



**DEPARTMENT OF DESIGN, MANUFACTURING AND  
ENGINEERING MANAGEMENT**

**Eta ( $\eta$ ) Phase Precipitation during Forging and Heat  
Treatment of ATI 718Plus<sup>®</sup>**

**Doctoral Thesis**

Engineering Doctorate in Advanced Manufacturing:  
Forging and Forming

**Bilal Hassan**

Registration Number: 201374736

**First academic supervisor:**  
**Second academic supervisor:**  
**Industrial supervisors:**

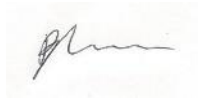
Professor Jonathan Corney  
Dr Salah Rahimi  
Mr Sebastien Nouveau and Dr Yann Jansen

## **Declaration of Authenticity and Author's Rights**

This thesis is the result of the author's original research. It has been composed by the author and has not been previously submitted for examination which has led to the award of a degree.

The copyright of this thesis belongs to the author under the terms of the United Kingdom Copyright Acts as qualified by University of Strathclyde Regulation 3.50. Due acknowledgement must always be made of the use of any material contained in, or derived from, this thesis.

Signed:

A handwritten signature in black ink, appearing to be 'J. M. ...', written on a light-colored rectangular background.

Dated: 04/06/2023

## **Abstract**

ATI 718Plus components are heat treated to optimised proportions of  $\gamma'$  and  $\eta$  phases.  $\eta$  phase is utilised in controlling the grain size during hot working processes. When  $\eta$  phase is fully solutioned, the grain size is free to increase, and the material properties can become detrimental.

In this study, the aims and objectives were to study the effect of strain and strain rate on the precipitation kinetics of  $\eta$  phase at a temperature range between 925°C to 975°C, at strains between 0 and 0.4 and strain rates of 0.1 s<sup>-1</sup> and 0.01 s<sup>-1</sup>. In addition, the effect of the initial grain size on  $\eta$  phase precipitation kinetics was also studied at the same temperature, strain and strain rate ranges. The  $\eta$  phase at the equilibrium state was studied too, at a temperature range of 850°C to 975°C.

TTT diagrams were produced for the  $\eta$  phase in strain-free recrystallised material, deformed material, and larger initial grain size material. Also, the equilibrium  $\eta$  phase content, aspect ratio, length and width were determined. The  $\eta$  phase precipitate aspect ratio, length and width were investigated in the strain-free recrystallised material and in the larger initial grain size material.

Some of the key findings that were observed were:

- Induced strain considerably hastens the  $\eta$  phase precipitation kinetics in comparison to that in the strain-free recrystallised material. No substantial difference was observed between the strain levels explored in this study. Increasing the strain rate has the effect of making the  $\eta$  phase precipitation kinetics faster in comparison to a slower strain rate.
- Increasing the initial grain size produces slower  $\eta$  phase precipitation kinetics, Interestingly, with the same study, incrementally increasing the strain also increases the  $\eta$  phase precipitation kinetics between the strain levels.

It is hoped that the findings from this study will assist in the manufacture of components made with ATI 718Plus with optimised microstructures fit for application.

## **Acknowledgements**

In the Name of God, the Most Beneficent, the Most Merciful.

All praise is due to God.

Firstly, I would like to thank my parents and wife as well as my family and in-laws for giving me all their love and support during this project. Without this and their encouragement, guidance and motivation, I would not have been able to follow my life ambitions and be where I am today. It is hard to imagine where I would be without them, and for this I am forever grateful.

My utmost thanks and appreciation go to Professor Jonathan Corney, Mr Sebastien Nouveau, Dr Yann Jansen, Dr Salah Rahimi and Dr Christian Dumont, who have assisted me throughout this project. I would also like to thank Mr Ryan O'Neill, Ms Kornelia Kondziolka, Mr Duncan Rodger and Ms Jacqueline Schramm who have helped me during the experimental stages of this project.

I also would like to give my thanks to my friends and colleagues from the AFRC who have encouraged and supported me along the way in this project.

# Table of Contents

<b>List of Tables and Figures .....</b>	<b>i</b>
<b>Nomenclature.....</b>	<b>x</b>
<b>1 Introduction.....</b>	<b>1</b>
1.1 Context .....	1
1.2 Background .....	2
1.3 Aims, Objectives and Scope.....	4
1.4 Structure of Thesis.....	5
<b>2 Literature Review.....</b>	<b>7</b>
2.1 Overview of Superalloys .....	7
2.1.1 <i>Background</i> .....	7
2.1.2 <i>Nickel Based Superalloys</i> .....	10
2.1.3 <i>Iron-Nickel Based Superalloys</i> .....	11
2.1.4 <i>Cobalt Based Superalloys</i> .....	12
2.1.5 <i>Applications of Superalloys</i> .....	12
2.2 Mechanisms of Property Improvement .....	14
2.2.1 <i>Strengthening Mechanisms</i> .....	14
2.2.2 <i>Creep and Fatigue Resistance</i> .....	23
2.2.3 <i>Role of Elements</i> .....	26
2.2.4 <i>Specific Strengthening Mechanisms of ATI 718Plus</i> .....	28
2.3 Phases .....	30
2.3.1 <i><math>\gamma</math> phase</i> .....	30
2.3.2 <i><math>\gamma'</math> phase</i> .....	31
2.3.3 <i><math>\gamma''</math> phase</i> .....	32
2.3.4 <i><math>\delta</math> phase</i> .....	34

2.3.5	<i>η phase</i> .....	37
2.3.6	<i>TCP phases</i> .....	44
2.4	Effect of Strain .....	45
2.5	Review of Precipitation Kinetics .....	48
2.6	Effect of Grain Boundary Precipitation on Mechanical Properties .....	50
2.7	Summary .....	52
<b>3</b>	<b>Experimental Methods .....</b>	<b>54</b>
3.1	Material .....	54
3.2	Mechanical Testing .....	54
3.3	Heat Treatment .....	56
3.4	Sample Preparation .....	57
3.5	Microscopy .....	60
3.6	Microstructural Analysis .....	62
<b>4</b>	<b>Precipitation at the Equilibrium State .....</b>	<b>63</b>
4.1	Introduction .....	63
4.2	Equilibrium Area Fraction .....	66
4.3	Aspect Ratio .....	70
4.4	Length .....	72
4.5	Thickness .....	73
4.6	Discussion .....	74
4.7	Summary .....	76
<b>5</b>	<b>Precipitation Kinetics in Strain-Free Recrystallised Microstructure .....</b>	<b>78</b>
5.1	Introduction .....	78
5.2	Area Fraction and TTT Diagram .....	82
5.3	Aspect Ratio, Length and Thickness .....	93
5.3.1	<i>Overall Data</i> .....	93

5.3.2	<i>Intergranular Data</i> .....	98
5.3.3	<i>Intragranular Data</i> .....	102
5.4	Discussion .....	106
5.4.1	<i>TTT Diagram</i> .....	106
5.4.2	<i>Aspect Ratio, Length and Thickness</i> .....	114
5.5	Summary .....	117
<b>6</b>	<b>Effect of Deformation on Precipitation Kinetics</b> .....	<b>119</b>
6.1	Introduction .....	119
6.2	Precipitation Kinetics at 0.1 s <sup>-1</sup> Strain Rate .....	123
6.3	Precipitation Kinetics at 0.01 s <sup>-1</sup> Strain Rate .....	131
6.4	Discussion .....	139
6.4.1	<i>Effect of Strain</i> .....	139
6.4.2	<i>Effect of Strain Rate</i> .....	144
6.4.3	<i>Effect of n and k Parameters</i> .....	145
6.5	Summary .....	152
<b>7</b>	<b>Effect of Initial Grain Size on Precipitation Kinetics</b> .....	<b>153</b>
7.1	Introduction .....	153
7.2	Precipitation Kinetics at 0.01 s <sup>-1</sup> Strain Rate.....	157
7.3	Aspect Ratio, Length and Thickness .....	164
7.4	Discussion .....	168
7.4.1	<i>Effect of Strain</i> .....	168
7.4.2	<i>Effect of Initial Grain Size</i> .....	169
7.4.3	<i>Aspect Ratio, Length and Thickness</i> .....	173
7.4.4	<i>Effect of n and k Parameters</i> .....	175
7.5	Summary .....	182
<b>8</b>	<b>Conclusions</b> .....	<b>183</b>

8.1	Introduction .....	183
8.2	Equilibrium Study .....	183
8.2.1	<i>Equilibrium Area Fraction</i> .....	183
8.2.2	<i>Aspect Ratio, Length and Thickness</i> .....	183
8.3	Recrystallised $\eta$ Phase Precipitation Kinetics .....	184
8.3.1	<i>TTT Diagram</i> .....	184
8.3.2	<i>Aspect Ratio, Length and Thickness</i> .....	184
8.4	Effect of Deformation on $\eta$ Phase Precipitation Kinetics .....	185
8.4.1	<i>Effect of Strain</i> .....	185
8.4.2	<i>Effect of Strain Rate</i> .....	186
8.4.3	<i>Effect of <math>n</math> and <math>k</math> Parameters</i> .....	186
8.5	Effect of Initial Grain Size on $\eta$ Phase Precipitation Kinetics .....	187
8.5.1	<i>Effect of Strain</i> .....	187
8.5.2	<i>Effect of Initial Grain Size</i> .....	187
8.5.3	<i>Aspect Ratio, Length and Thickness</i> .....	188
8.5.4	<i>Effect of <math>n</math> and <math>k</math> Parameters</i> .....	188
8.6	Future Work .....	189
	<b>References .....</b>	<b>191</b>



## List of Tables and Figures

<i>Figure 1.1 – Typical class of materials used in various parts of aerospace engine (1)</i> .....	1
<i>Figure 1.2 – Schematic diagram of the Brayton cycle. “C” is the compressor stage, “CC” is the combustion chamber and “T” is the turbine stage.....</i>	4
<i>Figure 2.1 – Process flow diagram for manufacturing nickel alloy products (10) .....</i>	9
<i>Figure 2.2 – Size factor of various elements for solid solution formation against atomic number (11).....</i>	15
<i>Figure 2.3 – Plan and side views of (a). before shearing and (b). after shearing (15)</i> .....	17
<i>Figure 2.4 - Schematic diagram displaying the morphological evolution of <math>\gamma'</math> as an increasing level of ageing (from (a) to (f)) (6).....</i>	18
<i>Figure 2.5 – (a). an ordered particle (b). sheared particle with new interfaces and anti-phase boundary (16).....</i>	20
<i>Figure 2.6 – Schematic diagram of the different stages in Orowan looping (15) ....</i>	22
<i>Figure 2.7 – Comparison between experimental data and calculations of yield strength (Orowan mechanism and precipitate shearing) (25).....</i>	29
<i>Figure 2.8 – Schematic diagram of the crystallographic and atomic structure of the <math>\gamma</math> phase (5).....</i>	31
<i>Figure 2.9 – Schematic diagram of the crystal structure of the <math>\gamma'</math> phase. (5).....</i>	32
<i>Figure 2.10 – Schematic diagram of the crystal structure of the <math>\gamma''</math> phase (42) .....</i>	33
<i>Figure 2.11 – Diagram displaying the prototype orthorhombic crystal structure of the <math>\delta</math> phase with nickel and niobium atom positions (31).....</i>	34
<i>Figure 2.12 – Schematic diagram displaying the globulisation mechanism of <math>\delta</math> phase (45).....</i>	35
<i>Figure 2.13 – Differences in precipitate morphology. Top: acicular precipitates, Bottom: globular precipitates (48).....</i>	36
<i>Figure 2.14 – Diagram displaying the prototype HCP crystal structure of the <math>\eta</math> phase with Ni, Nb and Al/Ti atom positions (30) .....</i>	39

<i>Figure 2.15 – Frequency of <math>\eta</math> phase precipitation with respect to grain boundary misorientation (66)</i> .....	40
<i>Figure 2.16 – Illustration displaying the stages of discontinuous precipitation (67)</i>	41
<i>Figure 2.17 – Concentration gradients for (a) diffusion through advancing grain boundary (b) diffusion across lattice in front of proceeding precipitate (67)</i> .....	42
<i>Figure 2.18 – Schematic diagram of the forces at the triple junction between the parent grain (<math>\gamma_1</math>), the neighbouring grain (<math>\gamma_2</math>), and the <math>\eta</math> phase precipitate (30)</i> .....	43
<i>Figure 2.19 – Microstructure containing <math>\eta</math> phase and <math>\gamma'</math> phase. <math>\gamma'</math> denuded zone can be observed around <math>\eta</math> precipitates (58)</i> .....	44
<i>Figure 2.20 – Growth and coarsening of <math>\delta</math> precipitates (a) 875°C at 100 s (b) 875°C at 1000 s (c) 975°C at 100 s (d) 975°C at 1000 s (73)</i> .....	47
<i>Figure 2.21 – Effect of cold rolling on the precipitation kinetics of <math>\delta</math> phase in Inconel 718 (71)</i> .....	48
<i>Figure 3.1 – Furnace, flat dies and test piece used in hot compression testing</i> .....	56
<i>Figure 3.2 – Carbolite RHF 1400 furnace chamber</i> .....	57
<i>Figure 3.3 – SimpliMet 3000 mounting machine</i> .....	58
<i>Figure 3.4 – EcoMet 300 Pro grinding/polishing machine</i> .....	59
<i>Figure 3.5 – FEI Quanta FEG 250 scanning electron microscope</i> .....	61
<i>Figure 4.1 – Tensile test sample prior to deformation with labelled working zone dimensions</i> .....	64
<i>Figure 4.2 – <math>\eta</math> phase area fraction against temperature in the equilibrium state</i> .....	66
<i>Figure 4.3 – Microstructure of ATI 718Plus at 0.1 strain with 0.00083 s<sup>-1</sup> strain rate and after heat treatment at 850°C for 75 hours</i> .....	67
<i>Figure 4.4 – Microstructure of ATI 718Plus at 0.1 strain with 0.00083 s<sup>-1</sup> strain rate and after heat treatment at 875°C for 75 hours</i> .....	67
<i>Figure 4.5 – Microstructure of ATI 718Plus at 0.1 strain with 0.00083 s<sup>-1</sup> strain rate and after heat treatment at 900°C for 72 hours</i> .....	68
<i>Figure 4.6 – Microstructure of ATI 718Plus at 0.1 strain with 0.00083 s<sup>-1</sup> strain rate and after heat treatment at 925°C for 74 hours</i> .....	68
<i>Figure 4.7 – Microstructure of ATI 718Plus at 0.1 strain with 0.00083 s<sup>-1</sup> strain rate and after heat treatment at 950°C for 72 hours</i> .....	69

<i>Figure 4.8 – Microstructure of ATI 718Plus at 0.1 strain with 0.00083 s<sup>-1</sup> strain rate and after heat treatment at 975°C for 72 hours</i> .....	69
<i>Figure 4.9 – <math>\eta</math> phase precipitate aspect ratio against temperature in the equilibrium state</i> .....	70
<i>Figure 4.10 – <math>\eta</math> phase precipitate length against temperature in the equilibrium state</i> .....	72
<i>Figure 4.11 – <math>\eta</math> phase precipitate thickness against temperature in the equilibrium state</i> .....	73
<i>Figure 4.12 – Equilibrium <math>\eta</math> phase area fraction compared to published data</i> .....	74
<i>Figure 4.13 – Equilibrium <math>\eta</math> phase area fraction compared to data from simulations</i> .....	75
<i>Figure 5.1 – EBSD grain size map of initial microstructure after solution heat treatment at 990°C after 180 minutes</i> .....	79
<i>Figure 5.2 – Example samples used in the strain-free precipitation kinetics study.</i> .	80
<i>Figure 5.3 – Schematic diagram of sample divided into three sections.</i> .....	80
<i>Figure 5.4 – <math>\eta</math> phase area fraction against time in strain-free material</i> .....	82
<i>Figure 5.5 – <math>\eta</math> phase area fraction against temperature in strain-free material</i> .....	82
<i>Figure 5.6 – Microstructure of ATI 718Plus in the as-received condition</i> .....	87
<i>Figure 5.7 – Microstructure of ATI 718Plus after heat treatment at 990°C for 180 minutes</i> .....	87
<i>Figure 5.8 – Microstructure of ATI 718Plus after heat treatment at 925°C after 30 minutes</i> .....	88
<i>Figure 5.9 – Microstructure of ATI 718Plus after heat treatment at 925°C after 60 minutes</i> .....	88
<i>Figure 5.10 – Microstructure of ATI 718Plus after heat treatment at 925°C after 180 minutes</i> .....	89
<i>Figure 5.11 – Microstructure of ATI 718Plus after heat treatment at 925°C after 720 minutes</i> .....	89
<i>Figure 5.12 – TTT diagram for 3% and 5% <math>\eta</math> phase area fractions in strain-free material, experimental values only</i> .....	91
<i>Figure 5.13 – TTT diagram for 3% and 5% <math>\eta</math> phase area fractions in strain-free material with modelling curves</i> .....	92

<i>Figure 5.14 – <math>\eta</math> phase precipitate aspect ratio against time in strain-free material .</i>	<i>94</i>
<i>Figure 5.15 – <math>\eta</math> phase precipitate length against time in strain-free material .....</i>	<i>96</i>
<i>Figure 5.16 – <math>\eta</math> phase precipitate thickness against time in strain-free material .....</i>	<i>97</i>
<i>Figure 5.17 – Areas of new precipitates in microstructure after heat treatment at 850°C for 720 mins .....</i>	<i>98</i>
<i>Figure 5.18 – <math>\eta</math> phase (intergranular) precipitate aspect ratio against time in strain-free material .....</i>	<i>99</i>
<i>Figure 5.19 – <math>\eta</math> phase (intergranular) precipitate length against time in strain-free material .....</i>	<i>100</i>
<i>Figure 5.20 – <math>\eta</math> phase (intergranular) precipitate thickness against time in strain-free material .....</i>	<i>101</i>
<i>Figure 5.21 – <math>\eta</math> phase (intragranular) precipitate aspect ratio against time in strain-free material .....</i>	<i>103</i>
<i>Figure 5.22 – <math>\eta</math> phase (intragranular) precipitate length against time in strain-free material .....</i>	<i>104</i>
<i>Figure 5.23 – <math>\eta</math> phase (intragranular) precipitate thickness against time in strain-free material .....</i>	<i>105</i>
<i>Figure 5.24 – Comparison with Casanova et al. (77) at 1% area fraction .....</i>	<i>107</i>
<i>Figure 5.25 – Comparison with Casanova et al. (77) at 4% area fraction .....</i>	<i>107</i>
<i>Figure 5.26 – Comparison with Cao (22) at 0.5% area fraction .....</i>	<i>110</i>
<i>Figure 5.27 – Comparison with Cao (22) at 2% area fraction .....</i>	<i>110</i>
<i>Figure 5.28 – Comparison with Cao (22) at 5% area fraction .....</i>	<i>111</i>
<i>Figure 5.29 – Comparison with Stotter et al. (85) at 2% area fraction .....</i>	<i>112</i>
<i>Figure 5.30 – Comparison with Radis et al. (36) at 2% area fraction .....</i>	<i>113</i>
<i>Figure 5.31 – Comparison with Radis et al. (36) at 5% area fraction .....</i>	<i>113</i>
<i>Figure 5.32 – Intergranular (solid) &amp; intragranular (dashed) precipitate aspect ratio .....</i>	<i>114</i>
<i>Figure 5.33 – Intergranular (solid) &amp; intragranular (dashed) precipitate length ..</i>	<i>115</i>
<i>Figure 5.34 – Intergranular (solid) &amp; intragranular (dashed) precipitate thickness .....</i>	<i>115</i>
<i>Figure 6.1 – Typical ATI 718Plus cylindrical test piece after heat treatment at 990°C for 180 minutes but prior to isothermal compression testing .....</i>	<i>120</i>

<i>Figure 6.2 – Sectioning of sample after isothermal compression testing .....</i>	<i>120</i>
<i>Figure 6.3 – Strain map at 0.6 global strain with 0.1 s<sup>-1</sup> strain rate .....</i>	<i>122</i>
<i>Figure 6.4 – Strain map at 0.6 global strain with 0.01 s<sup>-1</sup> strain rate .....</i>	<i>122</i>
<i>Figure 6.5 – η phase area fraction against time at 0.1 s<sup>-1</sup> strain rate for zero to 0.4 strain and for 900°C to 975°C .....</i>	<i>123</i>
<i>Figure 6.6 – η phase area fraction against temperature at 0.1 s<sup>-1</sup> strain rate for zero to 0.4 strain and for 30 mins to 720 mins .....</i>	<i>123</i>
<i>Figure 6.7 – η phase area fraction against time at 0.1 s<sup>-1</sup> strain rate for zero to 0.8 strain and at 950°C .....</i>	<i>127</i>
<i>Figure 6.8 – TTT diagrams for 5% η phase area fraction for strain-free material, 0.2 strain and 0.4 strain with 0.1 s<sup>-1</sup> strain rate.....</i>	<i>128</i>
<i>Figure 6.9 – Microstructure of ATI 718Plus at 0.2 strain with 0.1 s<sup>-1</sup> strain rate and after heat treatment at 950°C for 720 minutes .....</i>	<i>129</i>
<i>Figure 6.10 – Microstructure of ATI 718Plus at 0.4 strain with 0.1 s<sup>-1</sup> strain rate and after heat treatment at 950°C for 720 minutes .....</i>	<i>129</i>
<i>Figure 6.11 – Microstructure of ATI 718Plus at 0.6 strain with 0.1 s<sup>-1</sup> strain rate and after heat treatment at 950°C for 720 minutes .....</i>	<i>130</i>
<i>Figure 6.12 – Microstructure of ATI 718Plus at 0.8 strain with 0.1 s<sup>-1</sup> strain rate and after heat treatment at 950°C for 720 minutes .....</i>	<i>130</i>
<i>Figure 6.13 – η phase area fraction against time at 0.01 s<sup>-1</sup> strain rate for zero to 0.4 strain and for 900°C to 975°C .....</i>	<i>131</i>
<i>Figure 6.14 – η phase area fraction against temperature at 0.01 s<sup>-1</sup> strain rate for zero to 0.4 strain and for 30 mins to 720 mins .....</i>	<i>131</i>
<i>Figure 6.15 – η phase area fraction against time at 0.01 s<sup>-1</sup> strain rate for zero to 0.8 strain and at 950°C .....</i>	<i>135</i>
<i>Figure 6.16 – TTT diagrams for 5% η phase area fraction for strain-free material, 0.2 strain and 0.4 strain with 0.01 s<sup>-1</sup> strain rate.....</i>	<i>136</i>
<i>Figure 6.17 – Microstructure of ATI 718Plus at 0.2 strain with 0.01 s<sup>-1</sup> strain rate and after heat treatment at 950°C for 720 minutes .....</i>	<i>137</i>
<i>Figure 6.18 – Microstructure of ATI 718Plus at 0.4 strain with 0.01 s<sup>-1</sup> strain rate and after heat treatment at 950°C for 720 minutes .....</i>	<i>138</i>

<i>Figure 6.19 – Microstructure of ATI 718Plus at 0.6 strain with 0.01 s<sup>-1</sup> strain rate and after heat treatment at 950°C for 720 minutes</i> .....	138
<i>Figure 6.20 – Microstructure of ATI 718Plus at 0.8 strain with 0.01 s<sup>-1</sup> strain rate and after heat treatment at 950°C for 720 minutes</i> .....	139
<i>Figure 6.21 – TTT diagrams for 5% η phase area fraction for strain-free material, 0.2 strain and 0.4 strain with 0.1 s<sup>-1</sup> and 0.01 s<sup>-1</sup> strain rates</i> .....	144
<i>Figure 6.22 – ln – ln1 – yfeq vs time at 950°C and at 0.1 s<sup>-1</sup> strain rate</i> .....	146
<i>Figure 6.23 – ln – ln1 – yfeq vs time at 950°C and at 0.01 s<sup>-1</sup> strain rate</i> .....	146
<i>Figure 6.24 – The value of n against strain with 0.1 s<sup>-1</sup> strain rate</i> .....	147
<i>Figure 6.25 – The value of n against strain with 0.01 s<sup>-1</sup> strain rate</i> .....	148
<i>Figure 6.26 – The value of ln(k) against 1/T for 0.1 s<sup>-1</sup> strain rate</i> .....	149
<i>Figure 6.27 – The value of ln(k) against 1/T for 0.01 s<sup>-1</sup> strain rate</i> .....	150
<i>Figure 7.1 – EBSD grain size map of initial microstructure after solution heat treatment at 1010°C after 180 minutes</i> .....	154
<i>Figure 7.2 – Torsion test strain map at 0.6 global strain with 0.01 s<sup>-1</sup> strain rate (middle cut)</i> .....	155
<i>Figure 7.3 – Torsion test strain map at 0.6 global strain with 0.01 s<sup>-1</sup> strain rate (end cut)</i> .....	155
<i>Figure 7.4 – η phase area fraction against time at 0.01 s<sup>-1</sup> strain rate for zero to 0.4 strain and for 900°C to 975°C</i> .....	157
<i>Figure 7.5 – η phase area fraction against temperature at 0.01 s<sup>-1</sup> strain rate for zero to 0.4 strain and for 30 mins to 720 mins</i> .....	157
<i>Figure 7.6 – TTT diagrams for 5% η phase area fraction for material with larger initial grain size (LIGS) at zero strain, 0.2 strain and 0.4 strain with 0.01 s<sup>-1</sup> strain rate</i> .....	161
<i>Figure 7.7 – Microstructure of ATI 718Plus at zero strain with 0.01 s<sup>-1</sup> strain rate and after heat treatment at 950°C for 720 minutes and with larger initial grain size</i> ...	162
<i>Figure 7.8 – Microstructure of ATI 718Plus at 0.2 strain with 0.01 s<sup>-1</sup> strain rate and after heat treatment at 950°C for 720 minutes and with larger initial grain size</i> ...	163
<i>Figure 7.9 – Microstructure of ATI 718Plus at 0.4 strain with 0.01 s<sup>-1</sup> strain rate and after heat treatment at 950°C for 720 minutes and with larger initial grain size</i> ...	163
<i>Figure 7.10 – η phase precipitate aspect ratio against time in larger initial grain size material at zero strain</i> .....	164

<i>Figure 7.11 – <math>\eta</math> phase precipitate length against time in larger initial grain size material at zero strain</i> .....	166
<i>Figure 7.12 – <math>\eta</math> phase precipitate thickness against time in larger initial grain size material at zero strain</i> .....	167
<i>Figure 7.13 – <math>\eta</math> phase area fraction against time at 900°C for as-received initial grain size material and larger initial grain size material (LIGS)</i> .....	170
<i>Figure 7.14 – <math>\eta</math> phase area fraction against time at 925°C for as-received initial grain size material and larger initial grain size material (LIGS)</i> .....	170
<i>Figure 7.15 – <math>\eta</math> phase area fraction against time at 950°C for as-received initial grain size material and larger initial grain size material (LIGS)</i> .....	171
<i>Figure 7.16 – <math>\eta</math> phase area fraction against time at 975°C for as-received initial grain size material and larger initial grain size material (LIGS)</i> .....	171
<i>Figure 7.17 – TTT diagrams for 5% <math>\eta</math> phase area fraction comparing as-received initial grain size material with larger initial grain size material (LIGS)</i> .....	172
<i>Figure 7.18 – <math>\eta</math> phase aspect ratio against time for as-received initial grain size material and larger initial grain size material (LIGS)</i> .....	173
<i>Figure 7.19 - <math>\eta</math> phase length against time for as-received initial grain size material and larger initial grain size material (LIGS)</i> .....	173
<i>Figure 7.20 - <math>\eta</math> phase thickness against time for as-received initial grain size material and larger initial grain size material (LIGS)</i> .....	174
<i>Figure 7.21 – <math>\ln - \ln 1 - yfeq</math> vs time at 950°C and at 0.01 s<sup>-1</sup> strain rate with larger initial grain size</i> .....	176
<i>Figure 7.22 – The n-value against strain with 0.01 s<sup>-1</sup> strain rate and with larger initial grain size</i> .....	177
<i>Figure 7.23 – n against strain for material with larger initial grain size (LIGS) and smaller initial grain size</i> .....	178
<i>Figure 7.24 – The value of <math>\ln(k)</math> against 1/T for material with larger initial grain size</i> .....	179
<i>Figure 7.25 – <math>\ln(k)</math> against 1/T for material with larger initial grain size (LIGS) and smaller initial grain size</i> .....	180
 <i>Table 2.1 – List of superalloy components used in different industries (5)</i> .....	13

<i>Table 2.2 – Microstructural effects from elements (5).....</i>	<i>27</i>
<i>Table 2.3 – Chemistry comparison between Inconel 718 and ATI 718Plus with key differences highlighted in yellow (22).....</i>	<i>27</i>
<i>Table 3.1 – Chemical composition of as-received ATI 718Plus material.....</i>	<i>54</i>
<i>Table 3.2 – Grinding procedure used for ATI 718Plus .....</i>	<i>60</i>
<i>Table 3.3 – Polishing procedure used for ATI 718Plus.....</i>	<i>60</i>
<i>Table 4.1 – Experimental matrix for <math>\eta</math> phase precipitation at the equilibrium state.</i>	<i>64</i>
<i>Table 4.2 – Results of <math>\eta</math> phase area fraction in the equilibrium state .....</i>	<i>66</i>
<i>Table 4.3 – Numerical results of <math>\eta</math> phase aspect ratio in the equilibrium state .....</i>	<i>70</i>
<i>Table 4.4 – Numerical results of <math>\eta</math> phase length in the equilibrium state .....</i>	<i>72</i>
<i>Table 4.5 – Results of <math>\eta</math> phase thickness in the equilibrium state.....</i>	<i>73</i>
<i>Table 5.1 – Experimental matrix for <math>\eta</math> phase precipitation kinetics in strain free material .....</i>	<i>78</i>
<i>Table 5.2 – <math>\eta</math> phase precipitation kinetics in strain-free material.....</i>	<i>83</i>
<i>Table 5.3 – Adjusted <math>R^2</math> values for Equations 5.2 to 5.7.....</i>	<i>86</i>
<i>Table 5.4 – Calculated time taken to precipitate 3% and 5% area fractions at each temperature .....</i>	<i>91</i>
<i>Table 5.5 – Results of strain-free <math>\eta</math> phase precipitate aspect ratio .....</i>	<i>94</i>
<i>Table 5.6 – Results of strain-free <math>\eta</math> phase precipitate length .....</i>	<i>96</i>
<i>Table 5.7 – Results of strain-free <math>\eta</math> phase precipitate thickness.....</i>	<i>97</i>
<i>Table 5.8 – Results of strain-free <math>\eta</math> phase precipitate aspect ratio (intergranular) ..</i>	<i>99</i>
<i>Table 5.9 – Results of strain-free <math>\eta</math> phase precipitate length (intergranular) .....</i>	<i>101</i>
<i>Table 5.10 – Results of strain-free <math>\eta</math> phase precipitate thickness (intergranular) ..</i>	<i>102</i>
<i>Table 5.11 – Results of strain-free <math>\eta</math> phase precipitate aspect ratio (intragranular) .....</i>	<i>103</i>
<i>Table 5.12 – Results of strain-free <math>\eta</math> phase precipitate length (intragranular).....</i>	<i>104</i>
<i>Table 5.13 – Results of strain-free <math>\eta</math> phase precipitate thickness (intragranular) ..</i>	<i>105</i>
<i>Table 6.1 – Experimental matrix for <math>\eta</math> phase precipitation kinetics in deformed strained material .....</i>	<i>121</i>
<i>Table 6.2 – <math>\eta</math> phase precipitation kinetics at 0.2 strain with <math>0.1\text{ s}^{-1}</math> strain rate.....</i>	<i>124</i>
<i>Table 6.3 – <math>\eta</math> phase precipitation kinetics at 0.4 strain with <math>0.1\text{ s}^{-1}</math> strain rate.....</i>	<i>124</i>
<i>Table 6.4 – Adjusted <math>R^2</math> values for Equation 6.1 to Equation 6.8 .....</i>	<i>126</i>



<i>Table 6.5 – <math>\eta</math> phase precipitation kinetics at 950°C with 0.1 s<sup>-1</sup> strain rate.....</i>	127
<i>Table 6.6 – <math>\eta</math> phase precipitation kinetics at 0.2 strain with 0.01 s<sup>-1</sup> strain rate.....</i>	132
<i>Table 6.7 – <math>\eta</math> phase precipitation kinetics at 0.4 strain with 0.01 s<sup>-1</sup> strain rate.....</i>	132
<i>Table 6.8 – Adjusted R<sup>2</sup> values for Equation 6.11 to Equation 6.18 .....</i>	134
<i>Table 6.9 – <math>\eta</math> phase precipitation kinetics at 950°C with 0.01 s<sup>-1</sup> strain rate.....</i>	135
<i>Table 6.10 – Values of a<sub>1</sub>, b<sub>1</sub> and adjusted R<sup>2</sup> for Equation 6.22 at 0.1 s<sup>-1</sup> strain rate .....</i>	148
<i>Table 6.11 – Values of a<sub>1</sub>, b<sub>1</sub> and adjusted R<sup>2</sup> for Equation 6.22 at 0.01 s<sup>-1</sup> strain rate .....</i>	149
<i>Table 6.12 – Values of E<sub>a</sub> for each strain and strain rate with adjusted R<sup>2</sup> values .</i>	152
<i>Table 7.1 – Experimental matrix for <math>\eta</math> phase precipitation kinetics in material with larger initial grain size .....</i>	156
<i>Table 7.2 – <math>\eta</math> phase precipitation kinetics at 0.0 strain with 0.01 s<sup>-1</sup> strain rate.....</i>	158
<i>Table 7.3 – <math>\eta</math> phase precipitation kinetics at 0.2 strain with 0.01 s<sup>-1</sup> strain rate.....</i>	158
<i>Table 7.4 – <math>\eta</math> phase precipitation kinetics at 0.4 strain with 0.01 s<sup>-1</sup> strain rate.....</i>	158
<i>Table 7.5 – Adjusted R<sup>2</sup> values for Equation 7.1 to Equation 7.12 .....</i>	161
<i>Table 7.6 – Results of <math>\eta</math> phase precipitate aspect ratio in larger initial grain size material at zero strain.....</i>	165
<i>Table 7.7 – Results of <math>\eta</math> phase precipitate length in larger initial grain size material at zero strain .....</i>	166
<i>Table 7.8 – Results of <math>\eta</math> phase precipitate thickness in larger initial grain size material at zero strain .....</i>	167
<i>Table 7.9 – Values of a<sub>1</sub>, b<sub>1</sub> and adjusted R<sup>2</sup> for material with larger initial grain size .....</i>	178
<i>Table 7.10 – Values of E<sub>a</sub> for the larger initial grain size material for each strain at 0.01 s<sup>-1</sup> strain rate with adjusted R<sup>2</sup> values.....</i>	181

## Nomenclature

a	Constant related to nucleation
a <sub>1</sub>	Constant
ASTM	American Society for Testing and Materials
b	Width or breadth (also constant related to the growth kinetics of the $\eta$ phase)
b <sub>1</sub>	Constant
BCC	Body centred cubic
BCT	Body centred tetragonal
C	Specific heat generalised constant
CO <sub>2</sub>	Carbon dioxide
d	Grain diameter
D <sub>gb</sub>	Grain boundary diffusion coefficient
D0 <sub>a</sub>	Strukturbericht designation of crystal structure
D0 <sub>22</sub>	Strukturbericht designation of crystal structure
D0 <sub>24</sub>	Strukturbericht designation of crystal structure
d <sub>i</sub>	Diameter of elemental atom
d <sub>Ni</sub>	Diameter of nickel atom
D <sub>v</sub>	Lattice diffusion coefficient
E	Modulus of elasticity for axial loading (Young's modulus)
E <sub>A</sub>	Apparent activation energy
EBSD	Electron backscattered diffraction
f	Volume fraction of dispersed phase
FCC	Face centred cubic
f <sub>eq</sub>	$\eta$ phase area fraction at the thermodynamic equilibrium
F <sub>1</sub>	Complex function of stacking fault width and particle size
G	Modulus of elasticity in shear (modulus of rigidity)
$\Delta G$	Difference in shear modulus between particle phase and matrix phase
HCP	Hexagonal close packed

k	Boltzmann's constant (also time independent coefficient)
$k_0$	Frequency factor
$k(\alpha)$	Partial dislocation separating force times the separation distance
LIGS	Larger initial grain size
MPa	Megapascals
n	Time independent coefficient
ODS	Oxide Dispersion Strengthening
r	Radius
R	Universal gas constant
$R^2$	Coefficient of determination
SEM	Scanning electron microscope
$S_m$	Stacking fault energy in matrix
$S_p$	Stacking fault energy in particle
t	Time
T	Temperature
TCP	Topologically closed packed phases
$T_{melt}$	Melting temperature
$T_{oper}$	Operating temperature
TTT	Time Temperature Transformation
y	$\eta$ phase area fraction percentage
$\beta$	Numerical constant
$\gamma$	Gamma
$\gamma'$	Gamma prime
$\gamma''$	Gamma double prime
$\gamma_{apb}$	Anti-phase boundary energy
$\gamma_s$	Particle-matrix surface energy
$\gamma_1$	Parent grain
$\gamma_2$	Neighbouring grain
$\delta$	Delta
$\varepsilon$	Measure of the strain field

$\dot{\epsilon}_s$	Minimum creep rate
$\eta$	Eta
$\eta_{\text{solv}}$	$\eta$ phase solvus temperature
$\theta$	Contact angle
$\mu$	Mu phase
$\sigma$	Strain (also Sigma phase)
$\sigma_{\eta\gamma 1}$	Interfacial energy between $\eta$ precipitate and parent grain
$\sigma_{\eta\gamma 2}$	Interfacial energy between $\eta$ precipitate and neighbouring grain
$\sigma_{\gamma 1\gamma 2}$	Interfacial energy between parent grain and neighbouring grain
$\Delta\sigma$	Strain field
$\tau$	Stress (also time in hours)

# 1 Introduction

## 1.1 Context

Modern aircraft engines have to be designed so that they can aim to achieve the highest levels in terms of reliability, weight, performance, low carbon emissions, and general service life. The materials that are used in today's aircraft engines play a very important role in achieving these high standards. Figure 1.1 shows the typical class of materials that are generally used for various sections of the aerospace engine.

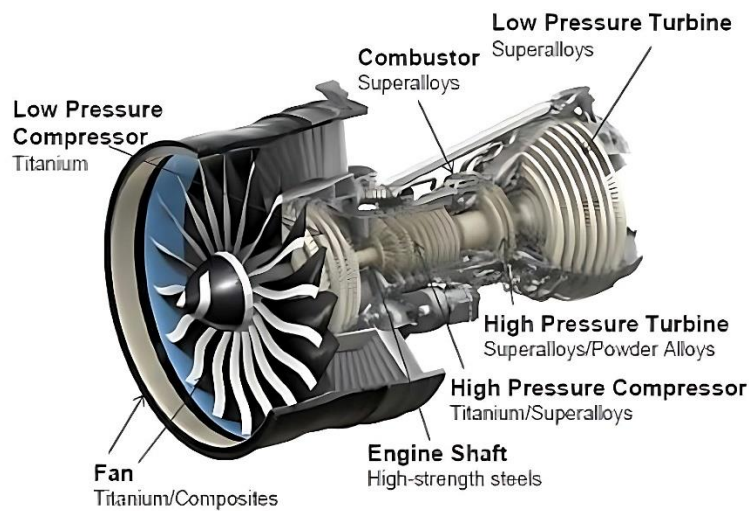


*Figure 1.1 – Typical class of materials used in various parts of aerospace engine (1)*

Aerospace materials are used in billet or bar form initially before they are put through high temperature manufacturing processes (such as closed die forging, super plastic forming, and ring rolling to name a few) so that actual components can be produced from the original billet or bar. The reason why these manufacturing processes are performed at high temperature is because phase transformations take place within the microstructure of the material. This has a great impact on the final mechanical properties of the component being produced. Different experimental parameter values have different effects on the microstructure of the material, which leads to differences in the mechanical properties. Another reason why manufacturing processes occur at high temperature is due to the easier formability of metals as the temperature increases.

Therefore, it is imperative during the high temperature manufacturing stage that the correct parameters (e.g., temperature, load, strain rate) are used so that the most suitable microstructure is obtained. This leads to the acquisition of the desired properties of the final component. Sometimes, further heat treatments are required after high temperature processes in order to optimise the microstructure. This is the case with some nickel superalloys, in which further heat treatments are necessary after forging to obtain the optimum proportions of  $\delta$  (delta) and  $\gamma''$  (gamma double prime) phases.

If the wrong parameters are used during the high temperature manufacturing process, the microstructure obtained would be deficient and would compromise the mechanical properties of the material. In safety critical applications such as aerospace or marine applications, this compromise is unacceptable. Therefore, it is crucial to understand and characterise the microstructural transformations that alloys go through during the high temperature manufacturing process so that the mechanical properties of the material can be optimised.

Suitable materials need to be utilised at the turbine stage of the aircraft engine so that the high temperatures (that come from the combustor) can be safely handled. The use of ATI 718Plus<sup>®</sup> (hereafter referred to as ATI 718Plus) allows for higher efficient engines to be designed and manufactured due to the maximum temperature advantage it possesses. Some engine manufacturers are currently considering implementing ATI 718Plus into use within their current production of aerospace engines.

## **1.2 Background**

ATI 718Plus is a relatively new nickel superalloy that has been developed by Allegheny Technologies Incorporated. It was designed to improve and replace its predecessor material Inconel<sup>®</sup> 718 (hereafter referred to as IN 718) in applications including aerospace gas turbine engines and power generation engines. More specifically, it is a very good candidate material for implementation as static and rotating structural components within aerospace gas engines. It also has many

advantages over IN 718 in terms of mechanical properties and process ability. The aerospace engine parts that could be produced from ATI 718Plus include (1):

- Cases and rings
- Discs
- Structural casings
- Blades
- Fasteners
- Sheet fabrications

However, one of the most important advantages of ATI 718Plus is that the maximum temperature that it can be used at is 55°C greater than that of IN 718 (2,3). ATI 718Plus can be used at up to 704°C whereas IN 718 is restricted to 649°C (2). This is due to the characteristic primary strengthening phase in both materials. Within IN 718, the primary strengthening phase is the  $\gamma''$  phase, whereas in the case of ATI 718Plus, the phase responsible for its primary strengthening is the gamma prime ( $\gamma'$ ) phase.

Above each phases' particular temperature limit, the phase begins to transform into a secondary phase. For IN 718, the  $\gamma''$  phase transforms into the  $\delta$  phase, whereas in the case of ATI 718Plus, the  $\gamma'$  phase transforms into the eta ( $\eta$ ) phase. Both the  $\eta$  phase and the  $\delta$  phase are advantageous (at low area fractions) for controlling grain growth, as well as improving notch sensitivity; however, they intrinsically possess less strength than the primary strengthening phases in their respective alloys. Therefore, they reduce the strength of the alloy in which they precipitate in. However, a trade off needs to be achieved between strength, grain size and notch sensitivity, and hence for the case of ATI 718Plus, a correct balance of  $\eta$  phase and  $\delta$  phase needs to be obtained.

It is well known that increasing the turbine entry temperature (i.e., the temperature at Stage 3 in Figure 1.2) has the effect of increasing the thermodynamic efficiency ( $\eta_{th}$ ) of an aerospace gas engine. This is the reason why the difference in maximum temperature capability is an important advantage for ATI 718Plus.

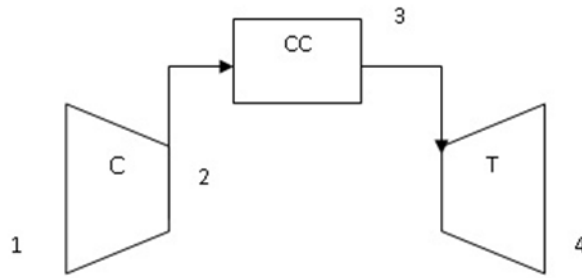


*Figure 1.2 – Schematic diagram of the Brayton cycle. “C” is the compressor stage, “CC” is the combustion chamber and “T” is the turbine stage*

By using materials that allow for higher temperatures to be used within the aerospace engine, the overall thermodynamic efficiency of the engine can be increased. Therefore, the implementation of ATI 718Plus will allow aerospace engines to have higher thermodynamic efficiency in comparison to engines with parts made from IN 718. This provides advantages for airline operators in the form of savings on fuel costs. Also, as controls for CO<sub>2</sub> emissions become more stringent and concerning, using materials such as ATI 718Plus could be beneficial for engine manufacturers in order to meet environmental standards.

### **1.3 Aims, Objectives and Scope**

The aim of this study is to characterise and analyse the precipitation behaviour of  $\eta$  phase during forging and heat treatment. To meet this aim, the following objectives are defined and will be studied:

1.  $\eta$  phase precipitation at the equilibrium state
2.  $\eta$  phase precipitation kinetics in the strain-free recrystallised state
3. Effect of deformation on  $\eta$  phase precipitation kinetics
4. Effect of initial grain size on  $\eta$  phase precipitation kinetics

Various strains will be investigated as well as different strain rates. In order to characterise the  $\eta$  phase precipitation, equations will be obtained to model the  $\eta$  phase behaviour for a particular temperature, strain and strain rate. From these equations, a set of TTT (Time-Temperature-Transformation) graphs can be produced for both



strain-free and strained conditions. From these graphs, approximate modelling equations can be fitted on to the TTT graphs, which would therefore provide a method of estimating the time taken precipitate a certain area fraction of  $\eta$  phase at different temperatures, strains and strain rates. The maximum amount of  $\eta$  phase precipitation from experimental results will be compared to results from simulations and current literature. Also, the effects of initial grain size on the  $\eta$  phase precipitation kinetics will be explored.

All the above constitutes the scope of this project. However, the industrial application of these findings is not included in the scope of this project and is suggested for potential future work.

#### **1.4 Structure of Thesis**

The context and background, as well as the aims and objectives of this study are presented in this introductory chapter (Chapter 1).

Chapter 2 presents and discusses elementary metallurgical concepts, such as the basic metallurgy of ATI 718Plus and other nickel superalloys, as well as a review of the current literature regarding the precipitation kinetics of ATI 718Plus and similar nickel superalloys and the impact of grain boundary precipitation on the mechanical properties.

In Chapter 3, the various experimental techniques and processes that were employed in this study are described.

In Chapter 4, a study is presented to show the maximum possible area fraction of  $\eta$  phase, or otherwise known as the equilibrium area fraction, at different temperatures.

Chapter 5 describes the  $\eta$  phase kinetics of recrystallised strain-free ATI 718Plus material.

In Chapter 6, the precipitation kinetics of  $\eta$  phase is presented for deformed strained ATI 718Plus material.

In Chapter 7, the effect of different initial grain size on the precipitation kinetics of  $\eta$  phase is investigated.

Chapter 8 concludes the thesis by presenting the final conclusions from the study as well as including the final remarks of the thesis.

## **2 Literature Review**

### **2.1 Overview of Superalloys**

In this section, an overall general perspective of superalloys is provided, which includes the background of superalloys, their categorisation and also their applications in the real world.

#### **2.1.1 Background**

The development of superalloys came about in the early 1940's (4) as a response for the demand for materials that would be able to withstand the high temperature and demanding conditions in aircraft engine gas turbines. The materials available at this time were not good enough to be used and so there was a requirement for materials with improved properties (4). These properties included higher strength, greater corrosion resistance and enhanced creep and fatigue properties at higher temperatures. In the beginning, attempts were made to achieve these improved properties through enhancements made in stainless steels (4), since these were the leading high temperature alloys at the time. Further advancements were then made by the development of nickel, iron-nickel and cobalt superalloys which were intended for operating temperatures exceeding 540°C (5).

There are three distinct characteristics that constitute a 'high temperature material'. These are (6):

1. "An ability to withstand loading at an operating temperature close to its melting point" (in this case of ATI 718Plus, up to the  $\gamma'$  solvus temperature)
2. "A substantial resistance to mechanical degradation over extended periods of time"
3. "Tolerance of severe operating environments"

Regarding the first characteristic, for materials to be classed as being 'high temperature materials', a particular criterion has to be satisfied. This criterion states that if the ratio

of the operating temperature ( $T_{oper}$ , in Kelvin) to the material melting point ( $T_{melt}$ , in Kelvin) is greater than or equal to 0.6, then the material can be categorised as a 'high temperature material' (6). In mathematical terms:

$$\frac{T_{oper}}{T_{melt}} = 0.6$$

ATI 718Plus has a melting temperature range between 1533 K (1260°C) and 1616 K (1343°C) (7,8). The operating temperature is 977 K (704°C) (9). This means that the ratio of operating temperature to melting temperature ranges from 0.605 to 0.637, which clearly places ATI 718Plus as a high temperature material since it satisfies the aforementioned criteria.

Secondly, high temperature materials must be designed such that they are particularly creep resistant, i.e. they are resistant to time-dependant, plastic and irretrievable deformation (6). This is very important in safety critical applications.

Thirdly (and finally), severe operating environments must be tolerated. For example, corrosive fuels, lubricants and liquids must have a minimal impact on the high temperature material. Environments that promote oxidation, surface degradation or any microstructural mechanism that can reduce component life should be tolerated by the material (6).

Figure 2.1 (10) displays the general process flow diagram for the manufacture of nickel alloys in its various final product forms. As it can be observed, the route of manufacturing nickel alloy products involves a large number of technological processes. The final product form of superalloys are usually available as three types (10):

1. Rod, bar, sections, and wire products
2. Plate, strip, and sheet products
3. Tubing products

Since the original superalloy invention, many superalloys with different chemical compositions have been designed and produced. Most of these have been patented by their creators and are usually produced with specific properties in mind to target (5).

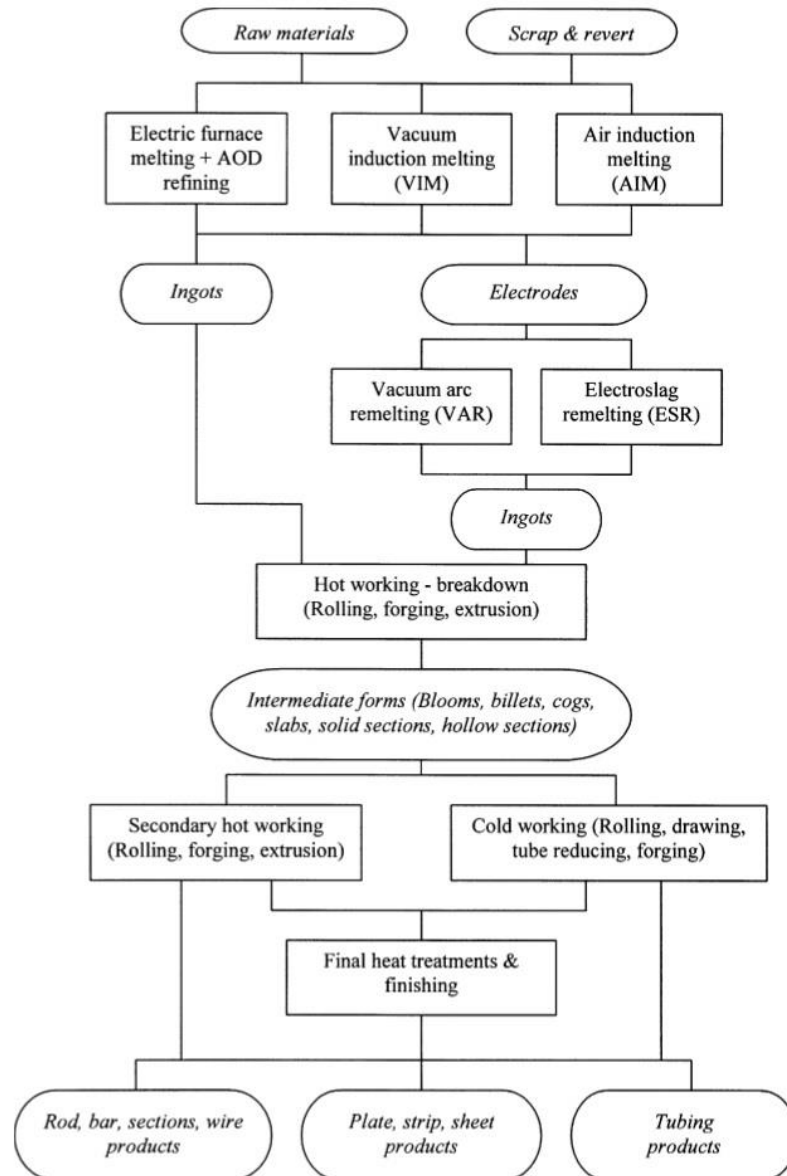


Figure 2.1 – Process flow diagram for manufacturing nickel alloy products (10)

As well as being categorised into different final product form, superalloys can also be divided into three main groups depending on the elements that are fundamentally used to produce the superalloy, and which are present in significantly high concentrations. These groups are (5):

- Nickel based superalloys
- Iron-nickel based superalloys
- Cobalt based superalloy

The following sections in this sub-chapter will describe these main superalloy groups. This is followed by a description of the general applications that superalloys are implemented in.

### 2.1.2 Nickel Based Superalloys

The majority of nickel-based superalloys are primarily strengthened by the precipitation of intermetallic compounds within an austenitic face centred cubic (FCC) matrix. This is achieved through the use of the elements aluminium, titanium and niobium. (4). These three elements are used to produce two different principal strengthening precipitates, namely  $\gamma'$  and  $\gamma''$ . These phases are explained in more detail in Section 2.3.2 and Section 2.3.3 respectively. However, there are some nickel based superalloys which are primarily strengthened through solid solution hardening and there also exists another group of nickel based superalloys which are strengthened by oxide dispersion (5). Hence, nickel-based superalloys could be classified into three main groups:

1. Precipitation strengthened
  - a.  $\gamma'$  strengthened
  - b.  $\gamma''$  strengthened
2. Solid solution strengthened
3. Oxide dispersion strengthened (ODS)

One subgroup of precipitation strengthened nickel based superalloys are those that primarily strengthened by the  $\gamma'$  phase (5). Examples of  $\gamma'$  strengthened nickel based superalloys include Waspaloy, Astroloy, U-700 and U-720 (5). ATI 718Plus also belongs within this group since it is also primarily strengthened via the  $\gamma'$  phase (4). Another group of precipitation strengthened nickel-based superalloys are those that are principally strengthened by the  $\gamma''$  phase. An example of a superalloy which is

principally strengthened by  $\gamma''$  is IN 718 (5), which is very well known and is commonly used in many applications. In addition, some nickel-based superalloys are strengthened by both  $\gamma'$  and  $\gamma''$  phase. Examples of such superalloys include IN 706 and IN 909. Due to the high iron content within IN 718, IN 706 and IN 909, they are sometimes classed as iron-nickel based superalloys (4,5).

The second type of nickel-based superalloys are those that are mainly strengthened by solid solution strengthening. Examples of such superalloys include Hastelloy X and IN 625. This group of superalloys can also obtain further strengthening via the precipitation of carbides and intermetallic compounds (5). Therefore, the strengthening mechanisms are a combination of solid solution strengthening, carbides, and intermetallic precipitates.

As for the third type, known as oxide dispersion strengthened (ODS) superalloys, these superalloys are strengthened via the dispersion of inert particles such as yttria. Examples of these unique superalloys include IN-MA-754 and IN-MA-6000E. Some superalloys within this class can also be strengthened in combination with  $\gamma'$ , as is the case with the superalloy IN-MA-6000E (5).

### 2.1.3 Iron-Nickel Based Superalloys

Another category of superalloys is those that contain significant proportions of both iron and nickel. Similarly, to nickel-based superalloys, the iron-nickel superalloys can also be divided into two main groups:

1. Precipitation strengthened
2. Solid solution strengthened

The most significant iron-nickel superalloys are those that are strengthened via the precipitation of intermetallic compounds, more commonly being the  $\gamma'$  phase. Examples include A-286, V-57 and Incoloy 901. Some iron-nickel based superalloys are essentially improved forms of stainless steels which are strengthened via solid solution strengthening (5).

#### 2.1.4 Cobalt Based Superalloys

Cobalt based superalloys are always strengthened through the use of solid solution strengthening and the precipitation of carbides. Strengthening by intermetallic compound precipitation is not a mechanism that exists in cobalt-based superalloys. An intermetallic precipitate which has the same usefulness as the  $\gamma'$  phase has never been found in cobalt-based superalloy systems. They are manufactured in both cast and wrought forms, X-40 being in cast form and L-605 being in wrought form (5).

#### 2.1.5 Applications of Superalloys

Superalloys are implemented in the form of components for a wide and broad range of applications such as aerospace engines, power generation engines, and chemical/petrochemical plants to name a few. As superalloys are high temperature and high strength materials, they are often used as parts within the hot sections of gas turbine engines. However, that being said, not all superalloy applications require high temperature strength properties. Due to the good corrosion resistance of superalloys, it has been possible to implement particular grades of superalloys within biomedical devices. There are also cryogenic applications for superalloys (5).

Figure 1.1 (1) shows the class of materials that are used as different components within the aerospace engine. As mentioned previously, superalloys are used extensively in the hot parts of the aerospace engine. This includes the:

- High pressure compressor
- Combustor
- High pressure turbine
- Low pressure turbine

Table 2.1 (5) lists many of the widespread uses of superalloys in terms of the components that are manufactured from them, along with the industries that these superalloy components are employed in.



<b><u>Industry</u></b>	<b><u>Components</u></b>
Aircraft/industrial gas turbine components	Disks
	Bolts
	Shafts
	Cases
	Blades
	Vanes
	Combustors
	Afterburners
	Thrust reversers
Steam turbine power plant components	Bolts
	Blades
	Stack-gas reheaters
Selected automotive components	Turbochargers
	Exhaust valves
Metal processing	Hot work tools and dies
	Casting dies
Medical components	Dentistry
	Prosthetic devices
Space vehicle components	Aerodynamically heated skins
	Rocket engine parts
Heat treating equipment	Trays
	Fixtures
	Conveyor belts
Nuclear power systems	Control-rod drive mechanisms
	Valve stems
	Springs
	Ducting
Chemical and petrochemical industries	Bolts
	Valves
	Reaction vessels
	Piping
	Pumps

*Table 2.1 – List of superalloy components used in different industries (5)*

## 2.2 Mechanisms of Property Improvement

Within this section, some of the mechanisms of how superalloys are strengthened are explained, which includes solid solution hardening and precipitation strengthening. This section also describes the mechanisms by which fatigue and creep properties are derived from. Also, the specific role that elements have in improving the material microstructure and properties are shown. Lastly, the specific strengthening mechanisms that are used with ATI 718Plus are mentioned in light of the available literature.

### 2.2.1 Strengthening Mechanisms

#### 1. Solid Solution Hardening

The primary purpose of solid solution hardening elements is to build strength into the parent matrix phase of the superalloy. The element nickel has an extensive range of solubility, and it can alloy with most metallic elements. Tungsten, molybdenum, titanium, tantalum, niobium, vanadium, rhenium, and technetium are elements that have favourable characteristics for strengthening the  $\gamma$  matrix phase via solid solution hardening (11). Also, chromium and cobalt are also used for the purpose of solid solution strengthening (12). The difference in atomic diameter of the aforementioned elements in comparison to nickel causes a lattice expansion in the  $\gamma$  matrix which in turn causes it to strengthen.

The size factor function describes the solubility of any particular element  $i$  in nickel, which is shown below in Equation 2.1 (11).

$$\text{Size factor} = \frac{100(d_i - d_{Ni})}{d_{Ni}} \quad \text{Equation 2.1}$$

The size factor for a particular element  $i$  that results from Equation 2.1 can be plotted against its atomic number, which is shown below in Figure 2.2.

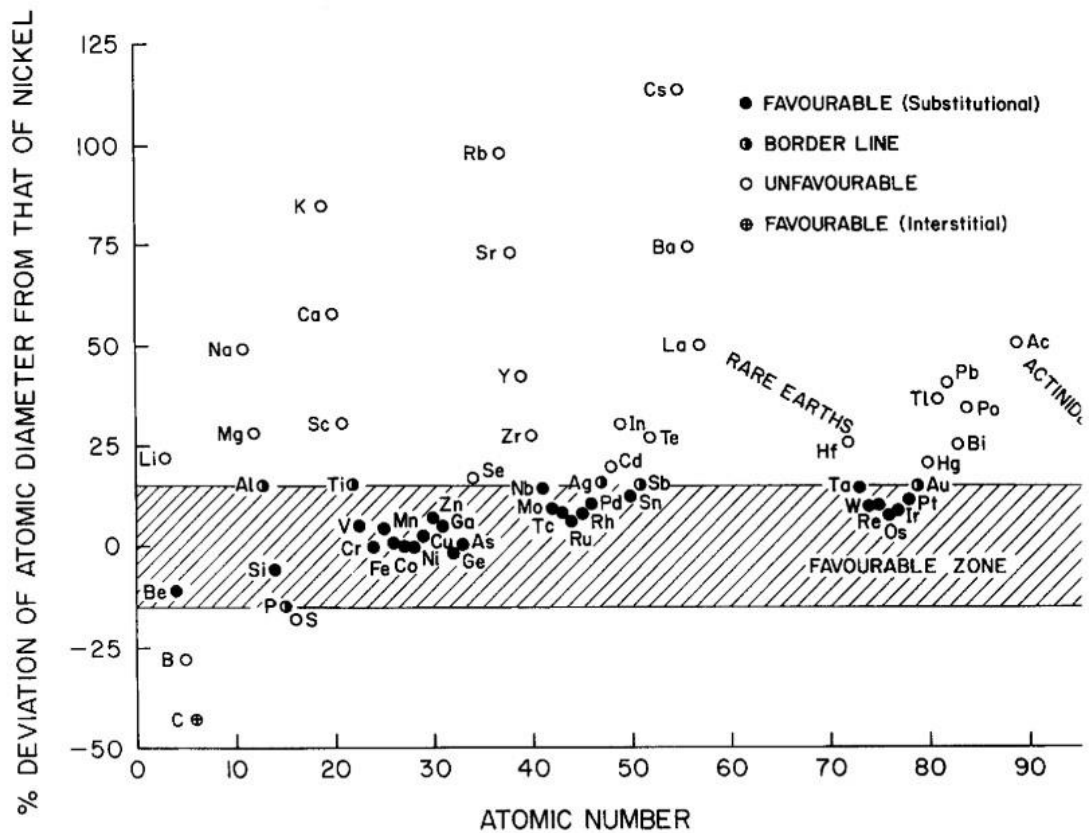


Figure 2.2 – Size factor of various elements for solid solution formation against atomic number (11)

In the above Figure 2.2, the shaded area is known as the “favourable zone” and is defined as the area which lies between a size factor of -15 and +15. If the size factor that arises from Equation 2.1 falls into this favourable zone, then it is expected that the element will have considerable solid solubility in nickel. The strength of the solid solution is enhanced via the solid solution hardening elements by increasing the resistance to the movement of dislocations. This movement resistance originates from changes in shear modulus and distortions in the lattice due to the presence of solute atoms (11). The presence of solute atoms in the host solvent structure causes to strain the nickel crystal structure. This produces a barrier to the movement of dislocations which inevitably causes an amount of hardening and strengthening of the  $\gamma$  matrix phase. The nickel crystal lattice changes as a result of the solute atoms having a

different size to the nickel atoms. Due to this, dislocations are either attracted to or repelled by the solute atoms, although both cases bring an increase in strength. In the case when a dislocation is attracted to a solute atom, the increase in strength arises from the additional force necessary to pull the dislocation away from the solute atom. When the dislocation is repelled by a solute atom, an additional force is necessary to push the dislocation past the solute atom (13).

## 2. Precipitation Strengthening

Nickel is inclined to associate with other certain elements to produce intermetallic compounds that contribute to the strengthening of the  $\gamma$  matrix phase. In nickel-based superalloys, the elements aluminium, niobium and titanium are commonly observed as the main elements in secondary intermetallic precipitate phases. There are a number of mechanisms through which intermetallic precipitates are used to enhance the strength of superalloys. These strengthening mechanisms are obtained through (14):

- Coherency strains
- Stacking-fault energy
- Ordered structure
- Modulus effect
- Interfacial energy
- Orowan looping.

Most of these mechanisms involve the shearing of precipitate particles by dislocations (Figure 2.3). Although, as will be explained later, dislocations can also ‘bow’ around secondary phase precipitate particles.

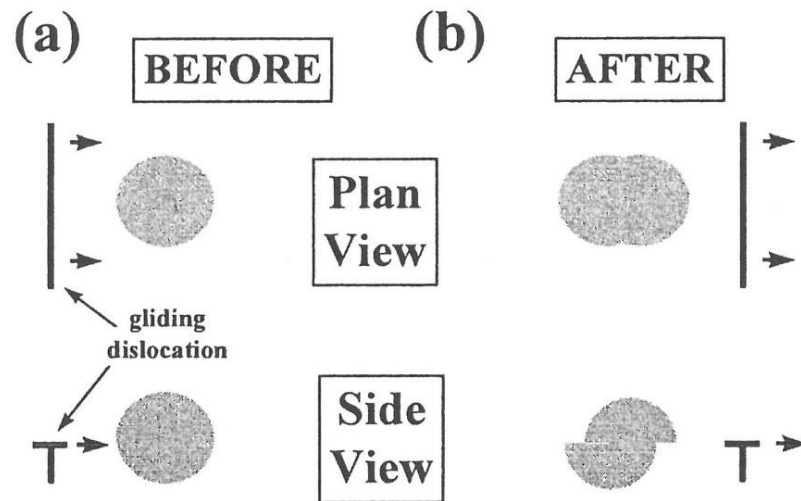


Figure 2.3 – Plan and side views of (a). before shearing and (b). after shearing (15)

#### a. Coherency Strains

The degree of mismatch is a measure of difference in the size of crystal lattice between the precipitate phase and the matrix phase (5). Due to this difference, strain fields are created around the precipitates which can fight the movement of dislocations when the material is undergoing deformation (16). The degree of mismatch can be used to classify precipitates as coherent, semi-coherent or incoherent (15).

From the literature, an expression exists which derives the yield stress that results from the degree of mismatch (14).

$$\Delta\sigma \approx 2G\varepsilon f \quad \text{Equation 2.2}$$

The effect of coherency strains and mismatch are observed in the  $\gamma'$  phase within nickel-based superalloys. The morphology changes as the amount of mismatch between the  $\gamma$  and  $\gamma'$  phases increases. The degree of  $\gamma - \gamma'$  mismatch can be calculated from Equation 2.3 (17).

$$\varepsilon = \frac{\alpha_{\gamma'} - \alpha_{\gamma}}{\alpha_{\gamma}} \quad \text{Equation 2.3}$$

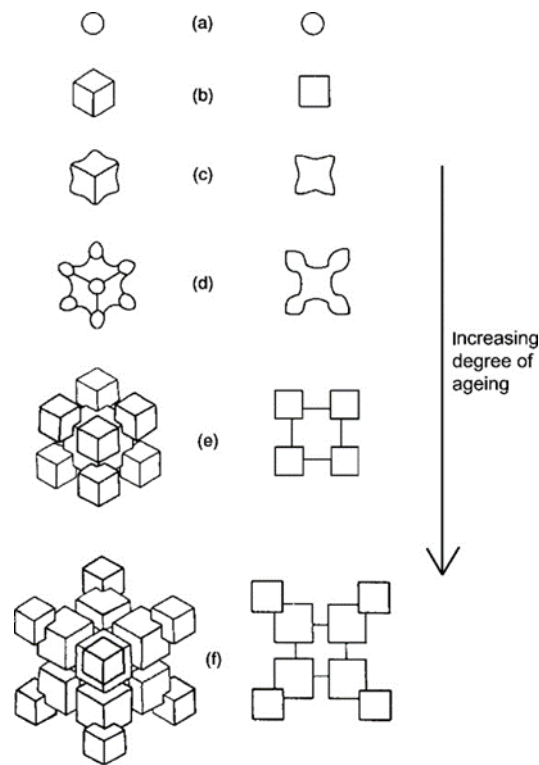


Figure 2.4 - Schematic diagram displaying the morphological evolution of  $\gamma'$  as an increasing level of ageing (from (a) to (f)) (6)

It is known that spherical precipitates of  $\gamma'$  form when then the mismatch is less than 0.4%. Between 0.4% and 1.0% of mismatch,  $\gamma'$  becomes cubical. The cubical morphology is sometimes considered as spherical with a minor deviation because of elastic anisotropy. Above 1.0%,  $\gamma'$  precipitation becomes cellular. Plate or rod morphology of  $\gamma'$  is observed after 3% of mismatch (11).

#### b. Stacking Fault Energy

In some alloys, there is a difference in crystal structure between the matrix phase and the secondary precipitate phase. Due to this, both phases will have different stacking fault energies. If the difference in stacking fault is significant, then considerable strengthening is possible (18).

If the stacking fault energy of the precipitate is higher than that of the matrix phase, the intrusion of a dislocation into the precipitate will increase the dislocation elastic line energy. This causes there to be a repulsive force between the precipitate and

dislocation when they meet. This repulsive force is at its maximum at the halfway point through the matrix. Therefore, the dislocation goes through the precipitate and is not prevented from movement during deformation (18).

However, if the stacking fault energy of the matrix phase is higher than that of the precipitate, the dislocation is attracted towards to the centre of the precipitate because it is at that point in which the dislocation elastic line energy will be minimised. Therefore, the dislocation ends up residing within the precipitate. The maximum resistance to the movement of the dislocation will exist when the dislocation tries to go through the precipitate (18). The increase in flow stress that is required to force the dislocation out of the precipitate is governed by the following equation (14):

$$\Delta\sigma \approx C \left( \frac{\Delta S}{b} \right) \left\{ \frac{3k(\alpha)\ln(S_m - S_p)}{E} \right\} F_1 f^{2/3} \quad \text{Equation 2.4}$$

### *c. Ordered Structure*

Ordered particles are those precipitate particles in which individual atoms have a preferred position and arrangement (5) (see Figure 2.5). When a dislocation goes through and shears an ordered particle, this causes a change in the atomic arrangement across the slip plane within the particle (16). The shearing of the particle causes the creation of an interface known as an anti-phase boundary within the particle (14). Ordered particles require a larger energy to shear by dislocations in comparison to normal disordered or randomly ordered particles (5).

The hardening from ordered particles arises from three causes (16):

1. the energy necessary to create an additional interface between the particle and matrix
2. the additional energy necessary to create an anti-phase boundary within the ordered particle
3. the change in width of a dissociated dislocation as it passes through the ordered particle where the stacking fault energy differs from the matrix.

Therefore, for a dislocation to shear through a ordered precipitate, higher applied force or stress is required to cause material deformation (5).

Figure 2.5 (16) illustrates the shearing of an ordered particle.

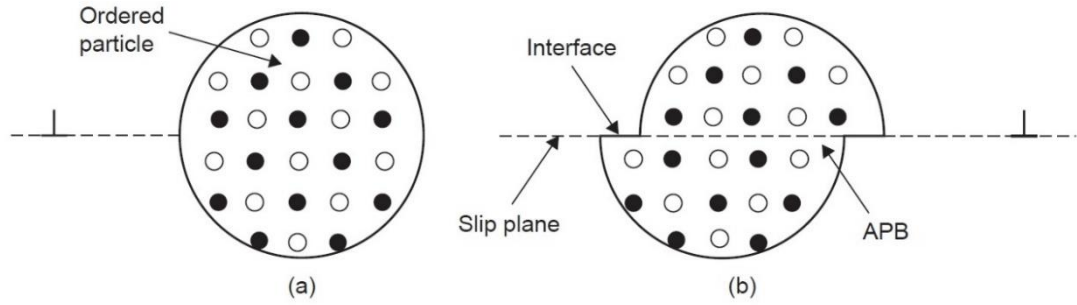


Figure 2.5 – (a). an ordered particle (b). sheared particle with new interfaces and anti-phase boundary (16)

Notice from Figure 2.5 (16) that two new interfaces are created between the particle and the matrix phase. The energy that is required to create the anti-phase boundary is given by the stress required to shear the particle (16)

$$\tau \cong \frac{\beta \gamma_{apb} \frac{3}{2} (fr)^{\frac{1}{2}}}{Gb^2} \quad \text{Equation 2.5}$$

The increase in strength that is provided from this mechanism is given by the following equation (14):

$$\Delta\sigma \approx \frac{2}{\sqrt{\pi E}} \left( \frac{\gamma_{apb}}{b} \right)^{\frac{3}{2}} r^{\frac{1}{2}} f^{\frac{1}{2}} \quad \text{Equation 2.6}$$

#### d. Modulus Effect

The modulus effect comes as a result of the difference between the particle and matrix phase in terms of shear modulus. The energy of a dislocation has a linear relationship



with the local modulus. This means that if a particle has a significantly different modulus in comparison to the matrix phase, the energy of a dislocation will change significantly as it attempts to go through the particle (14). The increase of strength that arises due to this modulus effect is described by the following equation (14):

$$\Delta\sigma \approx \frac{\Delta G}{2\pi^2} \left[ \frac{3|\Delta G|}{Gb} \right]^{\frac{1}{2}} \left[ 0.8 - 0.143 \ln \left( \frac{r}{b} \right) \right]^{\frac{3}{2}} r^{\frac{1}{2}} f^{\frac{1}{2}} \quad \text{Equation 2.7}$$

*e. Interfacial Energy*

When a dislocation shears through the particles in its pathway, some of the atomic bonds within the particle become broken. This causes to form an interface between the particle and the matrix, and this is linked with an increase in interfacial energy between the particle and matrix phase. The increase in strength that is associated with this is given by Equation 2.8 (14).

$$\Delta\sigma = \frac{2\sqrt{6}}{\pi} \gamma_s \frac{f}{r} \quad \text{Equation 2.8}$$

*f. Orowan Strengthening*

Orowan strengthening is a concept of dislocation-particle interaction. When a dislocation moves and interacts with a particle (in this case a precipitate), if the particle is hard enough to resist the associated shearing between itself and the dislocation, the dislocation bypasses the particle and leaves a dislocation loop around the particle (14). This is also known as Orowan looping.

Figure 2.6 displays a schematic diagram showing the different stages in Orowan strengthening (15). In stage (i), a straight line of dislocations moves towards some particles within the material. At stage (ii), the dislocation line begins to bend, whereas at stage (iii), a critical amount of bending has been reached. At stage (iv), the bending

continues around the majority of the particles. At the end at stage (v), the dislocations around both sides of the particles meet each other complete a dislocation loop around the particles. This process is repeated every time a dislocation line passes through these particles. This results in multiple loops around the particles and therefore this makes further material deformation increasingly difficult (14).

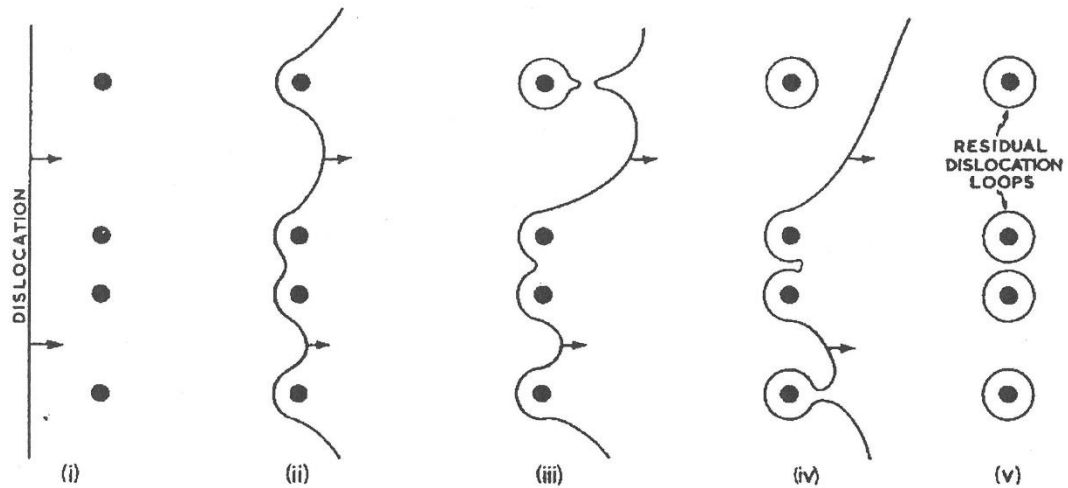


Figure 2.6 – Schematic diagram of the different stages in Orowan looping (15)

### 3. Carbide Strengthening

Carbides that are present in the microstructure of the material can also provide limited strengthening effects. They can impede the movement of dislocations much like how precipitates do. The typical carbides that are found in nickel-based superalloys include  $MC$ ,  $M_6C$ ,  $M_{23}C_6$  and  $M_7C_3$ . The elements that make up these carbides consist of a combination of titanium, chromium, tungsten, tantalum, molybdenum, niobium and hafnium. Carbides that form on the grain boundaries of the material have a number of advantages. They can be used for enhancing the strength of the grain boundary, preventing grain boundary sliding, and stress relaxation (5).

### 2.2.2 Creep and Fatigue Resistance

For high temperature applications of materials, creep and fatigue are two of the most important mechanical properties that one needs to consider. This is especially true for aerospace applications, particularly within the jet engine. This is because the jet engine involves compressing air to high pressure and then igniting this compressed air to extremely high temperatures by burning fuel with it. This produces high temperature and high-pressure gases which thrust the aircraft forward. The materials used in this application must be able to withstand high temperatures and stresses for lengthy periods of time, and therefore must offer good creep and fatigue resistance (19).

Creep is defined as the “*slow and progressive deformation of the material with time under a constant stress*” (20). The mechanisms of creep deformation can be divided into three main types (14):

1. Dislocation glide
2. Dislocation creep
3. Diffusion creep

Each of these three types of creep apply for an approximate range of stress to shear modulus ratio  $\left(\frac{\sigma}{G}\right)$ .

Dislocation glide involves the movement of dislocations that move along slip planes. They overcome movement barriers via thermal activation processes. This particular creep mechanism occurs at high stress to shear modulus ratio  $\left(\frac{\sigma}{G} > 10^{-2}\right)$  (14).

In dislocation creep, the dislocations also use thermally assisted mechanisms to overcome barriers similar to dislocation glide, but they are also assisted by the diffusion of vacancies and/or interstitials. The range of stress to shear modulus ratio is typically  $10^{-4} > \frac{\sigma}{G} > 10^{-2}$  (14).

Diffusion creep involves the movement of vacancies and interstitials through the crystal structure while under the impact of the applied stress on the material. This creep mechanism applies for low stress levels approximately  $\frac{\sigma}{G} < 10^{-4}$ , but also with high temperatures. There are two equations used to determine the creep rate for diffusion creep, which are shown below (14).

$$\dot{\epsilon}_s \approx \frac{14\sigma b^3 D_v}{kT d^2} \quad \text{Equation 2.9}$$

$$\dot{\epsilon}_s \approx \frac{50\sigma b^4 D_{gb}}{kT d^3} \quad \text{Equation 2.10}$$

Equation 2.9 is called the Nabarro-Herring creep equation, while Equation 2.10 is known as the Coble creep equation. The Nabarro-Herring equation says that the creep rate is related to the crystal lattice diffusion coefficient and is inversely proportional to the square of the grain size. The Coble creep equation applies for low temperatures and says that the creep rate is related to the grain boundary diffusion coefficient and is inversely proportional to the cube of the grain size. From both equations, this means that better creep resistance is achieved as the grain size increases.

Generally speaking, the higher the melting point of a metal the higher the creep resistance it possesses. This is because the rate of self-diffusion is lower in metals with a higher melting temperature (14). As dislocation cross slip is an important mechanism in dislocations climbing to avoid obstacles, metals with a low stacking-fault energy have a higher resistance to creep because extended partial dislocations have difficulty in cross slipping. High valence solid solution alloying additions are very useful because they produce a large reduction in stacking fault energy. Solid solutioning additions can increase creep resistance by a number of mechanisms such as (14):

- Segregation to stacking faults
- Elastic interactions of solute atoms with moving dislocations
- Interaction with vacancies and dislocation jogs

- Segregation to grain boundaries in order to influence grain boundary sliding and migration

Fine precipitates are also required for higher resistance to creep. Nickel based superalloys generally produce intermetallic precipitates such as  $\gamma'$  or  $\gamma''$  (14). These fine precipitates will impede the movement of dislocations and hence will result in slower dislocation glide through the alloy. Therefore, the rate of dislocation creep will be reduced. The resistance to creep will be stronger as the dispersion of  $\gamma'$  is finer.

Fatigue is a phenomenon in which metals that are subjected to a repetitive or fluctuating stress will fail at a stress much lower than that required to cause fracture on a single application of load (16). It has been said that good resistance to fatigue can be obtained by homogenising slip deformation in order for local concentrations of plastic deformation to be avoided. This complements the theory that fatigue strength is directly proportional to the resistance of dislocation cross slip. Materials with high stacking fault energy allow dislocations to cross slip more effortlessly, which encourages slip band formation and large plastic zones at the crack tips. This allows crack initiation and propagation due to fatigue to happen with less difficulty. However, in materials with low stacking fault energy, cross slip is more problematic since dislocations are restricted to travel in a more planar path. This means that local concentrations of plastic deformation are restricted and therefore fatigue crack initiation is stifled (14).

However, influencing fatigue strength by changing stacking fault energy has pragmatic constraints. A better way to increase fatigue strength would be to control the microstructure via the use of thermomechanical processing to encourage homogenous slip with a high number of small regions of plastic deformation instead of a low amount of regions of extensive slip (14).

There is also evidence that the fatigue life can be linked to the grain size of the material, depending on the deformation mode. The strongest evidence of grain size influence on fatigue can be observed in the low-stress and high-cycle regime which is where stage

I cracking occurs. In materials that possess a high stacking fault energy such as aluminium and copper, cross-slip of dislocations is relatively easy, and a dislocation cell structure is formed in fatigue. This dislocation cell structure masks the grain boundaries and controls the stage I crack propagation, making fatigue life insensitive to grain size (14,21).

On the other hand, in materials that possess low stacking fault energy, such as  $\alpha$  brass, dislocations go through planar slip which restricts dislocations to intergranular bands. The grain boundaries resist the propagation of fatigue cracks since dislocations cannot easily penetrate them. Therefore, increasing the number of grain boundaries (by reducing the grain size) increases the resistance of the material to fatigue (14,21).

### 2.2.3 Role of Elements

In any superalloy, the elements that make up the chemical composition of the superalloy have certain advantages that effect the material behaviour. Table 2.2 (5) shows the role that particular elements play in improving the material and inducing desired effects.

<i>Effect</i>	<i>Iron based</i>	<i>Cobalt based</i>	<i>Nickel based</i>
Solid solution strengtheners	Cr, Mo	Nb, Cr, Mo, Ni, W, Ta, Ni	Co, Cr, Fe, Mo, W, Ta
FCC matrix stabilisers	C, W, Ni	Ni	
<i>Carbides:</i>			
MC	Ti	Ti	W, Ta, Ti, Mo, Nb
M <sub>7</sub> C <sub>3</sub>		Cr	Cr
M <sub>23</sub> C <sub>6</sub>	Cr	Cr	Cr, Mo, W
M <sub>6</sub> C	Mo	Mo, W	Mo, W
<i>Carbonitrides</i>			
M(CN)	C, N	C, N	C, N
Promotes general precipitation of carbides	P		
Forms $\gamma'$	Al, Ni, Ti		Al, Ti
Retards formation of hexagonal $\eta$	Al, Zr		
Raises solvus temperature of $\gamma'$			Co

Hardening precipitates and/or intermetallics	Al, Ti, Nb	Al, Mo, Ti, W, Ta	Al, Ti, Nb
Oxidation resistance	Cr	Al, Cr	Al, Cr, Y, La, Ce
Improve hot corrosion resistance	La, Y	La, Y, Th	La, Th
Sulfidation resistance	Cr	Cr	Cr, Co, Si
Improves creep properties	B		B, Ta
Increases rupture strength	B	B, Zr	B
Grain boundary refiners			B, C, Zr, Hf
Facilitates working		Ni <sub>3</sub> Ti	
Retard $\gamma'$ coarsening			Re

Table 2.2 – Microstructural effects from elements (5)

A nominal chemistry comparison of Inconel 718 and ATI 718Plus is shown below in Table 2.3.

Alloy	Chemistry											
	Ni	C	Cr	Mo	W	Co	Fe	Nb	Ti	Al	P	B
<b>Inconel 718</b>	Bal	0.025	18.1	2.90	-	-	18.0	5.40	1.00	0.45	0.007	0.004
<b>ATI 718Plus</b>	Bal	0.025	18	2.70	1.0	9.0	10.0	5.40	0.70	1.45	0.007	0.004

Table 2.3 – Chemistry comparison between Inconel 718 and ATI 718Plus with key differences highlighted in yellow (22)

The main differences in chemistry between ATI 718Plus and its predecessor Inconel 718 are the additions of cobalt and tungsten, the increase in aluminium content and the decrease in titanium and iron content, as highlighted in yellow in Table 2.3.

The chemical composition of ATI 718Plus arose as a result of a comprehensive study conducted by Cao and Kennedy (23), in which the effect of alloying elements in 718-type alloys was investigated. It was found that a small addition of 1% of tungsten in combination with approximately 2.8% of molybdenum gave the best result in terms of stress rupture life (23).

The addition of cobalt was found increase the  $\gamma$ - $\gamma'$  mismatch, which considerably enhanced stress rupture properties. This effect was saturated with an addition of 9% of cobalt. However, the authors had warned against the addition of too much cobalt as

this has the effect of larger quantities of precipitation of TCP phases which is detrimental to the alloy mechanical properties (23).

Contrarily, iron was found to promote the formation of Laves phase and actually decrease the  $\gamma$ - $\gamma'$  mismatch. The precipitation of all phases in the work ( $\gamma'$ ,  $\gamma''$ ,  $\delta$  and  $\eta$ ) was accelerated by increasing the amounts of iron and cobalt. It was found by the authors that an optimal iron content of 10% gave the best results in terms of thermal stability and stress rupture properties (23).

Increasing the content of aluminium and titanium (Al+Ti) has the effect of increasing the volume fraction of  $\gamma'$  at the cost of  $\gamma''$ , until the alloy becomes a primarily  $\gamma'$  strengthened superalloy. Due to the larger value of Al+Ti in ATI 718Plus in comparison to Inconel 718, the main strengthening phase in ATI 718Plus is  $\gamma'$ , not  $\gamma''$  which is the main strengthening phase in Inconel 718. Another important parameter is the aluminium to titanium ratio (Al/Ti ratio). Low Al/Ti ratios provide a lower thermal stability due to significant formation of  $\delta$  and  $\eta$  phases which lead to considerable degradation of mechanical properties after long-term heat treatment. As ATI 718Plus has a higher Al/Ti ratio in comparison to Inconel 718, the thermal stability of ATI 718Plus is much improved over Inconel 718 (23).

#### 2.2.4 Specific Strengthening Mechanisms of ATI 718Plus

In the initial years after its development, the exact strengthening mechanisms of ATI 718Plus were not very clear (24). However, in more recent years, studies have been performed to investigate the specific precipitation strengthening mechanisms via the interactions between dislocations and precipitates (as briefly described in the preceding sections). In one such study (25), a comparison of yield strength as a function of aging time is performed in which experimental data, yield strength from Orowan looping, and yield strength from particle shearing are all compared. The yield strength from Orowan looping and particle shearing are obtained from equations that are mentioned in the literature. The graph that is obtained from the study is shown in Figure 2.7 (25).



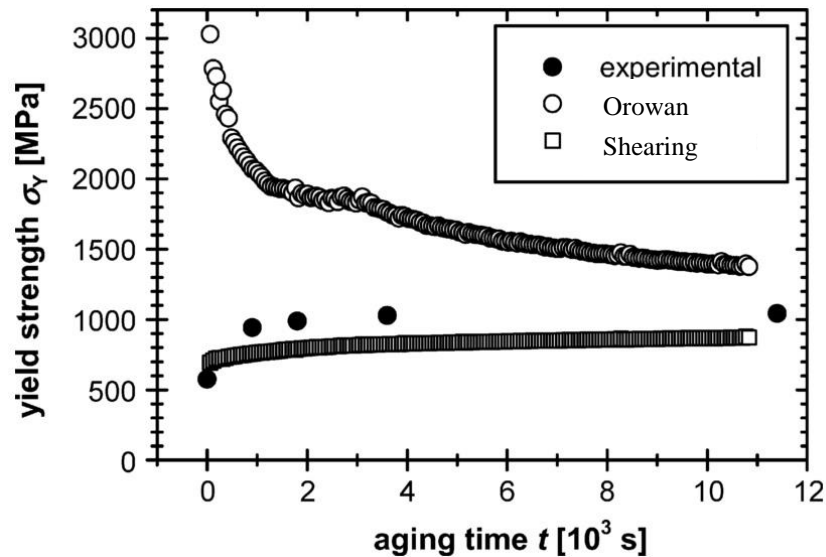


Figure 2.7 – Comparison between experimental data and calculations of yield strength (Orowan mechanism and precipitate shearing) (25)

It can be observed from the above graph that the experimental data has a good tendency with the shearing yield strength during the early stages of aging. However, the shearing mechanism shows a decrease in yield strength from approximately 3000 MPa to about 1300 MPa with increasing aging time, which is clearly not observed in the experimental data. During the later stages of aging, the shearing mechanism tends towards the experimental data. This indicates that the Orowan strengthening may occur only during the later stages of aging, and strengthening via particle shearing takes place during the early stages of aging (25).

A similar result is obtained in another study (26) in which the yield strength is simulated using integrated physical models that include intrinsic, grain boundary, solid solution and precipitate strengthening mechanisms. It was found within this study that during aging at 788°C, before 10 hours the operative strengthening mechanism is via particle shearing. Beyond 10 hours, the strengthening is provided by Orowan looping, which is a non-shearing mechanism (26).

Although, as described in Section 2.2.1, there are many strengthening phenomena that involve the shearing of particles. Specifically, for ATI 718Plus, it was found in the previously mentioned study (26) that coherency strain strengthening (see a. Coherency

Strains in Section 2.2.1) and anti-phase boundary strengthening (see c. Ordered Structure in Section 2.2.1) are the two most predominant strengthening mechanisms (26,27). However, it is unclear which of the two strengthening mechanisms has the most effect (26,27).

### **2.3 Phases**

As with other superalloys, ATI 718Plus contains various different phases within its microstructure and each of these distinct phases possesses a particular type of crystal structure. The most common crystal structures found within nickel-based superalloys are the face centred cubic (FCC) structure, the hexagonal close packed (HCP) structure and the body centred cubic (BCC) structure. The body centred tetragonal (BCT) crystal structure is also observed in nickel-based superalloys but on a smaller scale when compared to the aforementioned crystal structures (5).

Within ATI 718Plus, the main phases in the microstructure that are of significant interest and that are considerably influential on the material behaviour and the mechanical properties are (28):

- $\gamma$  phase
- $\gamma'$  phase
- $\eta$  phase

These are the main phases that make up the microstructure of ATI 718Plus. In this section, a brief overview of each of these phases will be described. Also, other various intermetallic and precipitate phases that are found in the superalloy class of materials (but not necessarily found specifically in ATI 718Plus) will be described in this section.

#### **2.3.1 $\gamma$ phase**

The  $\gamma$  phase is made up of a face centred cubic (FCC) disordered crystal structure (29). This phase is also termed as being 'austenitic'. It is also referred to as the 'matrix'

phase or the ‘parent’ phase. It forms a continuous matrix from which other intermetallic and precipitates nucleate and grow from. Although it consists primarily of nickel atoms, the  $\gamma$  matrix contains within itself significant concentrations of cobalt, chromium, molybdenum, ruthenium and rhenium, as this is where, thermodynamically speaking, these elements prefer to reside in (6). Figure 2.8 shows a schematic diagram of the FCC crystal structure and a spherical atomic model of the  $\gamma$  phase (5).

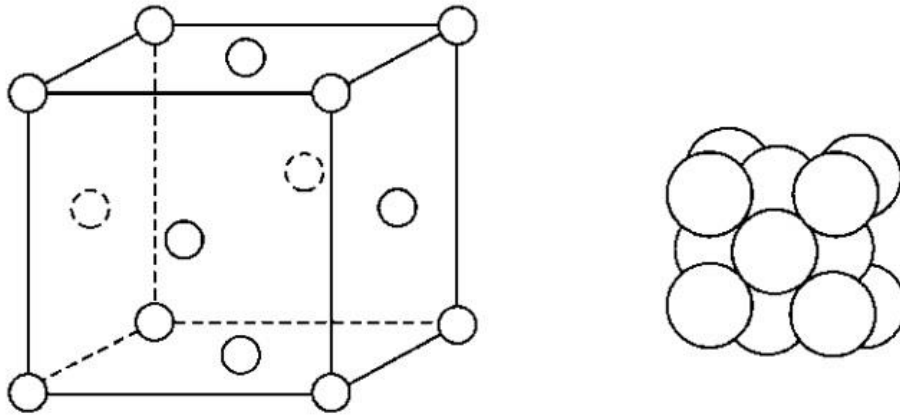


*Figure 2.8 – Schematic diagram of the crystallographic and atomic structure of the  $\gamma$  phase (5)*

### 2.3.2 $\gamma'$ phase

The  $\gamma'$  phase is a nanometre-sized intermetallic phase constituting primarily of nickel atoms but also with additions of aluminium, titanium and niobium atoms, with its chemical structure being  $\text{Ni}_3(\text{Al, Ti, Nb})$ . The chemical structure has also been referred to as being  $\text{Ni}_3(\text{Al/Ti})$  (5,30),  $\text{Ni}_3\text{Al}$  (31), and  $(\text{Ni, Co})_3(\text{Al, Ti, Cr, Nb})$  (32). However, most literature sources mention this phase as being  $\text{Ni}_3(\text{Al, Ti, Nb})$  (29,33–36), and therefore it will be stated as this chemical structure within this work.

In terms of crystal structure, the  $\gamma'$  phase has an  $L1_2$  ordered FCC crystal structure. This is the same crystal structure that is shown in Figure 2.8, but with nickel atoms located at the face centres of the unit cell and aluminium, titanium and niobium positioned in the corners of the unit cell (35). Figure 2.9 displays a schematic diagram of the crystal structure of the  $\gamma'$  phase (5).

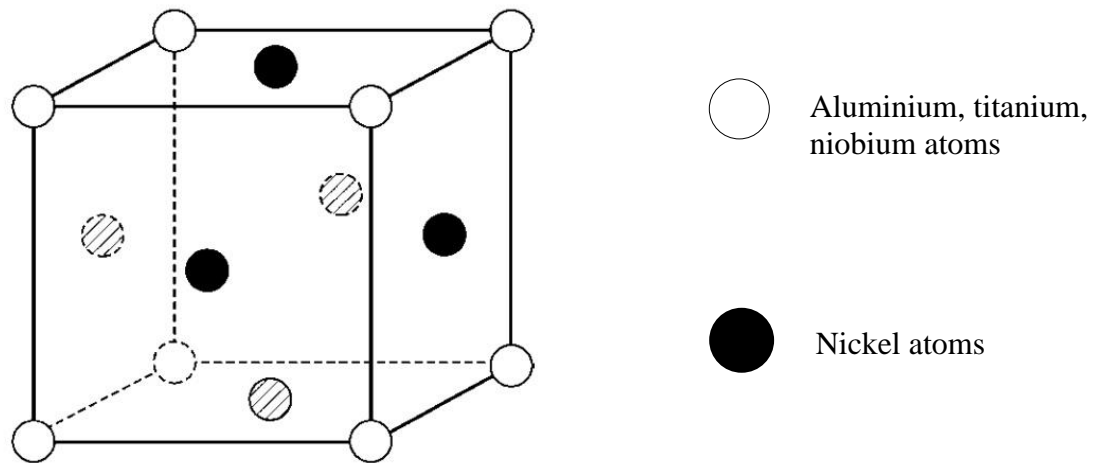


Figure 2.9 – Schematic diagram of the crystal structure of the  $\gamma'$  phase. (5)

The  $\gamma'$  phase has a roughly spherical morphology when existing at low volume fractions. While at higher volume fraction,  $\gamma'$  tends to have a more cuboidal morphology (29,32,35). This is also observed as the degree of ageing is increased (Figure 2.4). For ATI 718Plus (as well as other superalloys), the  $\gamma'$  phase is termed as being the principal strengthening phase – meaning that the primary source of strength that the material possesses is through the use of the  $\gamma'$  phase (24). The  $\gamma'$  phase is the principal strengthening phase for many superalloys including Nimonic 80A, Waspaloy (4,37), René 65 (38) and AD730 (39).

The main advantage of the  $\gamma'$  phase is that due to its high temperature stability, ATI 718Plus is able to retain high strength at temperatures up to 704°C. In comparison, IN 718 has a temperature limit of 650°C due to the presence of the metastable  $\gamma''$  phase. At and after 650°C, the  $\gamma''$  phase rapidly transforms into the more stable  $\gamma'$  phase. Due to this quick conversion, IN 718 suffers a significant detrimental drop in mechanical properties (40).

### 2.3.3 $\gamma''$ phase

The  $\gamma''$  phase is a metastable intermetallic phase consisting of nickel and niobium atoms which are arranged in a chemical structure of  $\text{Ni}_3\text{Nb}$  and possesses a  $\text{D}_{022}$  body centred tetragonal (BCT) crystal structure (41). Figure 2.10 displays a schematic

diagram of the crystal structure of the  $\gamma''$  phase as well as its atomic arrangement (42). It can be seen that the arrangement of atoms in this phase is closely related to that of the  $L1_2$  of the  $\gamma'$  phase. The relationship between the lattice parameters is  $a = b \neq c$  with the magnitude of  $c$  almost being double of the same parameter in the  $\gamma'$  phase. It is from this that the term  $\gamma''$  arises (6).

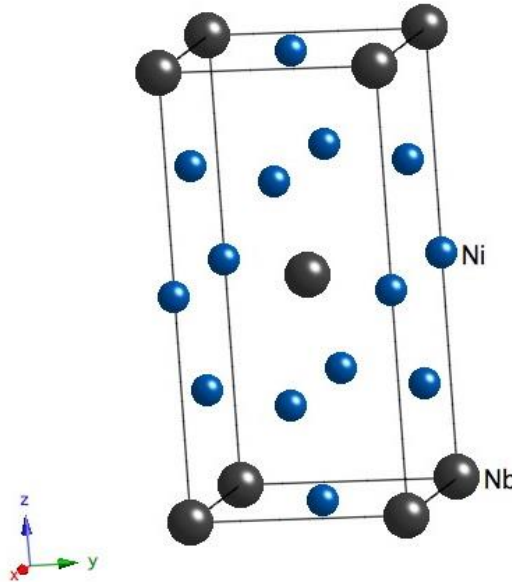


*Figure 2.10 – Schematic diagram of the crystal structure of the  $\gamma''$  phase (42)*

The morphology of  $\gamma''$  is disc shaped with typical thicknesses being around 10 nm and the diameter being approximately 50 nm. There is good coherency between  $\gamma''$  particles and the  $\gamma$  parent phase. As mentioned previously, IN 718 is primarily strengthened with  $\gamma''$  phase particles. The excellent mechanical properties that IN 718 possesses at high temperature are due to the large coherency strains between  $\gamma''$  and the  $\gamma$  matrix, as well as the restricted amount of slip systems that function in  $\gamma''$ . Due to the aforementioned high coherency strains, the precipitation kinetics of the  $\gamma''$  phase are known to be sluggish (6).

Within IN 718, the  $\gamma''$  phase particularly influences the tensile and creep properties, while the dislocation shearing mechanism within  $\gamma''$  is associated with fatigue softening at high temperatures (41).

The main disadvantage of the  $\gamma''$  phase is that in the overaged condition and above 650°C,  $\gamma''$  phase transforms into the stable equilibrium  $\delta$  phase (6,43). This brings a general reduction in strength as it is incoherent with the  $\gamma$  matrix and it does bring any improvement in strength even at significant quantities (5,6).

#### 2.3.4 $\delta$ phase

The  $\delta$  phase has a chemical structure of  $\text{Ni}_3\text{Nb}$  with an orthorhombic  $\text{D0}_a$  crystal structure (44–47). It is an incoherent phase in relation to the  $\gamma$  matrix (45,46). Figure 2.11 displays a prototype crystallographic structure for the  $\delta$  phase (31).

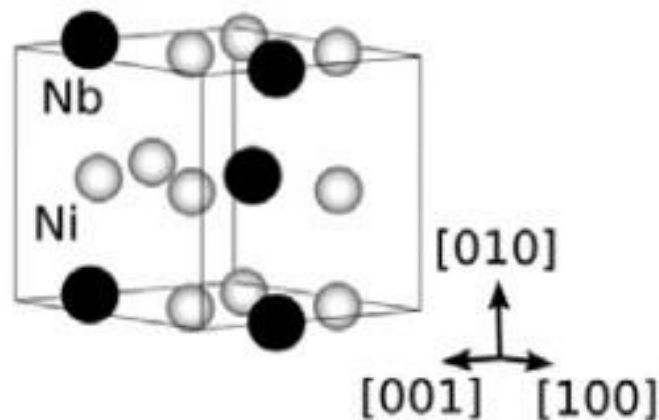


*Figure 2.11 – Diagram displaying the prototype orthorhombic crystal structure of the  $\delta$  phase with nickel and niobium atom positions (31)*

It is well known that the  $\delta$  phase exists in the form of grain boundary precipitates within IN 718 (44–46,48,49). However, in the case of ATI 718Plus, the  $\delta$  phase is not the main phase of the grain boundary precipitates. As explained later (see Section 2.3.5), the main phase of the grain boundary precipitates within ATI 718Plus is in fact the  $\eta$  phase. However, interwoven layers of  $\delta$  phase are found within the  $\eta$  grain boundary precipitates in ATI 718Plus such that the constituents of the grain boundary precipitates are technically  $\eta + \delta$  phase (30). The percentage of  $\delta$  phase that is found in the grain boundary precipitates within the whole material is very small and is estimated to be less than 1% (30), which means the majority of the grain boundary precipitates consist of the  $\eta$  phase.

Within the literature, it seems that the range in which the  $\delta$  phase precipitates within is disputed, with some authors mentioning it to be between 700°C to 1000°C (44), 750°C to 1020°C (46). The solvus temperature of the  $\delta$  phase is also uncertain as it has been reported to be in the range of 990°C to 1020°C (48). The dispersion in  $\delta$  phase solvus temperature is said to be due to the fluctuations in chemical composition of the alloy, with the niobium content having the most influence on the  $\delta$  phase solvus temperature (48).

The fastest rate of  $\delta$  phase precipitation occurs at approximately 900°C (44,46). It usually nucleates and precipitates starting at the grain boundaries of the  $\gamma$  phase (44) through a discontinuous reaction (47). It then grows into thin plates along the grain boundary and eventually elongating into the  $\gamma$  phase grains (44).  $\delta$  phase precipitation can also occur along intragranular to the  $\gamma$  matrix grains when  $\gamma''$  phase is present (44).

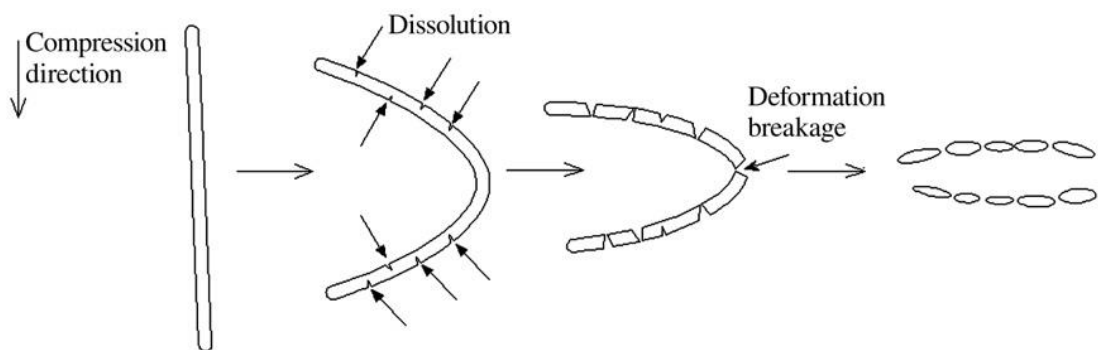
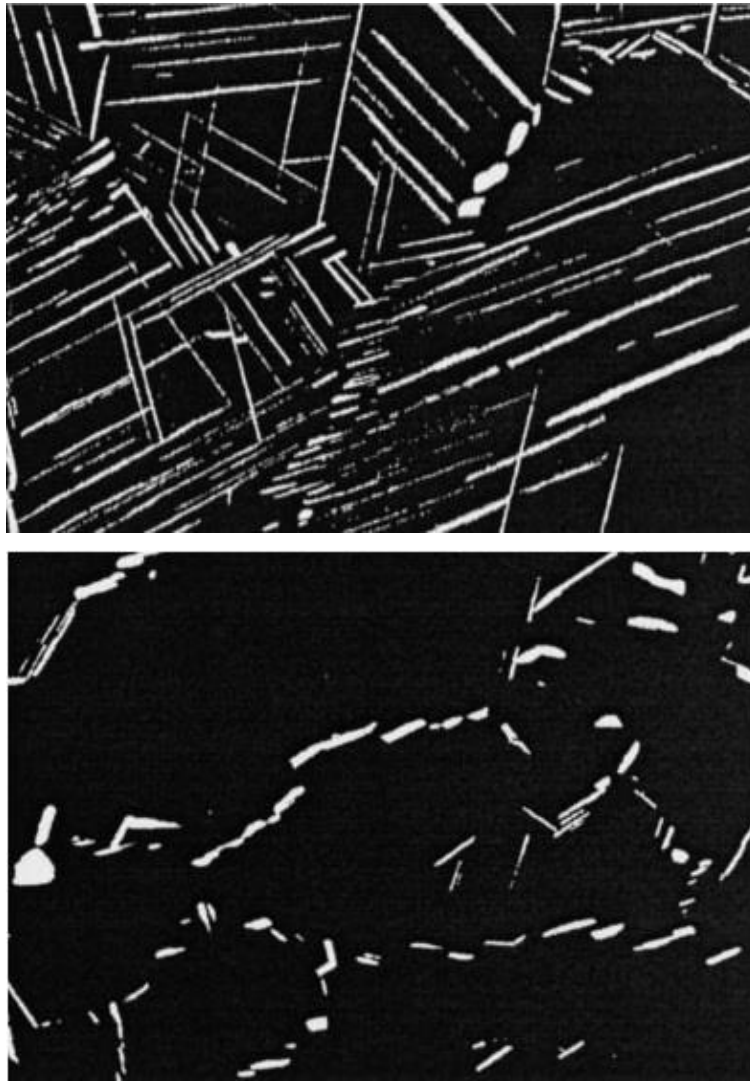


Figure 2.12 – Schematic diagram displaying the globulisation mechanism of  $\delta$  phase (45)



*Figure 2.13 – Differences in precipitate morphology. Top: acicular precipitates, Bottom: globular precipitates (48)*

In material that has been thermo-mechanically processed, the  $\delta$  phase precipitates can exist as equiaxed and relatively coarse particles, which are termed as ‘globular  $\delta$  phase’ (44,50). These globular  $\delta$  phase particles arise due to the fragmentation of originally pre-existing  $\delta$  phase plates (44). This is schematically depicted in Figure 2.12 (45). Figure 2.13 shows the difference in precipitate morphology (48).

As mentioned previously, the metastable  $\gamma''$  transforms into the stable  $\delta$  phase under certain temperature and time conditions (6,43). Even though the  $\delta$  phase is thermodynamically more stable than the  $\gamma''$  phase, the slowness of the precipitation of the  $\delta$  phase allows the  $\gamma''$  phase to precipitate before it. This is the case up to 900°C,



but beyond this the limit of  $\gamma''$  phase is reached and therefore further precipitation of the  $\gamma''$  phase is not possible. Both the  $\gamma''$  phase and the  $\delta$  phase have the same chemical structure and therefore both phases contain niobium. This suggests that the growth of the  $\delta$  phase precipitates occurs at the expense of the  $\gamma''$  phase up to 900°C. As mentioned previously, this cannot be the case after 900°C since  $\gamma''$  phase does precipitate beyond this (44).

The existence of  $\delta$  phase means a loss of strength and hardenability because of a reduction of the amount of  $\gamma''$  phase in the microstructure (44,51). On the contrary, at room temperature at least, it has been reported that the  $\delta$  phase does not make any negative or positive difference on the tensile strength, yield strength and hardness of IN 718 (51). However, the  $\delta$  phase is known to be a hard brittle phase and it has been reported to have an adverse effect on the plasticity of Inconel 718 at high temperatures. As the  $\delta$  phase content increases, the plasticity at high temperature reduces (52).

Studies have also shown that the presence of  $\delta$  phase does neither improve or weaken the grain boundary resistance to environmental cracking (53), although it has been said that the  $\delta$  phase does make the alloy more susceptible to hot cracking (44). Moreover, within IN 718, it has shown that the plasticity of the alloy at high temperatures is reduced as the amount of  $\delta$  phase content is increasing (52). Without any  $\delta$  phase present in the microstructure, the stress rupture life is doubled, while the creep elongation to failure is multiplied between 4 to 5, when in comparison to microstructures exposed to heat treatment processes that encourage  $\delta$  phase precipitation (54). However, it has been reported elsewhere in the literature that the presence of grain boundary  $\delta$  phase can improve stress rupture ductility (50). Also, at low but sufficient volume fractions, the  $\delta$  phase is beneficial to restrict the growth of  $\gamma$  phase grains (44,49,55)

### 2.3.5 $\eta$ phase

In the early literature regarding ATI 718Plus, it was initially thought that the grain boundary precipitates were orthorhombic  $\text{Ni}_3\text{Nb}$   $\delta$  phase (2,25,40,56–60) (see Section

2.3.4). Although, some authors had reported the existence of an hexagonal closed pack (HCP) phase (22,61–63). However, the vast majority of the available literature had referred to the grain boundary precipitates in ATI 718Plus as the  $\delta$  phase. It was suggested that the reported presence of an HCP phase was in fact a new plate-like phase which consisted of a chemical structure of  $\text{Ni}_3\text{Al}_{0.5}\text{Nb}_{0.5}$ . It was implied that this new phase nucleates within the same microstructure in which the  $\delta$  phase precipitates in, such that both the  $\delta$  phase and the  $\text{Ni}_3\text{Al}_{0.5}\text{Nb}_{0.5}$  phase coexist within ATI 718Plus (22,62,63). However, more work was required at this stage to elaborate on this new phase (22).

A very detailed study was done on the grain boundary precipitates, which had clarified the issue very well. It was found the grain boundary precipitates in ATI 718Plus are in fact a modified version of the  $\eta$  phase (30). Usually, the  $\eta$  phase is defined as having a chemical structure of  $\text{Ni}_3\text{Ti}$  with a  $\text{D}_{024}$  HCP crystal structure (5). Interestingly, in the case of ATI 718Plus, the grain boundary precipitates are consistent with the  $\text{D}_{024}$  HCP structure, however the chemistry of these precipitates was found to be  $\text{Ni}_6\text{AlNb}$ , which is different to the chemical definition of  $\eta$  phase as mentioned previously. In this ‘modified’  $\eta$  phase, the aluminium and niobium atoms are accommodated in the position where the titanium atoms are usually located in the original  $\eta$  phase. Figure 2.14 displays the chemical and crystallographic prototype structure of the  $\eta$  phase found in ATI 718Plus (30).

Interestingly, it was found that that  $\delta$  phase was present in the form of small interwoven strips which were located in the niobium rich areas of the  $\eta$  phase precipitates and were coherent between itself and the  $\eta$  phase. These  $\delta$  phase strips are in very insignificant quantities such that it is difficult to quantify them. In fact, these  $\delta$  phase layers have been found to be only a few atomic layers thick in some cases. It is probable that the balance of niobium, aluminium and titanium is held by a combination of both  $\delta$  and  $\eta$  phase (30)

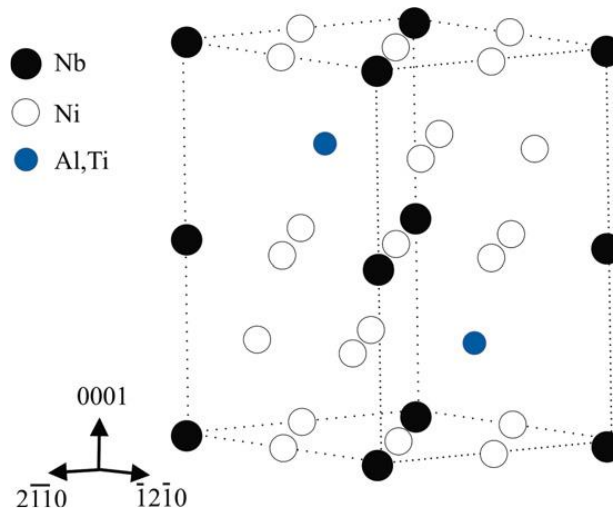


Figure 2.14 – Diagram displaying the prototype HCP crystal structure of the  $\eta$  phase with Ni, Nb and Al/Ti atom positions (30)

A number of studies (30,64,65) have shown the general order of  $\eta$  phase precipitation locations in ATI 718Plus; random grain boundaries, twin boundaries and then within the grains (intragranular precipitation). However, it must be mentioned that although the  $\eta$  phase primarily nucleates and grows on grain boundaries, it does not appear to grow on every single grain boundary.

A couple of studies (30,66) have tried to investigate the relationship between grain boundary misorientation angle and the presence of  $\eta$  phase precipitates. In one study conducted by Alabbad and Tin (66), a distribution of grain boundary misorientations was shown based on the number of grain boundaries (see Figure 2.15). As the misorientation angle increases in ranges of  $10^\circ$ , the frequency of grain boundaries (black columns) increases in each class. It is also observed that the frequency of the grain boundaries with  $\eta$  phase precipitates (grey column) generally increases as the misorientation angle class increases. However, at  $0^\circ - 10^\circ$ , it can be seen that almost half of the grain boundaries contain  $\eta$  phase precipitates. Whereas at  $50^\circ - 60^\circ$ , the relative proportion of grain boundaries with  $\eta$  phase is comparatively less but still considerable in absolute terms.  $\eta$  phase precipitation is observed on grain boundaries in every class of grain boundary misorientation angle. Therefore, there does not seem to be any link between grain boundary misorientation angle and  $\eta$  phase precipitation.

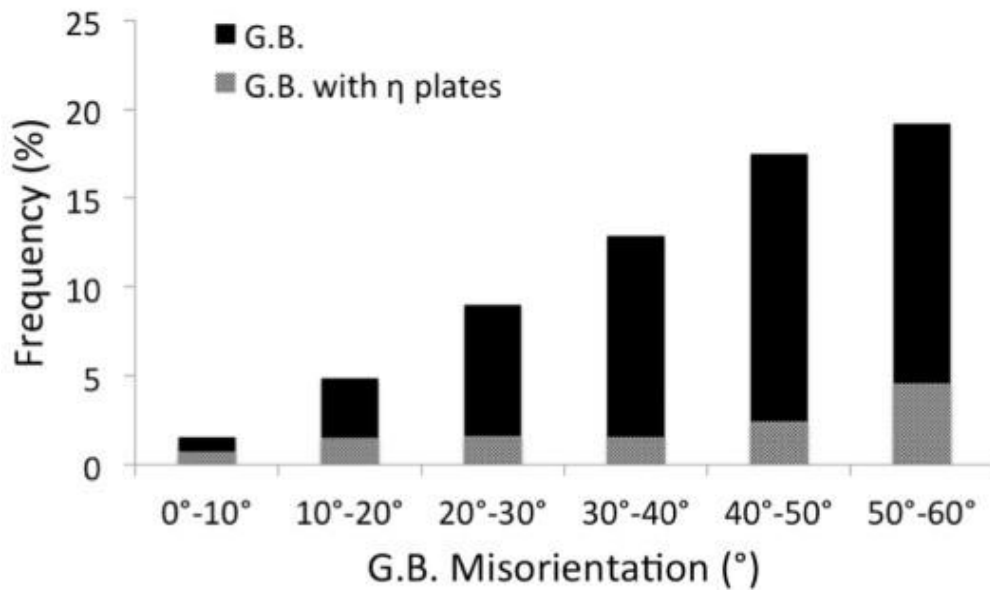


Figure 2.15 – Frequency of  $\eta$  phase precipitation with respect to grain boundary misorientation (66)

Likewise, in the other study by Pickering et al. (30), it was also seen that a decent percentage of low angle and low energy grain boundaries contained  $\eta$  phase precipitates, while at the same time, there were some high angle and high energy grain boundaries that were precipitate free. This further support the idea that there is no strong indication for a distinct link between the misorientation of grain boundaries and  $\eta$  phase precipitation. However, within the study it was mentioned by the author that from the grain boundaries that were precipitate free, approximately half of those were twin boundaries and the remaining precipitate-free grain boundaries had misorientation angles that were spread over a wide range. This finding may indicate that twin boundaries have a little more resistance to  $\eta$  phase nucleation. No explanation for this observation was given by the author for this finding and nothing was found to explain this from already published literature.

It was also observed that grain boundaries appear to become serrated at locations in which there are  $\eta$  phase precipitates. This suggests that the precipitation of  $\eta$  phase is predominantly through a discontinuous precipitation mechanism. Discontinuous precipitation reactions are usually characterised and recognised distinctively because the grain boundary tends to move with the growing precipitate tips. Figure 2.16 shows

the possible sequence of steps during the development of discontinuous precipitation (67).

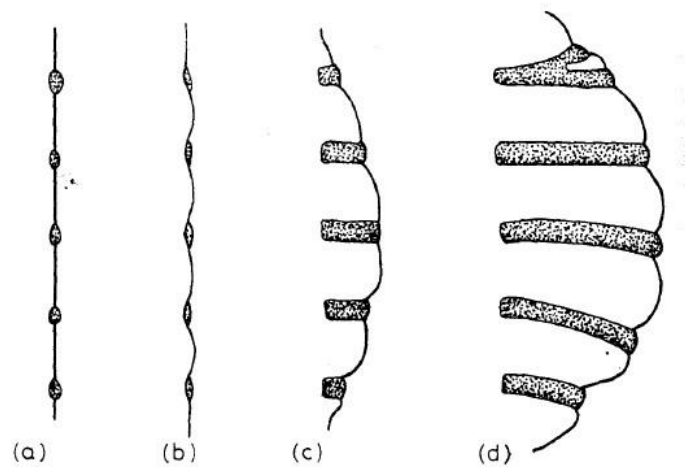


Figure 2.16 – Illustration displaying the stages of discontinuous precipitation (67)

Discontinuous precipitation necessitates that solute atoms are partitioned to the precipitate tips that are in contact with the preceding grain boundary (67). In essence, the movement of the grain boundary is enabled by the consumption of supersaturated material ahead of the grain boundary, along with the precipitation of a stable phase behind it (30). There are two mechanisms by which this can occur (67):

1. Diffusion through the lattice in front of the preceding precipitate front
2. Diffusion within the moving grain boundary

Discontinuous precipitation is driven by an overall reduction in free energy of the system (30). If diffusion through the lattice of the precipitate front is the main mechanism of discontinuous precipitation, then one can expect a gradient of solute concentration from the precipitate face into the matrix phase (67). An example of this type of solute concentration gradient is shown in Figure 2.17 (b) (67) for a particular Mg–Al alloy whereby the Al concentration profile in the  $\alpha$  phase matrix between two equilibrium  $\beta$  phase precipitates is displayed. If the process of diffusion in the discontinuous precipitation reaction is occurring through the advancing grain boundary, then the composition in the matrix should be constant right until the precipitate face (67). Figure 2.17 (a) (67) displays an example of this type of

concentration gradient between a supersaturated matrix phase ( $\alpha'$ ) and the  $\alpha$  matrix (which is the same phase as  $\alpha'$  but has a lower thermodynamic excess of solute).

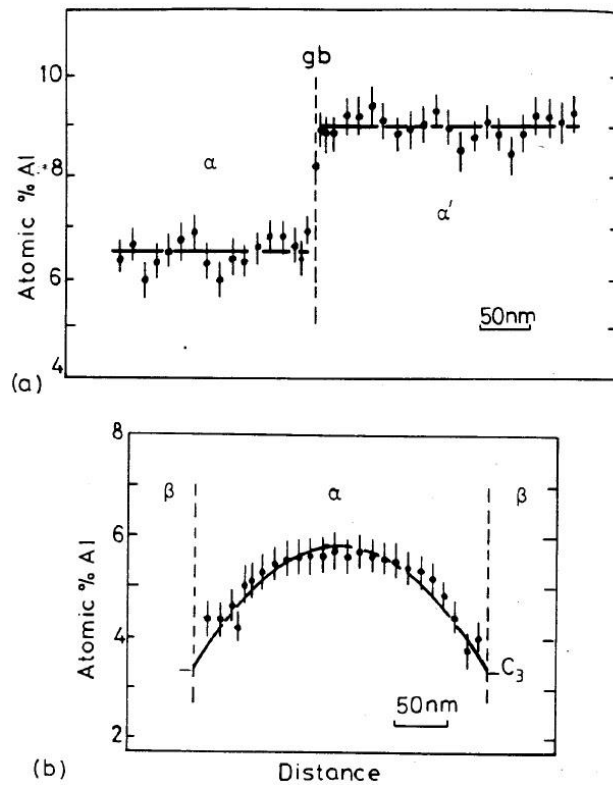


Figure 2.17 – Concentration gradients for (a) diffusion through advancing grain boundary (b) diffusion across lattice in front of proceeding precipitate (67)

The unique grain boundary curvatures observed in the discontinuous precipitation reactions in ATI 718Plus is a result of the interaction between three main parameters (30):

1. The interfacial energies of the boundaries between the two  $\gamma$  matrix grains and  $\eta$  phase
2. Changes in free energy across the grain boundary due to differences in composition
3. Diffusion of the precipitate forming elements (Al, Nb, Ti) along the grain boundary

The contact angle ( $\theta$ ) between the grain boundary and the  $\eta$  phase precipitate is determined as a result of the interfacial energy terms that are present at the tripartite

junction between the  $\eta$  phase precipitate, the parent grain ( $\gamma_1$ ) (in which the  $\eta$  precipitate is nucleating into), and the neighbouring grain ( $\gamma_2$ ) next to the  $\eta$  precipitate (30). This is schematically displayed in Figure 2.18 (30).

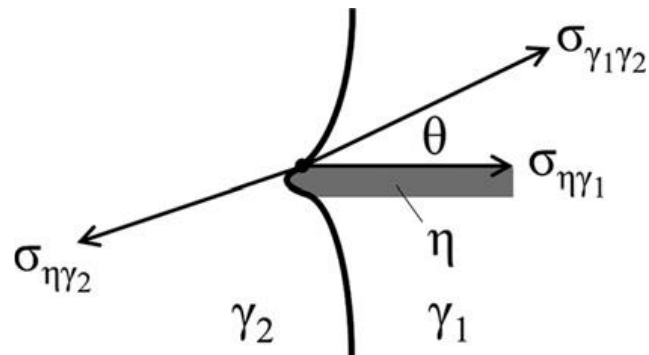


*Figure 2.18 – Schematic diagram of the forces at the triple junction between the parent grain ( $\gamma_1$ ), the neighbouring grain ( $\gamma_2$ ), and the  $\eta$  phase precipitate (30)*

The interfacial energy between the  $\eta$  precipitate and its own parent grain ( $\sigma_{\eta\gamma_1}$ ) will be relatively low and constant because there is a good coherency between them. The other interfacial terms, specifically between the two grains ( $\sigma_{\gamma_1\gamma_2}$ ) and between the  $\eta$  precipitate and the neighbouring grain ( $\sigma_{\eta\gamma_2}$ ) are a function of the grain boundary plane and misorientation, however they would still be larger than the interfacial energy between the  $\eta$  precipitate and its own parent grain ( $\sigma_{\eta\gamma_1}$ ). As a consequence, it is beneficial for the grain boundary to move forward with the growing precipitate in order to avoid the development of a high interfacial energy interface between the  $\eta$  precipitate and the neighbouring grain ( $\sigma_{\eta\gamma_2}$ ) (30). Therefore, the grain boundary at the location of the  $\eta$  phase precipitate becomes serrated.

However, there have been observations of very long precipitates that extend deep into the  $\gamma$  matrix grains. This suggests that there is also another precipitate growth mechanism in addition to the discontinuous precipitation, which is the transformation of the  $\gamma'$  phase into  $\eta$  phase and the accumulation of diffusing elements into the  $\eta$  phase precipitate (30).

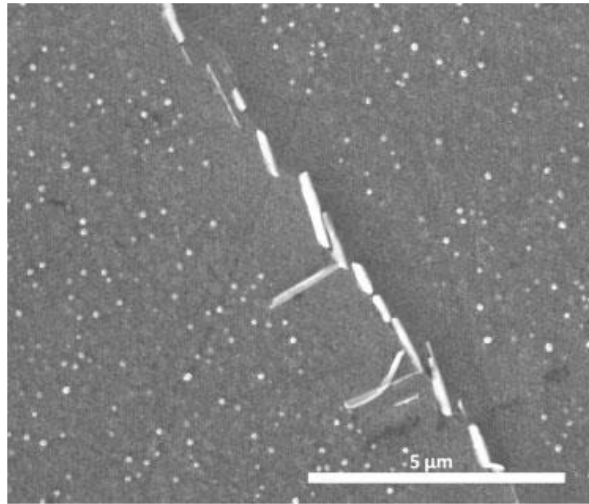


*Figure 2.19 – Microstructure containing  $\eta$  phase and  $\gamma'$  phase.  $\gamma'$  denuded zone can be observed around  $\eta$  precipitates (58)*

The  $\gamma'$  phase and the  $\eta$  phase both contain elements that exist in both phases, namely aluminium and niobium. In ATI 718Plus, both the  $\gamma'$  and  $\eta$  phase can precipitate simultaneously under certain temperatures and times. Due to this simultaneous precipitation, there is a competition between both phases for aluminium and niobium (36). Within ATI 718Plus, the microstructure contains a fine distribution of circular  $\gamma'$  phase particles. However, it can be observed that around the vicinity of the  $\eta$  phase precipitates, there is a zone which is devoid of  $\gamma'$  precipitates, which can be observed in Figure 2.19 (58). This indicates the competition between both phases (58). Due to shared chemical elements within their respective composition, a higher amount of  $\eta$  phase precipitation means a lower amount of  $\gamma'$  phase precipitation since the amount of  $\gamma'$  depleted zones would increase. This means that a higher amount of  $\eta$  phase precipitation would lower the intrinsic strength and hardness of the alloy (64).

### 2.3.6 TCP phases

Another group of phases that are sometimes found are those that are known as the ‘topologically closed packed’ (TCP) phases. These are generally detrimental to the mechanical properties and behaviour of nickel-based superalloys, and they are characteristically brittle. In trace amounts, these phases are not damaging. Anything



exceeding trace amounts can damage and weaken the mechanical properties of the superalloy. The TCP phases are namely (5):

- Sigma ( $\sigma$ ) phase
- Mu ( $\mu$ ) phase
- Laves phase

These phases (in particular, the  $\sigma$  phase) can be controlled by manipulating and adjusting the chemical composition of the superalloy. Interestingly, these phases are not necessarily always disadvantageous. Very minute amounts of  $\sigma$  phase can be advantageous for creep rupture strength. There have even been efforts to produce superalloys with the  $\sigma$  phase being the strengthening phase in the material (5).

The detrimental effects of the TCP phases do not arise solely from their brittleness. The disadvantageous properties can arise from the TCP phase morphology, volume fraction, and the degree to which the TCP phases diminish the  $\gamma$  matrix of elements that are needed for precipitation strengthening (5).

With high temperature homogenisation and thermo-mechanical processing, the TCP phases are generally not found in the as-received form of ATI 718Plus (3,4). However, without high temperature treatment and processing, the presence of Laves phase in the as-received condition of ATI 718Plus has been reported in the literature (68).

## **2.4 Effect of Strain**

A few studies have shown that induced strain within the microstructure does indeed affect the precipitation kinetics of grain boundary precipitates in nickel-based superalloys. This is especially important for manufacturers since the amount of  $\delta$  phase that is precipitated depends on the thermomechanical history of the material. Chamanfar et al. (69) found that in a non-isothermal forged billet of Inconel 718, the  $\delta$  phase precipitation during a subsequent heat treatment was considerably varied from the centre to the edge of the as-forged billet. This can be attributed to the variation in stress applied across the billet. Although it must be mentioned that the authors data was found to be highly scattered.

Liu et al. (70) and Mei et al. (71) carried out an extensive study of the cold rolling effect on the precipitation behaviour of the  $\delta$  phase within Inconel 718. It was found that cold rolling promotes the precipitation of  $\delta$  phase. The authors found that at 960°C, the recrystallisation of the  $\gamma$  matrix is completed well before the commencement of  $\delta$  precipitation. However, the increase in  $\delta$  phase precipitation kinetics from cold rolling is still observed. Due to the recrystallisation, dislocations created from cold rolling have been eradicated before the start of precipitation. Therefore, the theory that dislocations created from cold rolling increases the density of nucleation sites and increases the diffusivities of precipitate forming elements cannot be applied here. Instead, the authors attributed the faster kinetics of  $\delta$  phase to niobium segregation. At lower temperatures in which no or less recrystallisation occurs, the faster precipitation kinetics are a result of both niobium segregation and higher dislocation density from deformation, which leads to even faster  $\delta$  precipitation kinetics (23).

Huang and Langdon (46) looked at the evolution of  $\delta$  phase within Inconel 718 during optimum superplastic deformation conditions. The authors found that the total precipitation of  $\delta$  phase does increase with the level of strain during superplastic deformation, as it does with cold rolling (70,71).

A number of studies have found that the precipitate morphology gradually changes from needle/plate-like into blocky/globular as the strain increases (46,70–72). Differences in  $\delta$  phase morphology within Inconel 718 have been reported before in early literature (49), but the mechanisms by which this occurs was not well known. Zhang et al. (45) investigated the deformation characteristics of the  $\delta$  phase. During the deformation process, plate-like  $\delta$  phase develops into spherical  $\delta$  particles (44,45,50). This occurs due to two mechanisms. Firstly, the dissolution of plate-like  $\delta$  phase takes place while simultaneously, newer spherical  $\delta$  phase particles are precipitated. Secondly, as a result of dissolution breakage (in which parts of  $\delta$  plates are dissolved at high density dislocation zones) and deformation breakage (where  $\delta$  plates are broken as a result of deformation), the  $\delta$  plates are essentially broken into spherical  $\delta$  particles. Figure 2.12 (45) shows a schematic diagram of this process. Figure 2.20 (73) shows microscopy images of the growth and coarsening of  $\delta$

precipitates after heat treatment which was preceded by deformation. Also, in agreement with previously mentioned literature (46,70,71), the zone with the highest strain had seen all  $\delta$  plates transformed into spherical  $\delta$  particles.

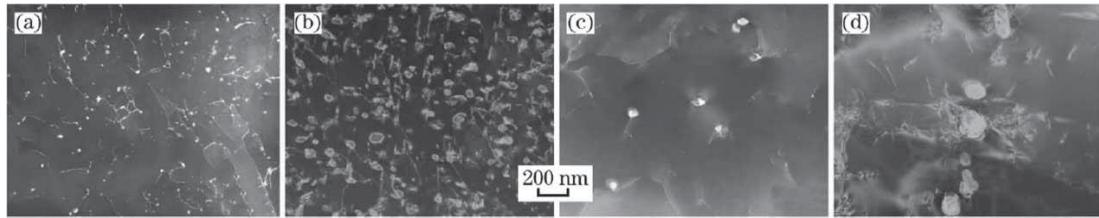


*Figure 2.20 – Growth and coarsening of  $\delta$  precipitates (a) 875°C at 100 s (b) 875°C at 1000 s (c) 975°C at 100 s (d) 975°C at 1000 s (73)*

Similar to Inconel 718, increasing the level of strain also causes increased  $\eta$  phase precipitation within ATI 718Plus (74,75). Casanova et al. (76) found that within the microstructure of components made with ATI 718Plus, two main morphologies co-exist together; coarse plates and thin lamellae, and the origin of these were investigated by the author.  $\eta$  phase precipitates are present within the microstructure of the billet prior to forging. During sub-solvus forging, these precipitates are deformed and unpinned from their initial nucleation locations. As a result of this, the interface between the  $\eta$  precipitates and the  $\gamma$  matrix becomes incoherent, which gives the  $\eta$  precipitates increased mobility. During following processing operations, these precipitates develop a coarse morphology. Also, their direction is more aligned with the local forging flow, which is an indication of their increased mobility. However, during the post-forging processing operations, new coherent  $\eta$  phase precipitates are formed. Since they are coherent, they grow into a fine lamellar morphology and thus, two morphologies of  $\eta$  phase exist within the final microstructure (76).

Another study from the same author (77) found that these morphologies even exist in different locations within the wrought billet during heating before sub-solvus forging takes place. The surface of the billet had coarse  $\eta$  plates which are result of high lattice rotations and high dislocation densities that come from the production process of the wrought billet. On the other hand, the centre of the billet consisted of large, recrystallised grains, which meant that there was no inherent strain in these zones. As

a result, the precipitates in the billet centre grew coherently into thin lamellae (77). It is interesting to note that the  $\eta$  phase does not become spherical nor does it go under the same mechanisms of becoming spherical like the  $\delta$  phase does within Inconel 718.

## 2.5 Review of Precipitation Kinetics

Inconel 718 has been in use since 1965 and within that time many authors have studied the  $\delta$  phase precipitation kinetics over the years (48,78–84). There seems to be a general acceptance that the nose of precipitation occurs between 910 and 920°C, although Beaubois et al. (48) disputes this and suggests that the nose of precipitation should be higher, somewhere between 960 and 980°C. The authors also suggest that the start of  $\delta$  phase precipitation starts earlier than what is mentioned in previous literature. The authors also investigated the precipitation kinetics with and without  $\delta$  phase in the initial microstructure and suggest that the difference in precipitation kinetics can be scaled according to the change in grain size (48). Azadian et al. (44) suggests 900°C as the nose temperature of  $\delta$  precipitation. It has been well established that deformation imposed on Inconel 718 can significantly cause  $\delta$  phase precipitation more rapidly (46,49,69–71). Figure 2.21 (71) shows the effect of cold rolling on the precipitation kinetics of  $\delta$  phase in Inconel 718.

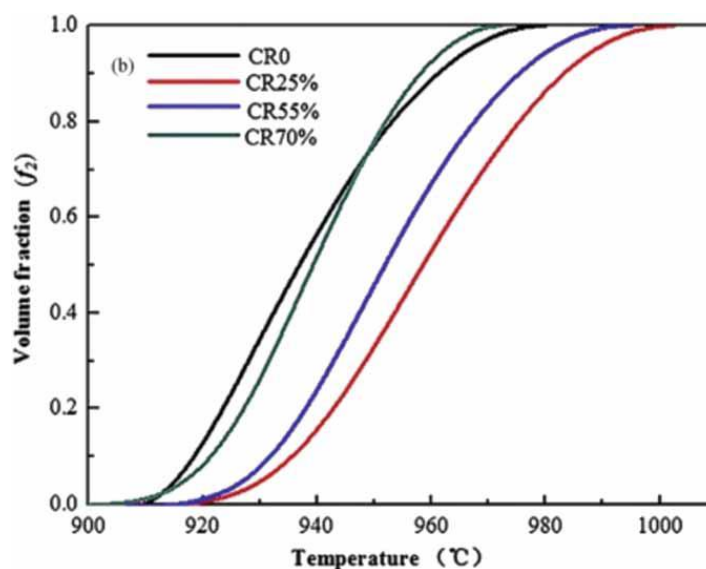


Figure 2.21 – Effect of cold rolling on the precipitation kinetics of  $\delta$  phase in Inconel 718 (71)

In regard to ATI 718Plus, Xie et al. (63) completed an early study into the  $\eta$  phase precipitation kinetics and compared them to the  $\delta$  phase precipitation kinetics. The authors had studied the growth kinetics from a 'clean' state, meaning that there were no  $\eta$  precipitates in the initial microstructures of Inconel 718 and ATI 718Plus. The grain size in the ATI 718Plus samples were 79  $\mu\text{m}$ , whereas within the Inconel 718 samples the grain size was 44  $\mu\text{m}$ . One would expect the kinetics in the ATI 718Plus samples to be slower since there is less grain boundary area for precipitation to occur. However, the difference in grain size in this study did not seem to matter as the precipitation kinetics of  $\eta$  phase in ATI 718Plus was faster than that of the  $\delta$  phase in Inconel 718. Stotter et al. (57) and Sommitsch et al. (85) also characterised the  $\eta$  phase precipitation kinetic behaviour. The authors found that the precipitation is sensitive to the nucleation sites, as precipitation occurred firstly on grain boundaries, then twin boundaries and then followed by precipitation within the bulk. Simulations can also be performed to determine precipitation kinetics. Zickler et al. (86) used the thermo-kinetic software MatCalc to perform simulations at different temperatures of the precipitation kinetics of both the  $\eta$  phase and the  $\gamma'$  phase. The simulations of  $\eta$  phase precipitation had good agreement with experimental data. However, discontinuities in the simulated TTT curves were observed at lower temperatures where precipitation of both  $\gamma'$  and  $\eta$  phases occurs simultaneously. This has been attributed to a competition of the diffusional transport of elements that constitute both phases namely aluminium and niobium (33,36,86). However, it would be of interest to obtain experimental volume fraction data at lower temperatures to see if these discontinuities can be validated. McDevitt (74) investigated the effect of thermomechanical processing on  $\eta$  phase precipitation in ATI 718Plus and found that the kinetics of precipitation are increased as the level of strain is increased. Casanova et al. (77) also reached the same conclusion in that areas with higher levels of strain produced faster precipitation kinetics. McDevitt (74) also found that  $\eta$  phase precipitation is inadequate during annealing after deforming the material at temperature above the  $\eta$  solvus temperature.

## **2.6 Effect of Grain Boundary Precipitation on Mechanical Properties**

The  $\delta$  and  $\eta$  phases within nickel superalloys are particularly useful for controlling the grain size, which significantly impacts the mechanical properties. This is done by a mechanism known as Zener pinning (55,87). However, it is established within the field that low quantities of  $\delta$  and  $\eta$  precipitation are sufficient for grain boundary control and that excessive amounts are actually detrimental to the mechanical properties of alloy.

Within ATI 718Plus, some studies have shown that the precipitation of  $\eta$  phase on the grain boundary can be very important in reducing the notch sensitivity of the alloy (22,61). Likewise for Inconel 718, it has been found that a lack of  $\delta$  phase causes an increase in notch sensitivity (50). The reason that brings about the notch sensitivity in both Inconel 718 and ATI 718Plus is due to the amount and distribution of  $\eta$  phase precipitates within the microstructure. Within ATI 718Plus, the  $\gamma'$  phase and the  $\eta$  phase both contain similar constituent elements, namely niobium, titanium and aluminium. As explained earlier (see Section 2.3.5), this causes a competition for these elements when simultaneous precipitation of both the  $\gamma'$  and  $\eta$  phases occurs. As a result, there is a  $\gamma'$  denuded zone around  $\eta$  phase precipitates (see Figure 2.19). This  $\gamma'$  depleted zone can behave as a micro-plastic zone. Therefore, in notch sensitivity testing, the high stress concentration at the root of the notch can be partially relaxed by the micro-plastic zone which would reduce notch sensitivity. Conversely, with no or too little  $\eta$  phase precipitates, there would be no  $\gamma'$  depleted zone and so the high stress concentration at the root of the notch cannot be relaxed, thereby increasing notch sensitivity and leading to the creation and growth of cracks (50).

The formation of  $\eta$  phase in ATI 718Plus can create serrated grain boundaries (30,88). Some studies find that these serrated grain boundaries can enhance resistance to intergranular fatigue cracking (22,62,89,90). It has been suggested that this occurs by the serrated grain boundaries forcing the intergranular cracks to take a more meandering path. However, other studies suggest that  $\eta$  phase in ATI 718Plus has no substantial effect on grain boundary resistance to environmental cracking during

rupture tests (53,91). The authors go on to propose that the factors that have more impact are grain dislocation substructure and grain boundary misorientation. Serrated grain boundaries have been found to prolong the creep life within Inconel 718 (92).

Conflicting reports have been reported regarding the effect of grain boundary precipitation on tensile properties and hardness. It has often been said that the precipitation of  $\delta$  phase within Inconel 718 and ATI 718Plus causes a degradation in mechanical properties (44,47,93–95). This is due to the transformation of  $\gamma''$  into  $\delta$  phase within the microstructure. Since  $\gamma''$  is the main strengthening phase, one would expect a loss in mechanical properties with a loss in  $\gamma''$ . However, Valle et al. (51) conducted a study regarding the effect of the  $\delta$  phase upon the tensile properties and hardness of Inconel 718. Intriguingly,  $\delta$  phase did not show much effect on the tensile strength, yield strength and hardness at room temperature, although the ductility was observed to decrease as the  $\delta$  phase volume fraction increases. However, a criticism of this work is the fact that the authors chose to study the mechanical properties over a very small range of  $\delta$  phase volume fraction, from 0.30 to 1.38%. This range may not be sufficient enough to observe a significant impact on the tensile properties and hardness. A study conducted by Zhang et al. (52) also agrees with Valle et al. (51) regarding the reduced ductility as  $\delta$  phase volume fraction increases. Zhang et al. (52) also found that the plasticity of Inconel 718 at high temperatures is reduced as the amount of  $\delta$  phase content is increased. Moreover, within Inconel 718, it has been shown that without any  $\delta$  phase present in the microstructure, the stress rupture life is doubled, while the creep elongation to failure is multiplied between 4 and 5, when in comparison to microstructures with  $\delta$  phase precipitation (54).

As mentioned previously, due to its morphology, the  $\eta$  phase does not add to the alloy hardness. Instead, the presence of  $\eta$  phase means a reduction in hardness as the  $\eta$  phase shares the same elemental composition as  $\gamma'$  phase, which is the primary strengthening phase in ATI 718Plus. A higher amount of  $\eta$  phase precipitation would mean a reduction in  $\gamma'$  content via more  $\gamma'$  depleted zones in the microstructure, which would cause a reduction in the strength and hardness of the alloy (64).

## 2.7 Summary

In this chapter, a literature review was given in which a broad range of aspects of superalloys are discussed. This included some background knowledge of superalloys and a review of the current literature in regard to the precipitation kinetics of secondary phases within Inconel 718 and ATI Plus. The effect of strain on the precipitation kinetics and the effect of secondary phases on the mechanical properties was also explored.

There is little work available in the literature regarding the effect on the  $\delta$  phase precipitation kinetics from forging strain, strain rate and initial grain size within Inconel 718. Considering that Inconel 718 predates ATI 718Plus considerably, no work has been published to date which has created TTT diagrams showing the effect of different strains, strain rates and initial grain sizes on the precipitation kinetics of  $\eta$  phase in ATI 718Plus. This work will intend to investigate the effect of strain, strain rate and initial grain size on the  $\eta$  phase precipitation kinetics within ATI 718Plus. Also, this work will also attempt to investigate  $\eta$  phase precipitation at the equilibrium state, as no work to date has been published in the current literature regarding this.

In the work carried out by Casanova et al. (77), it was concluded that the local strain conditions along a billet of ATI 718Plus material have a major influence on the  $\eta$  phase precipitate fraction, morphology and location. It was found that the centre of the billet has slower precipitation kinetics than the surface of the billet since the centre has primarily a structure consisting of large, recrystallised grains. Whereas the surface of the billet is mostly made up of smaller unrecrystallised grains and larger amounts of strain. However, within the work of Casanova et al. (77), it could be argued that the difference in grain size could have a larger impact on  $\eta$  phase precipitation kinetics than the amount of inherent strain. The author does not quantitatively investigate how strain and strain rate affect the  $\eta$  phase precipitation kinetics.

In the work carried out by McDevitt (74), it was concluded that the  $\eta$  phase precipitation is considerably affected by increasing amounts of strain within the



austenitic  $\gamma$  matrix. The author observed that by decreasing the amount of total height reduction (i.e., thereby increasing the amount of strain) or reducing the forging temperature has the effect of increasing the amount of  $\eta$  phase precipitation during subsequent solution annealing. However, in this work, the author looks at the effect of the 'global' strain of the sample on the  $\eta$  phase precipitation kinetics, rather than investigating the local strain within the sample. Also, the author does not investigate the effect of the strain rate and the effect of the initial grain size.

### 3 Experimental Methods

#### 3.1 Material

The raw material that was used in this study was as-received ATI 718Plus wrought hot rolled bar material with a diameter of 2.5 cm. The as-received material was provided in the solution treated condition in which the material had undergone heat treatment at 1750°F (approximately 954°C) for 1 hour and then air cooled. The material was melted and manufactured in the United States of America by ATI Speciality Materials Ltd and provided by Rolls-Royce Plc. The chemical composition of the as-received material was determined by ATI Specialty Materials Ltd as is shown in Table 3.1.

<b>C</b>	<b>S</b>	<b>Mn</b>	<b>Si</b>	<b>Cr</b>	<b>Mo</b>	<b>Co</b>	<b>Ti</b>	<b>Al</b>	<b>B</b>
0.020	<0.0003	0.030	0.050	18.000	2.690	9.170	0.750	1.460	0.005
0.020	<0.0003	0.030	0.050	18.000	2.690	9.170	0.750	1.460	0.005
<b>Zr</b>	<b>Fe</b>	<b>Cu</b>	<b>Ni</b>	<b>P</b>	<b>Nb</b>	<b>Ta</b>	<b>W</b>	<b>V</b>	<b>Y</b>
<0.01	9.350	0.010	51.550	0.005	5.500	<0.01	1.030	0.020	-
<0.01	9.370	0.010	51.580	0.006	5.490	<0.01	1.030	0.020	-
<b>Bi</b>	<b>Ca</b>	<b>Pb</b>	<b>Mg</b>	<b>Se</b>	<b>Ag</b>	<b>Sn</b>	<b>O</b>	<b>N</b>	
<0.00001	<0.001	<0.0001	0.0011	<0.00005	0.0001	<0.0005	<0.0005	0.0058	
<0.00001	<0.001	<0.0001	0.0014	<0.00005	<0.0001	<0.0005	<0.0005	0.0064	

*Table 3.1 – Chemical composition of as-received ATI 718Plus material*

The as-received material originated from heat number B91J and was produced using vacuum induction melting which was then followed by vacuum arc remelting. The grain size of the material was determined using EBSD and was found to be 12.8  $\mu\text{m} \pm 4.7 \mu\text{m}$  (standard deviation) which corresponds to ASTM 9.5.

#### 3.2 Mechanical Testing

To emulate the hot working process of forging, hot isostatic uniaxial compression testing was performed using cylindrical samples. Cylindrical samples with dimensions of 16 mm diameter and 24 mm height were machined from the as-received raw material. The specimens for the compression tests were taken from the middle area of

the as-received wrought bar, as this is where the material has a homogenous microstructure.

Hot compression tests were performed at the Advanced Forming Research Centre at the University of Strathclyde, Glasgow. The hot compression tests were performed at 990°C and at a global strain of 0.6. This strain was chosen after performing preliminary simulations of the hot compression test at different global strains using the DEFORM simulation software. These simulations were performed using the same test temperature and using the same sample dimensions as the real compression test and were performed by the R&D department at Aubert & Duval. From these simulations, it was decided that the simulation at 0.6 global strain would be best used for the actual hot compression tests as it provided a wide range of local strains within the sample which could be investigated. The test temperature (990°C) was chosen in order to replicate as much as possible the industrial forging process for ATI 718Plus at Aubert & Duval production facilities.

A servo-hydraulic Zwick/Roell Amsler HA machine was used to perform the hot compression tests and had a maximum load capacity of 250 kN. The machine was equipped with flat compression dies which were produced from single crystal CMSX-4 nickel alloy material, as well as a three-zone furnace (see Figure 3.1) which is used to perform elevated temperature testing.

As the intention of the hot compression testing is to imitate the hot forging process, the flat dies were heated to the same temperature as the sample to ensure isothermal conditions. Three thermocouples were placed inside the furnace to measure temperature; one at the top anvil, one at the anvil and lastly one was placed as close as possible to the test piece, which was approximately at mid-height of the furnace. The temperature was measured to  $\pm 5^\circ\text{C}$ .

Before the hot compression test, each sample top and bottom were coated with boron nitride in order to reduce the inevitable friction between the test piece and the flat dies. The cylindrical test piece was placed between the flat dies as the temperature of the

furnace was ramping up to 650°C. At this temperature, the furnace was positioned to envelop and surround the test piece as well as the flat dies. The furnace temperature was then increased to 990°C at a heating rate of 12°C per minute. Once the furnace temperature had reached 990°C, the test piece was soaked at temperature for 15 minutes after which the hot compression test was performed, with the strain rate staying constant via the use of the test machine software package. Upon completion of the test, the sample was taken out as quickly as possible and quenched in cold water.

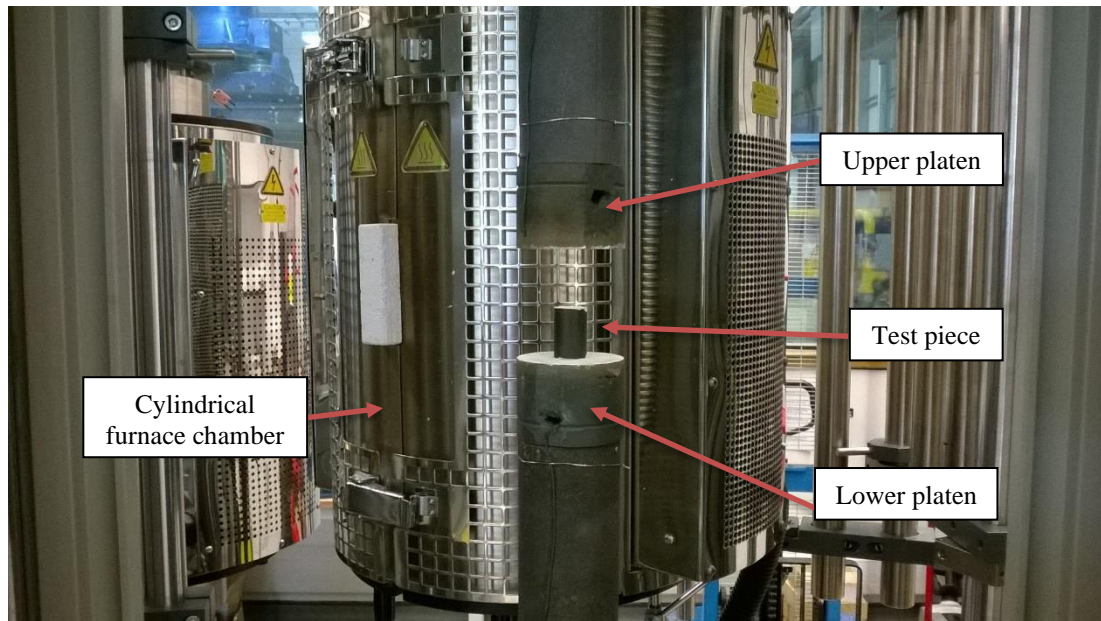


*Figure 3.1 – Furnace, flat dies and test piece used in hot compression testing*

Hot torsion testing was also performed in this study in Chapter 7. This was performed at the laboratory facilities at Aubert & Duval in Les Ancizes, France. Due to intellectual property reasons, some information in regard to the set-up of the testing apparatus cannot be disclosed here, however similar conditions involved in the hot compression testing were also pertinent to the hot torsion testing that was carried out.

### **3.3 Heat Treatment**

After hot compression or torsion testing, heat treatments were performed to promote  $\eta$  phase precipitation at different times and temperatures. The furnace that was used to apply such heat treatments was a Carbolite RHF 1400 furnace chamber (see Figure

3.2) The furnace machine was heated to the applicable temperature at a slow heating rate in order not to damage the heating filaments. In order for the furnace to reach the high temperatures used in this study, the furnace was programmed to ramp up to a particular temperature overnight until the desired temperature had been reached. In all the heat treatments performed within this study, the cooling method was always water quenching. Once the heat treatment had been finished, the sample was taken out promptly and inserted into a water bucket within 5 seconds.

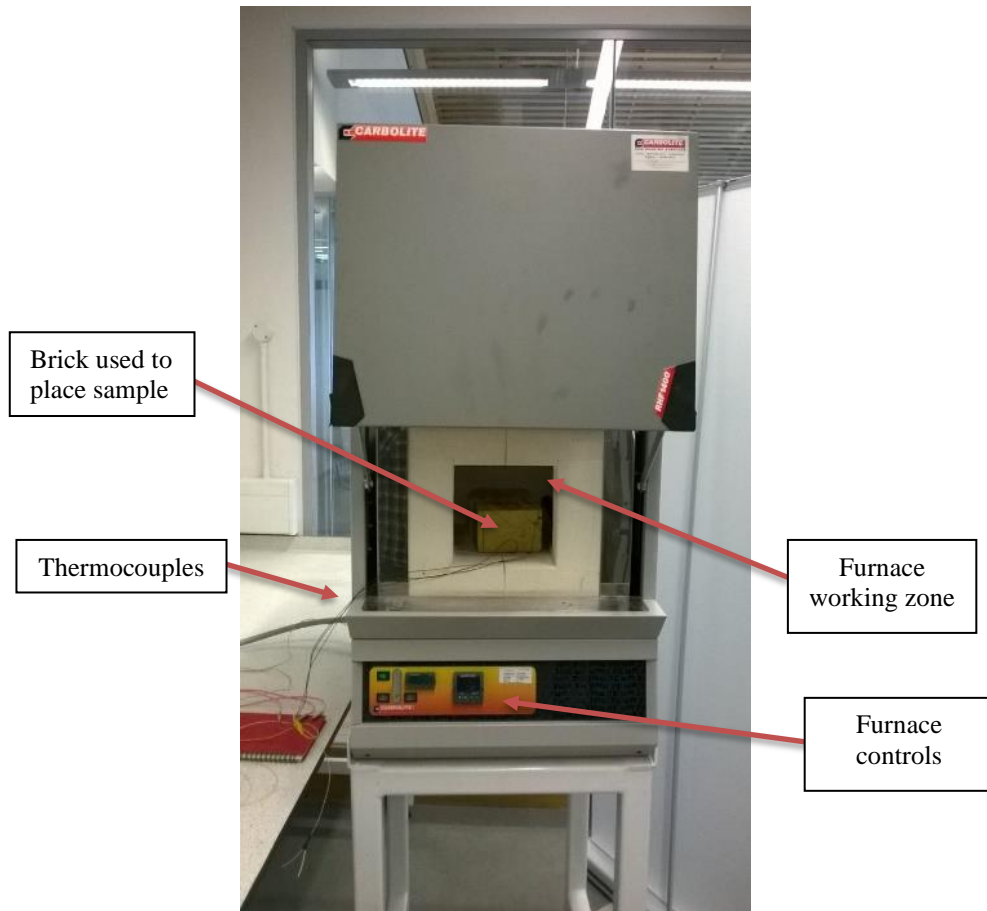


*Figure 3.2 – Carbolite RHF 1400 furnace chamber*

### **3.4 Sample Preparation**

After processing and heat treatment, it is necessary to mount the sample in a conductive resin so that the sample can be securely placed during the subsequent grinding, polishing and microscopy. Therefore, sample mounting was carried out via the use of a Buehler SimpliMet 3000 machine, which is shown in Figure 3.3. The

sample is placed on the centre of the mounting piston, with the face to be examined positioned face down. The mounting piston is then lowered, and a conductive resin powder is added, of which approximately 2 and ½ scoops are used. The commercial name of the conductive resin is ProbeMet and is also produced by Buehler. With the piston and conductive resin lowered, the shaft is then closed securely. The start button is then pressed which initiates the SimpliMet 3000 machine. The process requires 1 minute of heating, followed by 3 minutes of cooling after which the mounting process is complete. The heating is performed at 150°C with a pressure of 290 bar. After the mounting process is complete, piston is raised up and the mounted sample is removed. The diameter of the mounted sample was fixed to be 25 mm.



*Figure 3.3 – SimpliMet 3000 mounting machine*

Once the specimens have been mounted, it is necessary to grind and polish the samples so that they are flat and without any scratches. For this purpose, the Buehler EcoMet 300 Pro machine was utilised. This machine is shown in Figure 3.4. The specimens

are held together using a specimen holder (maximum capacity of 6 specimens at any one time) which rotates. Special abrasive grinding papers are used to grind the specimens, and then polishing cloths are used in the polishing stages. These grinding papers and polishing clothes rotate either in complimentary direction to that of the specimen holder or contrary direction to the specimen holder. The polishing and grinding cloths have different grit sizes and are of various types. During the grinding stages, water is used as a lubricant, whereas during the polishing stages, a special diamond paste lubricant is used. The preparation methods that were used for grinding and polishing the ATI 718Plus specimens are shown in Table 3.2 and Table 3.3 respectively. The samples were thoroughly rinsed in between stages and were also ultrasonic bathed after grinding and after polishing.



*Figure 3.4 – EcoMet 300 Pro grinding/polishing machine*

<b>Grinding Paper</b>	<b>Rotation</b>	<b>Force (N)</b>	<b>Speed (rpm)</b>	<b>Time (minutes)</b>
CarbiMet SiC P240	Comp	27	260	Until plane
CarbiMet SiC P400	Comp	27	260	Until plane
CarbiMet SiC P800	Comp	27	260	Until place
CarbiMet SiC P1200	Comp	27	260	Until plane

*Table 3.2 – Grinding procedure used for ATI 718Plus*

<b>Polishing Cloth</b>	<b>Rotation</b>	<b>Force (N)</b>	<b>Speed (rpm)</b>	<b>Time (minutes)</b>
UltraPol 9 $\mu\text{m}$ with 9 $\mu\text{m}$ MetaDi Polycrystalline Diamond Suspension	Contra	25	150	4
Trident 3 $\mu\text{m}$ with 3 $\mu\text{m}$ MetaDi Polycrystalline Diamond Suspension	Contra	22	150	5
TexMet 1 $\mu\text{m}$ with 1 $\mu\text{m}$ MetaDi Polycrystalline Diamond Suspension	Contra	20	150	6
Microcloth 0.05 $\mu\text{m}$ with 0.02 $\mu\text{m}$ MasterMet Colloidal Silica	Contra	20	150	5

*Table 3.3 – Polishing procedure used for ATI 718Plus*

### **3.5 Microscopy**

To obtain microstructural images from the samples of ATI 718Plus, a scanning electron microscope (SEM) was utilised (see Figure 3.5). The model of the SEM was an FEI Quanta FEG 250. Backscattered electron (BSE) imaging was used as it provided the best imaging for the quantification of  $\eta$  phase precipitation. This is because  $\eta$  phase has a higher amount of niobium, and niobium inherently has a large atomic number. Therefore, the  $\eta$  phase is highly discernible in comparison to the austenitic  $\gamma$  matrix.

Backscattered electrons are produced when the incident electron beam is elastically scattered. They are highly energised and come from a larger volume of the material sample. If elastic scattering occurs with an atomically heavy element, the electrons can travel greater distance than in comparison to a lighter element. Therefore, the atomic number  $Z$  is represented via the contrast of the backscattered image. In all imaging that was conducted via the SEM, the working distance was always set to 10 mm, and



the magnification of the images that were used for quantification was always 3000X. The spot size of the electron beam was consistently set to 4.5.

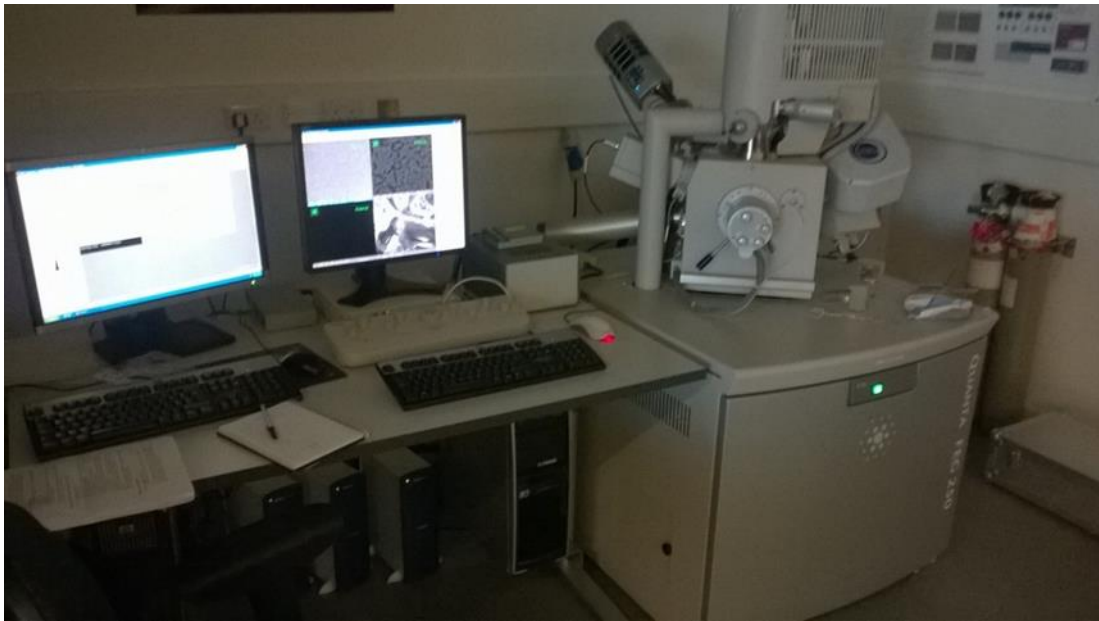


*Figure 3.5 – FEI Quanta FEG 250 scanning electron microscope*

Electron backscattered diffraction (EBSD) was also utilised during this study to obtain good approximations of the microstructural grain size. In EBSD, the sample is placed in the SEM and is tilted to  $70^\circ$ . An EBSD camera/detector is inserted via the use of a motorised carriage as close as possible to the tilted sample (usually within millimetres to the sample). The electron beam is directed towards the sample and as it impinges on the surface of the sample, the electron beam is incoherently and elastically scattered in all directions. The scattered electrons form a Kossel cone which represents a particular diffracted plane. The Kossel cone forms a Kikuchi line when the Kossel cone intersects with the phosphor screen of the EBSD camera/detector. Together the Kikuchi lines form a Kikuchi pattern which is particular to each crystal orientation. The Kikuchi pattern is then analysed and processed digitally by the EBSD camera/detector to index the pattern and determine the orientation and phase of the crystal.

In this study, the EBSD camera/detector that was used was produced from Oxford Instruments and the software used to index the sample was the Tango module of the

HKL Channel 5 software. To process the EBSD images after capture, another module of the HKL Channel 5 software package, known as Tango, was utilised. When performing EBSD, the voltage was set to 20 kV and the spot size was set to 4. After tilting the stage by 70°, the working distance was approximately 19.3 mm. The index rate during EBSD fluctuated between 90% to 95%.

When determining the grain size of any sample, twin boundaries were not considered as a grain boundary, however the EBSD maps shown in this work will also show twin boundaries.

### **3.6 Microstructural Analysis**

In order to quantify the  $\eta$  phase precipitates more easily, Adobe Photoshop was used to adjust the contrast and filtering of the image. The “Smart Sharpen” was first used to brighten the  $\eta$  phase precipitates, and then the “Dust & Scratches” feature was then used to remove as much of the background in the  $\gamma$  matrix as possible.

ImageJ analysis software was utilised to convert the microstructural images into binary format. To obtain more accurate data, the  $\gamma$  matrix was coloured black using the paint brush tool within ImageJ. This meant that only the  $\eta$  phase precipitates were left visible in the microstructural image. A threshold was set to distinguish between the  $\eta$  phase precipitate and the rest of the microstructural image to provide an area percentage of  $\eta$  phase precipitation relative to the whole microstructural image.

For the data where the length and width of the  $\eta$  phase precipitates was measured, the measurement tool within ImageJ was calibrated against the scale bar of the microstructural image. Then the length and width were then measured by clicking at the longitudinal and transverse ends of the  $\eta$  phase precipitate being measured.

## **4 Precipitation at the Equilibrium State**

### **4.1 Introduction**

In this study, the  $\eta$  phase precipitation was studied at their equilibrium point, meaning the point at which no further  $\eta$  phase precipitation can thermodynamically occur within the microstructure. To perform this study, strained and deformed samples of ATI 718Plus were heat treated at various temperatures for extended periods of time. SEM examination was then carried out to obtain an approximation of the  $\eta$  phase area fraction as well as average aspect ratio, length and thickness. The experimental matrix for this study is shown in Table 4.1.

The times (in hours) chosen for this study were selected to ensure that the  $\eta$  phase equilibrium state had been reached according to the published literature available. The only other work which has slightly touched upon this is the work conducted by Casanova et al. (77) in which samples of ATI 718Plus were heat treated for 81 hours. The author of the work investigated the  $\eta$  phase equilibrium state at both the core region and rim region of a wrought billet. The core region consisted of large, recrystallised grains (with either low or no strain levels) while the rim region consisted of smaller unrecrystallised grains with higher strain levels. The work confidently suggests that the equilibrium state had been reached at both the core and rim regions after 81 hours of heat treatment. Based on this, it was decided to use heat treatment times between 72 to 75 hours but with induced strain in the starting material to further accelerate the  $\eta$  phase precipitation kinetics to ensure that the equilibrium state had been reached.

Temperature (°C)	Time (hours)
850	75
875	75
900	72
925	74
950	72
975	72

*Table 4.1 – Experimental matrix for  $\eta$  phase precipitation at the equilibrium state*

In order to carry out this study, a number of tensile tests were performed with ATI 718Plus material. This was done in order to accelerate the rate of  $\eta$  phase precipitation so that the equilibrium state could be reached more quicker during the subsequent heat treatment. These tensile tests were performed at room temperature with 0.1 strain and with a strain rate of  $0.05 \text{ min}^{-1}$  (which translate to approximately  $0.00083 \text{ s}^{-1}$ ). No local necking was observed on the tensile test samples which indicates that the deformation occurred homogenously. Figure 4.1 displays an example of a tensile test sample prior to deformation with the dimensions of the working zone labelled.

The initial grain size of the material prior to tensile testing is the same as the material in the as-received condition, which is approximately ASTM 9.5. More details on the as-received material are found in Chapter 3 Section 3.1.

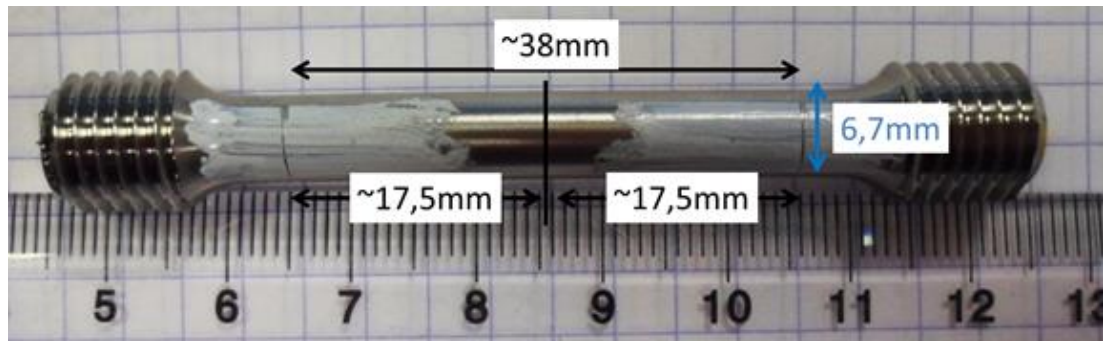


*Figure 4.1 – Tensile test sample prior to deformation with labelled working zone dimensions*

After carrying out these tensile tests, the subsequent samples were then machined to produce multiple sample pieces that could then be heat treated individually according to Table 4.1. These samples were not solutioned in order to ‘clean’ the initial

microstructure of  $\eta$  phase area fraction because the intention of this study is to obtain the maximum area fraction, length and thickness at each temperature.

After extended heat treatment (see Table 4.1), the samples were then mounted, ground and polished as described previously in Chapter 3 Section 3.4. SEM was then employed to obtain multiple microstructural images at random locations within the sample. From these images, the average  $\eta$  phase area fraction was calculated as well as the average  $\eta$  phase length and thickness at each temperature.

The average equilibrium area fraction values are obtained by averaging the measurements taken from three microstructural images. It was thought that three images would be sufficient to obtain a good representation of the sample. Also, using three images per data point was more feasible because the image processing technique used to obtain the  $\eta$  phase area fraction (as described in Chapter 3) was considerably time consuming, and due to time constraints more images per data point was not practically possible. For the aspect ratio, length and thickness measurements, ten values were used for each data point, again due to time constraints and feasibility issues.

## 4.2 Equilibrium Area Fraction

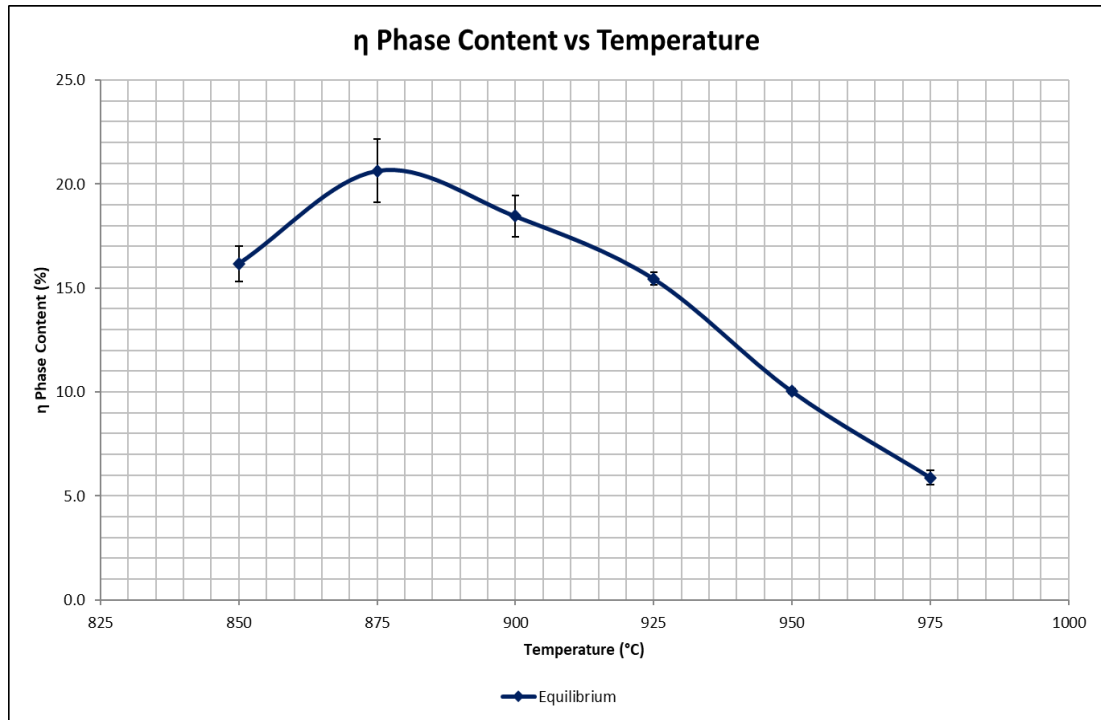


Figure 4.2 –  $\eta$  phase area fraction against temperature in the equilibrium state

Area Fraction (%)					
850°C	875°C	900°C	925°C	950°C	975°C
16.18 ± 0.85	20.64 ± 1.52	18.46 ± 0.98	15.45 ± 0.29	10.03 ± 0.13	5.88 ± 0.35

Table 4.2 – Results of  $\eta$  phase area fraction in the equilibrium state

In Figure 4.2, the  $\eta$  phase area fraction at each temperature in the equilibrium state is displayed with the numerical values shown in Table 4.2. The errors shown in Figure 4.2 and Table 4.2 are standard errors.

Microstructural images are displayed from Figure 4.3 to Figure 4.8. The equilibrium area fraction is observed to increase from 850°C to 875°C. Interestingly, the highest amount of equilibrium area fraction is found at 875°C. From there, a gradual decline is seen from 875°C to 975°C. As is shown in Figure 4.3 to Figure 4.8, many acicular precipitates are observed within the microstructures (especially at the lower temperatures), which makes it difficult to threshold properly and hence introduces a source of error within the results.

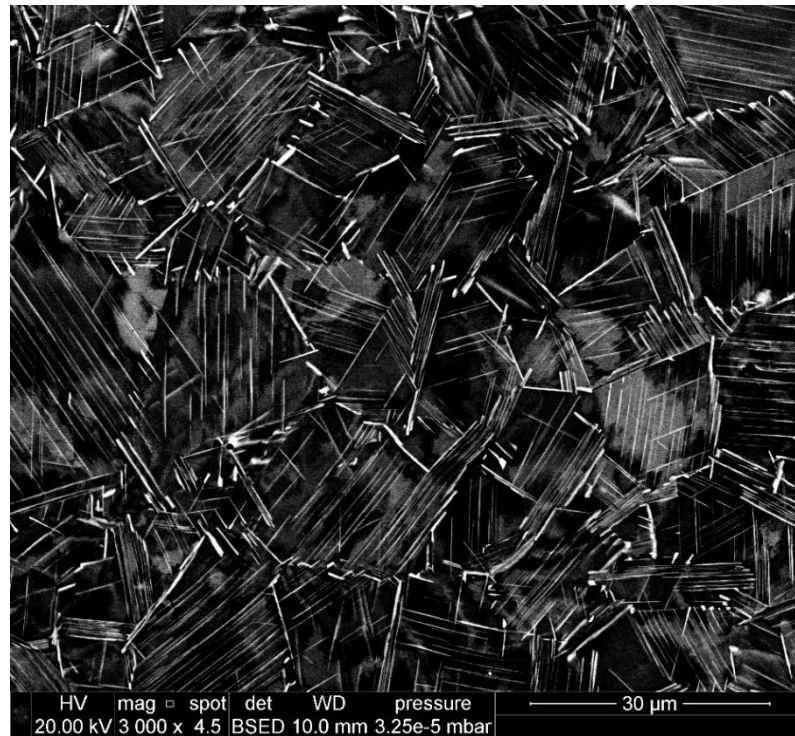


*Figure 4.3 – Microstructure of ATI 718Plus at 0.1 strain with  $0.00083\text{ s}^{-1}$  strain rate and after heat treatment at  $850^{\circ}\text{C}$  for 75 hours*

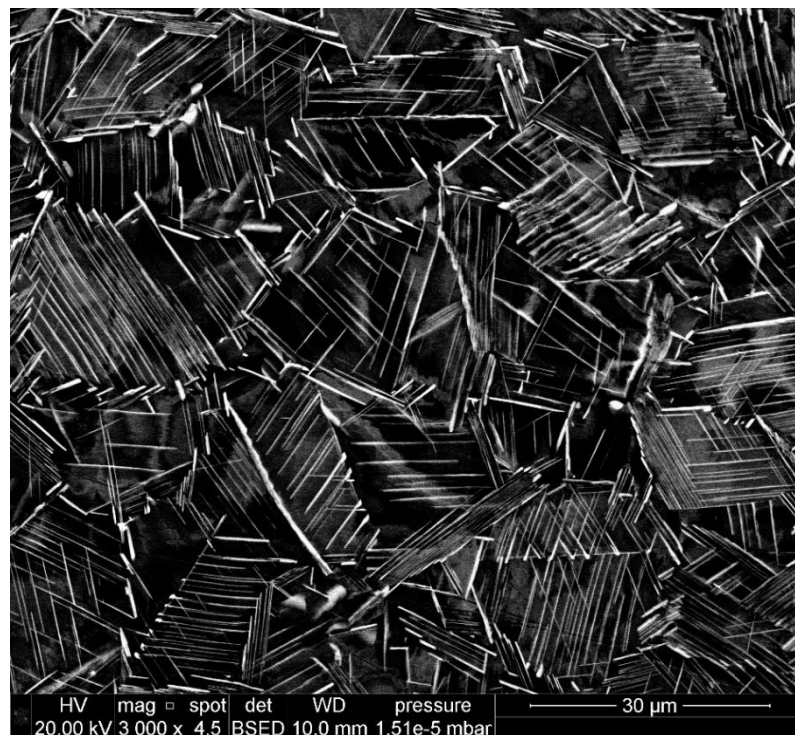


*Figure 4.4 – Microstructure of ATI 718Plus at 0.1 strain with  $0.00083\text{ s}^{-1}$  strain rate and after heat treatment at  $875^{\circ}\text{C}$  for 75 hours*

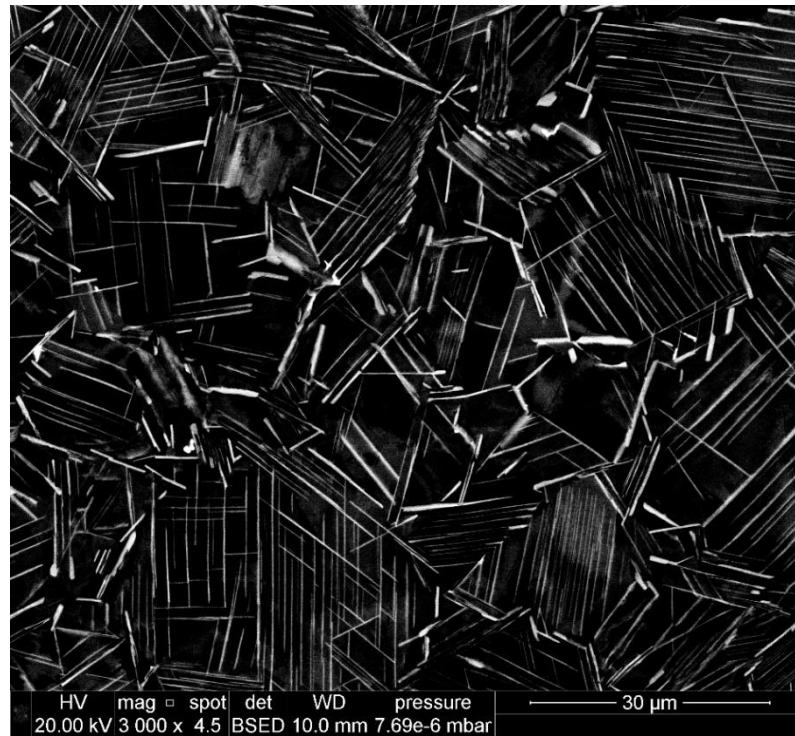


*Figure 4.5 – Microstructure of ATI 718Plus at 0.1 strain with  $0.00083\text{ s}^{-1}$  strain rate and after heat treatment at  $900^{\circ}\text{C}$  for 72 hours*

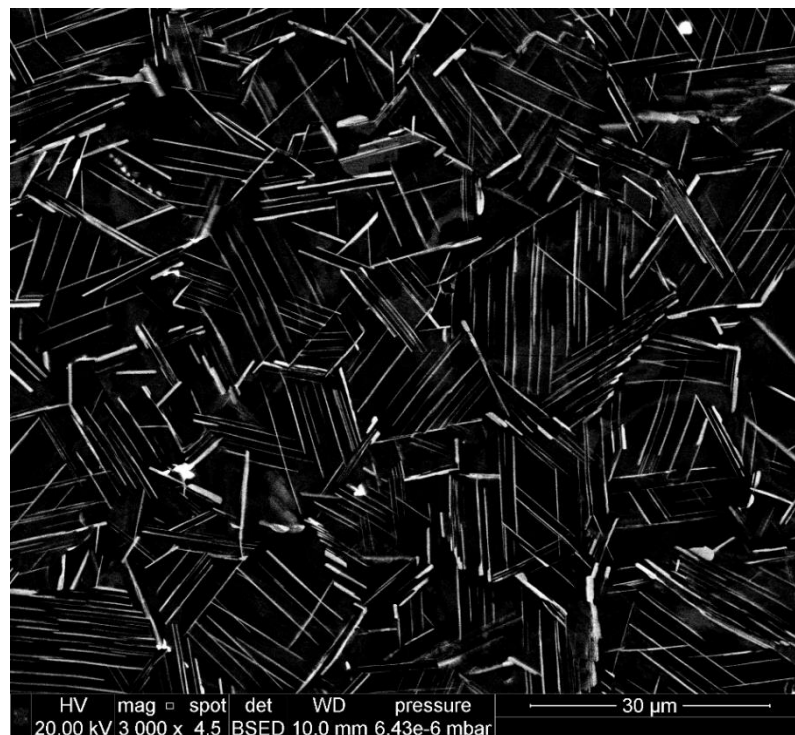


*Figure 4.6 – Microstructure of ATI 718Plus at 0.1 strain with  $0.00083\text{ s}^{-1}$  strain rate and after heat treatment at  $925^{\circ}\text{C}$  for 74 hours*



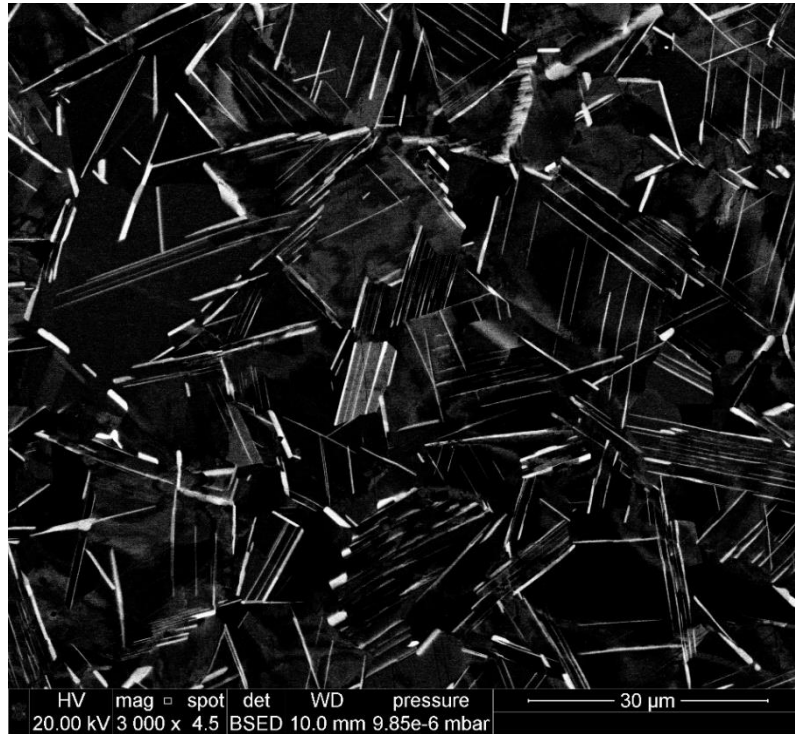


*Figure 4.7 – Microstructure of ATI 718Plus at 0.1 strain with  $0.00083\text{ s}^{-1}$  strain rate and after heat treatment at  $950^{\circ}\text{C}$  for 72 hours*

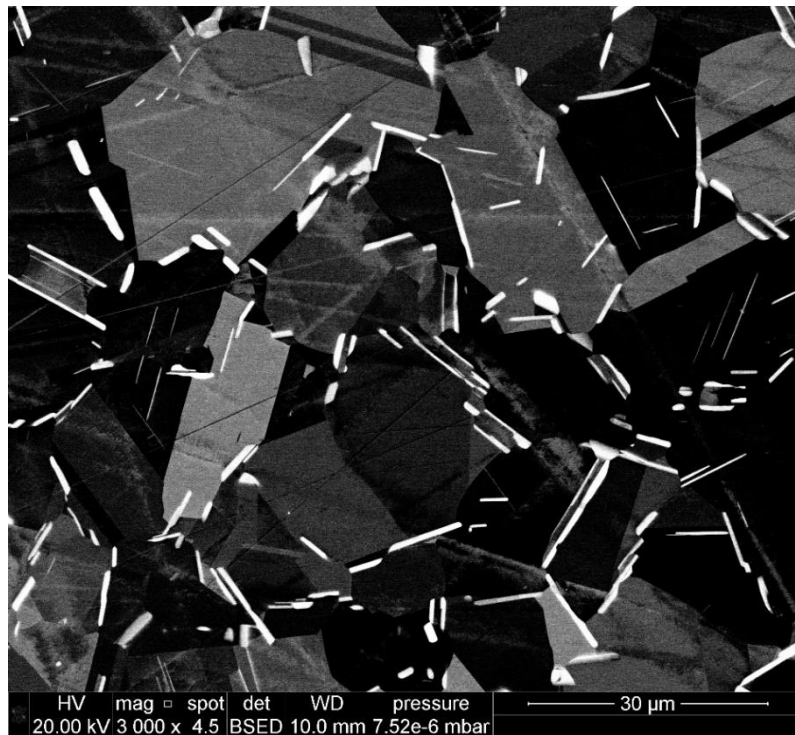


*Figure 4.8 – Microstructure of ATI 718Plus at 0.1 strain with  $0.00083\text{ s}^{-1}$  strain rate and after heat treatment at  $975^{\circ}\text{C}$  for 72 hours*

It is observed at all temperatures studied, intragranular precipitation occurs within the grains along preferred crystallographic planes. This suggests that  $\eta$  phase precipitation has occurred on slip bands that were formed during plastic deformation from the tensile test. The precipitation of  $\eta/\delta$  phase along slip bands has also been reported in other studies (96,97). Singh et al. (96) had discovered that slip bands that were produced from cold rolling were behaving as nucleation sites for  $\delta$  phase precipitation in Inconel 718. Gabb et al. (97) had also observed intragranular precipitation along preferred crystallographic planes in ATI 718Plus, which further supports that  $\eta$  phase precipitation occurs on slip bands formed from plastic deformation.

### 4.3 Aspect Ratio

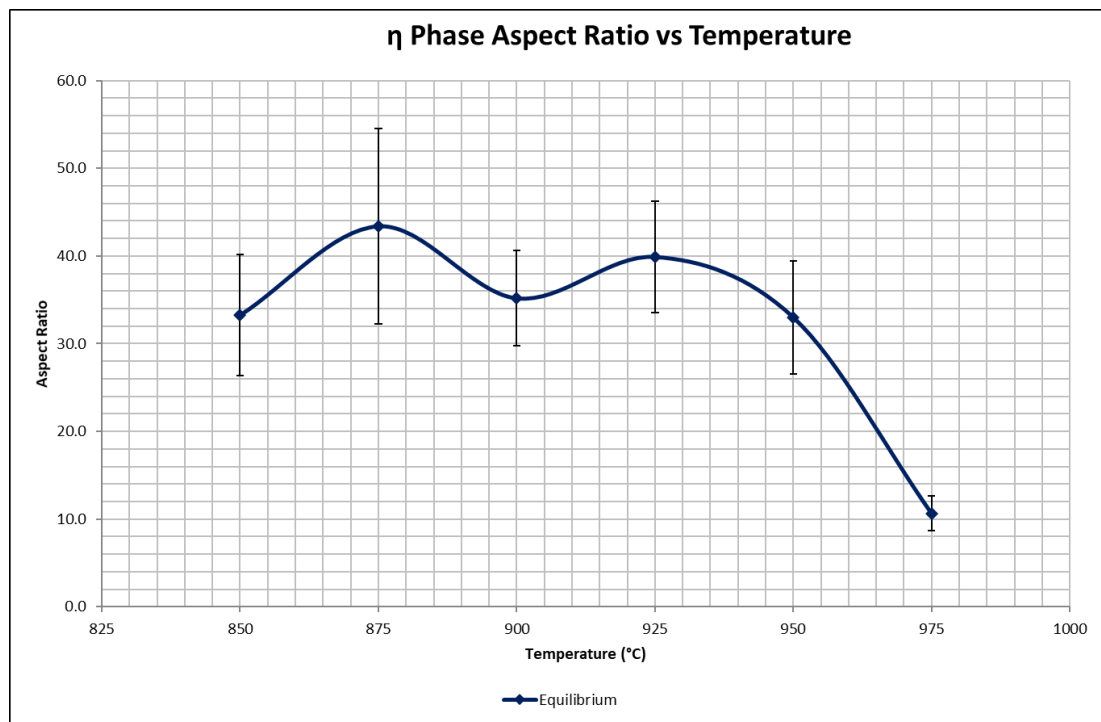


Figure 4.9 –  $\eta$  phase precipitate aspect ratio against temperature in the equilibrium state

Aspect Ratio					
850°C	875°C	900°C	925°C	950°C	975°C
33.25 ± 6.89	43.40 ± 11.12	35.18 ± 5.46	39.90 ± 6.32	33.02 ± 6.46	10.66 ± 2.02

Table 4.3 – Numerical results of  $\eta$  phase aspect ratio in the equilibrium state

Figure 4.9 shows the  $\eta$  phase aspect ratio at equilibrium between 850°C and 975°C and Table 4.3 shows the numerical results alongside the standard errors. The aspect ratio by and large stays the same between 850°C and 925°C, although fluctuations are observed in between the two temperatures. The aspect ratio is by definition the length of a single precipitate divided by its thickness. A higher aspect ratio implies the presence of more acicular needle shaped precipitates, whereas a lower aspect ratio implies the presence of more thicker or globular shaped precipitates. The fluctuations between 850°C and 925°C could be associated with the continuous precipitation occurring in the microstructure, which would start off more globular in nature and hence would have the effect of lowering the average aspect ratio. However, at the same time, earlier existing  $\eta$  phase precipitates would grow more longer in length which would be more acicular in nature, which has the effect of increasing the aspect ratio. Therefore, the final equilibrium aspect ratio could be essentially an amalgamation of these two phenomena. However, it can also be argued that the differences in aspect ratio from 850°C to 925°C are not significant enough to consider the values as completely different to each other. This is also supported by the fact that the values from 850°C to 925°C are all within each other's standard deviation. This suggests that equilibrium has in fact been achieved. The only reason why the value at 900°C is slightly lower than the values at 875°C and 925°C is that thickness at 900°C is very slightly higher in comparison to the previously mentioned temperatures.

From 925°C to 975°C, the average equilibrium aspect ratio is observed to decrease because the  $\eta$  phase equilibrium thickness is observed to increase during this temperature range. By looking at Figure 4.7 and Figure 4.8, it is observed that the precipitates within the microstructure are becoming thicker at equilibrium as the temperature increases.

#### 4.4 Length

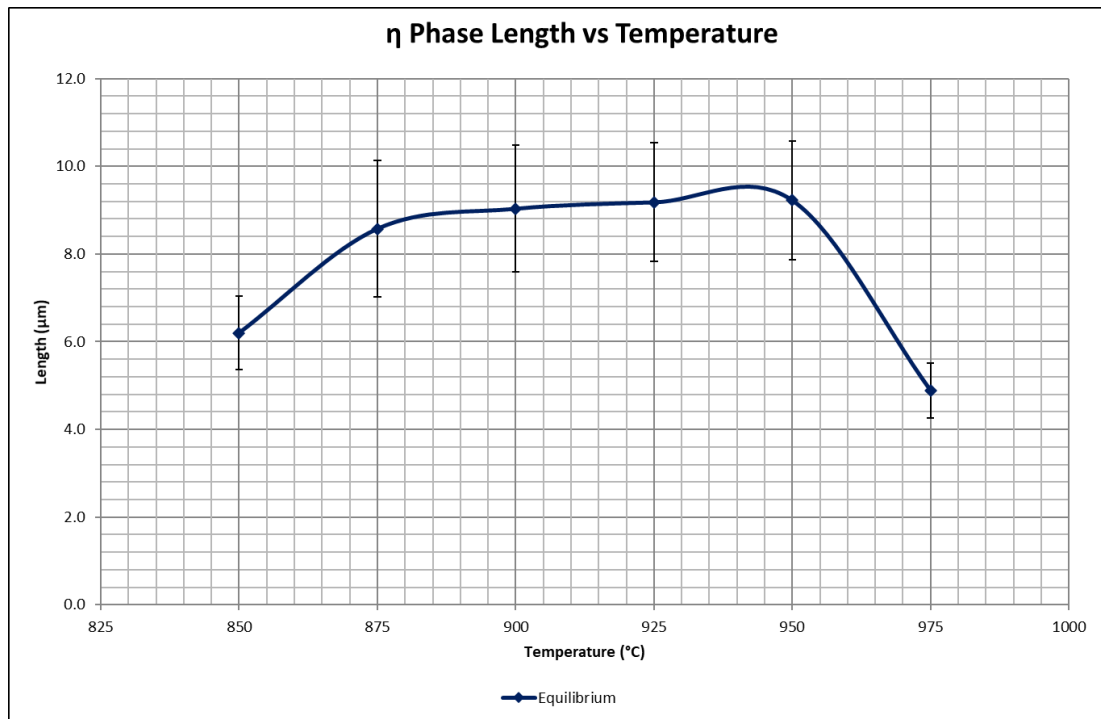


Figure 4.10 –  $\eta$  phase precipitate length against temperature in the equilibrium state

Length ( $\mu\text{m}$ )					
850°C	875°C	900°C	925°C	950°C	975°C
6.20 ± 0.84	8.58 ± 1.56	9.03 ± 1.44	9.18 ± 1.35	9.23 ± 1.36	4.89 ± 0.63

Table 4.4 – Numerical results of  $\eta$  phase length in the equilibrium state

The  $\eta$  phase length at equilibrium is shown as a function of temperature in Figure 4.10 with the tabulated results shown in Table 4.4. As observed, the  $\eta$  phase precipitate length increases from 850°C to 875°C, and then stays approximately constant between 875°C to 950°C. From 950°C to 975°C, a stark decline in precipitate length is observed and can be seen in Figure 4.8.

#### 4.5 Thickness

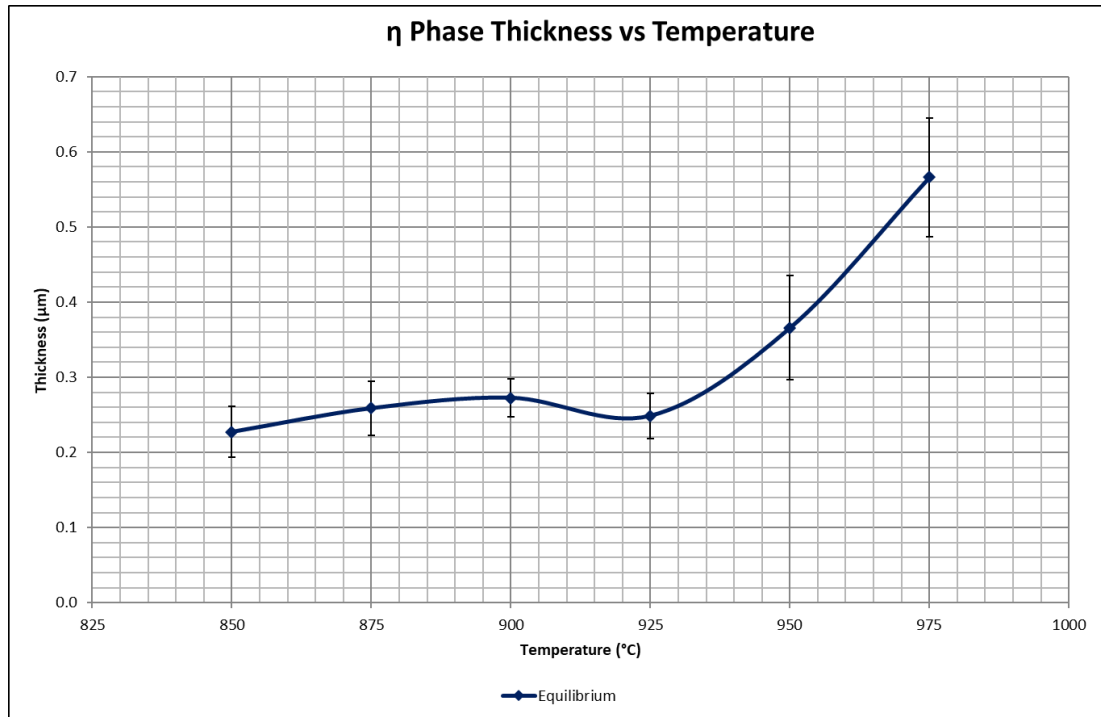


*Figure 4.11 – η phase precipitate thickness against temperature in the equilibrium state*

Thickness (μm)					
850°C	875°C	900°C	925°C	950°C	975°C
0.23 ± 0.03	0.26 ± 0.04	0.27 ± 0.03	0.25 ± 0.03	0.37 ± 0.07	0.57 ± 0.08

*Table 4.5 – Results of η phase thickness in the equilibrium state*

The η phase thickness at equilibrium is shown as a function of temperature in Figure 4.11 with the numerical results tabulated in Table 4.5. It can be seen that the maximum η phase precipitate thickness is approximately the same value between 850°C and 925°C. From 925°C to 975°C, the equilibrium η phase thickness increases. This gradual increase in thickness can be seen in Figure 4.6, Figure 4.7 and Figure 4.8.

## 4.6 Discussion

Within the published literature, very little existing data has been published regarding the equilibrium precipitation of ATI 718Plus. Only a couple of authors have published any work regarding the  $\eta$  phase equilibrium area fraction and in fact no published data has been found regarding the  $\eta$  phase aspect ratio, length and thickness at the equilibrium state. Equilibrium  $\eta$  phase area fraction data has been published by Casanova et al. (77) in which heat treatments were performed for 81 hours. However, only two temperatures were studied in this work: 900°C and 960°C. Also, the location of measurement was also considered in the work of Casanova et al. (77) in which the equilibrium  $\eta$  phase area fraction was measured at both the rim and core locations of the as received wrought billet. Cao (22) studied the equilibrium  $\eta$  phase area fraction quite early on in the development of ATI 718Plus. The author mentions that isothermal annealing experiments were conducted to obtain the experimental data, but no further details are provided such as the length of time taken in heat treatment for example. The author also produced calculated results via modelling but only the experimental data is shown in Figure 4.12.

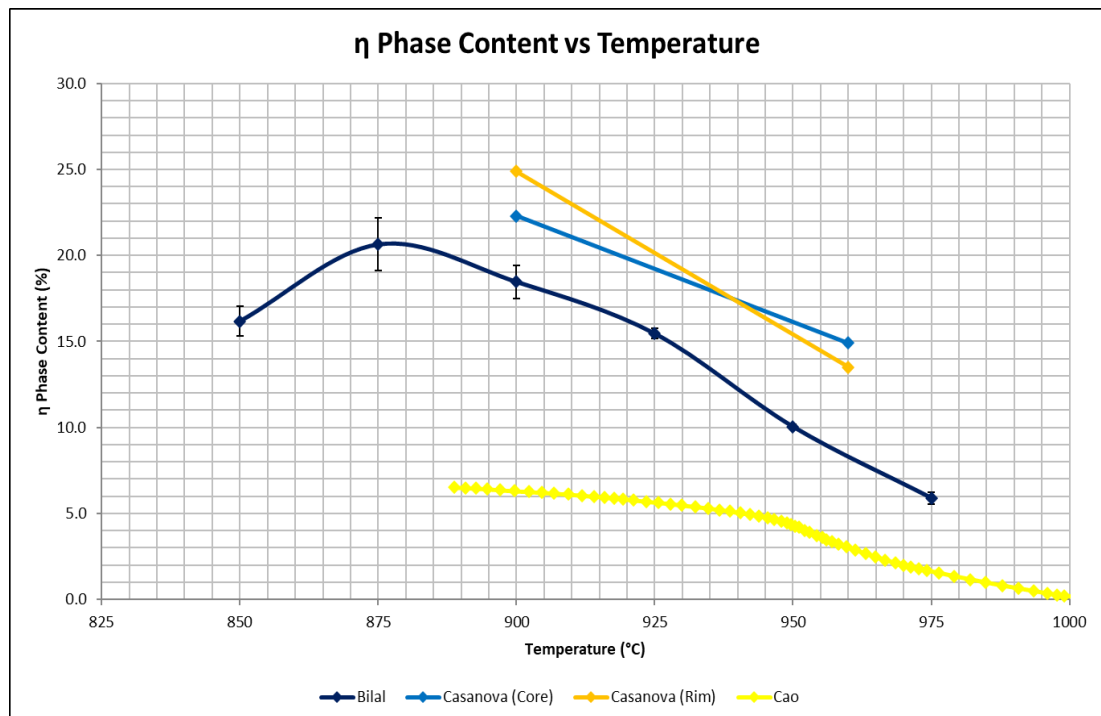


Figure 4.12 – Equilibrium  $\eta$  phase area fraction compared to published data

The close proximity of the equilibrium  $\eta$  phase content data from the core and rim locations of the as-received wrought billet studied in Casanova et al. (77) suggests that the equilibrium point has been reached at both locations (77). It is observed that the data from Casanova et al. (77) follows the same trajectory as the data obtained in the current work for the same temperature range that Casanova et al. (77) had studied. However, there are considerable quantitative differences between the two sets of data. This potentially could be due to the fact that in the study by Casanova et al. (77), the samples were electrolytically etched in 10% phosphoric acid in distilled water at 2.5V. This accentuates the  $\eta$  phase precipitates which falsely increases the  $\eta$  phase area fraction, hence the quantitative difference with the data obtained in this work. As for the Cao (22) curve, it is more flatter initially but then decreases more starkly from 950°C onwards. The quantitative differences between the data from Cao (22) and the data obtained in this study are significantly and surprisingly large. The author does not mention much information regarding the experimental methodology and the data capture method, apart from mentioning that isothermal annealing experiments were conducted. Due to the lack of details, it is difficult to theorise why such large differences are found between the authors data and the data within the current study.

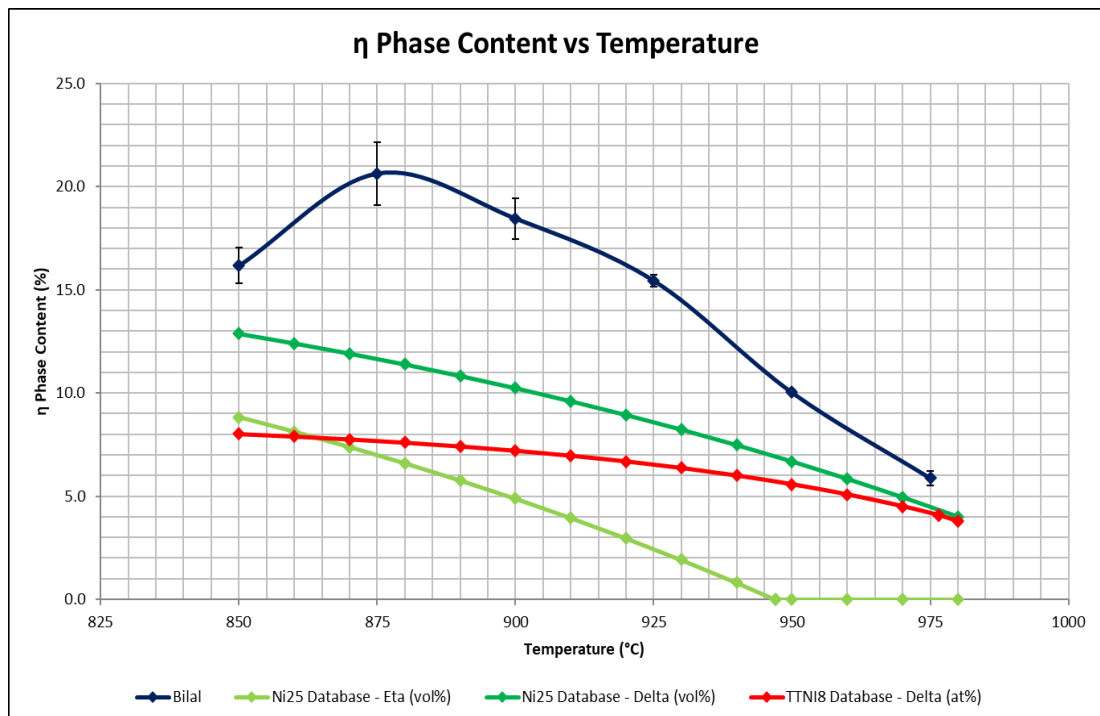


Figure 4.13 – Equilibrium  $\eta$  phase area fraction compared to data from simulations

In Figure 4.13, the experimental data obtained in this study is compared to data obtained from simulations that were performed using the Thermo-Calc kinetic software package. These simulations were performed by and provided by the R&D department in Aubert & Duval. Thermo-Calc software uses complex thermodynamic equations in conjunction with material databases to perform thermodynamic calculations and calculations for phase equilibria and diffusion-controlled transformations. The databases contain thermodynamic, kinetic and properties data specific to different classes of alloys. Two material databases were used in conjunction with the Thermo-Calc simulation software namely Ni25 (which is an internal database to Aubert & Duval) and TTNI18. The latter provides results in atomic percentage whereas the former is able to produce results in volume percentage. However, it is clear from Figure 4.13 that the  $\eta$  phase content data produced by simulations are considerably underestimated in comparison to the experimental data produced by this study, although the general trend of both sets of data are the same between 875°C and 975°C. The reason for the discrepancy between the experimental data and simulated data could be due to the simulation software having models that are not accurate enough to represent real precipitation kinetic behaviour. There could be some assumptions or simplifications incorporated into the model calculations that do not represent the actual conditions. Experimental results are supposed to represent the real behaviour of  $\eta$  phase precipitation kinetics with its associated measuring errors. On the other hand, simulation results are supposed to represent the  $\eta$  phase precipitation kinetics based on its mathematical and theoretical model. The discrepancy between the experimental and simulated values shows that there is an issue with the mathematical and theoretical model of the  $\eta$  phase precipitation kinetics in that it lacks to represent real world behaviour. The implication for this is that it is not sufficient to solely rely upon simulation results for  $\eta$  phase precipitation kinetics.

#### **4.7 Summary**

In this chapter, the precipitation of  $\eta$  phase has been characterised at the equilibrium state. The equilibrium area fraction has been determined experimentally for a temperature range between 850°C to 975°C and the length, thickness and aspect ratio



at the equilibrium state has been measured at the same temperature range. Comparisons have been made to thermodynamic simulations and other published results from the available literature. The equilibrium  $\eta$  phase area fraction is important to determine as this is used to produce TTT diagrams for the other studies in this work, namely the  $\eta$  phase precipitation kinetics in the strain-free recrystallised state, the deformed strained material and material with a larger initial grain size.

## **5 Precipitation Kinetics in Strain-Free Recrystallised Microstructure**

### **5.1 Introduction**

In this study, the  $\eta$  phase precipitation kinetics were studied in the recrystallised strain-free condition. To do this, samples of ATI 718Plus were required to be heat treated at various times and temperatures, after which microscopic examination (using an SEM) was to be performed to determine an estimation of the  $\eta$  phase area fraction. The experimental matrix for this study is shown below in Table 5.1.

Temperature (°C)	Time (minutes)			
850	30	60	180	720
875	30	60	180	720
900	30	60	180	720
925	30	60	180	720
950	30	60	180	720
975	30	60	180	720

*Table 5.1 – Experimental matrix for  $\eta$  phase precipitation kinetics in strain free material*

As mentioned earlier in this thesis, the as-received material, in extruded bar form, was shipped in the recrystallised strain-free condition. Before shipment, the as-received material had undergone a solution heat treatment for 1 hour at 1750°F (approximately 954°C) and was then subsequently air cooled.

Samples for this study were produced by sectioning the extruded bar into approximately 1 cm thick pieces, as shown in Figure 5.2. After undergoing the necessary heat treatments shown in Table 5.1, the samples were then mounted, ground and polished as described previously in Chapter 3.

The samples went through another solutioning heat treatment which was performed at 990°C for 180 minutes. This was done in order to try and bring the constituents of the initial  $\eta$  phase precipitates back into the austenitic matrix but without significantly

changing the initial as-received grain size. EBSD was then utilised in order to obtain the initial grain size of the samples prior to carrying out the experiments in Table 5.1. The resultant grain size map is shown in Figure 5.1. The grain size obtained from this EBSD analysis was  $13.2 \mu\text{m} \pm 5.3 \mu\text{m}$  (standard deviation). This corresponds to a grain size of ASTM 9.5 which is the same as the grain size of the material in the as-received state. Also, the  $\eta$  phase area fraction had reduced from  $1.78\% \pm 0.25\%$  to  $0.93\% \pm 0.14\%$ , which demonstrates that the objective of the solutioning heat treatment had been met.

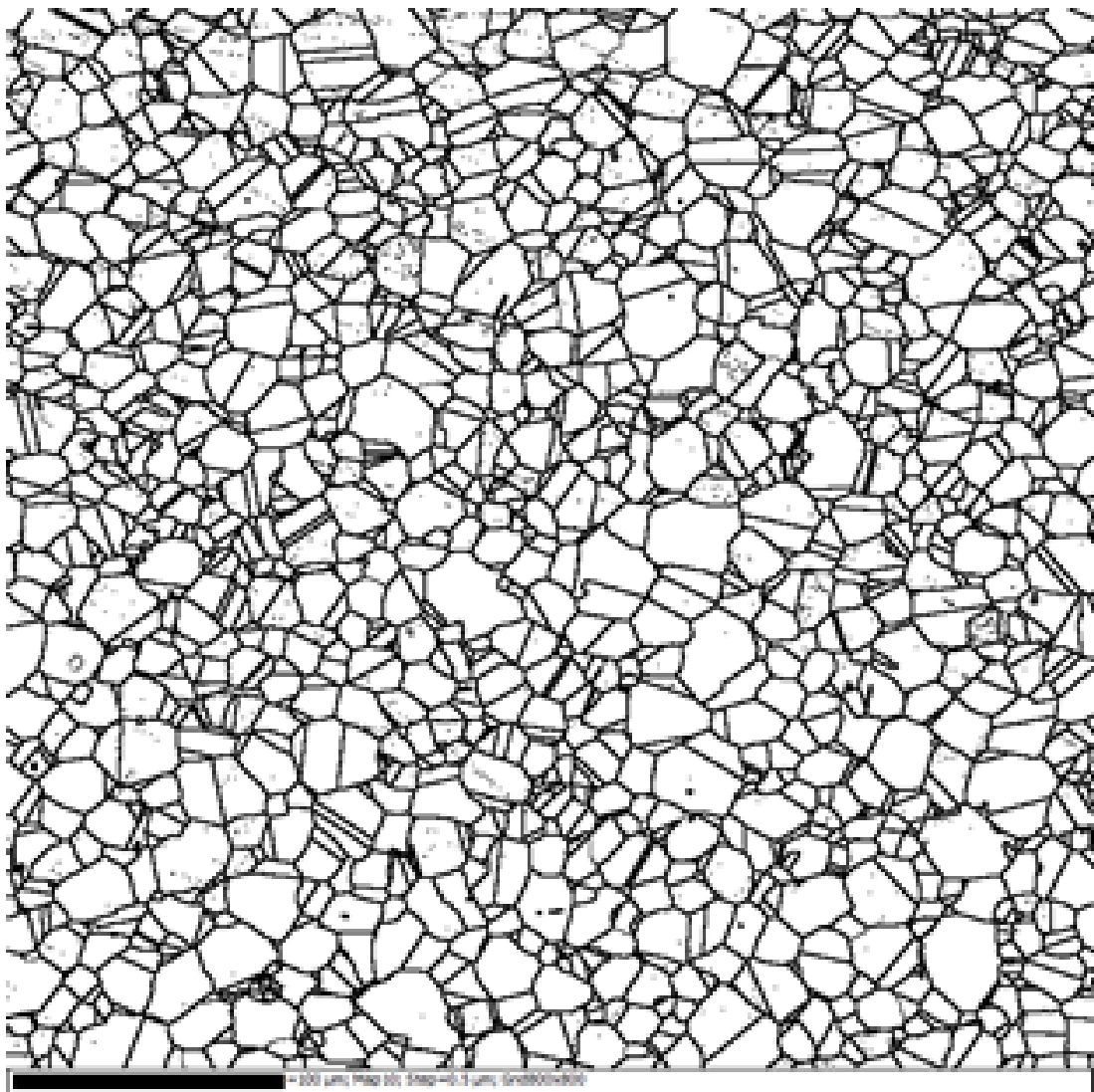


*Figure 5.1 – EBSD grain size map of initial microstructure after solution heat treatment at 990°C after 180 minutes*

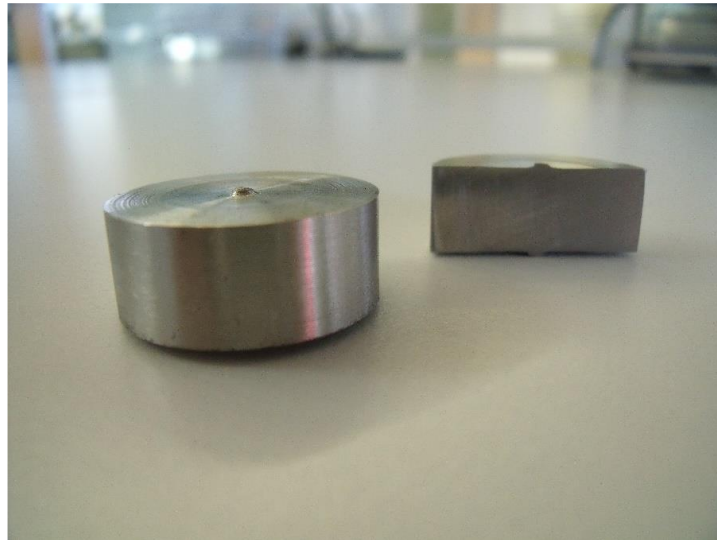


*Figure 5.2 – Example samples used in the strain-free precipitation kinetics study.*

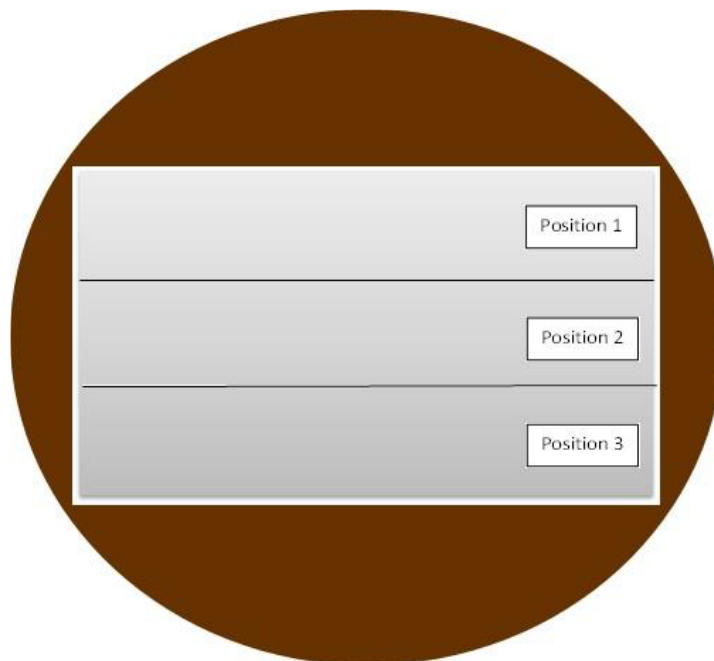


*Figure 5.3 – Schematic diagram of sample divided into three sections.*

The surface area of the resultant sample was then divided into three ‘positions’, as schematically represented in Figure 5.3. SEM was then utilised to obtain microstructural images from each position. The area fraction measurements shown in Section 5.2 are an average of three microstructural images: one image from each position. This was done so that a good representation of the sample is included within the area fraction measurements described in Section 5.2. Also, using three images per data point was more feasible because the image processing technique used to obtain

the  $\eta$  phase area fraction (as described in Chapter 3) was considerably time consuming, and due to time constraints more images per data point was not practically possible.

For the aspect ratio, length, and thickness measurements, six measurements were taken from each position, which meant that eighteen measurements were taken for each data point (since there are three positions from Figure 5.3). From these eighteen measurements, nine measurements were taken from intergranular precipitates and nine measurements were taken from intragranular precipitates. This sample size was considered practical as it was thought this would be a good representation of the sample while being feasible at the same time.

## 5.2 Area Fraction and TTT Diagram

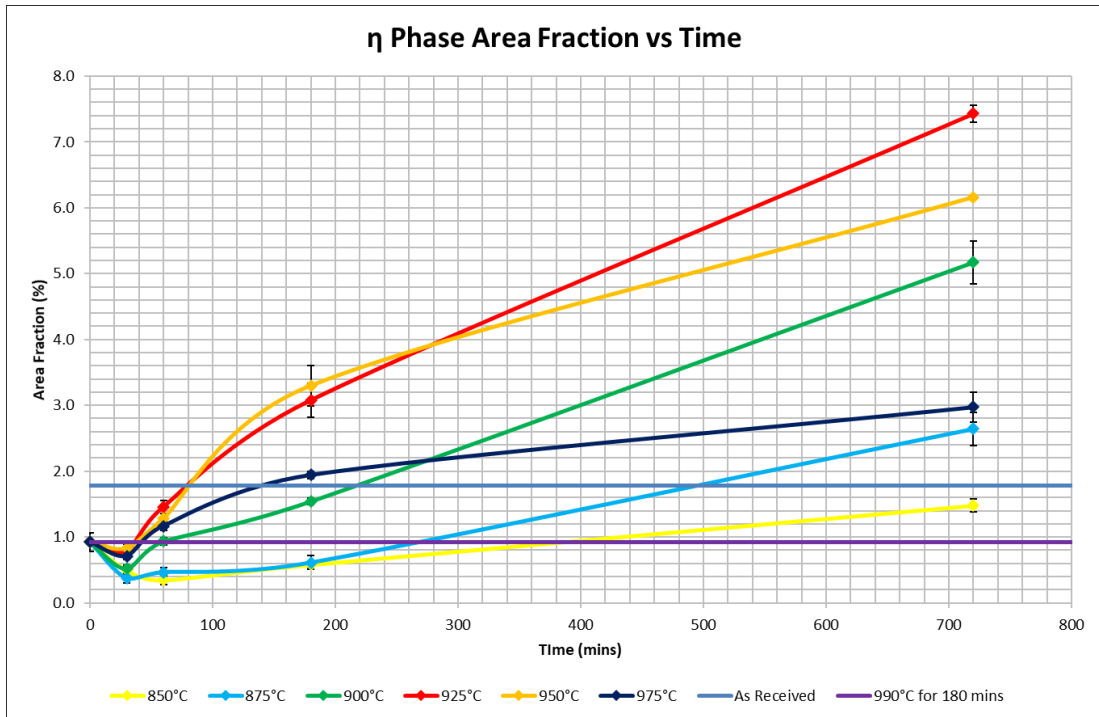


Figure 5.4 – η phase area fraction against time in strain-free material

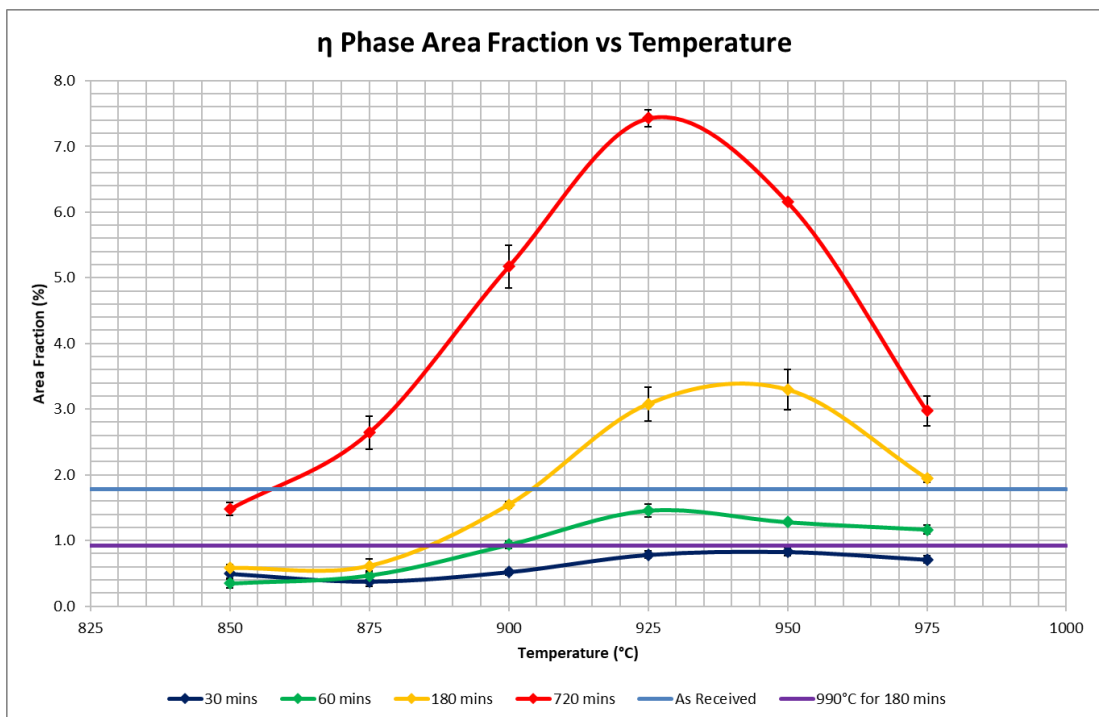


Figure 5.5 – η phase area fraction against temperature in strain-free material

Time (mins)	Area Fraction (%)					
	850°C	875°C	900°C	925°C	950°C	975°C
0	0.93 ± 0.14	0.93 ± 0.14	0.93 ± 0.14	0.93 ± 0.14	0.93 ± 0.14	0.93 ± 0.14
30	0.50 ± 0.07	0.38 ± 0.08	0.52 ± 0.04	0.78 ± 0.05	0.83 ± 0.06	0.71 ± 0.06
60	0.34 ± 0.07	0.47 ± 0.07	0.93 ± 0.05	1.45 ± 0.10	1.28 ± 0.01	1.17 ± 0.07
180	0.58 ± 0.05	0.61 ± 0.10	1.54 ± 0.05	3.08 ± 0.25	3.29 ± 0.31	1.94 ± 0.06
720	1.48 ± 0.09	2.65 ± 0.25	5.17 ± 0.32	7.43 ± 0.13	6.16 ± 0.01	2.97 ± 0.23

*Table 5.2 –  $\eta$  phase precipitation kinetics in strain-free material*

In Figure 5.4, the  $\eta$  phase area fraction as a function of time is displayed with the numerical values shown in Table 5.2. The errors shown in Figure 5.4 and Table 5.2 are standard errors. The as-received material was heat treated for 3 hours at 990°C in order to cause dissolution of the initial  $\eta$  phase while simultaneously preventing grain growth as much as possible. It is important to try to keep the grain size the same while solution treating the as-received material from  $\eta$  phase so that the starting condition is as close to the as-received condition as much as possible but without the presence of the initial  $\eta$  phase precipitates. Around 0.93% area fraction of  $\eta$  phase was remaining in the microstructure after the initial heat treatment at 990°C for 180 minutes. Therefore, the resultant microstructure was not completely “clean” of  $\eta$  phase precipitates.

It is observed that the amount of precipitation generally increases as a function of time, which is expected from the literature. It is noticed at all temperatures that the  $\eta$  phase area fraction decreases from 0 minutes to 30 minutes, before going on to increase as the time increases. This initial decrease between 0 minutes and 30 minutes is currently unexplained for, but it is surprising to notice as this is not observed in other studies on grain boundary kinetics in the published literature.

One potential reason could be that since the  $\eta$  phase area fraction is low in the beginning, some grain growth might occur which means there are less grain boundaries per field of view. As  $\eta$  phase precipitation occurs first from grain boundaries, this is would mean that there is less  $\eta$  phase per field of view. However, this theory would

need to be substantiated further by investigating the grain size and  $\eta$  phase area fraction at small intervals of time between 0 to 30 minutes. Also, by comparing the EBSD analysis that was done on ATI 718Plus in both the as-received condition as well as after heat treatment at 990°C for 180 minutes, the difference in grain size that occurred does not suggest that it would make much difference to the amount of  $\eta$  phase per field of view.

Another possible explanation could be that the new  $\eta$  phase precipitation that occurs initially is acicular in nature, consisting of very thin lamellae. This makes it especially difficult to threshold accurately and hence may not be reflected in the final  $\eta$  phase area fraction value. However, even if this was considered, the  $\eta$  phase area fraction at 30 minutes should still be closer to that after heat treatment at 990°C for 180 minutes, especially for the data at 850°C, 875°C and 900°C.

From Figure 5.4, after 720 minutes of heat treatment, the area fraction of  $\eta$  phase increases as the temperature increases from 850°C to 925°C, before reducing as the temperature increases from 925°C to 975°C. Therefore, the peak of precipitation looks to occur at 925°C. However, from 0 minutes to 180 minutes, the temperature with the highest  $\eta$  phase area fraction fluctuates between 925°C and 950°C.

This is also observed in Figure 5.5, in which the  $\eta$  phase area fraction is plotted against temperature. After 720 minutes, the peak of precipitation looks to occur just above 925°C. At 925°C after 720 minutes, the rate of nucleation and precipitation decreases as the temperature increases. This is because thermodynamically, the driving force for nucleation decreases as the temperature increases (67) above 925°C. Similarly, after 30 minutes, 60 minutes and 180 minutes, the peak of precipitation looks likely to be reached somewhere between 925°C and 950°C. This suggests that the peak or ‘nose’ of  $\eta$  phase precipitation (i.e., the temperature at which the fastest rate of precipitation occurs) is between 925°C and 950°C.

It is also noticed from Figure 5.4 that the lowest and slowest  $\eta$  phase precipitation occurs at 850°C and 875°C at all times studied. From Figure 5.4, the levels of  $\eta$  phase



precipitation are somewhat close together between 0 minutes and 180 minutes, but the difference between 850°C and 875°C becomes more pronounced after 180 minutes onwards, as can be seen by the values at 720 minutes. This is also seen in Figure 5.5. Although the levels of  $\eta$  phase precipitation are close together for 850°C and 875°C for 30 minutes, 60 minutes and 180 minutes, the difference in  $\eta$  phase precipitation between 850°C and 875°C is much more manifest after 720 minutes. From Figure 5.6 to Figure 5.11, the microstructural evolution is shown from the as-received condition until 720 minutes of heat treatment at 925°C. After solutioning at 990°C for 180 minutes (Figure 5.7), it can be observed that there is a gradual increase in  $\eta$  phase area fraction at 30 minutes (Figure 5.8), 60 minutes (Figure 5.9), 180 minutes (Figure 5.10) and onwards to 720 minutes (Figure 5.11).

In Figure 5.4, for each of the area fraction curves at their respective temperatures, the Avrami equation (Equation 5.1) was used as the basis for the mathematical fitting of each area fraction curve. The mathematical fitting allows us to obtain an equation for each temperature, which can be used to extrapolate to obtain an  $\eta$  phase area fraction for any given time. Conversely, the equation could also be used to derive the length of time required (in minutes) to precipitate a particular amount of  $\eta$  phase. From the latter, a TTT curve could be produced which would describe the times and temperatures at which a particular percentage of  $\eta$  phase is present within the material.

$$y = f_{eq}(1 - \exp(-kt^n)) \quad \text{Equation 5.1}$$

Where  $y$  is the  $\eta$  phase area fraction percentage,  $t$  is the time in minutes,  $f_{eq}$  is the  $\eta$  phase area fraction at the thermodynamic equilibrium for that temperature and  $k$  and  $n$  are time independent coefficients.

Using the Origin 2021 software, the non-linear curve fittings were performed and obtained using the Levenberg-Marquardt iteration algorithm. The Avrami equations for each of the temperatures experimentally studied are shown on the next page and the coefficients of determination for each of the equations are shown in Table 5.3.

$$850^{\circ}\text{C} \quad y = 16.18(1 - \exp(-0.00133t^{0.64935})) \quad \text{Equation 5.2}$$

$$875^{\circ}\text{C} \quad y = 20.64(1 - \exp(-0.000432484t^{0.87328})) \quad \text{Equation 5.3}$$

$$900^{\circ}\text{C} \quad y = 18.46(1 - \exp(-0.00124t^{0.8468})) \quad \text{Equation 5.4}$$

$$925^{\circ}\text{C} \quad y = 15.45(1 - \exp(-0.00394t^{0.7772})) \quad \text{Equation 5.5}$$

$$950^{\circ}\text{C} \quad y = 10.03(1 - \exp(-0.00819t^{0.72662})) \quad \text{Equation 5.6}$$

$$975^{\circ}\text{C} \quad y = 5.88(1 - \exp(-0.02958t^{0.48602})) \quad \text{Equation 5.7}$$

Temperature ( $^{\circ}\text{C}$ )	Adjusted $R^2$ Value
850	0.99173
875	0.95476
900	0.98749
925	0.9997
950	0.98776
975	0.98128

*Table 5.3 – Adjusted  $R^2$  values for Equations 5.2 to 5.7*

The adjusted  $R^2$  values for the fitted Avrami equations for strain-free material is shown in Table 5.3. The adjusted  $R^2$  values are all above 0.95, which shows that a very good mathematical fit to the experimental data has been achieved. This shows confidence in the obtained equations and will give confidence to the eventual TTT curve that will be derived as a result of these fitted Avrami equations.

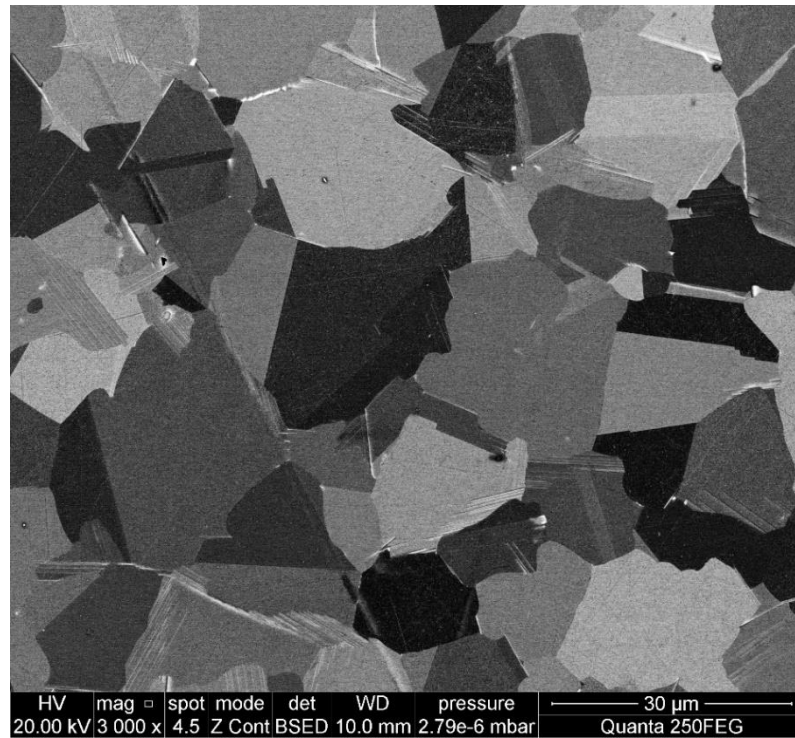


*Figure 5.6 – Microstructure of ATI 718Plus in the as-received condition*

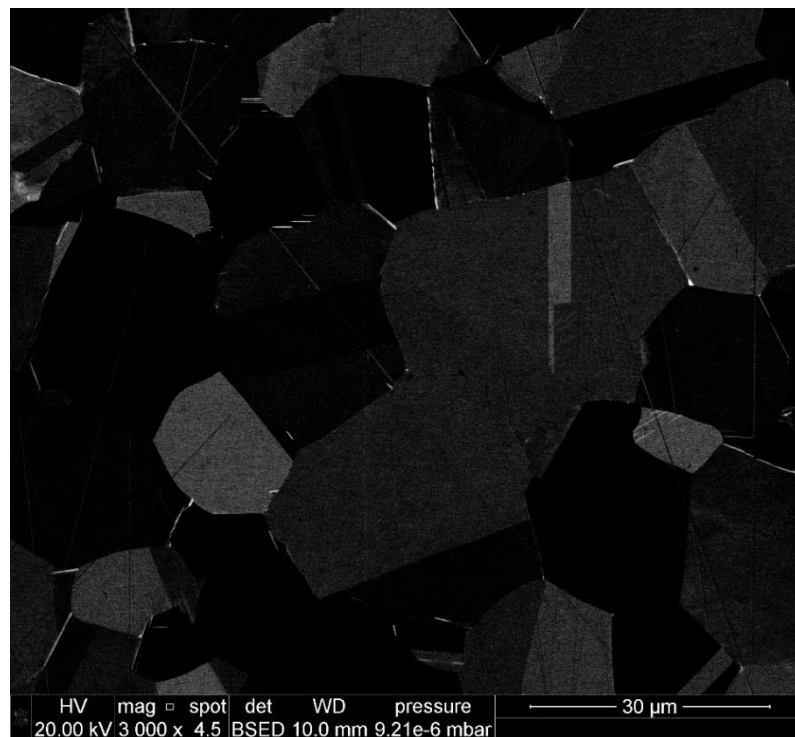


*Figure 5.7 – Microstructure of ATI 718Plus after heat treatment at 990°C for 180 minutes*

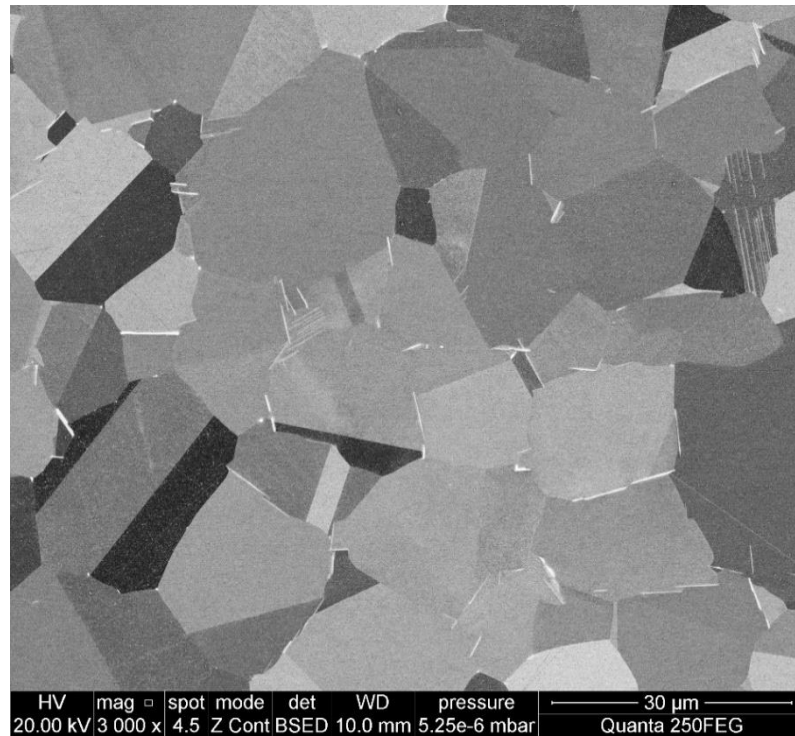


*Figure 5.8 – Microstructure of ATI 718Plus after heat treatment at 925°C after 30 minutes*

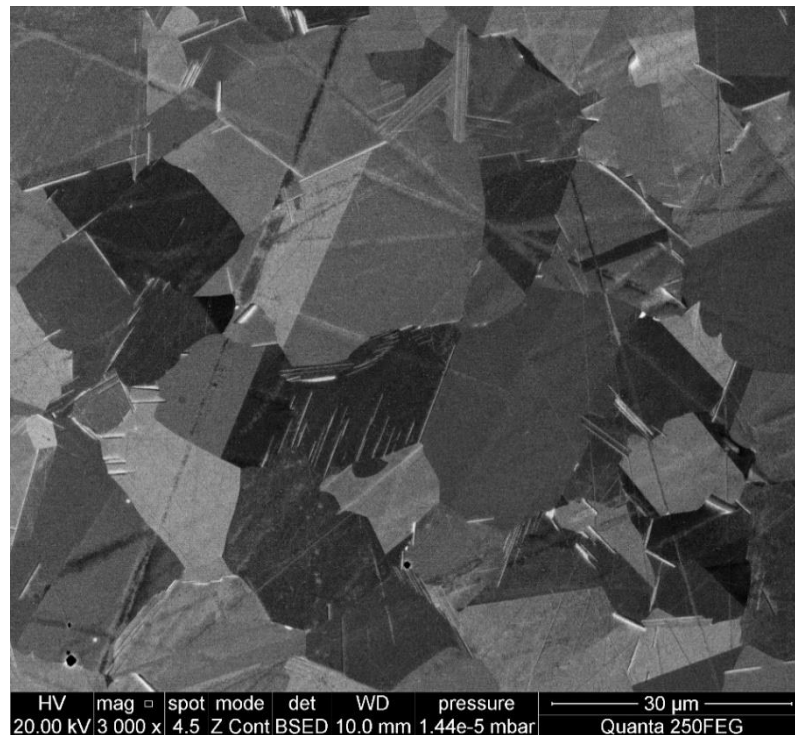


*Figure 5.9 – Microstructure of ATI 718Plus after heat treatment at 925°C after 60 minutes*

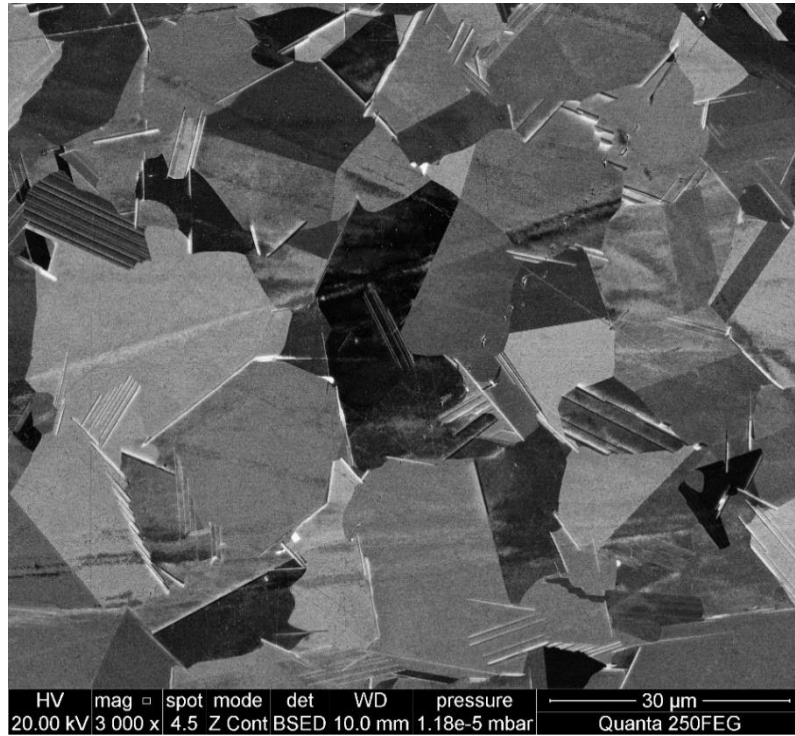


*Figure 5.10 – Microstructure of ATI 718Plus after heat treatment at 925°C after 180 minutes*

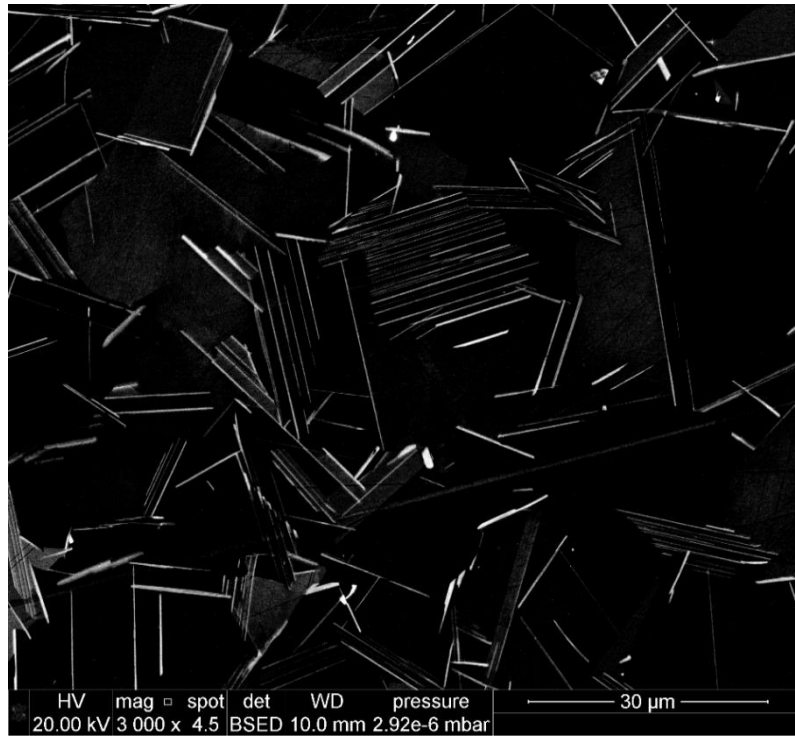


*Figure 5.11 – Microstructure of ATI 718Plus after heat treatment at 925°C after 720 minutes*

Using the fitted Avrami equations (Equation 5.2 to Equation 5.7), a TTT curve can be derived for the strain-free condition of ATI 718Plus. To do this, Equation 5.1 firstly needs to be reverse engineered in order that the time (in minutes) is a mathematical function of  $f_{eq}$  ( $\eta$  phase area fraction at the thermodynamic equilibrium),  $y$  ( $\eta$  phase area fraction), and time independent coefficients  $k$  and  $n$ . This is derived as follows:

$$y = f_{eq}(1 - \exp(-kt^n))$$

$$\frac{y}{f_{eq}} = 1 - \exp(-kt^n)$$

$$\exp(-kt^n) = 1 - \frac{y}{f_{eq}}$$

$$-kt^n = \ln \left[ 1 - \frac{y}{f_{eq}} \right]$$

$$t^n = \frac{\ln \left[ 1 - \frac{y}{f_{eq}} \right]}{-k}$$

$$t = \left[ \frac{\ln \left[ 1 - \frac{y}{f_{eq}} \right]}{-k} \right]^{1/n}$$

Equation 5.8

By applying Equation 5.8 for each of the temperatures involved in this study, we can obtain the time taken in minutes ( $t$ ) to precipitate a particular amount of  $\eta$  phase ( $y$ ) at a particular temperature. This can then be plotted on TTT diagram of temperature against time.

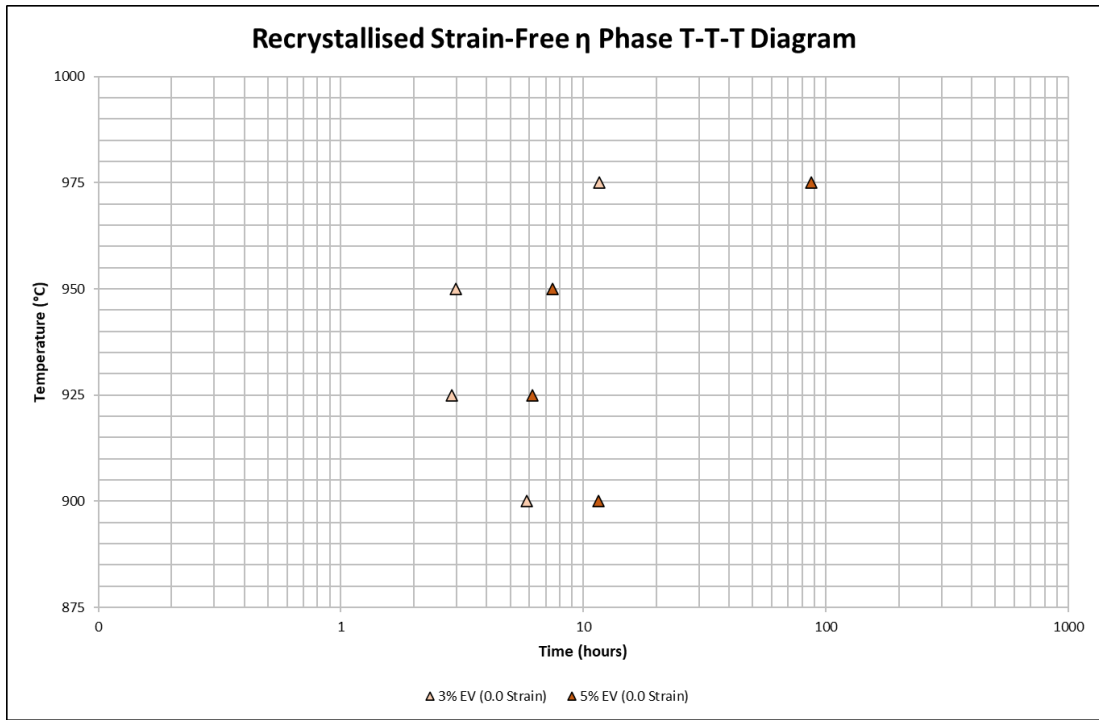


Figure 5.12 – TTT diagram for 3% and 5%  $\eta$  phase area fractions in strain-free material, experimental values only

Temperature (°C)	Time (hours)	
	3%	5%
850	39.0362	96.72
875	14.2377	27.31
900	5.8507	11.568
925	2.8776	6.1791
950	2.9877	7.4476
975	11.6547	87.311

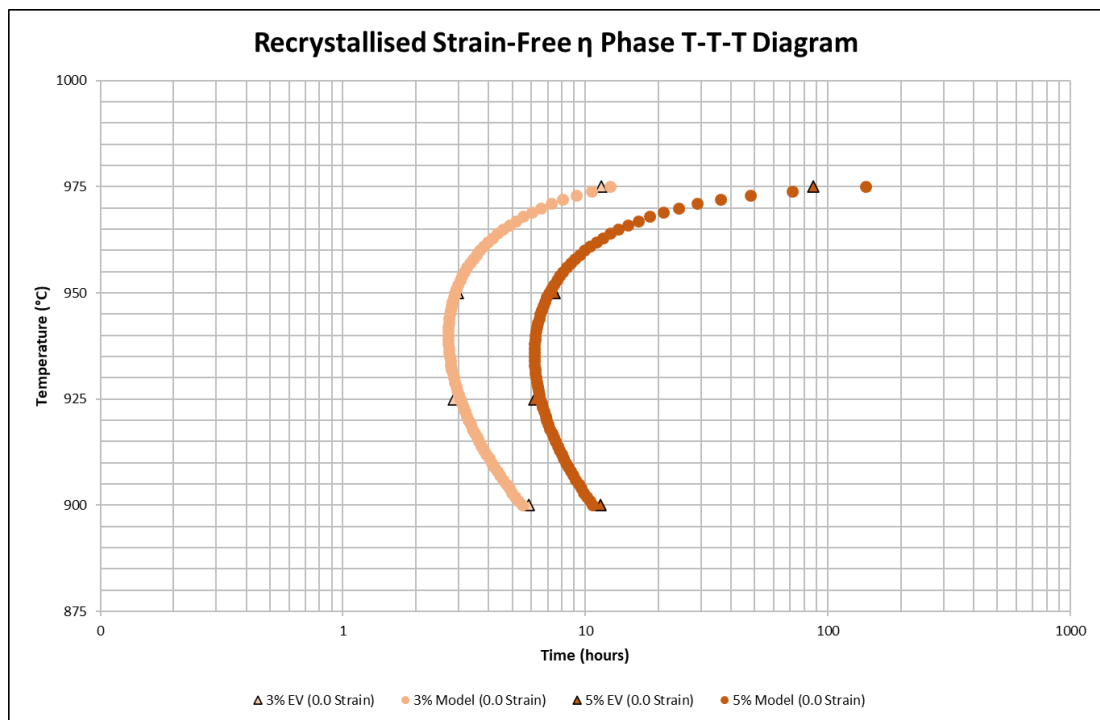
Table 5.4 – Calculated time taken to precipitate 3% and 5% area fractions at each temperature

Figure 5.12 displays the TTT data to precipitate 3% and 5% of  $\eta$  phase in the strain-free recrystallised condition of ATI 718Plus, with the numerical values displayed in Table 5.4. Of course, it takes longer to precipitate 5% than 3% hence the 5% curve is to the right of the 3% curve. Note, the time values obtained from Equation 5.8 are in minutes. These are converted into hours before plotting into Figure 5.12.

The TTT curves themselves can be modelled using a second order polynomial equation as the basis. This would allow us to obtain the time required to precipitate a specific amount of  $\eta$  phase at any particular temperature. The basic equation used to model or fit the TTT data shown in Figure 5.12 is shown below.

$$\tau^{-1} = a(\eta_{solv} - T)\exp\left[-\frac{(\eta_{solv} - T)^b}{T + 273}\right] \quad \text{Equation 5.9}$$

Where  $\tau$  is the time in hours,  $\eta_{solv}$  is the  $\eta$  phase solvus temperature,  $T$  is the temperature in Celsius,  $a$  is a constant related to nucleation, and  $b$  is a constant related to the growth kinetics of the  $\eta$  phase.



*Figure 5.13 – TTT diagram for 3% and 5%  $\eta$  phase area fractions in strain-free material with modelling curves*

As Figure 5.13 shows, the data derived from the fitted Avrami equations (Equation 5.2 to Equation 5.7) are themselves modelled as close as possible using Equation 5.9. The equations that were obtained as a result from this modelling are shown in Equation 5.10 and Equation 5.11 below.



$$\text{3\% Model} \quad \tau^{-1} = 0.016(980 - T)\exp \left[ -\frac{(980 - T)^{1.765}}{T + 273} \right] \quad \text{Equation 5.10}$$

$$\text{5\% Model} \quad \tau^{-1} = 0.007(976 - T)\exp \left[ -\frac{(976 - T)^{1.76}}{T + 273} \right] \quad \text{Equation 5.11}$$

From Figure 5.13, it can be seen that the ‘nose’ or peak of the curves lies between 925°C to 950°C, as was suggested earlier from Figure 5.5.

In order to make the fitting of Equation 5.10 and Equation 5.11 more accurate and as close as possible to the experimental values, the  $\eta$  phase solvus temperature was made to be a variable parameter instead of being fixed at a particular temperature. Within the literature, there does seem to be a debate regarding the true value of the  $\eta$  phase solvus temperature. However, in order to produce better fitting modelling equations in this study, the  $\eta$  phase solvus was subject to change accordingly to produce the best fit.

### 5.3 Aspect Ratio, Length and Thickness

#### 5.3.1 Overall Data

As well as studying the  $\eta$  phase precipitation kinetics in the recrystallised strain free condition, the kinetics of the  $\eta$  precipitate length, thickness and aspect ratio was also studied in the recrystallised strain-free condition. The behaviour of the average precipitate aspect ratio against time is shown in Figure 5.14 with the numerical values shown in Table 5.5. In addition, the average length against time is shown in Figure 5.15 with the numerical values shown in Table 5.6, and the average thickness against time is shown in Figure 5.16 with the numerical values shown in Table 5.7.

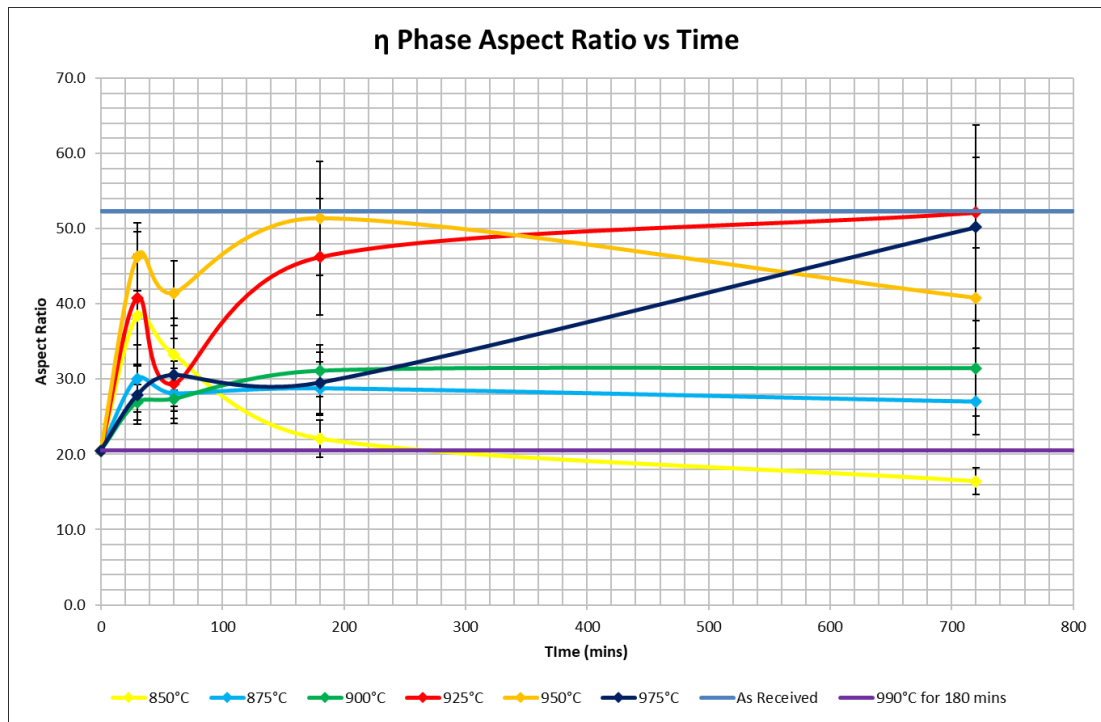


Figure 5.14 –  $\eta$  phase precipitate aspect ratio against time in strain-free material

Time (mins)	Aspect Ratio					
	850°C	875°C	900°C	925°C	950°C	975°C
0	20.48 ± 3.67	20.48 ± 3.67	20.48 ± 3.67	20.48 ± 3.67	20.48 ± 3.67	20.48 ± 3.67
30	38.40 ± 8.21	30.08 ± 4.47	26.93 ± 2.39	40.82 ± 8.81	46.24 ± 4.55	27.87 ± 3.90
60	33.30 ± 4.81	28.07 ± 3.32	27.35 ± 3.26	29.37 ± 3.05	41.43 ± 4.30	30.56 ± 4.83
180	22.11 ± 2.46	28.75 ± 3.58	31.08 ± 3.46	46.23 ± 7.71	51.35 ± 7.54	29.51 ± 4.10
720	16.43 ± 1.80	26.97 ± 4.37	31.45 ± 6.33	52.15 ± 11.65	40.77 ± 6.61	50.20 ± 9.25

Table 5.5 – Results of strain-free  $\eta$  phase precipitate aspect ratio

The average overall aspect ratio is observed to increase at all temperatures from the start until 30 minutes. This could be attributed to the growth of pre-existing  $\eta$  phase precipitates that are growing within the austenitic matrix which become more needle shaped. A high aspect ratio means that the precipitates are more needle shaped or acicular, whereas a low aspect ratio means that the precipitates are more globular in nature. From 30 minutes to 60 minutes, there is a decrease in aspect ratio at 850°C, 875°C, 925°C, 950°C whereas at 900°C the aspect ratio approximately stays the same. This is despite the fact that the precipitate length is observed to increase (or in the case of 925°C, approximately stay the same). However, the aspect ratio is decreased at this

time interval because the precipitate thickness is observed to increase noticeably within the same time interval at these temperatures. At 975°C the aspect ratio is observed to increase very slightly which is due to the length increasing slightly but the thickness decreasing at the same time. The decrease in thickness at 975°C can be attributed to the slower precipitation kinetics i.e., that new precipitates are nucleating and growing much slower relatively, which brings the average thickness down between 30 minutes to 60 minutes.

Between 60 minutes to 180 minutes, the  $\eta$  phase aspect ratio increases most noticeably at 925°C and 950°C, with the length and thickness also increasing at the same temperatures and time interval. At 925°C and 950°C, the quick increase in aspect ratio is due to the fast precipitation kinetics of the  $\eta$  phase, which is causing quick growth of the needle shaped precipitates in terms of its length. This is evident and matched with Figure 5.13 in which the fastest rate of precipitation occurs between 925°C and 950°C. The increase in thickness at 950°C between 60 and 180 minutes is minimal, so this would contribute to a larger aspect ratio as the difference in precipitate length is larger. Although the increase in thickness for 925°C is more substantial, the sizeable increase in precipitate length at 925°C provides an increase in aspect ratio. The growth of the precipitates at these temperatures could also be faster than the nucleation of new precipitates, which would provide a higher aspect ratio. The aspect ratio also increases (albeit less noticeably) at 900°C. At 900°C, the precipitation kinetics are slower (see Figure 5.13), so the increase in length of the precipitates (as well as the nucleation of new precipitates) will be slower too in comparison to 925°C and 950°C. Also, the length has increased noticeably between 60 minutes and 180 minutes, whereas the difference in thickness during the same time interval is extremely small. This would imply an increase in aspect ratio at 180 minutes than at 60 minutes, which is what is observed. At 875°C, the aspect ratio is somewhat the same. At this temperature, the precipitation kinetics are even slower, so the growth rate of  $\eta$  phase length will also be relatively slower. The precipitate length and thickness does increase very slightly, but the differences are not enough to cause the aspect ratio to change much. At 850°C the aspect ratio is seen to decrease substantially between 60 minutes and 180 minutes interval. It can be suggested that the nucleation of new precipitates dominates over the

growth of existing precipitates, which brings about a lower aspect ratio. This is also complemented by the fact that the precipitate length and thickness is also observed to decrease noticeably during the same time interval for the same suggested reason. The newly nucleated precipitates will be more globular in shape as they would not have had the time to grow in length.

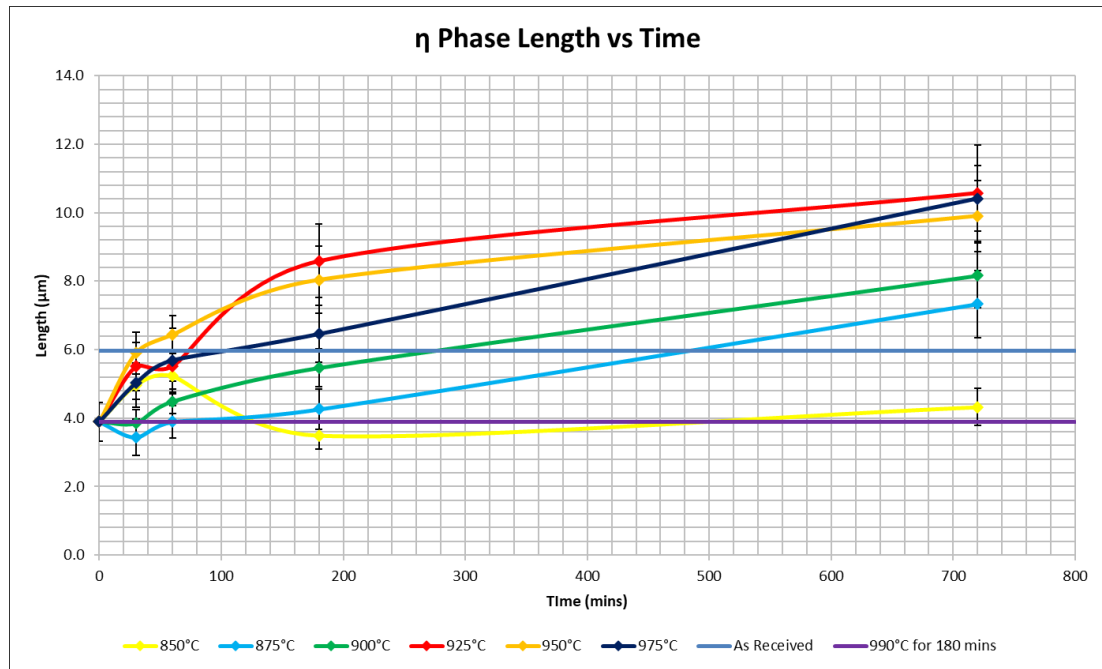


Figure 5.15 –  $\eta$  phase precipitate length against time in strain-free material

Time (mins)	Length ( $\mu\text{m}$ )					
	850°C	875°C	900°C	925°C	950°C	975°C
0	3.89 ± 0.56	3.89 ± 0.56	3.89 ± 0.56	3.89 ± 0.56	3.89 ± 0.56	3.89 ± 0.56
30	4.96 ± 0.64	3.44 ± 0.53	3.85 ± 0.39	5.51 ± 0.70	5.90 ± 0.61	5.02 ± 0.48
60	5.23 ± 0.53	3.89 ± 0.47	4.48 ± 0.36	5.52 ± 0.44	6.44 ± 0.55	5.69 ± 0.92
180	3.48 ± 0.40	4.26 ± 0.58	5.46 ± 0.55	8.58 ± 1.07	8.04 ± 0.98	6.46 ± 0.83
720	4.32 ± 0.54	7.33 ± 0.98	8.16 ± 0.94	10.57 ± 1.40	9.90 ± 1.04	10.41 ± 0.96

Table 5.6 – Results of strain-free  $\eta$  phase precipitate length

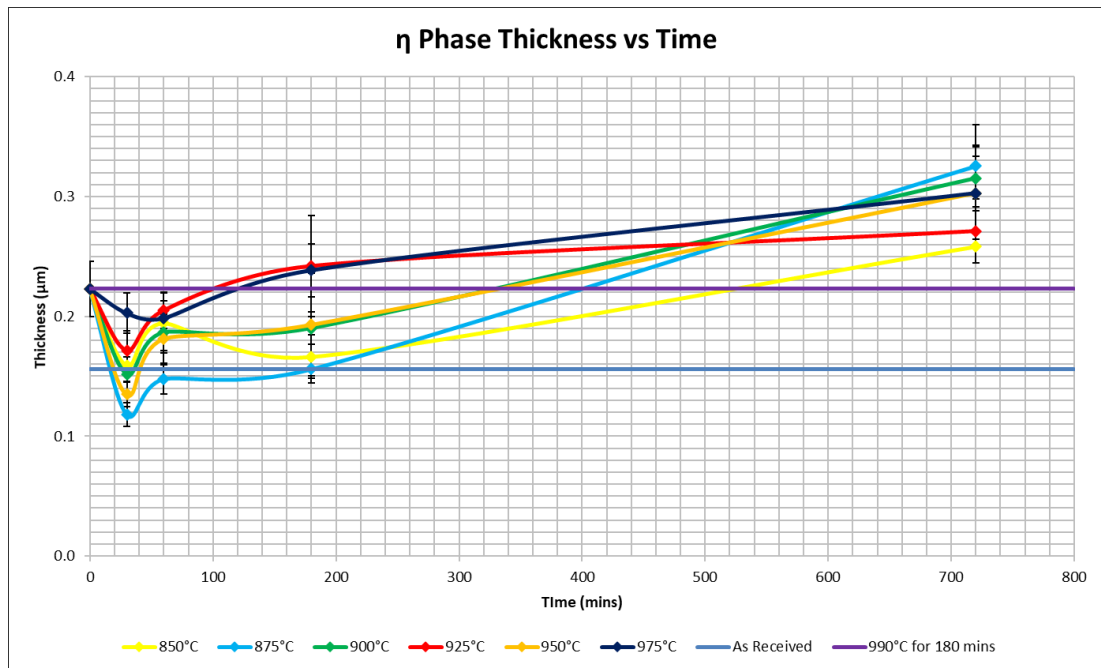


Figure 5.16 –  $\eta$  phase precipitate thickness against time in strain-free material

Time (mins)	Thickness ( $\mu\text{m}$ )					
	850°C	875°C	900°C	925°C	950°C	975°C
0	0.22 ± 0.02	0.22 ± 0.02	0.22 ± 0.02	0.22 ± 0.02	0.22 ± 0.02	0.22 ± 0.02
30	0.16 ± 0.01	0.12 ± 0.01	0.15 ± 0.01	0.17 ± 0.02	0.13 ± 0.01	0.13 ± 0.02
60	0.19 ± 0.03	0.15 ± 0.01	0.19 ± 0.02	0.20 ± 0.02	0.18 ± 0.02	0.18 ± 0.01
180	0.17 ± 0.02	0.16 ± 0.01	0.19 ± 0.01	0.24 ± 0.04	0.19 ± 0.04	0.19 ± 0.02
720	0.26 ± 0.01	0.33 ± 0.03	0.32 ± 0.03	0.27 ± 0.03	0.30 ± 0.03	0.30 ± 0.04

Table 5.7 – Results of strain-free  $\eta$  phase precipitate thickness

Between 180 minutes and 720 minutes, the aspect ratio continues to decrease noticeably at 850°C and slightly at 875°C. At 850°C, the precipitate length and thickness does increase a little. However, the increase in thickness is larger than the increase in length which provides an overall decrease in aspect ratio. Again, this is attributed to the nucleation of new precipitates that start off in a more globular fashion (see circled regions in Figure 5.17). This could be further verified in future work by investigating the length, thickness and aspect ratio at 850°C and 875°C at smaller time intervals between 180 minutes and 720 minutes. At 875°C and 900°C, the length and thickness both increase substantially, but this does not impact so much on the aspect ratio. At 925°C, the changes in length and thickness cause the aspect ratio to increase

a little, making the morphology of the precipitates more acicular. At 950°C, it is interesting to observe that the aspect ratio decreases markedly. The reasoning mentioned previously regarding the nucleation of new precipitates causing the aspect ratio to decrease could be applied. However, if this were the case, the same effect would also have been seen at 925°C. It would also have been seen at 950°C between 30 minutes and 60 minutes, but this is not the reality. It is not clear exactly why this particular result is observed, but it could be due to the prominent level of scatter or error within the data. At 975°C, the precipitate length and thickness can be seen to be increasing. The increase in length is larger than the increase in thickness which would give a larger aspect ratio.

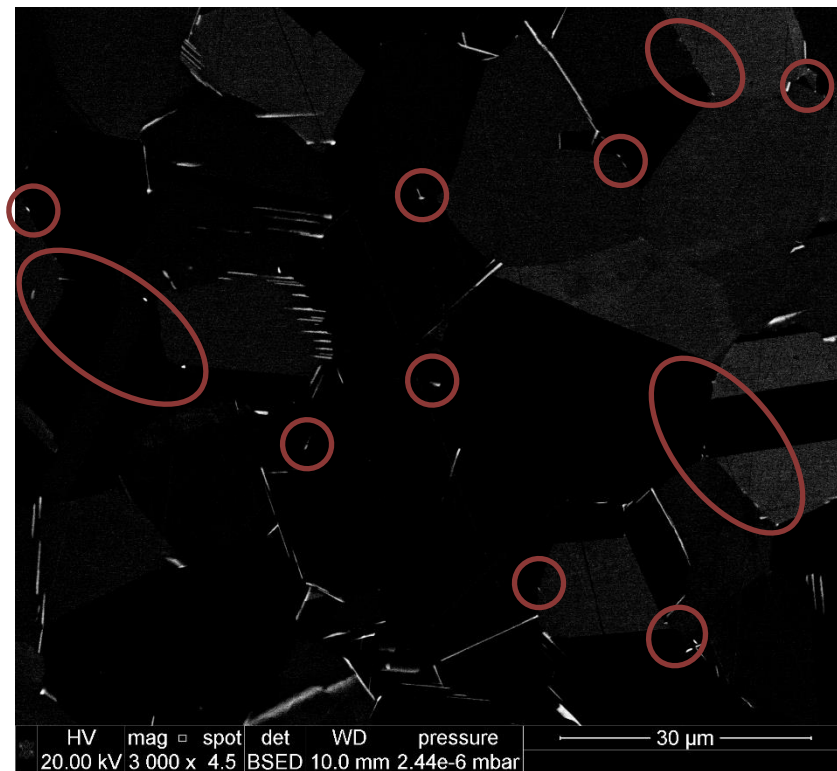


*Figure 5.17 – Areas of new precipitates in microstructure after heat treatment at 850°C for 720 mins*

### 5.3.2 Intergranular Data

In this study, intergranular precipitates are defined as those that nucleate at the grain boundary and grow along the grain boundary. Some precipitates are observed to start

growing along the grain boundary and then grow into the neighbouring grain. In these cases, if the majority of the precipitate is observed to be along the grain boundary, then it is classed as an intergranular precipitate. Conversely, if the majority of the precipitate is growing into the grain itself or into a neighbouring grain, then it is classed as an intragranular precipitate.

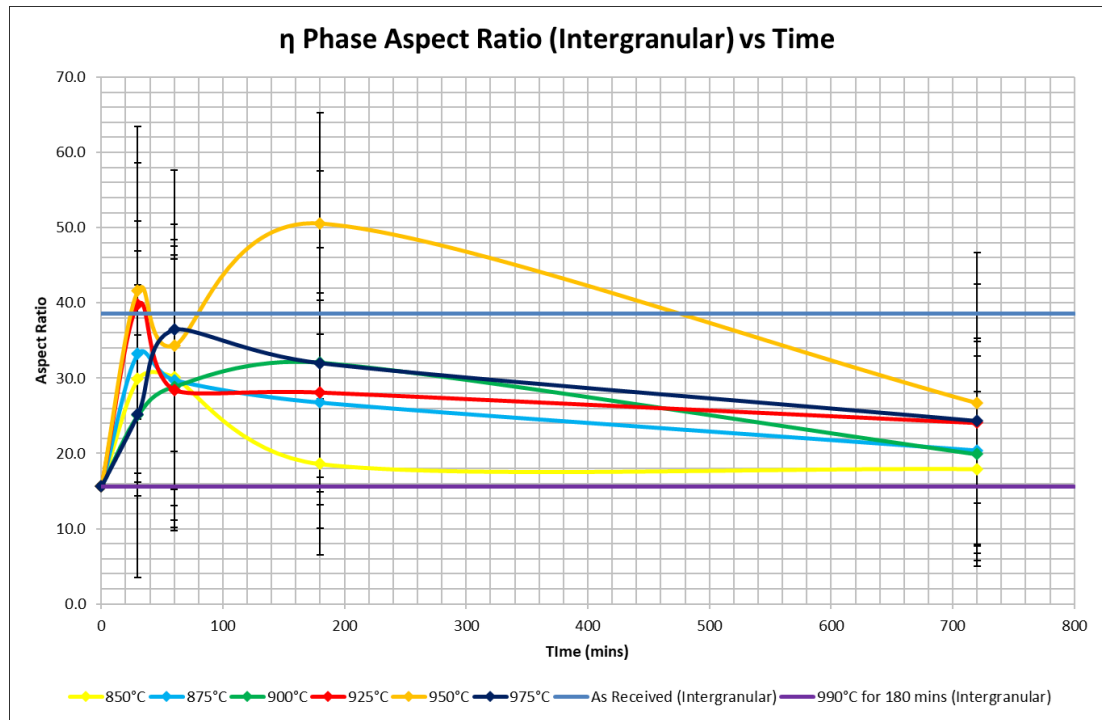


Figure 5.18 –  $\eta$  phase (intergranular) precipitate aspect ratio against time in strain-free material

Time (mins)	Aspect Ratio (Intergranular)					
	850°C	875°C	900°C	925°C	950°C	975°C
0	15.63 ± 10.54	15.63 ± 10.54	15.63 ± 10.54	15.63 ± 10.54	15.63 ± 10.54	15.63 ± 10.54
30	29.88 ± 12.55	33.22 ± 17.66	25.05 ± 10.68	39.79 ± 23.64	41.62 ± 17.02	25.20 ± 21.73
60	30.10 ± 20.34	29.74 ± 16.64	28.88 ± 18.69	28.47 ± 17.31	34.37 ± 14.09	36.43 ± 21.20
180	18.62 ± 8.61	26.76 ± 13.54	32.05 ± 15.23	28.12 ± 13.24	50.56 ± 14.69	32.00 ± 25.50
720	17.95 ± 10.29	20.41 ± 12.54	19.90 ± 14.93	24.08 ± 18.37	26.71 ± 19.97	24.33 ± 10.99

Table 5.8 – Results of strain-free  $\eta$  phase precipitate aspect ratio (intergranular)

In Figure 5.18, Figure 5.19 and Figure 5.20, the aspect ratio, length and thickness is shown against time for intergranular grain boundary precipitates respectively. While

the numerical values for the intergranular aspect ratio are shown in Table 5.8, the intergranular length numerical values are shown in Table 5.9 and the intergranular thickness numerical values are shown in Table 5.10.

The trajectories are similar at 850°C, 875°C, 900°C and 950°C. At 925°C, the  $\eta$  phase aspect ratio decreases between 60 minutes and 720 minutes for intergranular precipitates, whereas the  $\eta$  phase aspect ratio for the overall data increases during the same time interval. At 975°C, intergranular aspect ratio decreases between 180 minutes and 720 minutes, whereas for the overall data, the aspect ratio increases between the same time range.

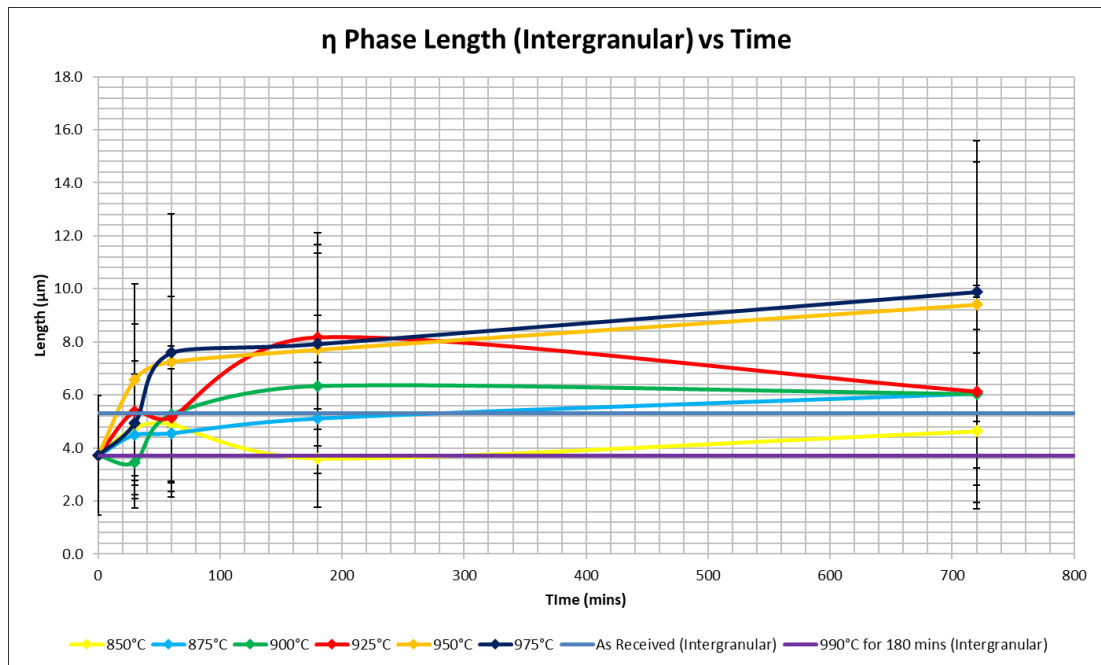


Figure 5.19 –  $\eta$  phase (intergranular) precipitate length against time in strain-free material



Time (mins)	Length ( $\mu\text{m}$ ) (Intergranular)					
	850°C	875°C	900°C	925°C	950°C	975°C
0	$3.72 \pm 2.26$	$3.72 \pm 2.26$	$3.72 \pm 2.26$	$3.72 \pm 2.26$	$3.72 \pm 2.26$	$3.72 \pm 2.26$
30	$4.78 \pm 2.00$	$4.50 \pm 2.78$	$3.47 \pm 1.22$	$5.39 \pm 3.30$	$6.57 \pm 3.62$	$4.94 \pm 2.35$
60	$4.91 \pm 2.21$	$4.56 \pm 2.42$	$5.26 \pm 2.59$	$5.16 \pm 2.42$	$7.26 \pm 2.47$	$7.59 \pm 5.24$
180	$3.62 \pm 1.84$	$5.12 \pm 2.09$	$6.33 \pm 2.66$	$8.17 \pm 3.48$	$7.71 \pm 3.63$	$7.93 \pm 4.18$
720	$4.63 \pm 2.94$	$6.06 \pm 2.40$	$6.03 \pm 4.10$	$6.14 \pm 3.54$	$9.41 \pm 6.17$	$9.89 \pm 4.90$

Table 5.9 – Results of strain-free  $\eta$  phase precipitate length (intergranular)

For the  $\eta$  phase length of the intergranular precipitates, the trends are similar at 850°C, 950°C and 975°C to that of the overall data. At 875°C, the intergranular precipitate length between 0 minutes and 30 minutes is observed to increase, whereas at the same time interval for the overall precipitate length, the length decreases. At 900°C, the length increases between 180 minutes and 720 minutes for the intergranular precipitates but stays roughly the same for the overall data. At 925°C, the intergranular precipitate length decreases between 180 minutes and 720 minutes, whereas the overall precipitate length increases during the same time interval.

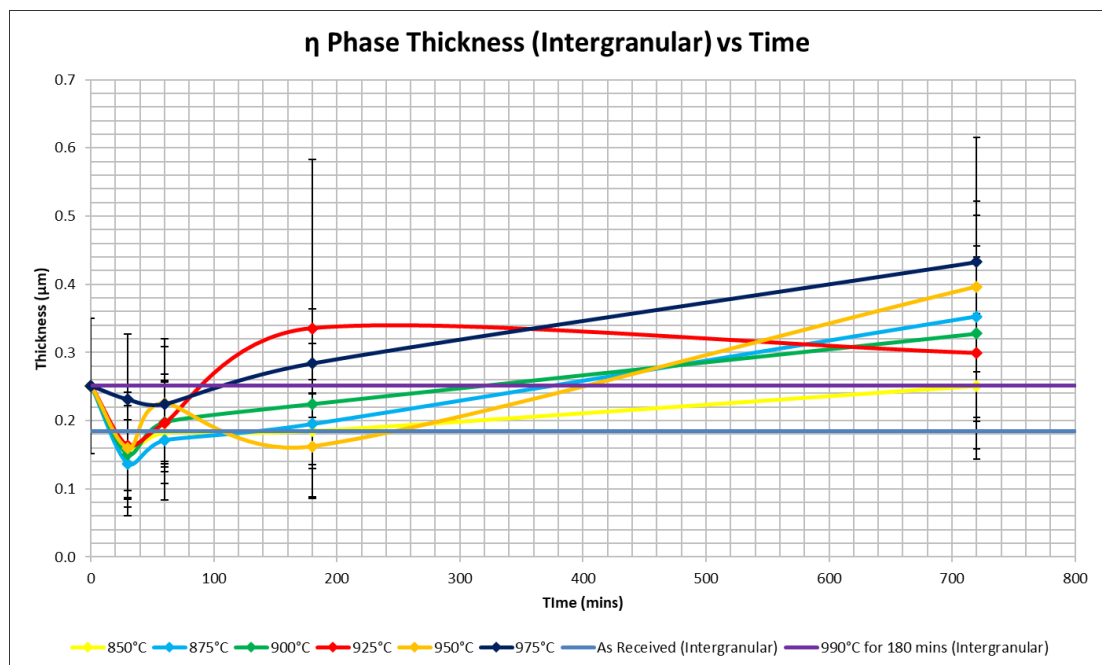


Figure 5.20 –  $\eta$  phase (intergranular) precipitate thickness against time in strain-free material

Time (mins)	Thickness ( $\mu\text{m}$ ) (Intergranular)					
	850°C	875°C	900°C	925°C	950°C	975°C
0	$0.25 \pm 0.10$	$0.25 \pm 0.10$	$0.25 \pm 0.10$	$0.25 \pm 0.10$	$0.25 \pm 0.10$	$0.25 \pm 0.10$
30	$0.16 \pm 0.06$	$0.14 \pm 0.06$	$0.15 \pm 0.09$	$0.16 \pm 0.08$	$0.16 \pm 0.07$	$0.23 \pm 0.10$
60	$0.18 \pm 0.07$	$0.17 \pm 0.09$	$0.20 \pm 0.06$	$0.20 \pm 0.07$	$0.23 \pm 0.09$	$0.22 \pm 0.08$
180	$0.18 \pm 0.06$	$0.20 \pm 0.06$	$0.22 \pm 0.09$	$0.34 \pm 0.25$	$0.16 \pm 0.08$	$0.28 \pm 0.08$
720	$0.25 \pm 0.11$	$0.35 \pm 0.15$	$0.33 \pm 0.13$	$0.30 \pm 0.14$	$0.40 \pm 0.13$	$0.43 \pm 0.18$

*Table 5.10 – Results of strain-free  $\eta$  phase precipitate thickness (intergranular)*

For the  $\eta$  phase thicknesses of the intergranular precipitates, the trends are almost exactly the same as the overall thickness measurements, except for the data at 925°C. At 925°C, the intergranular precipitate thickness is observed to decrease between 180 minutes and 720 minutes, while the overall precipitate thickness is seen to increase during the same time interval.

### 5.3.3 Intragranular Data

For the sake of this study, intragranular precipitates are defined as those that nucleate at the grain boundary and grow into the grain itself or into a neighbouring grain. The intragranular precipitate aspect ratios are shown in Figure 5.21 with the numerical values are shown in Table 5.11. The intragranular precipitate lengths are shown in Figure 5.22 with the numerical values are shown in Table 5.12. Lastly, the intragranular precipitate thicknesses are shown in Figure 5.23 with the numerical values shown in Table 5.13.

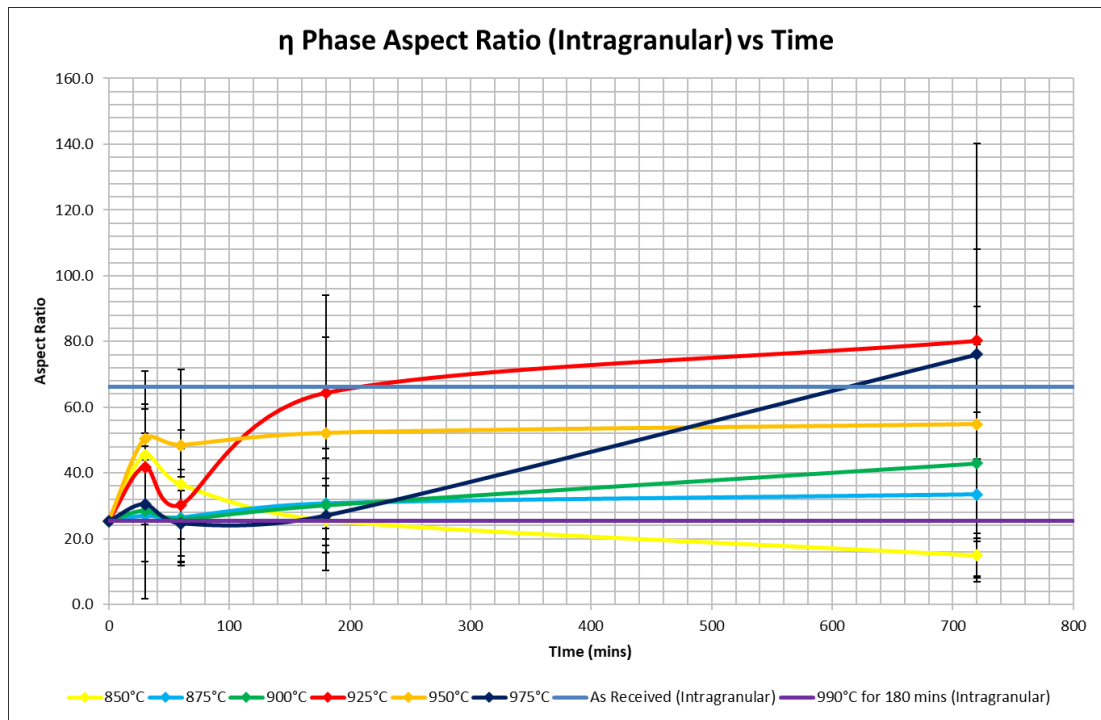


Figure 5.21 –  $\eta$  phase (intragranular) precipitate aspect ratio against time in strain-free material

Time (mins)	Aspect Ratio (Intragranular)					
	850°C	875°C	900°C	925°C	950°C	975°C
0	25.32 ± 21.59	25.32 ± 21.59	25.32 ± 21.59	25.32 ± 21.59	25.32 ± 21.59	25.32 ± 21.59
30	45.37 ± 15.50	26.93 ± 25.24	28.47 ± 15.55	41.86 ± 17.48	50.41 ± 20.66	30.53 ± 17.59
60	36.49 ± 16.47	26.40 ± 14.57	25.82 ± 13.12	30.27 ± 17.20	48.49 ± 23.06	24.68 ± 9.91
180	25.60 ± 5.61	30.73 ± 7.68	30.11 ± 14.28	64.35 ± 17.01	52.15 ± 41.87	27.02 ± 9.15
720	14.92 ± 6.69	33.52 ± 24.83	42.99 ± 36.00	80.22 ± 59.94	54.83 ± 35.69	76.07 ± 31.93

Table 5.11 – Results of strain-free  $\eta$  phase precipitate aspect ratio (intragranular)

Comparing the intragranular precipitate aspect ratio to the overall precipitate aspect ratio, the trajectories are similar at 850°C, 875°C and 925°C. At 900°C, the aspect ratio increases between 180 minutes and 720 minutes for the intragranular precipitates, whereas the overall aspect ratio approximately stays the same during the same time range. For the intragranular precipitates at 950°C, the aspect ratio slightly increases between 180 minutes and 720 minutes, whereas the overall aspect ratio is observed to decrease during the same time interval. At 975°C, the intragranular precipitate aspect

ratio decreases between 30 minutes and 60 minutes, whereas the overall aspect ratio increases for the same time period.

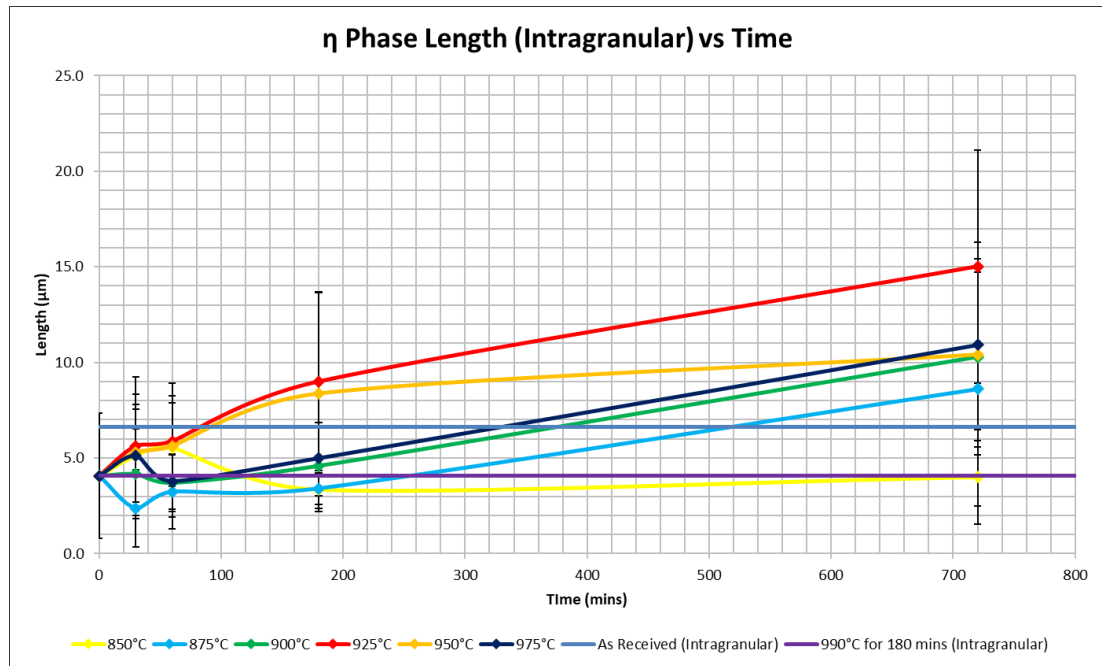


Figure 5.22 –  $\eta$  phase (intragranular) precipitate length against time in strain-free material

Time (mins)	Length ( $\mu\text{m}$ ) (Intragranular)					
	850°C	875°C	900°C	925°C	950°C	975°C
0	4.06 ± 3.27	4.06 ± 3.27	4.06 ± 3.27	4.06 ± 3.27	4.06 ± 3.27	4.06 ± 3.27
30	5.12 ± 2.43	2.37 ± 2.02	4.16 ± 2.35	5.62 ± 3.62	5.29 ± 3.06	5.11 ± 2.69
60	5.55 ± 2.32	3.23 ± 1.93	3.70 ± 1.50	5.88 ± 2.38	5.62 ± 3.31	3.78 ± 1.86
180	3.35 ± 1.14	3.40 ± 0.82	4.59 ± 2.24	9.00 ± 4.64	8.36 ± 5.33	4.98 ± 1.65
720	4.01 ± 2.46	8.60 ± 6.12	10.29 ± 5.11	15.01 ± 6.09	10.40 ± 4.50	10.93 ± 5.37

Table 5.12 – Results of strain-free  $\eta$  phase precipitate length (intragranular)

In terms of precipitate length, the intragranular data follows the same trajectories as those of the overall data. Although, between 30 minutes and 60 minutes at 900°C and 975°C, the intergranular precipitate length decreases. This is in contrast to the overall precipitate length which is shown to increase during the same time interval at both temperatures.

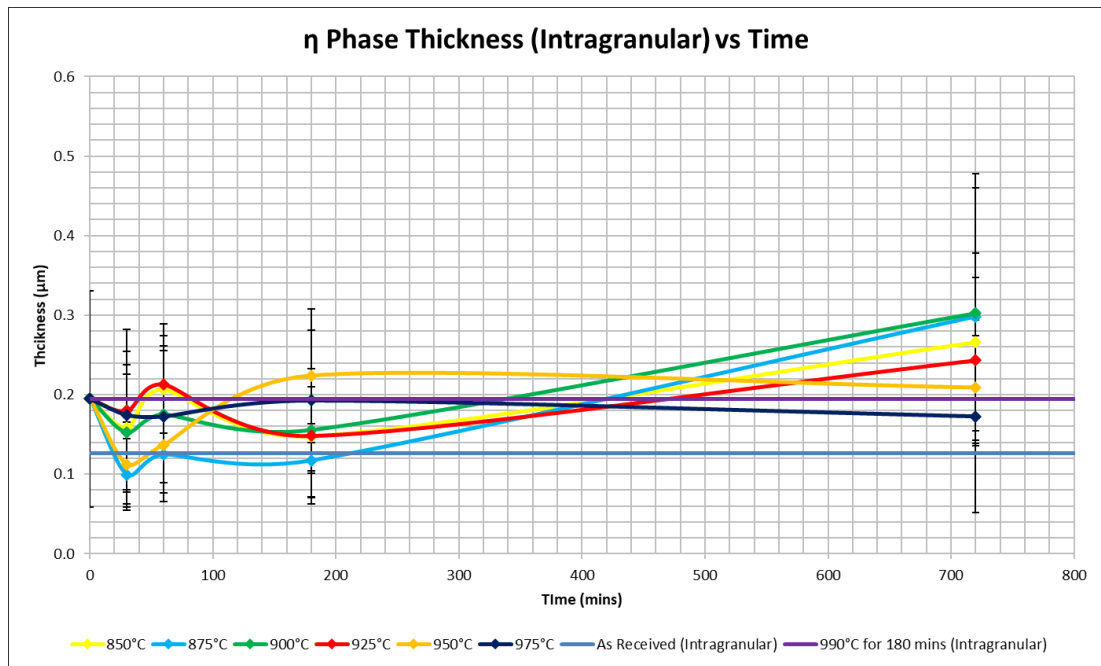


Figure 5.23 –  $\eta$  phase (intragranular) precipitate thickness against time in strain-free material

Time (mins)	Thickness ( $\mu\text{m}$ ) (Intragranular)					
	850°C	875°C	900°C	925°C	950°C	975°C
0	$0.19 \pm 0.14$	$0.19 \pm 0.14$	$0.19 \pm 0.14$	$0.19 \pm 0.14$	$0.19 \pm 0.14$	$0.19 \pm 0.14$
30	$0.16 \pm 0.10$	$0.10 \pm 0.05$	$0.15 \pm 0.07$	$0.18 \pm 0.10$	$0.11 \pm 0.05$	$0.17 \pm 0.06$
60	$0.21 \pm 0.05$	$0.12 \pm 0.05$	$0.18 \pm 0.10$	$0.21 \pm 0.08$	$0.14 \pm 0.07$	$0.17 \pm 0.08$
180	$0.15 \pm 0.09$	$0.12 \pm 0.05$	$0.16 \pm 0.05$	$0.15 \pm 0.08$	$0.22 \pm 0.08$	$0.19 \pm 0.09$
720	$0.27 \pm 0.11$	$0.30 \pm 0.16$	$0.30 \pm 0.18$	$0.24 \pm 0.10$	$0.21 \pm 0.07$	$0.17 \pm 0.12$

Table 5.13 – Results of strain-free  $\eta$  phase precipitate thickness (intragranular)

For the intragranular precipitate thickness data, the trajectories are similar at 850°C, 875°C and 900°C, but differences are observed at 925°C, 950°C and 975°C. At 925°C, the intragranular precipitate thickness can be seen to decrease between 60 minutes and 180 minutes which is contrast to the overall data where the overall precipitate thickness increases during the same time interval. At 950°C, the intragranular precipitate thickness increases between 60 minutes and 180 minutes while for the overall precipitate thickness data, the thickness increases but only slightly. Staying at 950°C, the intragranular precipitate thickness slightly decreases between 180 minutes and 720 minutes, while a large increase is observed during the same time interval at the same

temperature. At 975°C, the intragranular precipitate thickness is seen to slightly decrease between 180 minutes and 720 minutes, while during the same time range for the overall precipitate thickness data, the precipitate thickness is observed to increase.

## **5.4 Discussion**

### **5.4.1 TTT Diagram**

Within the literature, other authors have attempted to work on the precipitation kinetics of the  $\eta$  phase albeit with slightly different methodologies and in different conditions. In this discussion, a comparison will be made between the results obtained in this study to published data in literature.

In Figure 5.24 and Figure 5.25, a comparison is made between the data obtained in this study and the data obtained by Casanova et al. (77). Figure 5.24 shows the comparison for  $\eta$  phase area percentage at 1%, and Figure 5.25 shows the comparison for  $\eta$  phase area percentage at 4%.

In the study by Casanova et al. (77), the  $\eta$  phase precipitation kinetics was studied in two locations of an as-received wrought billet, namely the core and the rim regions of the wrought billet. The as-received wrought billet in the study by Casanova et al. (77) was not solutioned before starting the annealing heat treatments which implies that some percentage of  $\eta$  phase must have been present within the initial microstructure.

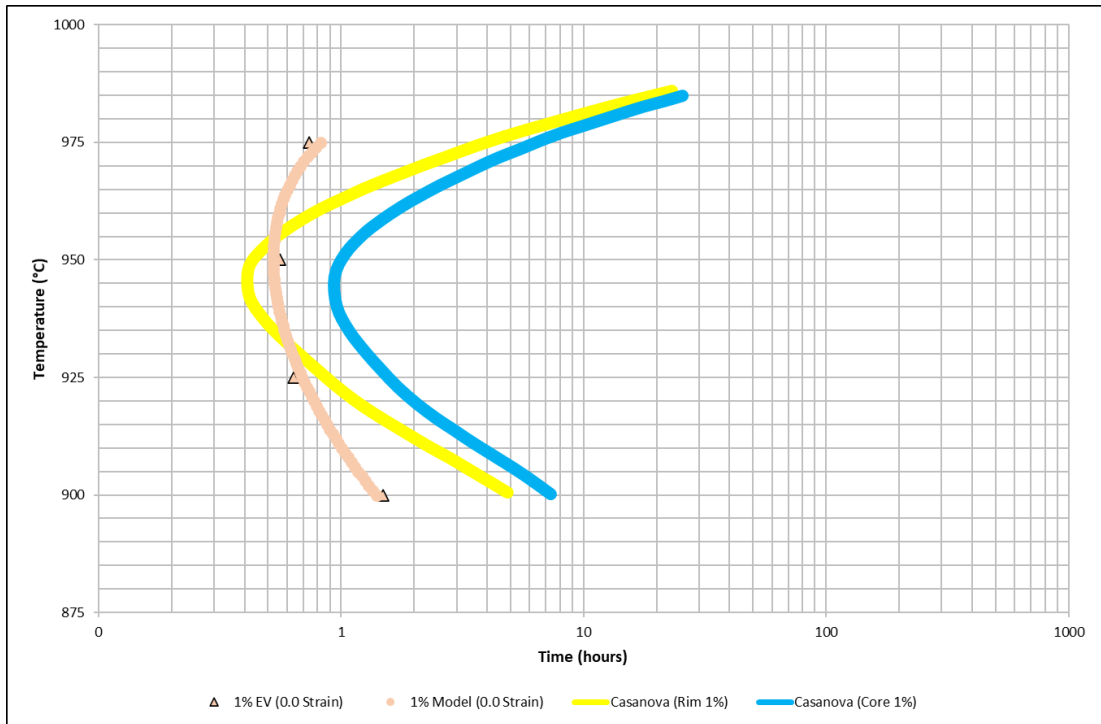


Figure 5.24 – Comparison with Casanova et al. (77) at 1% area fraction

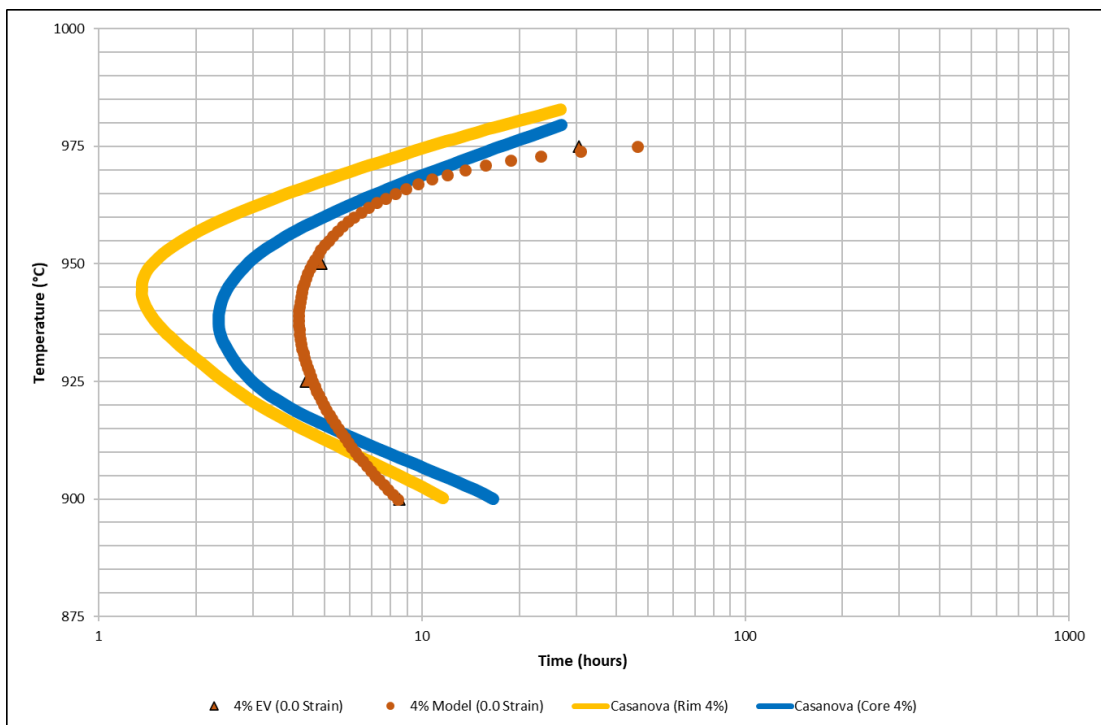


Figure 5.25 – Comparison with Casanova et al. (77) at 4% area fraction

Interestingly, the comparison provides mixed results at the two different area percentages. From Figure 5.24, the precipitation kinetics obtained in this study for 1% area fraction are somewhere in between the rim and core results at 1% area fraction by Casanova et al. (77), although it can be observed that the current study results are closer to the rim results by Casanova et al. (77). For the comparison at 4% area fraction (see Figure 5.25), the results obtained in this study are noticed to be slower in comparison to both the rim and core results by Casanova et al. (77).

It has been noted within the published literature that subsequent precipitation after solutioning strain-free ATI 718Plus material is slower in comparison to that in strained ATI 718Plus material (61). This seems to have been observed here in this study too with respect to the comparison at 4% area fraction, as the starting material in this study is recrystallised and strain-free. As stated earlier, the starting material that Casanova et al. (77) used is a wrought billet in the as-forged condition. Within this wrought billet, the core regions were observed to be mostly large sized recrystallised grains whereas the rim regions were smaller sized unrecrystallised deformed grains. This means that some amount of strain would have been present at the rim regions within the starting material which would have accelerated the  $\eta$  phase precipitation kinetics. Also, the smaller sized grains at the rim region would have provided more grain boundary area for precipitation to occur and hence would allow for higher area percentages of  $\eta$  phase at the rim region in comparison to the core region.

One could have expected a similarity between the data obtained in this study to that at the core region. Although not extremely far off from each other, a significant gap is observed between the two TTT curves. This could possibly be the result of different material preparation methods that were utilised in this study and in the study of Casanova et al. (77). In the study by Casanova et al. (77), the samples were electrolytically etched in 10% phosphoric acid in distilled water at 2.5 V in order to reveal the  $\eta$  phase precipitates more clearly. In contrast, and as explained in Chapter 3, the samples in the current study were viewed using a SEM under the use of a BSE detector and without the use of any etching methods. Etching can have the effect of accentuating certain features of interest within the microstructure. This has the impact



of giving higher area fraction results during subsequent image processing. While this would not impact the trend of the data, it may not provide comparable results as the data set may have been overvalued.

The effect of etching method as described above could be said for the data at 4% phase area fraction. However, for the comparison at 1%, the previous arguments do not seem to hold here as current results from this study are in between the rim and core results by Casanova et al. (77). It could be that the effects of different etching methods are only observed to be in effect at higher area fraction percentages, since 1% is a relatively too small of a percentage to compare against. However, the grain size of the microstructure at the core region in the study by Casanova et al. (77) is mentioned within the literature to be ASTM 8, whereas the average grain size of the starting material in the current study is approximately ASTM 9.5. This could explain why the precipitation kinetics in the current study at 1% is faster than the 1% precipitation kinetics from the core region in the work of Casanova et al. (77). The smaller starting grain size in the current study allows for more and quicker precipitation to occur and hence can reach 1% area fraction faster than the precipitation kinetics from a coarser grain size with less grain boundaries as is the case with study by Casanova et al. (77).

In the next three figures, a comparison is made between the precipitation kinetics from recrystallised strain-free material obtained in this study, to the precipitation kinetics that have been obtained by Cao (22). Figure 5.26 shows the comparison at 0.5% area fraction, Figure 5.27 displays the comparison at 2% area fraction, while Figure 5.28 shows the comparison at 5% area fraction. Figure 5.29 shows another comparison at 0.2% but against a different author than Figure 5.27.

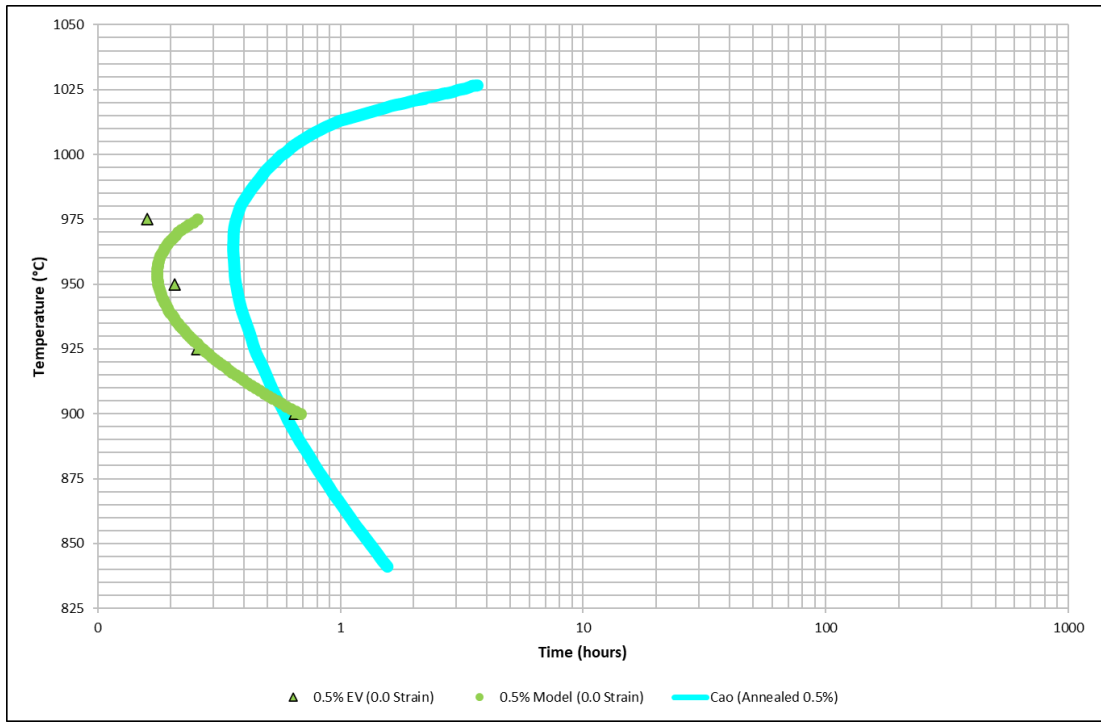


Figure 5.26 – Comparison with Cao (22) at 0.5% area fraction

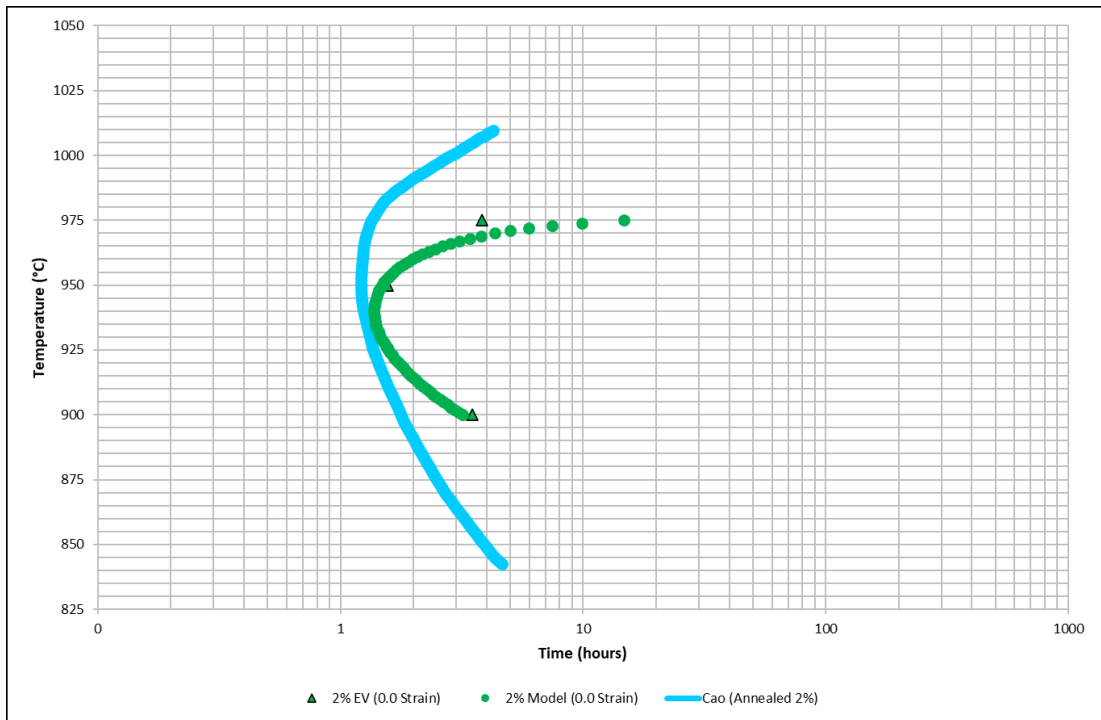


Figure 5.27 – Comparison with Cao (22) at 2% area fraction

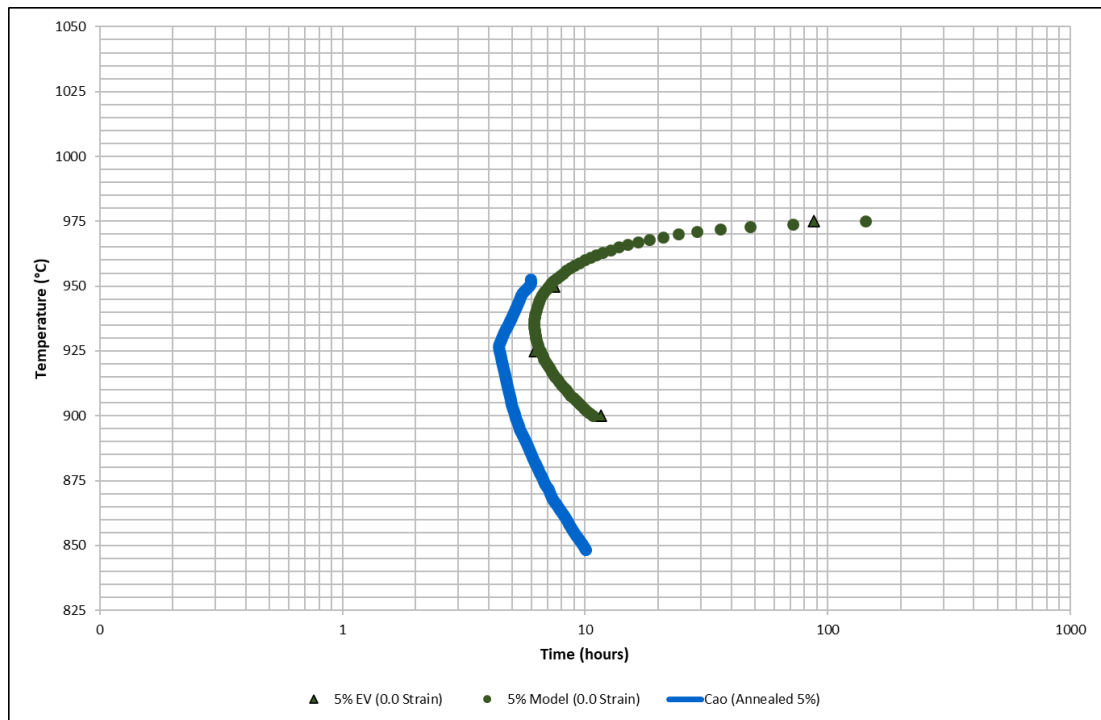


Figure 5.28 – Comparison with Cao (22) at 5% area fraction

In the study by Cao (22), the  $\eta$  phase precipitation kinetics was studied on ATI 718Plus material through the use of a simulation software package called JMatPro. The modelling analysis was performed to produce TTT curves for 0.5%, 2% and 5%  $\eta$  phase precipitate content. The modelling included a solutioning heat treatment that was performed above the  $\eta$  phase solvus temperature, specifically at 1038°C. After such heat treatment, no initial  $\eta$  phase precipitates should be in exist within the microstructure, as the elemental constituents should have dissolved back into the austenitic matrix. The TTT curves obtained from this study are somewhat close to the simulated curves obtained by Cao (22), although it is noticed that the nose of the simulated curves do not match with the nose of the curves obtained in this study. At 0.5% content, the nose of the simulated curve is a little higher than that of the experimental curve obtained in this study. The same is also true for the 2% content comparison in Figure 5.27. While at 5% content, the nose of the simulated curves is a little below the nose of the experimental curve from the current study. Although the difference in methodology, it is interesting to see a somewhat good correlation between simulated data from Cao (22), and the experimental data from this study,

albeit with some quantitative differences and differences in the nose temperature of the curves.

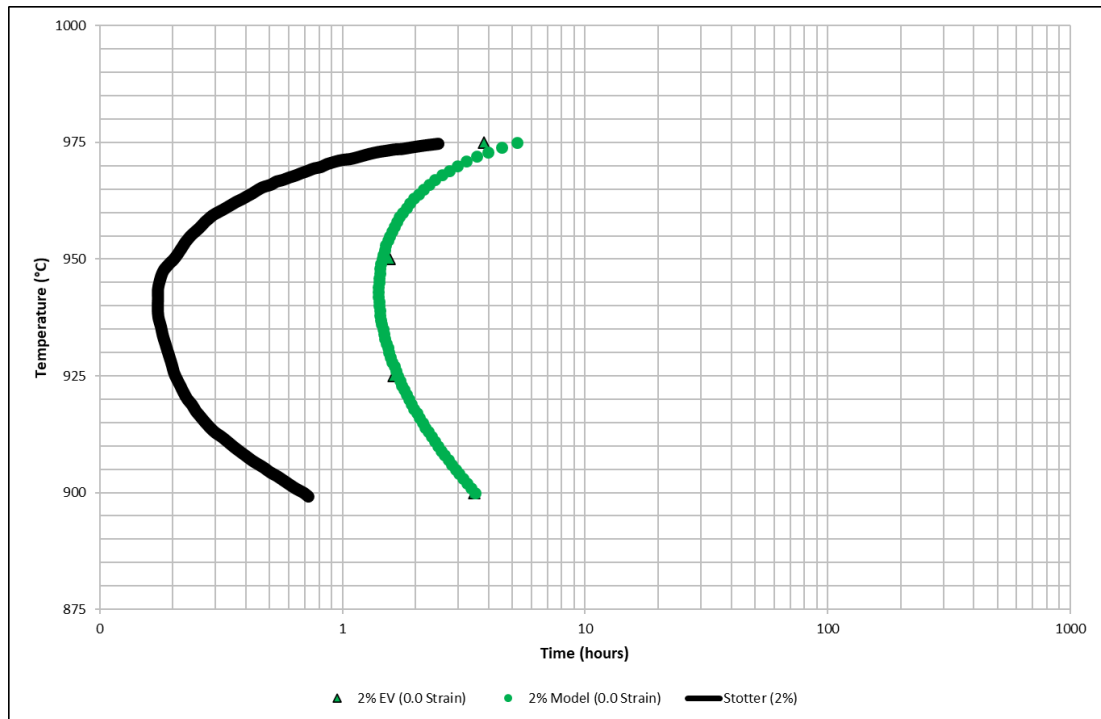


Figure 5.29 – Comparison with Stotter et al. (85) at 2% area fraction

In Figure 5.29, the  $\eta$  phase precipitation kinetics obtained in this study is compared to that obtained by Stotter et al. (85). In both studies, the TTT curves represent the precipitation behaviour at 2% area fraction. In the study by Stotter et al. (85), the samples that were used to produce the TTT diagram were taken from a super-solvus forged rod, which means that the starting material has some amount of strain within the microstructure (similar to the rim region in the study performed by Casanova et al. (77)). This explains how the curve by Stotter et al. (85) at 2% content is considerably faster than the 2% curve produced in this study. The strain in the material produced by forging has accelerated the precipitation kinetics of the  $\eta$  phase. Also, in the study by Stotter et al. (85) the samples were etched in a solution of 150 ml of water, 3 ml of hydrochloric acid and 1 ml of hydrofluoric acid. As has been mentioned previously, etching can emphasise the precipitate size which can give larger area fraction measurements than in reality. In this comparison, the difference between the two studies is expected due to the different starting material conditions.

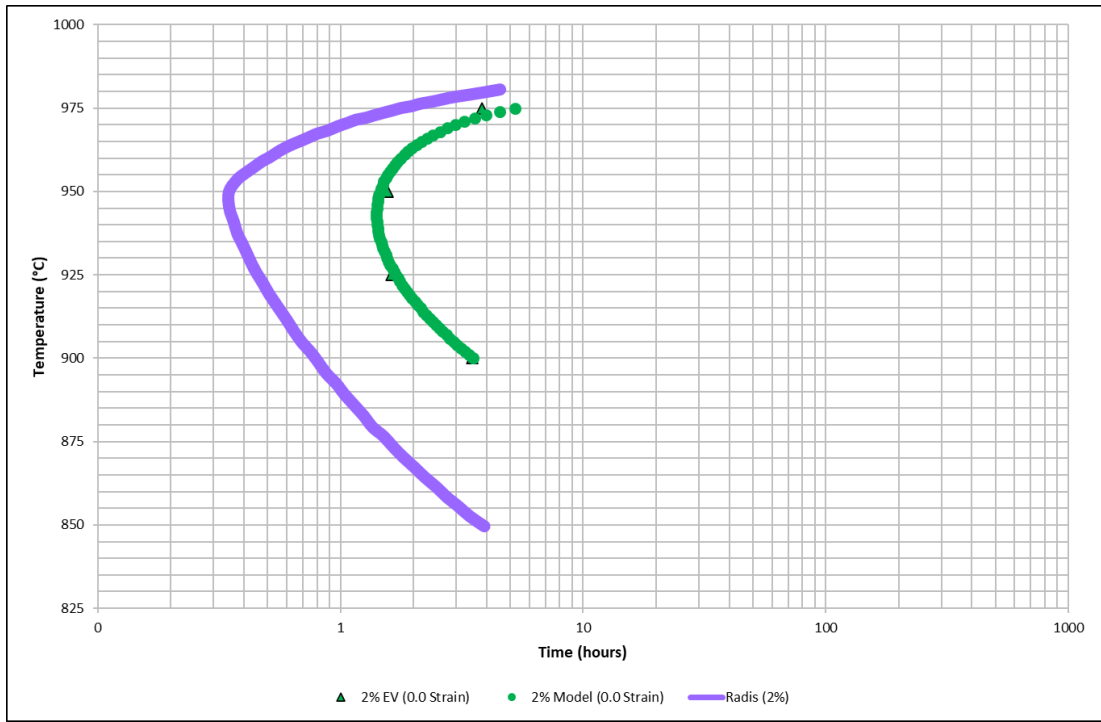


Figure 5.30 – Comparison with Radis et al. (36) at 2% area fraction

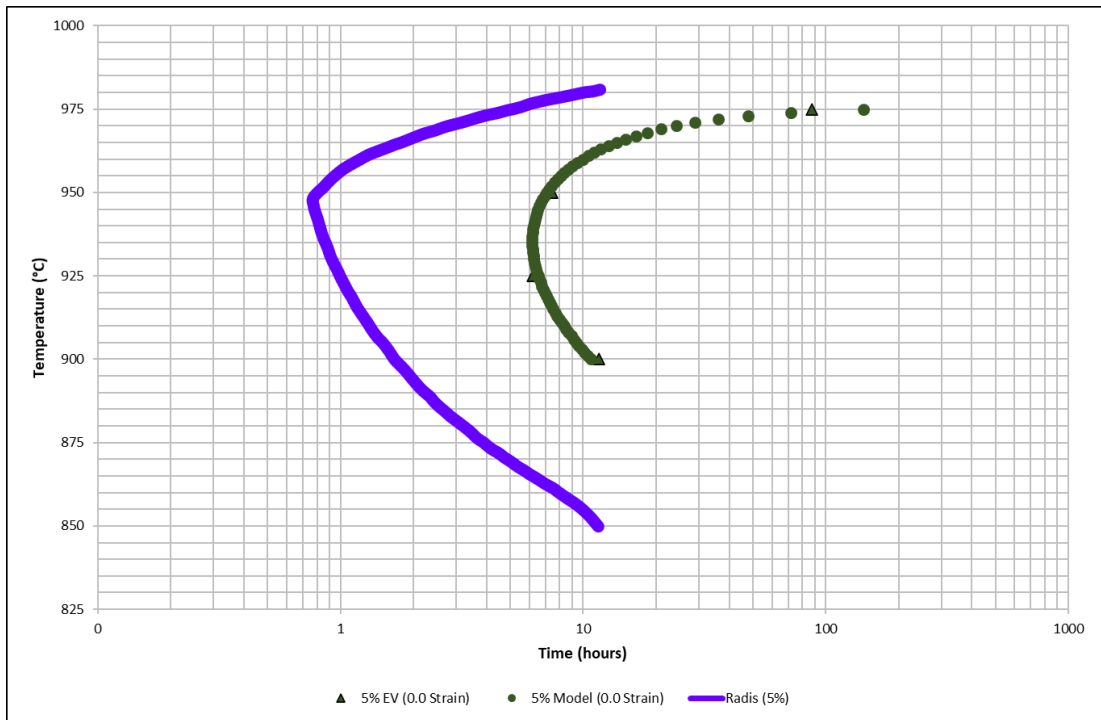


Figure 5.31 – Comparison with Radis et al. (36) at 5% area fraction

In Figure 5.30 and Figure 5.31, the recrystallised strain-free  $\eta$  phase precipitation kinetics studied in this work is compared to that published by Radis et al. (36). In the work by Radis et al. (36), the authors obtained their precipitation kinetics data through the use of a simulation software package called MatCalc. Thermodynamic adjustments and corrections are performed by the authors which provide simulated data which matches the authors experimental results very well. The simulations were performed in order to compare against the experimental data by Stotter et al. (85) and therefore the starting material conditions that were used in the study by Radis et al. (36) are the same as those in the study by Stotter et al. (85), in which samples were produced from super-solvus forged rods. Therefore, similar precipitation kinetic differences are observed between the strain-free precipitation kinetics produced by this study, and the precipitation kinetics obtained by Stotter et al. (85) and Radis et al. (36). The faster TTT precipitation kinetics from Radis et al. (36) are due to the fact that the starting material condition has strain within the microstructure, which has the effect of accelerating the precipitation kinetics, as mentioned previously.

#### 5.4.2 Aspect Ratio, Length and Thickness

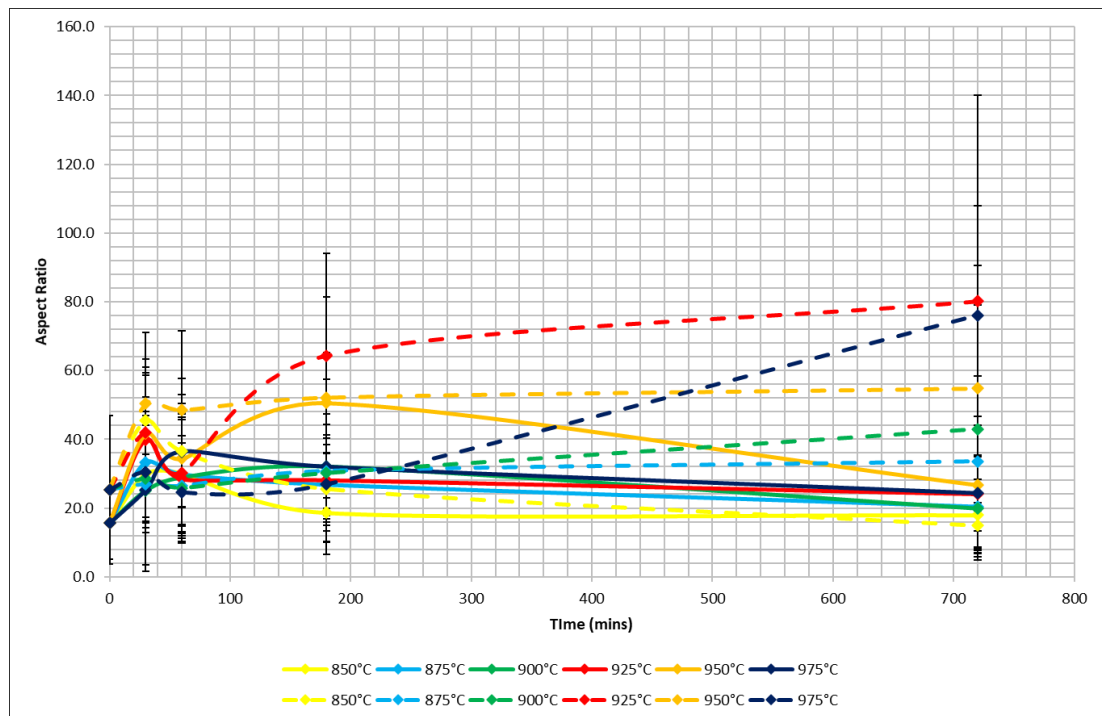


Figure 5.32 – Intergranular (solid) & intragranular (dashed) precipitate aspect ratio

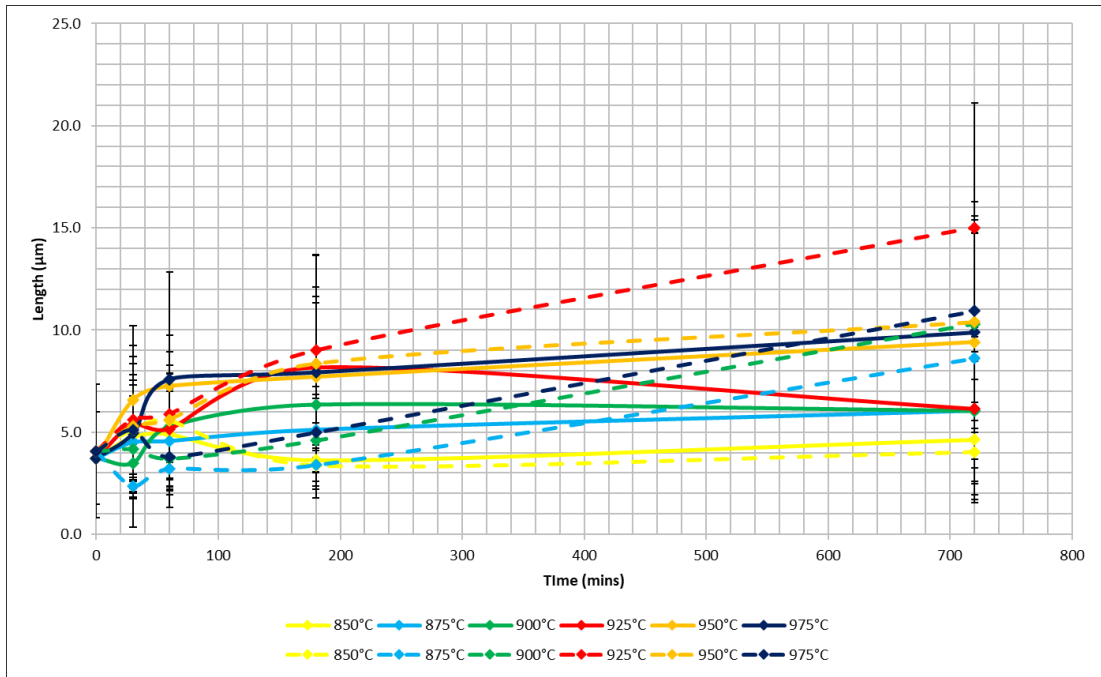


Figure 5.33 – Intergranular (solid) & intragranular (dashed) precipitate length

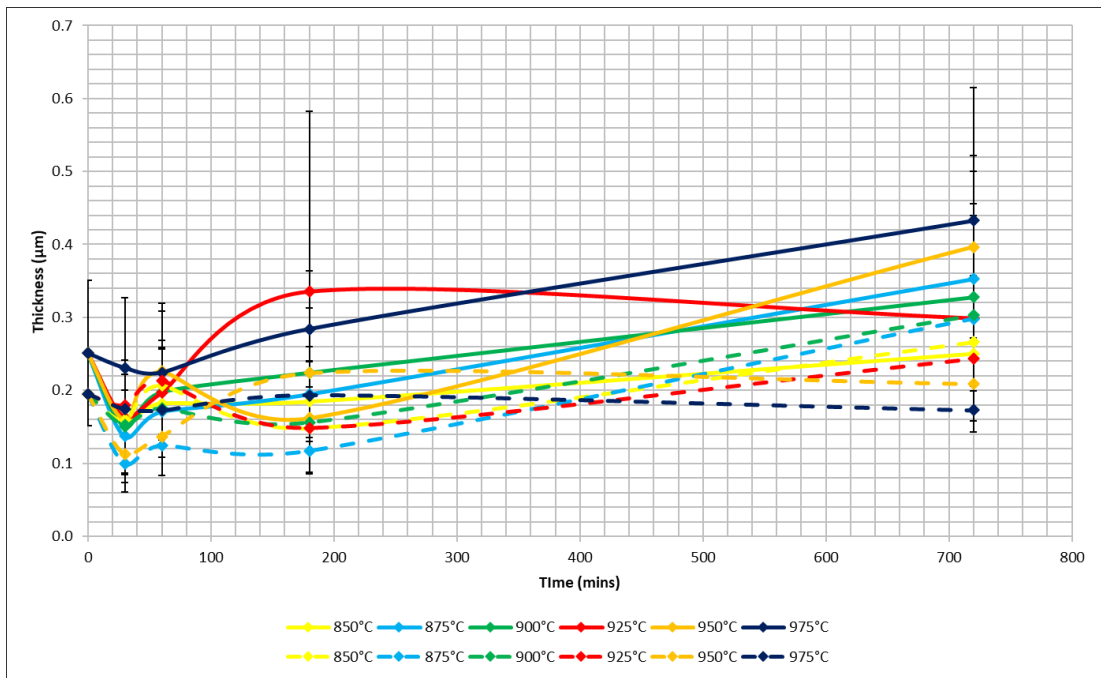


Figure 5.34 – Intergranular (solid) & intragranular (dashed) precipitate thickness

In Figure 5.32, Figure 5.33 and Figure 5.34, a comparison is made between intergranular and intragranular precipitates in terms of aspect ratio, length and thickness respectively. It is difficult to interpret the data and the differences between intergranular precipitates and intragranular precipitates due to the significantly large standard errors. However, it is observed that the thickness of intragranular precipitates tend to be thinner in comparison to intergranular precipitates. It is also observed that the intragranular precipitates have a larger aspect ratio in comparison to the intergranular precipitates. In some cases, the differences between intergranular and intragranular precipitates are considerably large (e.g., precipitate length after 720 minutes at 925°C) and in other cases the differences are quite small (e.g., precipitate aspect ratio after 720 minutes at 850°C).

Some general conclusions could be made regarding the aspect ratio, length and thickness by considering the data shown from Figure 5.14 to Figure 5.23. Looking at the data holistically, there is a general increase in aspect ratio, length and thickness after 720 minutes of heat treatment. The increases in precipitate length are larger than the increases in precipitate thickness, which therefore increases the aspect ratio. However, some exceptions are observed. For the aspect ratio, the average and intragranular data shows a decrease after 720 minutes at 850°C, while the intergranular data has approximately stayed the same after 720 minutes at 850°C. For the precipitate length, the average and intragranular precipitate length has stayed the same at 850°C after 720 minutes. In terms of precipitate thickness, the intergranular precipitate thickness has stayed the same at 850°C after 720 minutes. For the intragranular precipitates, the thickness has stayed approximately the same after 720 minutes at 950°C, while it has decreased after 720 minutes at 975°C.

It is seen that the data regarding the precipitate aspect ratio, length and thickness has significantly large standard errors associated with the data values. Some of the exceptions to the general trend (as described in the previous paragraph) could be explained due to the standard error within the data set. For example, the intragranular precipitate thickness after 720 minutes at 975°C is very close to that at 0 minutes. In fact, the thickness at 0 minutes is within the standard error of the value at 720 minutes,



which implies that the precipitate thickness has roughly stayed the same although the general curve shows a decrease. At 950°C, the intragranular precipitate thickness has decreased between 180 minutes and 720 minutes. However due to the large error bars, it can be assumed that the precipitate thickness has stayed the same from 180 minutes to 720 minutes at 950°C.

As mentioned before, the general trend of the aspect ratio, length and thickness is that they generally increase or stay the same after 720 minutes of heat treatment. Some exceptions are noted which have been mentioned before. The peaks and troughs in between 0 minutes and 720 minutes are difficult to explain definitively and conclusively but some suggestions are made in this study.

Very little literature regarding precipitate thickness, length or aspect ratio kinetics has been found in currently published studies. No studies were found in relation to ATI 718Plus however a study was found which was carried out by Azadian et al. (44) in which the  $\delta$  phase precipitation kinetics in Inconel 718 was investigated in different conditions. The authors studied the  $\delta$  phase precipitate thickness kinetics in two conditions of Inconel 718. Although directly comparing the results from that study to this work is of little benefit due to the different alloy and different material conditions, the overall findings by Azadian et al. (44) were that, generally speaking, the average  $\delta$  phase precipitate thickness increased as the temperature increased but had stayed relatively constant as time increased. In this study in relation to ATI 718Plus, it is holistically observed from the  $\eta$  phase precipitate thickness results (in Figure 5.16, Figure 5.20 and Figure 5.23) that the thickness increases slightly as time progresses. Correlating the  $\eta$  phase precipitate thickness with temperature is difficult as the results seem to be mixed. No trend or link is observed between  $\eta$  phase precipitate thickness and temperature.

## **5.5 Summary**

In this chapter, the  $\eta$  phase precipitation kinetics was studied in the strain-free recrystallised condition. A TTT diagram was created and comparisons were done of

the TTT diagram to those already published in the available literature. Length, thickness and aspect ratios were also investigated and any differences between intergranular and intragranular were explored. The data obtained from the study in this chapter will be used to compare the  $\eta$  phase precipitation kinetics in the strain-free recrystallised material to that from the deformed material (Chapter 6) and the larger initial grain size material (Chapter 7).

## **6 Effect of Deformation on Precipitation Kinetics**

### **6.1 Introduction**

In this chapter, the effects of deformation on the precipitation kinetics of the  $\eta$  phase in ATI 718Plus are studied. More specifically, the effect of strain as well as strain rate are explored in the current study. To carry out this study, a series of multiple isothermal compression tests were performed in order to induce deformation within the microstructure of the ATI 718Plus test pieces.

To begin with, a number of compression test pre-forms were made from the as-received ATI 718Plus extruded bar with a 16 mm diameter and a height of 24 mm. As was the case with the material used in Chapter 5, the compression test samples were heat treated at 990°C for 180 minutes before undergoing isothermal compression testing. This was done in order to ‘clean’ the microstructure from the initial  $\eta$  phase precipitates that are present within the material in the as-received condition. This led to an initial grain size roughly the same as that obtained in the previous chapter, approximately ASTM 9.5. Figure 5.1 shows the expected EBSD grain size map of the initial microstructure after heat treatment at 990°C after 180 minutes.

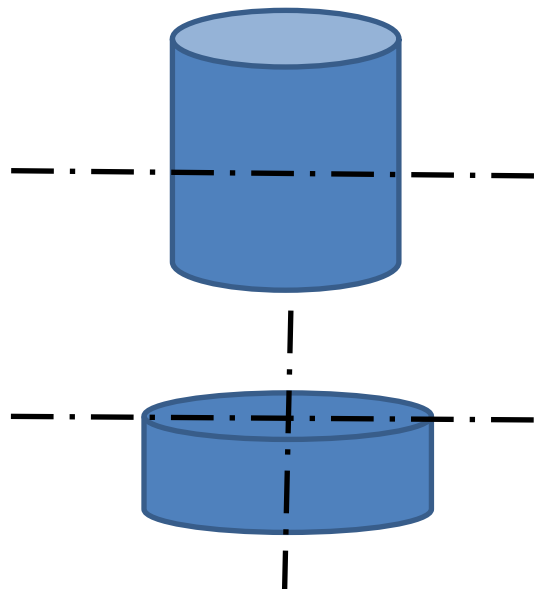
Two sets of isothermal compression tests were carried out, one set performed with a strain rate of  $0.1 \text{ s}^{-1}$  and the other performed with a strain rate of  $0.01 \text{ s}^{-1}$ . Both sets of isothermal compression tests were performed at a temperature of 990°C in order to represent the typical forging temperature used in the production of components made with ATI 718Plus at Aubert & Duval. Also, the global strain that was used in both sets of isothermal compression tests was 0.6. This was done because local regions of different strain values (0.2, 0.4, 0.6 and 0.8 strain) could be found within one compressed sample globally strained 0.6 strain. This is demonstrated in simulations that were performed in the DEFORM simulation software package using the flow curves produced from the isothermal compression tests. From these simulations, a strain map was produced for each strain rate ( $0.1 \text{ s}^{-1}$  and  $0.01 \text{ s}^{-1}$ ). These are shown in Figure 6.3 and

Figure 6.4. Further information regarding the experimental techniques used in these compression tests can be found in Chapter 3.



*Figure 6.1 – Typical ATI 718Plus cylindrical test piece after heat treatment at 990°C for 180 minutes but prior to isothermal compression testing*

After isothermal compression testing, the resultant deformed samples were machined into two halves through the mid-height section. These two halves were then cut into four quadrants, which gave a total of eight samples. This illustrated in Figure 6.2.



*Figure 6.2 – Sectioning of sample after isothermal compression testing*

Temperature (°C)	Time (minutes)							
	0.1 s <sup>-1</sup>				0.01 s <sup>-1</sup>			
900	30	60	180	720	30	60	180	720
925	30	60	180	720	30	60	180	720
950	30	60	180	720	30	60	180	720
975	30	60	180	720	30	60	180	720

*Table 6.1 – Experimental matrix for  $\eta$  phase precipitation kinetics in deformed strained material*

After sectioning the isothermal compression test samples into smaller samples, these smaller samples were then isothermally heat treated individually according to the experimental matrix which is shown above in Table 6.1. Each strain rate requires 16 samples, and since one isothermal compression test sample provides eight smaller samples, multiple isothermal compression tests had to be performed for each strain rate.

After the smaller samples had gone through the planned heat treatments described in Table 6.1, each smaller sample was then mounted, ground and polished using the techniques and procedures described previously in Chapter 3.

Using the strain maps mentioned earlier, a number of microstructural images were taken at regions of different strains, specifically 0.2, 0.4, 0.6 and 0.8 strain, via the use of SEM. For the area fraction measurements described later within this chapter, each data point is an average taken from the measurements of three images. It was thought that three images would be sufficient to obtain a good representation of the sample. Also, using three images per data point was more feasible because the image processing technique used to obtain the  $\eta$  phase area fraction (as described in Chapter 3) was considerably time consuming, and due to time constraints more images per data point was not practically possible.

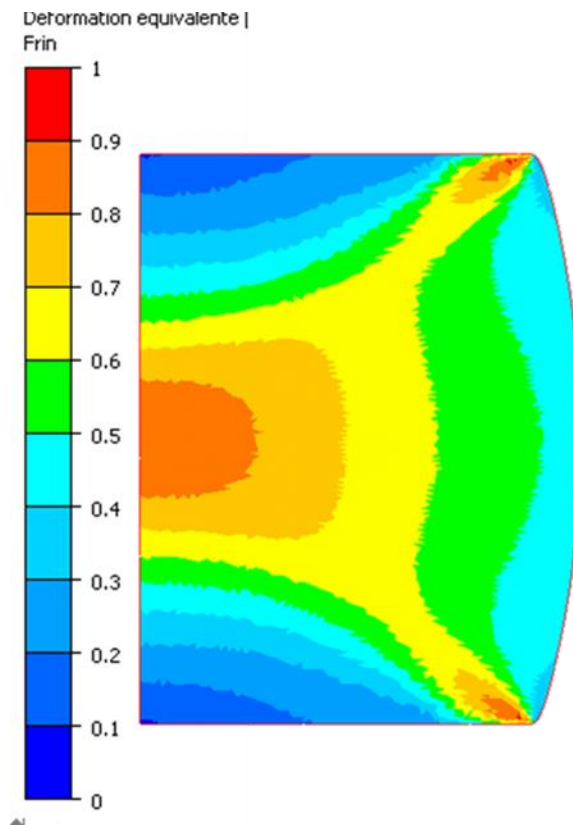


Figure 6.3 – Strain map at 0.6 global strain with  $0.1 \text{ s}^{-1}$  strain rate

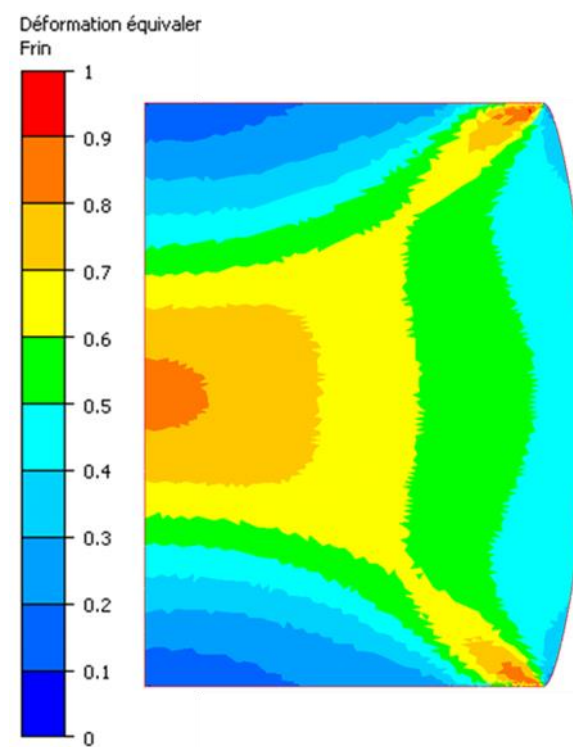


Figure 6.4 – Strain map at 0.6 global strain with  $0.01 \text{ s}^{-1}$  strain rate

## 6.2 Precipitation Kinetics at 0.1 s<sup>-1</sup> Strain Rate

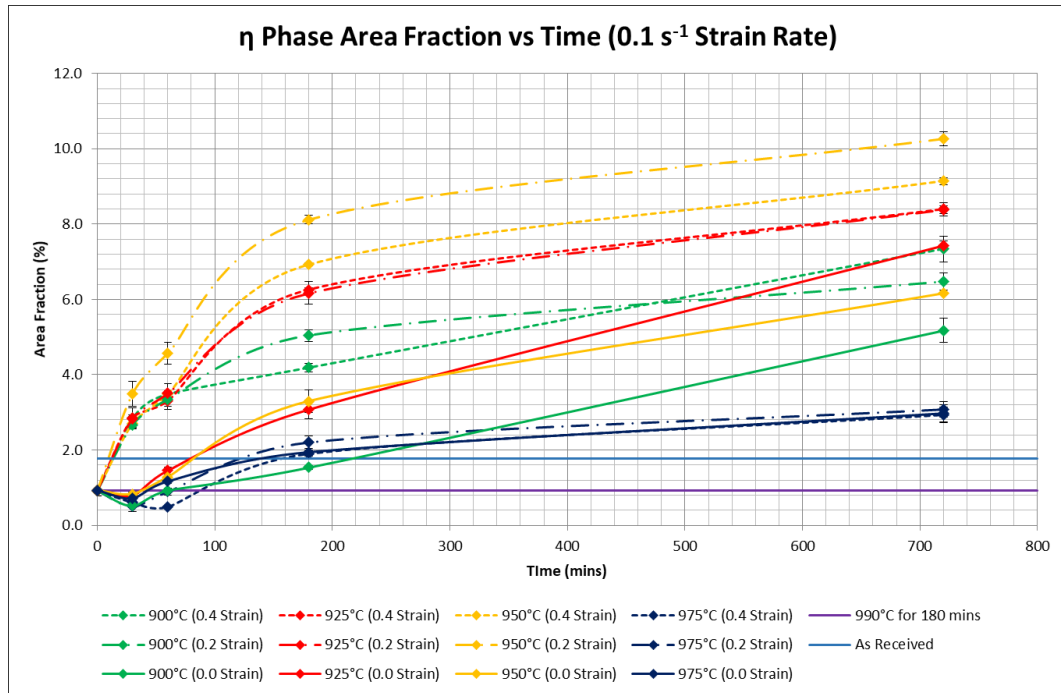


Figure 6.5 –  $\eta$  phase area fraction against time at 0.1 s<sup>-1</sup> strain rate for zero to 0.4 strain and for 900°C to 975°C

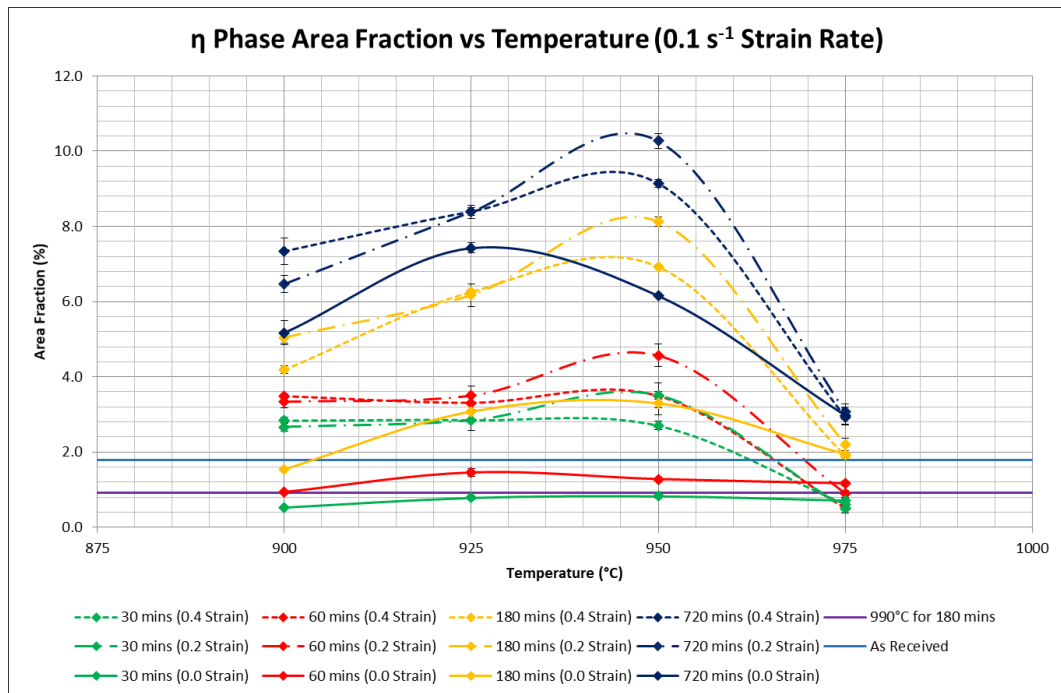


Figure 6.6 –  $\eta$  phase area fraction against temperature at 0.1 s<sup>-1</sup> strain rate for zero to 0.4 strain and for 30 mins to 720 mins

Time (mins)	Area Fraction (%)			
	900°C	925°C	950°C	975°C
0	0.93 ± 0.14	0.93 ± 0.14	0.93 ± 0.14	0.93 ± 0.14
30	2.67 ± 0.11	2.84 ± 0.05	3.50 ± 0.33	0.50 ± 0.13
60	3.34 ± 0.18	3.50 ± 0.25	4.57 ± 0.29	0.89 ± 0.09
180	5.04 ± 0.15	6.17 ± 0.30	8.12 ± 0.12	2.20 ± 0.16
720	6.47 ± 0.23	8.39 ± 0.10	10.27 ± 0.19	3.08 ± 0.21

Table 6.2 –  $\eta$  phase precipitation kinetics at 0.2 strain with  $0.1 \text{ s}^{-1}$  strain rate

Time (mins)	Area Fraction (%)			
	900°C	925°C	950°C	975°C
0	0.93 ± 0.14	0.93 ± 0.14	0.93 ± 0.14	0.93 ± 0.14
30	2.84 ± 0.09	2.85 ± 0.28	2.70 ± 0.11	0.61 ± 0.07
60	3.48 ± 0.07	3.31 ± 0.22	3.49 ± 0.09	0.49 ± 0.04
180	4.19 ± 0.11	6.26 ± 0.05	6.92 ± 0.04	1.90 ± 0.06
720	7.34 ± 0.35	8.39 ± 0.18	9.14 ± 0.10	2.93 ± 0.21

Table 6.3 –  $\eta$  phase precipitation kinetics at 0.4 strain with  $0.1 \text{ s}^{-1}$  strain rate

In this section, the results of the effect of strain on the  $\eta$  phase precipitation kinetics at  $0.1 \text{ s}^{-1}$  strain rate is presented. Figure 6.5 displays the  $\eta$  phase area fraction against time at 0 strain, 0.2 strain and 0.4 strain with a strain rate of  $0.1 \text{ s}^{-1}$ , whereas Figure 6.6 displays the  $\eta$  phase area fraction against temperature for the same strain levels at the same strain rate. Numerical values of  $\eta$  phase area fraction at 0.2 strain and 0.4 strain are shown in Table 6.2 and Table 6.3 respectively, while numerical values of  $\eta$  phase area fraction at 0.0 strain are shown in Table 5.2 in Chapter 5. As with the  $\eta$  phase area fraction data in the strain-free condition in Chapter 5, the errors shown in the above figures and tables are standard errors.

As is expected, the  $\eta$  phase area fraction increases as the time increases. It is also quite clear from both Figure 6.5 and Figure 6.6 that regardless of strain, the amount  $\eta$  phase precipitation increases in strained material in comparison to strain-free recrystallised material. Interestingly, no significant major difference has been observed between 0.2 strain and 0.4 strain in terms of the levels of  $\eta$  phase precipitation at 900°C, 925°C and



975°C. Some small differences are observed in which at some strains and times, the  $\eta$  phase area fraction is higher at 0.2 strain than 0.4 strain, and at other strains and times the contrarywise is true. It has been noticed however that at 950°C, the  $\eta$  phase area fraction at 0.2 strain is higher than that at 0.4 strain between 0 minutes to 720 minutes with the difference more pronounced than at other temperatures. However, it is not enough to conclusively say that one strain induces more  $\eta$  phase precipitation than the other. At 975°C, the  $\eta$  phase area fraction decreases between 0 minutes and 30 minutes at 0.2 strain and 0.4 strain. This not observed at the other temperatures in this study but is observed in the  $\eta$  phase precipitation kinetics in the strain-free material.

From Figure 6.6, for all times and strains studied, the peak of precipitation seems to either be at 925°C or 950°C, which is in agreement with the data for the strain-free microstructure. This reinforces the fact that the peak of  $\eta$  phase precipitation in ATI 718Plus lies somewhere in between 925°C and 950°C. As observed in Figure 6.5 as well as Figure 6.6, the  $\eta$  phase area fraction is larger at 0.2 strain than 0.4 strain for all times at 950°C. Interestingly, the peaks of precipitation at 0.2 strain and 0.4 strain after 720 minutes seem to shift to 950°C in contrast to 925°C for the strain-free material. However, this could be due to errors and fluctuations in measurements.

As was done in Chapter 5, non-linear curve fittings were completed using the Origin 2021 software package in which the Avrami equation was used as the basis for the curve fitting. The Levenburg-Marquardt iteration algorithm was used within the Origin 2021 software package for the fitting. These fittings were performed for the curves shown in Figure 6.5 for all the temperatures studied and at both 0.2 strain and 0.4 strain with 0.1 s<sup>-1</sup> strain rate. The resultant Avrami equations for 0.2 strain at 0.1 s<sup>-1</sup> strain rate are shown below from Equation 6.1 to Equation 6.4.

$$900^{\circ}\text{C} \quad y = 18.46(1 - \exp(-0.05840t^{0.30859})) \quad \text{Equation 6.1}$$

$$925^{\circ}\text{C} \quad y = 15.45(1 - \exp(-0.04994t^{0.42407})) \quad \text{Equation 6.2}$$

$$950^{\circ}\text{C} \quad y = 10.47371(1 - \exp(-0.02866t^{0.75410})) \quad \text{Equation 6.3}$$

$$975^{\circ}\text{C} \quad y = 5.88(1 - \exp(-0.01935t^{0.56484})) \quad \text{Equation 6.4}$$

For the  $\eta$  phase kinetics at 0.4 strain at  $0.1 \text{ s}^{-1}$  strain rate, the resultant Avrami equations are shown below from Equation 6.5 to Equation 6.8.

$$900^{\circ}\text{C} \quad y = 18.46(1 - \exp(-0.04438t^{0.36469})) \quad \text{Equation 6.5}$$

$$925^{\circ}\text{C} \quad y = 15.45(1 - \exp(-0.04771t^{0.43190})) \quad \text{Equation 6.6}$$

$$950^{\circ}\text{C} \quad y = 10.03(1 - \exp(-0.01886t^{0.78970})) \quad \text{Equation 6.7}$$

$$975^{\circ}\text{C} \quad y = 5.88(1 - \exp(-0.01182t^{0.62561})) \quad \text{Equation 6.8}$$

Temperature ( $^{\circ}\text{C}$ )	Adjusted $R^2$ Values	
	0.2 Strain ( $0.1 \text{ s}^{-1}$ Strain Rate)	0.4 Strain ( $0.1 \text{ s}^{-1}$ Strain Rate)
900	0.92171	0.92385
925	0.94901	0.94024
950	0.96267	0.91691
975	0.90615	0.83012

*Table 6.4 – Adjusted  $R^2$  values for Equation 6.1 to Equation 6.8*

The adjusted  $R^2$  values of the fitted Avrami equations for 0.2 strain and 0.4 strain at  $0.1 \text{ s}^{-1}$  strain rate are shown in Table 6.4. The adjusted  $R^2$  values range between 0.83012 and 0.96267, which although is generally lower than the values obtained for the  $\eta$  phase precipitation kinetics in strain-free material (see Table 5.3), it still indicates that good mathematical fits have been generated, which will reflect in the accuracy of the eventual TTT curves that will be produced from the fitted Avrami equations (Equation 6.1 to Equation 6.8).

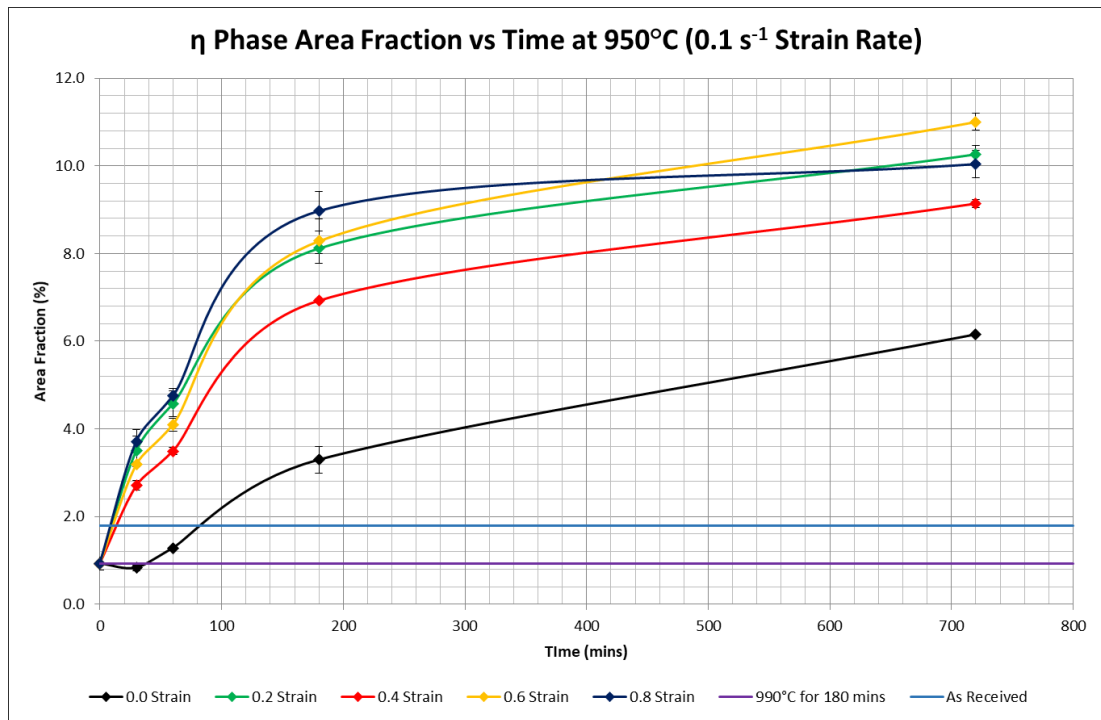


Figure 6.7 –  $\eta$  phase area fraction against time at  $0.1 \text{ s}^{-1}$  strain rate for zero to 0.8 strain and at  $950^\circ\text{C}$

Time (mins)	Area Fraction (%)			
	0.2 Strain	0.4 Strain	0.6 Strain	0.8 Strain
0	$0.93 \pm 0.14$	$0.93 \pm 0.14$	$0.93 \pm 0.14$	$0.93 \pm 0.14$
30	$3.50 \pm 0.33$	$2.70 \pm 0.11$	$3.19 \pm 0.05$	$3.71 \pm 0.27$
60	$4.57 \pm 0.29$	$3.49 \pm 0.09$	$4.10 \pm 0.15$	$4.75 \pm 0.17$
180	$8.12 \pm 0.12$	$6.92 \pm 0.04$	$8.28 \pm 0.50$	$8.97 \pm 0.45$
720	$10.27 \pm 0.19$	$9.14 \pm 0.10$	$11.01 \pm 0.20$	$10.04 \pm 0.31$

Table 6.5 –  $\eta$  phase precipitation kinetics at  $950^\circ\text{C}$  with  $0.1 \text{ s}^{-1}$  strain rate

Figure 6.7 shows the  $\eta$  phase area fraction against time at  $950^\circ\text{C}$  for strains from 0.0 to 0.8 strain with a  $0.1 \text{ s}^{-1}$  strain rate, with the numerical values shown in Table 6.5. It can be clearly observed that induced strain within the microstructure has a significant impact on the  $\eta$  phase precipitation kinetics within ATI 718Plus. The levels of  $\eta$  phase precipitation at 0.4 strain seems to be slightly lower in comparison to that at 0.2, 0.6 and 0.8 strain which is unexpected. However, the differences in  $\eta$  phase area fraction between the various levels of strain studied are so small that it becomes difficult to find a tangible correlation between 0.2 to 0.8 strain. Figure 6.9 to Figure 6.12 shows

the microstructures from 0.2 to 0.8 strain at  $0.1 \text{ s}^{-1}$  strain rate after 720 minutes of heat treatment at  $950^\circ\text{C}$ .

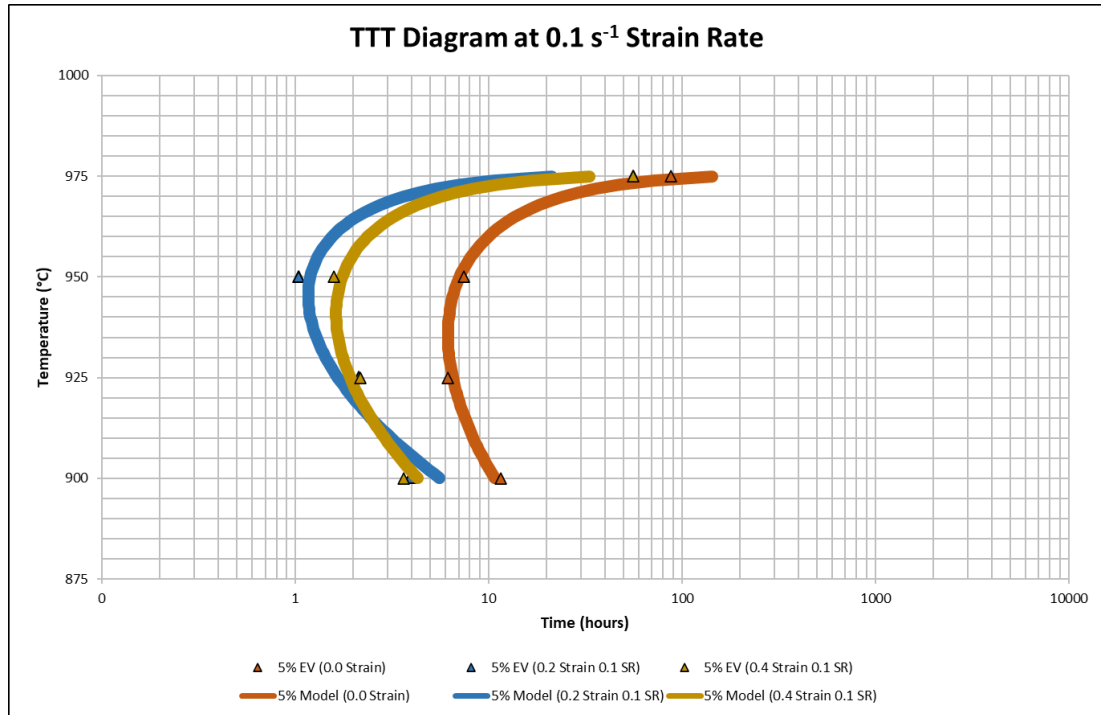
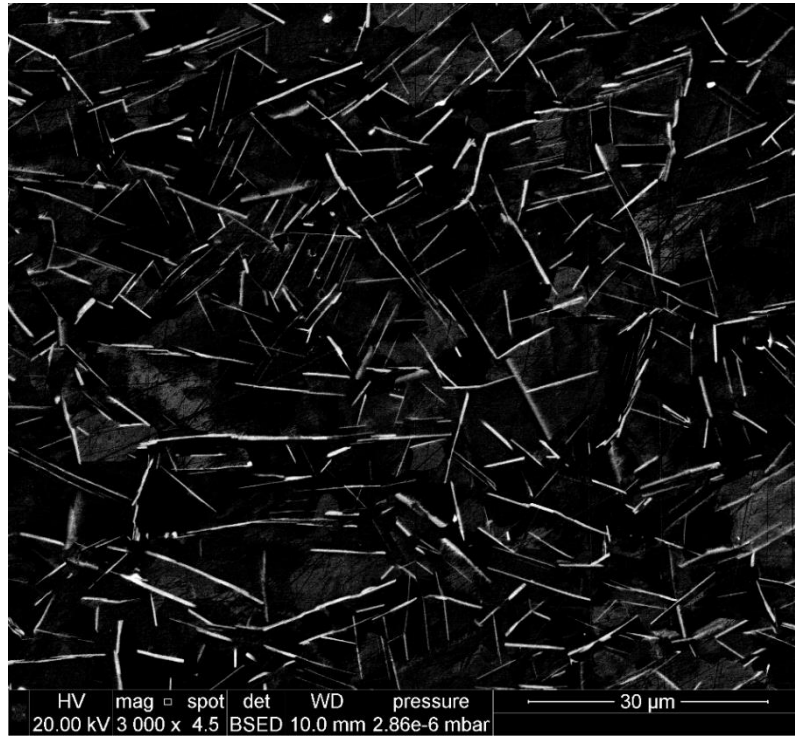


Figure 6.8 – TTT diagrams for 5%  $\eta$  phase area fraction for strain-free material, 0.2 strain and 0.4 strain with  $0.1 \text{ s}^{-1}$  strain rate

Using the Avrami equations obtained from Equation 6.1 to Equation 6.8, the TTT curves for 0.2 and 0.4 strain at  $0.1 \text{ s}^{-1}$  were produced and modelled using Equation 5.9 shown in Chapter 5. Figure 6.8 displays the TTT diagram for the  $\eta$  phase precipitation kinetics for 5% area fraction at 0.0, 0.2 and 0.4 strain with a  $0.1 \text{ s}^{-1}$  strain rate. The TTT equations that model the TTT curves at 0.2 and 0.4 strain are shown below in Equation 6.9 and Equation 6.10 respectively.

$$\begin{array}{l} \text{5\% Model} \\ \text{(0.2 strain)} \end{array} \quad \tau^{-1} = 0.048(976 - T) \exp \left[ -\frac{(976 - T)^{1.895}}{T + 273} \right] \quad \text{Equation 6.9}$$

$$\begin{array}{l} \text{5\% Model} \\ \text{(0.4 strain)} \end{array} \quad \tau^{-1} = 0.03(976 - T) \exp \left[ -\frac{(976 - T)^{1.822}}{T + 273} \right] \quad \text{Equation 6.10}$$



*Figure 6.9 – Microstructure of ATI 718Plus at 0.2 strain with 0.1 s<sup>-1</sup> strain rate and after heat treatment at 950°C for 720 minutes*

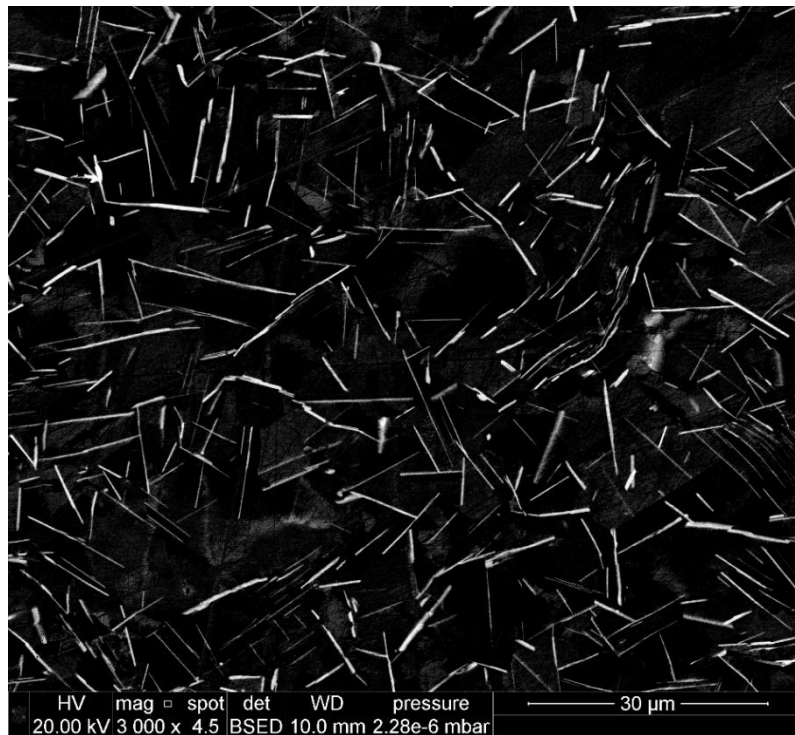


*Figure 6.10 – Microstructure of ATI 718Plus at 0.4 strain with 0.1 s<sup>-1</sup> strain rate and after heat treatment at 950°C for 720 minutes*

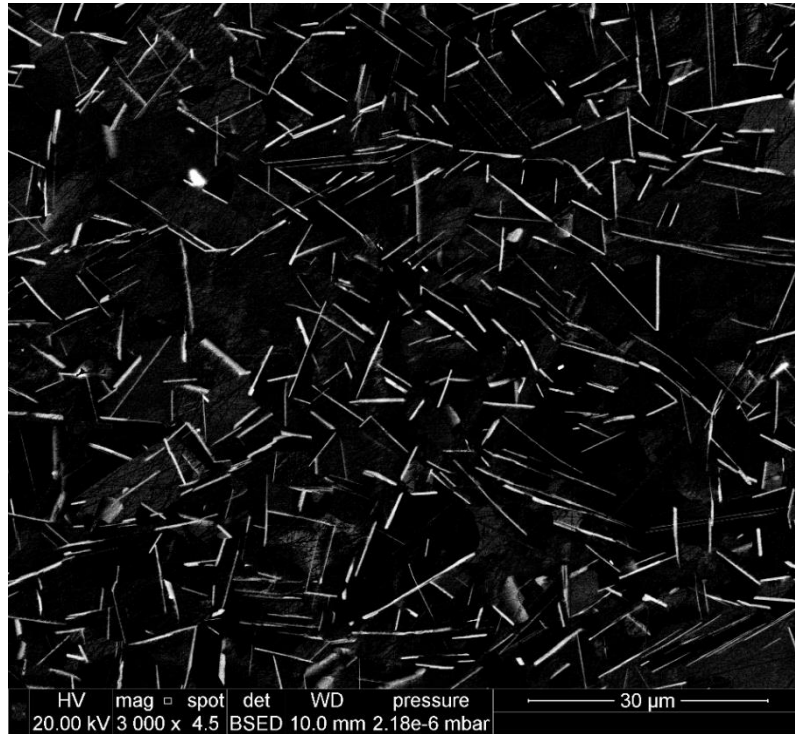


*Figure 6.11 – Microstructure of ATI 718Plus at 0.6 strain with 0.1 s<sup>-1</sup> strain rate and after heat treatment at 950°C for 720 minutes*

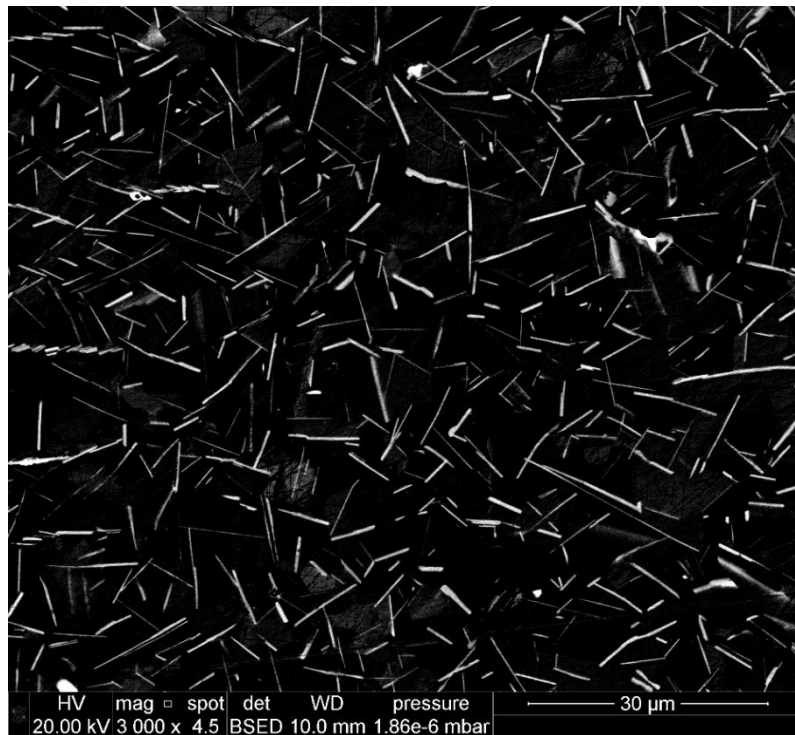


*Figure 6.12 – Microstructure of ATI 718Plus at 0.8 strain with 0.1 s<sup>-1</sup> strain rate and after heat treatment at 950°C for 720 minutes*

### 6.3 Precipitation Kinetics at 0.01 s<sup>-1</sup> Strain Rate

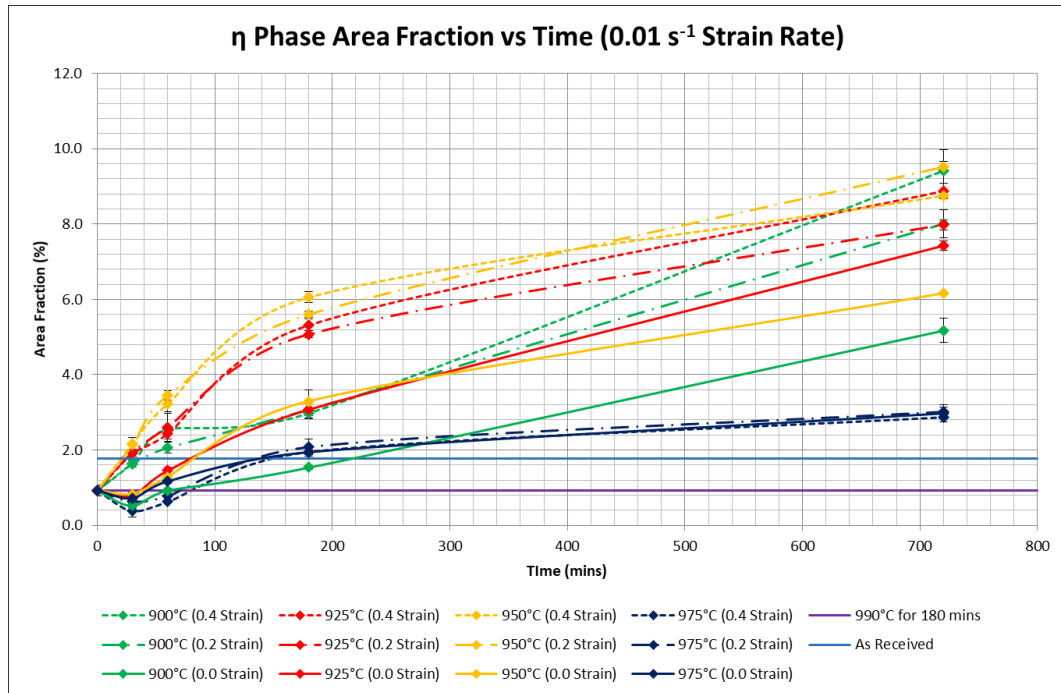


Figure 6.13 –  $\eta$  phase area fraction against time at 0.01 s<sup>-1</sup> strain rate for zero to 0.4 strain and for 900°C to 975°C

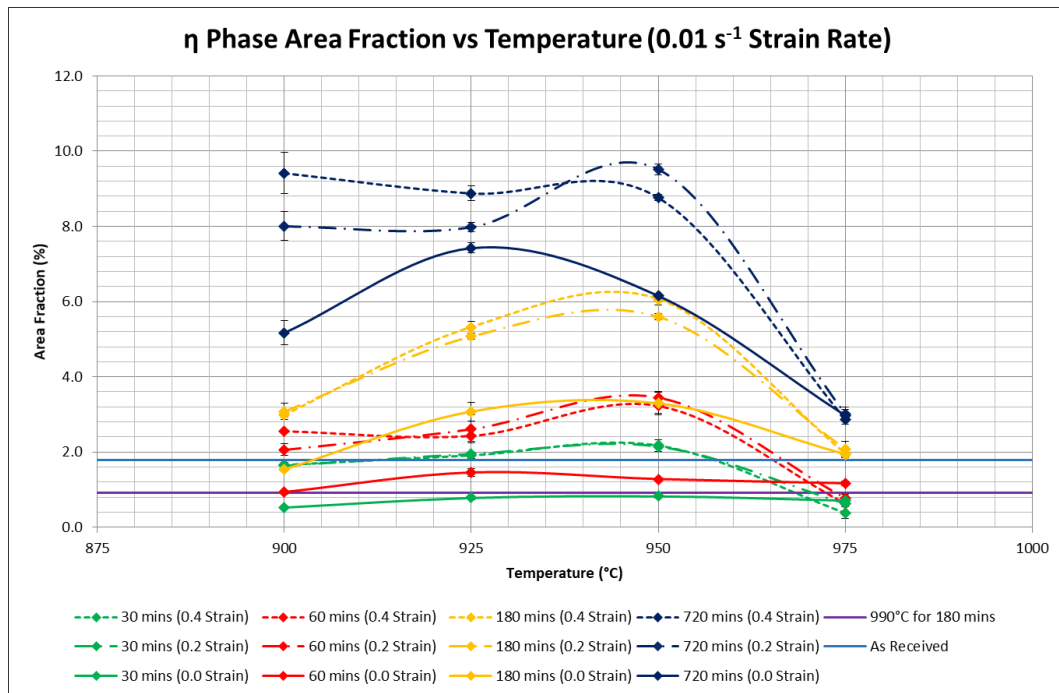


Figure 6.14 –  $\eta$  phase area fraction against temperature at 0.01 s<sup>-1</sup> strain rate for zero to 0.4 strain and for 30 mins to 720 mins

Time (mins)	Area Fraction (%)			
	900°C	925°C	950°C	975°C
0	0.93 ± 0.14	0.93 ± 0.14	0.93 ± 0.14	0.93 ± 0.14
30	1.63 ± 0.10	1.95 ± 0.01	2.14 ± 0.00	0.63 ± 0.05
60	2.06 ± 0.15	2.61 ± 0.37	3.45 ± 0.13	0.78 ± 0.09
180	3.08 ± 0.22	5.08 ± 0.09	5.60 ± 0.08	2.08 ± 0.21
720	8.01 ± 0.38	7.98 ± 0.13	9.52 ± 0.14	3.02 ± 0.13

Table 6.6 –  $\eta$  phase precipitation kinetics at 0.2 strain with  $0.01 \text{ s}^{-1}$  strain rate

Time (mins)	Area Fraction (%)			
	900°C	925°C	950°C	975°C
0	0.93 ± 0.14	0.93 ± 0.14	0.93 ± 0.14	0.93 ± 0.14
30	1.66 ± 0.03	1.91 ± 0.08	2.17 ± 0.15	0.38 ± 0.16
60	2.56 ± 0.05	2.43 ± 0.14	3.23 ± 0.21	0.63 ± 0.03
180	2.98 ± 0.06	5.32 ± 0.16	6.06 ± 0.15	1.95 ± 0.11
720	9.42 ± 0.55	8.88 ± 0.20	8.76 ± 0.08	2.86 ± 0.03

Table 6.7 –  $\eta$  phase precipitation kinetics at 0.4 strain with  $0.01 \text{ s}^{-1}$  strain rate

In this section, the results of the effect of strain on the  $\eta$  phase precipitation kinetics at  $0.01 \text{ s}^{-1}$  strain rate are presented. Figure 6.13 displays the  $\eta$  phase area fraction against time at 0 strain, 0.2 strain and 0.4 strain with a strain rate of  $0.01 \text{ s}^{-1}$ , whereas Figure 6.14 displays the  $\eta$  phase area fraction against temperature for the same strain levels at the same strain rate. Numerical values of  $\eta$  phase area fraction at 0.2 strain and 0.4 strain are shown in Table 6.6 and Table 6.7 respectively, while numerical values of  $\eta$  phase area fraction at 0.0 strain are shown in Table 5.2 in Chapter 5. As with the  $\eta$  phase area fraction data in the strain-free condition in Chapter 5, the errors shown in the above figures and tables are standard errors.

Similar to the  $\eta$  phase area fraction results obtained at  $0.1 \text{ s}^{-1}$  strain rate (see Figure 6.5 and Figure 6.6), the  $\eta$  phase area fraction increases as time increases and that regardless of the amount of strain, the amount of  $\eta$  phase precipitation substantially increases in strained material in comparison to strain-free recrystallised material, as Figure 6.13 shows. Also similar to the results with  $0.1 \text{ s}^{-1}$  strain rate, some differences between 0.2



and 0.4 strain are observed at certain temperatures and times in which one strain is higher or lower than the other but the differences are not substantial enough to make scientific conclusions. At 900°C and 925°C after 720 minutes, a visible difference is observed between 0.2 and 0.4 strain, with the  $\eta$  phase kinetics at 0.4 strain being higher than at 0.2 strain in both cases. It is difficult to say whether this is an effect of the strain or whether this is due to fluctuations and variability of the microstructures measured, especially since the differences between 0.2 and 0.4 strain are incredible small from 0 minutes to 180 minutes. At 950°C after 720 minutes of heat treatment, the area fraction at 0.2 strain is higher than at 0.4 strain, whereas at 180 minutes the area fraction at 0.4 strain is higher than at 0.2 strain. However, these differences are not significant enough to decisively say that the  $\eta$  phase precipitation kinetics at one strain are higher or lower than the  $\eta$  phase kinetics at another strain at 950°C. Rather, in the authors opinion, these differences are due to errors in measurements and the variability of microstructures as mentioned before. At 975°C, the differences in  $\eta$  phase precipitation kinetics at 0.0, 0.2 and 0.4 strain are so small that they are deemed to be negligible. Interestingly, the presence of strain within the material has no impact on the  $\eta$  phase precipitation kinetics at 975°C.

Figure 6.14 shows the  $\eta$  phase area fraction against temperature at 0.01 s<sup>-1</sup> strain rate. As was observed with the same graph at 0.1 s<sup>-1</sup> strain rate (see Figure 6.6), the peak of precipitation lies somewhere in between 925°C and 950°C, which is in agreement with the  $\eta$  phase TTT diagram for 0.1 s<sup>-1</sup> strain rate (see Figure 6.8) and the  $\eta$  phase TTT diagram for strain-free microstructure in ATI 718Plus (see Figure 5.13 in Chapter 5). It can be seen that the differences between 0.2 and 0.4 strain at 30 minutes, 60 minutes and 180 minutes are remarkable small, whereas some negligible differences are observed at 720 minutes as explained earlier.

Curve fittings were completed using the Origin 2021 software package in which the Avrami equation was used as the basis for the curve fitting, as has been done previously in this work. The Levenburg-Marquardt iteration algorithm was used within the Origin 2021 software package for the fitting. These fittings were performed for the curves shown in Figure 6.13 for all the temperatures studied and at both 0.2 strain and

0.4 strain with  $0.01 \text{ s}^{-1}$  strain rate. The resultant Avrami equations for 0.2 strain at  $0.01 \text{ s}^{-1}$  strain rate are shown below from Equation 6.11 to Equation 6.14.

$$900^{\circ}\text{C} \quad y = 18.46(1 - \exp(-0.00693t^{0.66574})) \quad \text{Equation 6.11}$$

$$925^{\circ}\text{C} \quad y = 15.45(1 - \exp(-0.02405t^{0.52184})) \quad \text{Equation 6.12}$$

$$950^{\circ}\text{C} \quad y = 10.16(1 - \exp(-0.02135t^{0.69998})) \quad \text{Equation 6.13}$$

$$975^{\circ}\text{C} \quad y = 5.88(1 - \exp(-0.01464t^{0.59515})) \quad \text{Equation 6.14}$$

For the  $\eta$  phase kinetics at 0.4 strain at  $0.01 \text{ s}^{-1}$  strain rate, the resultant Avrami equations are shown below from Equation 6.15 to Equation 6.18.

$$900^{\circ}\text{C} \quad y = 18.46(1 - \exp(-0.00502t^{0.74706})) \quad \text{Equation 6.15}$$

$$925^{\circ}\text{C} \quad y = 15.45(1 - \exp(-0.01742t^{0.59522})) \quad \text{Equation 6.16}$$

$$950^{\circ}\text{C} \quad y = 10.16(1 - \exp(-0.02540t^{0.67405})) \quad \text{Equation 6.17}$$

$$975^{\circ}\text{C} \quad y = 5.88(1 - \exp(-0.00775t^{0.67829})) \quad \text{Equation 6.18}$$

Temperature ( $^{\circ}\text{C}$ )	Adjusted $R^2$ Values	
	0.2 Strain ( $0.01 \text{ s}^{-1}$ Strain Rate)	0.4 Strain ( $0.01 \text{ s}^{-1}$ Strain Rate)
900	0.9399	0.92294
925	0.95474	0.96281
950	0.90372	0.96659
975	0.96944	0.97632

*Table 6.8 – Adjusted  $R^2$  values for Equation 6.11 to Equation 6.18*

The adjusted  $R^2$  values of the fitted Avrami equations for 0.2 strain and 0.4 strain at  $0.01 \text{ s}^{-1}$  strain rate are shown in Table 6.8. The adjusted  $R^2$  values range between 0.90372 and 0.97632, which is better than that obtained for the same strain values at

0.1 s<sup>-1</sup> strain rate, as shown in Table 6.4. This shows that good mathematical fits have been obtained, which will reflect in the accuracy of the eventual TTT curves that will be produced from the fitted Avrami equations (Equation 6.11 to Equation 6.18).

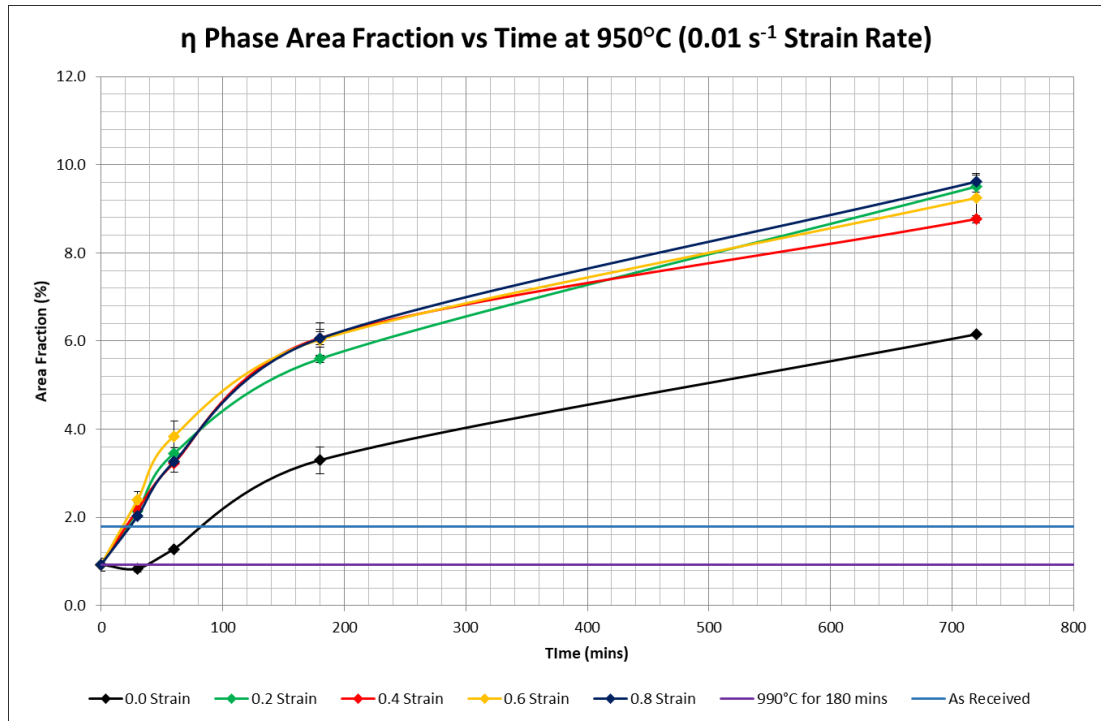


Figure 6.15 –  $\eta$  phase area fraction against time at 0.01 s<sup>-1</sup> strain rate for zero to 0.8 strain and at 950°C

Time (mins)	Area Fraction (%)			
	0.2 Strain	0.4 Strain	0.6 Strain	0.8 Strain
0	0.93 ± 0.14	0.93 ± 0.14	0.93 ± 0.14	0.93 ± 0.14
30	2.14 ± 0.00	2.17 ± 0.15	2.39 ± 0.18	2.03 ± 0.04
60	3.45 ± 0.13	3.23 ± 0.21	3.84 ± 0.34	3.26 ± 0.03
180	5.60 ± 0.08	6.06 ± 0.15	6.03 ± 0.38	6.06 ± 0.21
720	9.52 ± 0.14	8.76 ± 0.08	9.24 ± 0.56	9.62 ± 0.14

Table 6.9 –  $\eta$  phase precipitation kinetics at 950°C with 0.01 s<sup>-1</sup> strain rate

Figure 6.15 shows the  $\eta$  phase area fraction against time at 950°C for strains from 0.0 to 0.8 strain with a 0.01 s<sup>-1</sup> strain rate, with the numerical values shown in Table 6.9. Similar to the results at 0.1 s<sup>-1</sup> strain rate, it obvious to see that induced strain within

the microstructure has a significant impact on the  $\eta$  phase precipitation kinetics within ATI 718Plus.

The amounts of  $\eta$  phase precipitation at all strains from 0.2 strain to 0.8 strain are all similar to each other, with only slight fluctuations between the area fraction curves. This is in contrast to the same results obtained at  $0.1 \text{ s}^{-1}$  strain rate (see Figure 6.7) in which the area fraction curve for 0.4 strain was observed to be slightly lower than the area fraction curves at 0.2, 0.6 and 0.8 strain.

Figure 6.17 to Figure 6.20 shows the microstructures from 0.2 to 0.8 strain at  $0.01 \text{ s}^{-1}$  strain rate after 720 minutes of heat treatment at  $950^\circ\text{C}$ .

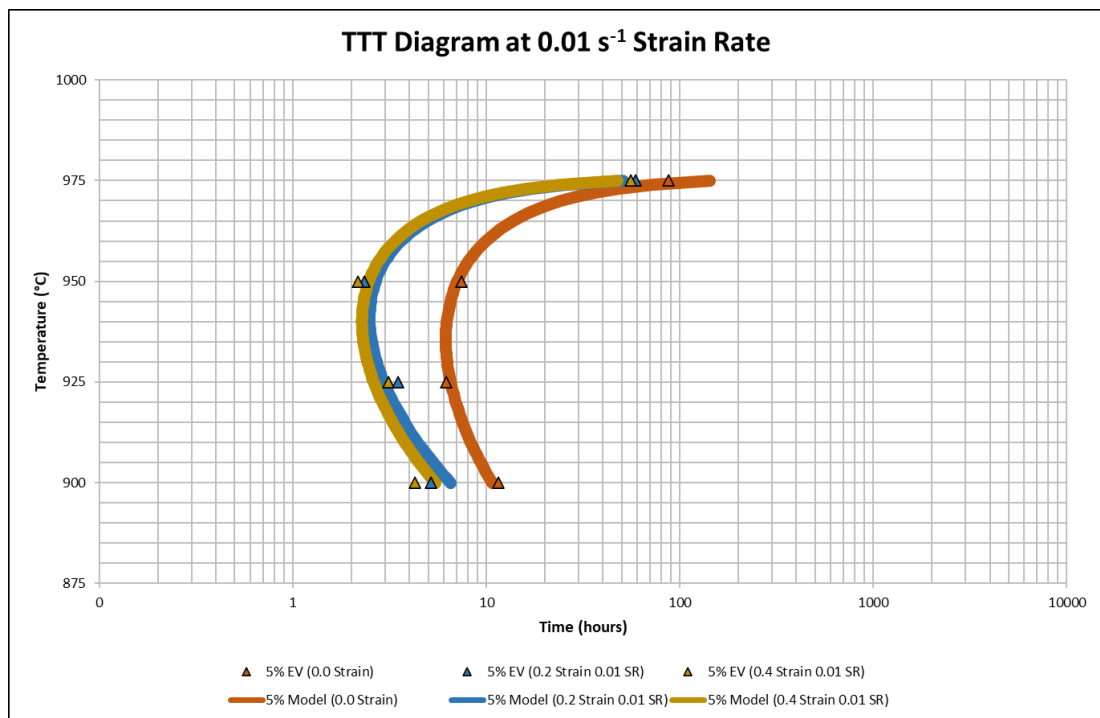


Figure 6.16 – TTT diagrams for 5%  $\eta$  phase area fraction for strain-free material, 0.2 strain and 0.4 strain with  $0.01 \text{ s}^{-1}$  strain rate

Using the Avrami equations obtained from Equation 6.11 to Equation 6.18, the TTT curves for 0.2 and 0.4 strain at  $0.01 \text{ s}^{-1}$  were produced and modelled using Equation 5.9 shown in Chapter 5. Figure 6.16 displays the TTT diagram for the  $\eta$  phase precipitation kinetics for 5% area fraction at 0.0, 0.2 and 0.4 strain with a  $0.01 \text{ s}^{-1}$  strain

rate. The TTT equations that model the TTT curves at 0.2 and 0.4 strain are shown below in Equation 6.19 and Equation 6.20 respectively.

$$\begin{array}{l} \text{5\% Model} \\ \text{(0.2 strain)} \end{array} \quad \tau^{-1} = 0.0196(976 - T) \exp \left[ -\frac{(976 - T)^{1.822}}{T + 273} \right] \quad \text{Equation 6.19}$$

$$\begin{array}{l} \text{5\% Model} \\ \text{(0.4 strain)} \end{array} \quad \tau^{-1} = 0.021(976 - T) \exp \left[ -\frac{(976 - T)^{1.810}}{T + 273} \right] \quad \text{Equation 6.20}$$

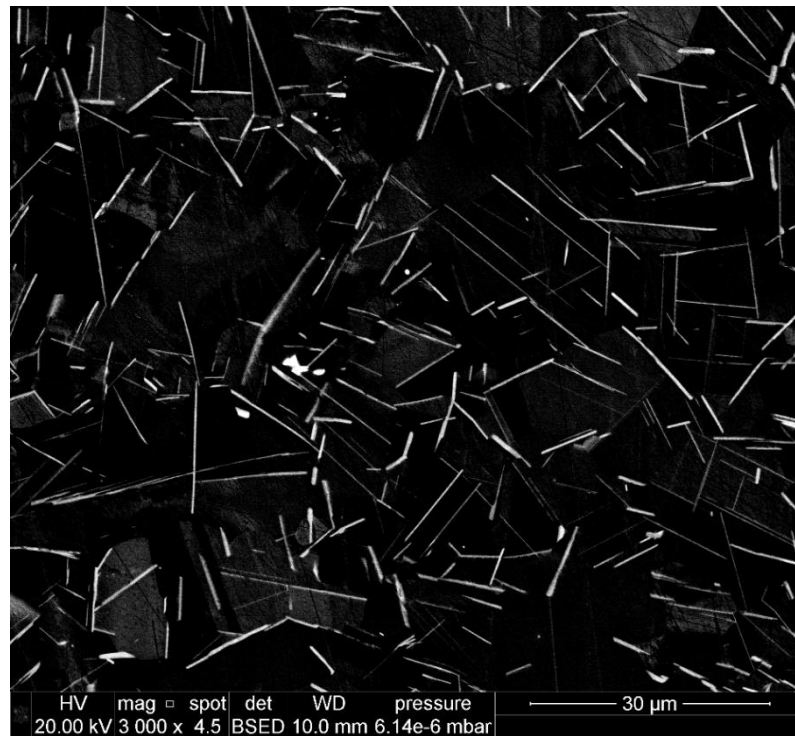


*Figure 6.17 – Microstructure of ATI 718Plus at 0.2 strain with  $0.01 \text{ s}^{-1}$  strain rate and after heat treatment at  $950^\circ\text{C}$  for 720 minutes*

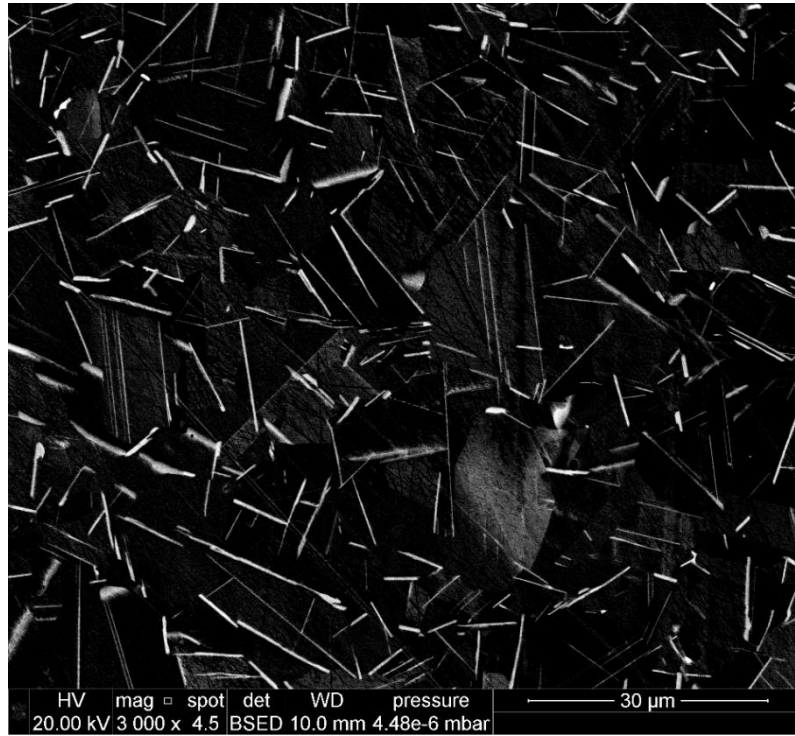


*Figure 6.18 – Microstructure of ATI 718Plus at 0.4 strain with 0.01 s<sup>-1</sup> strain rate and after heat treatment at 950°C for 720 minutes*

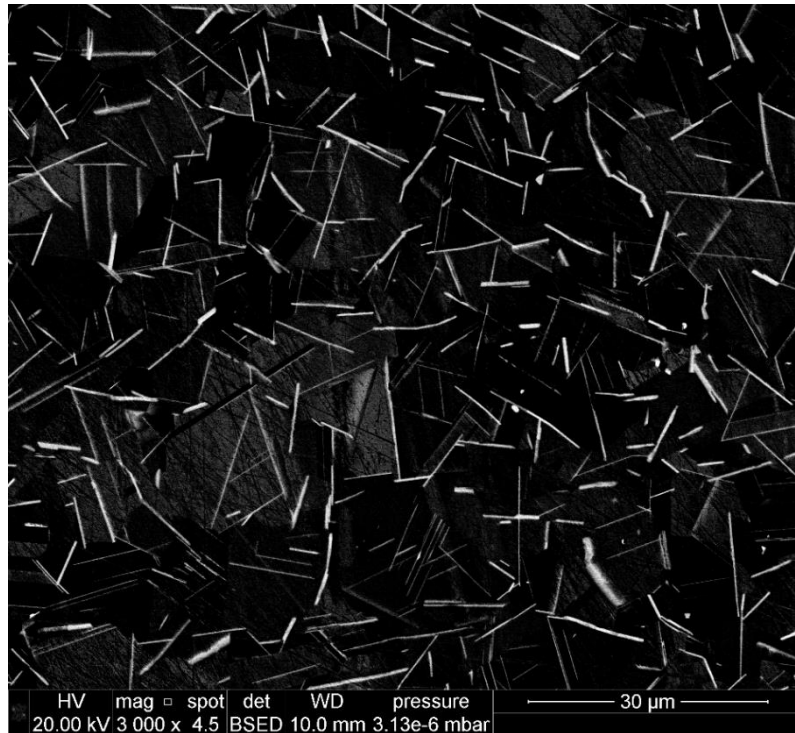


*Figure 6.19 – Microstructure of ATI 718Plus at 0.6 strain with 0.01 s<sup>-1</sup> strain rate and after heat treatment at 950°C for 720 minutes*

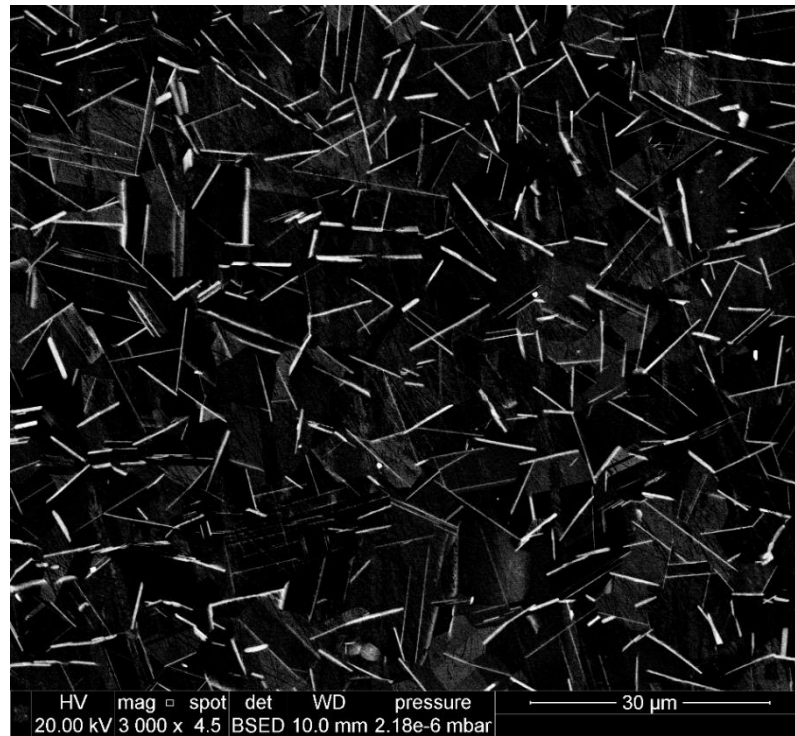


*Figure 6.20 – Microstructure of ATI 718Plus at 0.8 strain with  $0.01\text{ s}^{-1}$  strain rate and after heat treatment at  $950^{\circ}\text{C}$  for 720 minutes*

## **6.4 Discussion**

### **6.4.1 Effect of Strain**

As it can be clearly observed, induced strain in the microstructure via deformation has a significant impact on the precipitation kinetics of the  $\eta$  phase in ATI 718Plus. Deformation in ATI 718Plus considerably accelerates the precipitation kinetics of the  $\eta$  phase, as can be seen from the TTT diagrams at both  $0.01\text{ s}^{-1}$  and  $0.1\text{ s}^{-1}$  strain rate (shown in respectively) as well as the curves of area fraction against time at  $950^{\circ}\text{C}$  for both strain rates (Figure 6.7 for  $0.1\text{ s}^{-1}$  strain rate and Figure 6.15 for  $0.01\text{ s}^{-1}$  strain rate).

However, it is interesting to observe that from 0.2 strain onwards, the amount of strain does not substantially impact or differentiate the  $\eta$  phase precipitation kinetics at both strain rates studied. This is in contrast to published studies that are closely related to the current study, from which one would expect the rate of  $\eta$  phase precipitation to

increase as the strain increases. This phenomena is observed in the studies conducted by McDevitt (74) in which it was found that the volume of  $\eta$  phase precipitation increases as amount of forging reduction increases. Also, the same phenomena was also observed in studies conducted by Liu et al. (70) in which the  $\delta$  phase weight percentage was observed to increase as the amount of cold rolling increases in Inconel 718. As the amount of induced strain or deformation increases, the dislocation density would increase. This leads to an increase in the nucleation site density and the diffusivity of the precipitate-forming elements within the material. Hence, as the amount of strain increases, one would expect the amount of precipitation to increase. However, the same trend is not observed in the current study. As mentioned before, a significant increase in  $\eta$  phase precipitation kinetics is observed for strains above 0 in comparison to no strain. However, when strain is above zero, the  $\eta$  phase precipitation kinetics stays more or less the same which is in contradiction to previous studies.

From established nucleation theory, the nucleation rate is a result of the competition between the driving forces for nucleation against the retarding forces for nucleation. The retarding forces include the interfacial and strain energy that is involved with the creation of the precipitate phase. When second phase nucleation occurs, the interfacial energy retarding force (i.e., the interfacial energy between the second phase precipitate and the neighbouring grain) decreases while the parent phase grain boundary energy increases. This is assuming that the interfacial energy between the second phase precipitate and the parent phase is insignificant.

As the amount of strain increases within the austenitic microstructure from hot working, the number of dislocations would be expected to increase too. The dislocations will increase the amount of grain boundary defect structure present, and this will have the effect of increasing the interfacial energy of the austenitic grain boundaries, including low angle (low energy) grain boundaries. This effectively reduces the barrier to nucleation and therefore the nucleation rate for precipitation should increase on all grain boundaries as the level of strain increases (67).



However, in this study, although induced strain is observed to promote further precipitation, the amount of precipitation does not increase as the strain increases. In fact, this finding is contrary to published works with similar studies (70,74). Little research has been published regarding the effect of quantitatively increasing strain on the  $\delta$  phase precipitation in Inconel 718 and even less research exists with regards to the  $\eta$  phase precipitation in ATI 718Plus. Further fundamental studies are required to fully understand why the  $\eta$  phase precipitation stays approximately constant from 0.2 strain onwards.

It has been shown in the study conducted by Sommitsch et al. (98) (and visually observed in this study) that as the amount of strain present within the material increases, the volume percentage of recrystallised grains increases within the microstructure. When grains recrystallise, the dislocations present (and the associated dislocation density) within the grains become annihilated. This recrystallisation can impact the  $\eta$  phase precipitation kinetics depending on whether recrystallisation occurred before  $\eta$  phase precipitation or after. If recrystallisation within the austenite grain structure is completed prior to the onset of  $\eta$  phase precipitation, then recrystallisation will have no impact on the precipitation. However, if  $\eta$  phase precipitation starts before recrystallisation, then induced strain via deformation considerably increases the rate of precipitation (70).

Although the recrystallisation kinetics of ATI 718Plus were not studied in this work, it can be observed from Figure 6.5 and Figure 6.13 that the  $\eta$  phase precipitation kinetics at 975°C are almost identical for 0.0, 0.2 and 0.4 strains for both 0.1 s<sup>-1</sup> and 0.01 s<sup>-1</sup> strain rate respectively. This is an indicator that the recrystallisation of the austenite matrix grains has been completed before the initiation of  $\eta$  phase precipitation at 975°C and with the strains and strain rates mentioned.

As mentioned earlier, if  $\eta$  phase precipitation commences before recrystallisation, one would expect the amount of  $\eta$  phase precipitation to increase as the strain increases since the number of dislocations (and therefore dislocation density) increases as the strain increases. More dislocations would mean more potential nucleation sites and an

increase in the diffusion of precipitate-forming elements (71) which would lead to more  $\eta$  phase precipitation. At 900°C, 925°C and 950°C, there is a clear marked increase in  $\eta$  phase precipitation from zero strain to any strain above zero. This suggests that  $\eta$  phase precipitation occurs before recrystallisation at these temperatures. However, this is not enough to explain why mixed results and trends are observed as the strain increases from 0.2 onwards.

Liu et al. (70) extensively studied the effect of cold rolling on the precipitation kinetics of  $\delta$  phase in Inconel 718. The authors found that at 960°C, the austenite matrix was completely recrystallised before the start of  $\delta$  phase precipitation, similar to what has been suggested in this study in regard to the  $\eta$  phase precipitation at 975°C. However, Liu et al. had found that although the austenite matrix had recrystallised, the amount of  $\delta$  phase precipitation still increases as the level of cold rolling deformation increases. At 960°C, the enhancement effect of cold rolling is still observed on the  $\delta$  phase precipitation kinetics even though the austenite matrix has been completely recrystallised before the onset of  $\delta$  phase precipitation.

This finding by Liu et al. (70) puts into question the well-established theory that the increase in precipitation kinetics by deformation is attributed to the increase in dislocation density (which therefore increases the nucleation site density) because the dislocations formed during deformation would have been annihilated before the beginning of precipitation. To explain this interesting result, the authors theorise and explain that due to niobium segregation, niobium (which is one of the main constituents of the  $\delta$  phase) enriches the dislocation cell walls as well as twin and grain boundaries before recrystallisation occurs. As the dislocation cell walls and initial twin and grain boundaries are moved away and eliminated by the shifting boundaries of new recrystallised grains, the formed niobium distribution doesn't change. Therefore, this means that  $\delta$  phase precipitation still occurs at previous deformation bands as well as previous twin and grain boundaries.

However, the suggested theory and explanation by Liu et al. (70) for  $\delta$  phase kinetics at 960°C in cold rolled Inconel 718 does not work in the case of  $\eta$  phase precipitation

at 975°C in hot worked ATI 718Plus, or at least the idea of aluminium and niobium segregation in ATI 718Plus is not evidenced in this study. At 975°C, almost no difference is observed in the  $\eta$  phase precipitation kinetics at zero strain, 0.2 strain and 0.4 strain which, as mentioned earlier, suggests that the recrystallisation of the austenite matrix has been completed before the start of  $\eta$  phase precipitation with the dislocations produced from hot working being completely annihilated.

To explain the  $\eta$  phase precipitation kinetics from 0.2 strain and above, it could be suggested that the maximum allowable diffusion of  $\eta$  phase forming elements (i.e., aluminium and niobium) takes place at 0.2 strain and above for both strain rates studied. This leads to similar precipitation kinetics at any strain above 0.2, which is observed at 950°C at 0.1 s<sup>-1</sup> (Figure 6.7) and 0.01 s<sup>-1</sup> (Figure 6.15) strain rates. The maximum diffusion of  $\eta$  phase forming elements would be limited by the percentages of these elements within the elemental composition of the material. Essentially, in other words, the equilibrium state is reached for any given temperature, time, strain and strain rate. It can be observed from both Figure 6.5 and Figure 6.7 (at 0.1 s<sup>-1</sup> strain rate) that the results at 0.4 strain are strangely slightly below 0.2 strain. This observation is attributed to variance and error in data acquisition. In fact, the slight differences observed in Figure 6.13 and Figure 6.15 between the curves of 0.2 and 0.4 strain (at 0.01 s<sup>-1</sup> strain rate) could also be ascribed to experimental variance and error.

Another interesting phenomenon which was observed in the current study was the quick drop and subsequent rise in  $\eta$  phase area fraction between 0 minutes to 30 minutes. This rapid re-solutioning and precipitation is particularly observed for  $\eta$  phase area fraction kinetics at 975°C for both 0.2 and 0.4 strains with 0.1 s<sup>-1</sup> and 0.01 s<sup>-1</sup> strain rate. This trend is also observed at all temperatures for the  $\eta$  phase kinetics for the strain-free recrystallised material (see Figure 5.4). References to this phenomenon has not been found in the published literature as of writing but it is an interesting finding that could be explored further in future studies.

## 6.4.2 Effect of Strain Rate

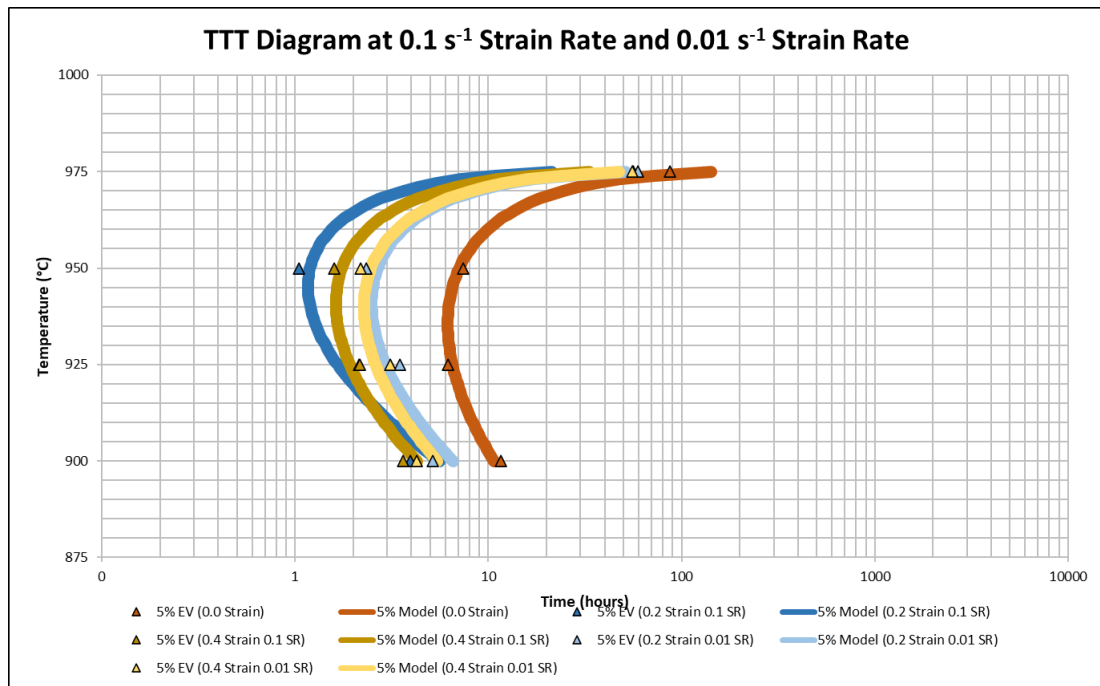


*Figure 6.21 – TTT diagrams for 5%  $\eta$  phase area fraction for strain-free material, 0.2 strain and 0.4 strain with 0.1 s<sup>-1</sup> and 0.01 s<sup>-1</sup> strain rates*

It can be observed from Figure 6.21 that the overall precipitation kinetics of  $\eta$  phase at 0.1 s<sup>-1</sup> are faster than the precipitation kinetics at 0.01 s<sup>-1</sup> for both 0.2 strain and 0.4 strain. It is inferred that reducing the deformation strain rate has the effect of slowing the kinetics of  $\eta$  phase precipitation in ATI 718Plus. It can be suggested that a lower strain rate slows the rate of dislocations produced within the material microstructure. Therefore, the dislocation density at a given time at 0.01 s<sup>-1</sup> strain rate would be lower than the dislocation density at the same time at 0.1 s<sup>-1</sup> strain rate. As mentioned previously, dislocations behave as nucleation sites for  $\eta$  phase precipitation, so a lower dislocation density would mean a lower amount of  $\eta$  phase precipitation.

Hence, it can be hypothesised that at the lower strain rate of 0.01 s<sup>-1</sup>, it takes a longer time to reach the same number of dislocations at a given point in comparison to that at 0.1 s<sup>-1</sup> strain rate. Therefore, at 0.01 s<sup>-1</sup> strain rate it takes a longer time to reach a particular amount of precipitation in comparison to 0.1 s<sup>-1</sup> strain rate. Hence the slower

$\eta$  phase precipitation kinetics at  $0.01 \text{ s}^{-1}$  strain rate in comparison to that at  $0.1 \text{ s}^{-1}$  strain rate, as observed in Figure 6.21.

### 6.4.3 Effect of n and k Parameters

In Equation 5.1 within Chapter 5, k and n are coefficients in which the former is the rate of  $\eta$  phase precipitation, and the latter is a constant dependant on the nucleation and growth of  $\eta$  phase precipitates. It is of interest to see how these coefficients behave over time and how they are influenced by time, temperature and strain.

To begin with, the Avrami equation in Equation 5.1 can be rearranged as follows:

$$y = f_{eq}(1 - \exp(-kt^n))$$

$$\frac{y}{f_{eq}} = 1 - \exp(-kt^n)$$

$$\exp(-kt^n) = 1 - \frac{y}{f_{eq}}$$

$$-kt^n = \ln \left[ 1 - \frac{y}{f_{eq}} \right]$$

$$\ln kt^n = \ln \left[ -\ln \left[ 1 - \frac{y}{f_{eq}} \right] \right] \quad \text{Equation 6.21}$$

By plotting  $\ln \left[ -\ln \left[ 1 - \frac{y}{f_{eq}} \right] \right]$  against time, we can observe how the constants k and n behave over time at different temperatures and strains. Figure 6.22 displays  $\ln \left[ -\ln \left[ 1 - \frac{y}{f_{eq}} \right] \right]$  against time at  $950^\circ\text{C}$  and at  $0.1 \text{ s}^{-1}$  strain rate while Figure 6.23 shows the same except at  $0.01 \text{ s}^{-1}$  strain rate.

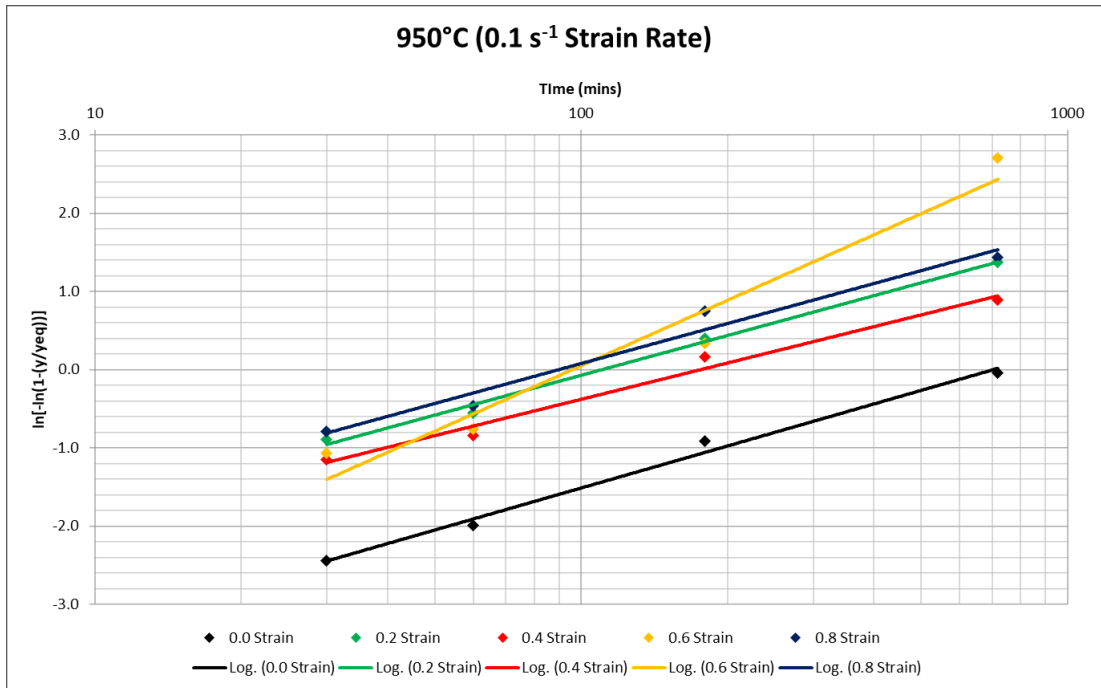


Figure 6.22 –  $\ln \left[ -\ln \left[ 1 - \frac{y}{f_{eq}} \right] \right]$  vs time at 950°C and at 0.1 s<sup>-1</sup> strain rate

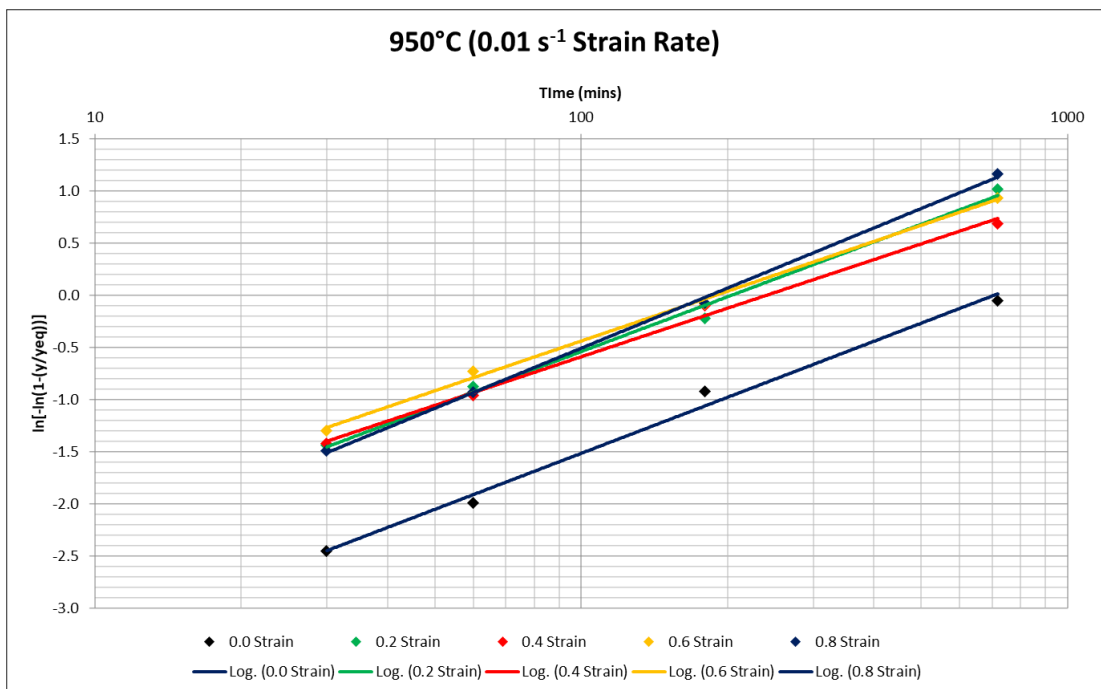


Figure 6.23 –  $\ln \left[ -\ln \left[ 1 - \frac{y}{f_{eq}} \right] \right]$  vs time at 950°C and at 0.01 s<sup>-1</sup> strain rate

Similar to the findings found from Section 6.4.1, the constants  $n$  and  $k$  at 0.2 to 0.8 strain differ from that at zero strain. However, at both strain rates, the differences between the strains from 0.2 to 0.8 do not corroborate to a particular trend and are not much different between each other to constitute a finding in the authors opinion. Most definitely however, there is a clear difference between the  $n$ - and  $k$ -values at any strain from 0.2 to 0.8 in comparison to that at zero strain. It must be mentioned here that although this is observed at 950°C in Figure 6.22 and Figure 6.23, the same findings have been observed at 900°C, 925°C and 975°C.

The effect of temperature and strain on the value of  $n$  can also be observed in Figure 6.24 and Figure 6.25 in which the  $n$ -value is plotted against strain at a strain rate of  $0.1 \text{ s}^{-1}$  and  $0.01 \text{ s}^{-1}$  respectively. It is observed at both strain rates that at 900°C and 925°C, the  $n$ -value decreases as the strain increases from 0 to 0.4 strain. At 950°C, the value of  $n$  stays more or less the same as the strain increases. Interestingly, at 975°C the value of  $n$  is observed to increase as the strain increases from 0 to 0.4 at both strain rates, which is an intriguing result as this contradicts the trend observed at 900°C and 925°C.

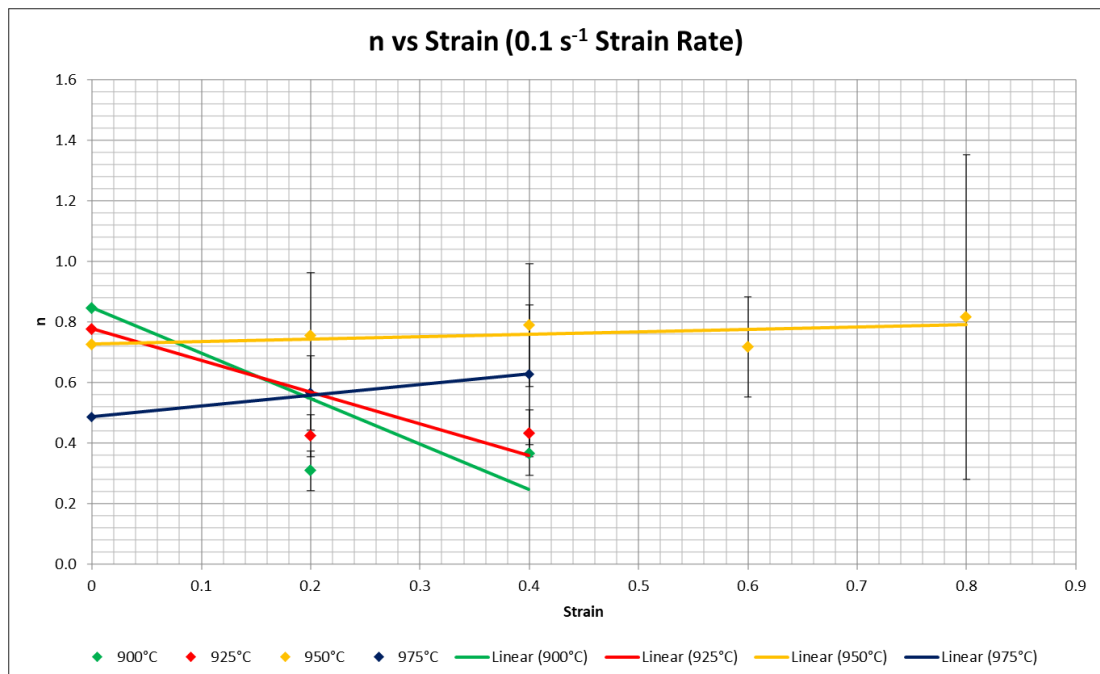


Figure 6.24 – The value of  $n$  against strain with  $0.1 \text{ s}^{-1}$  strain rate

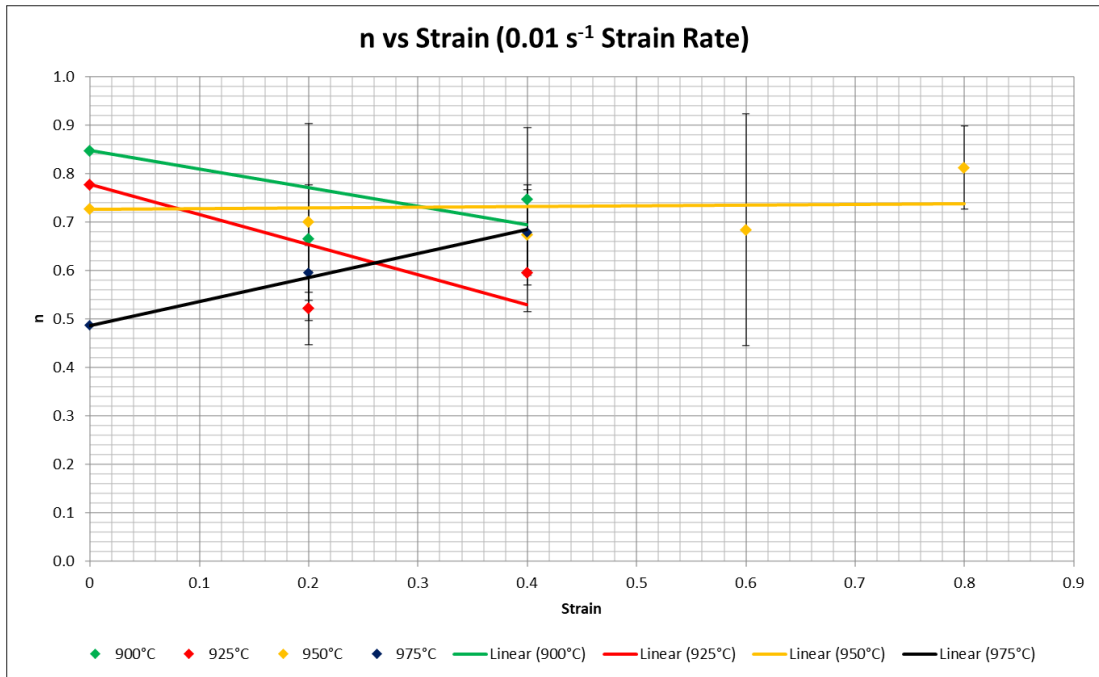


Figure 6.25 – The value of  $n$  against strain with  $0.01 \text{ s}^{-1}$  strain rate

From the data presented in Figure 6.24 and Figure 6.25, the relationship between the  $n$ -value and strain could be represented by the following equation:

$$n = a_1 + b_1 \varepsilon \quad \text{Equation 6.22}$$

Where  $a_1$  and  $b_1$  are constants and  $\varepsilon$  is the strain.

For the data obtained at the  $0.1 \text{ s}^{-1}$  strain rate, the numerical values of  $a_1$  and  $b_1$  as well as the adjusted  $R^2$  values are shown below in Table 6.10.

Temperature ( $^{\circ}\text{C}$ )	$a_1$	$b_1$	Adjusted $R^2$ Value
900	0.84680	$-1.50 \pm 0.42$	0.88791
925	0.77720	$-1.04 \pm 0.26$	0.95972
950	0.72662	$0.08 \pm 0.03$	0.99784
975	0.48602	$0.36 \pm 0.01$	0.99990

Table 6.10 – Values of  $a_1$ ,  $b_1$  and adjusted  $R^2$  for Equation 6.22 at  $0.1 \text{ s}^{-1}$  strain rate

For the data obtained at the  $0.01 \text{ s}^{-1}$  strain rate, the numerical values of  $a_1$  and  $b_1$  as well as the adjusted  $R^2$  values are shown in Table 6.11.



Temperature (°C)	$a_1$	$b_1$	Adjusted $R^2$ Value
900	0.84680	$-0.38 \pm 0.19$	0.98798
925	0.77720	$-0.62 \pm 0.23$	0.97366
950	0.72662	$0.01 \pm 0.05$	0.99401
975	0.48602	$0.49 \pm 0.02$	0.99981

Table 6.11 – Values of  $a_1$ ,  $b_1$  and adjusted  $R^2$  for Equation 6.22 at  $0.01 \text{ s}^{-1}$  strain rate

For both strain rates, it is noticed that the adjusted  $R^2$  values shown in Table 6.10 and Table 6.11 suggest that very good fittings have been obtained. It is seen that the value of  $b_1$  generally increases as the temperature increases, although there is an exception at  $925^\circ\text{C}$  at  $0.01 \text{ s}^{-1}$  strain rate. The value of  $a_1$  corresponds to the value of  $n$  in the strain-free recrystallised condition, i.e., zero strain. Temperature also effects the  $n$ -value such that the  $n$ -value is generally observed to increase as the temperature increases from  $900^\circ\text{C}$  to  $950^\circ\text{C}$ , although at  $975^\circ\text{C}$  the  $n$ -value is generally lower than that at  $950^\circ\text{C}$ .

Arrhenius plots of  $\ln(k)$  against  $1/T$  are displayed in Figure 6.26 and Figure 6.27 for  $0.1 \text{ s}^{-1}$  and  $0.01 \text{ s}^{-1}$  strain rates respectively.

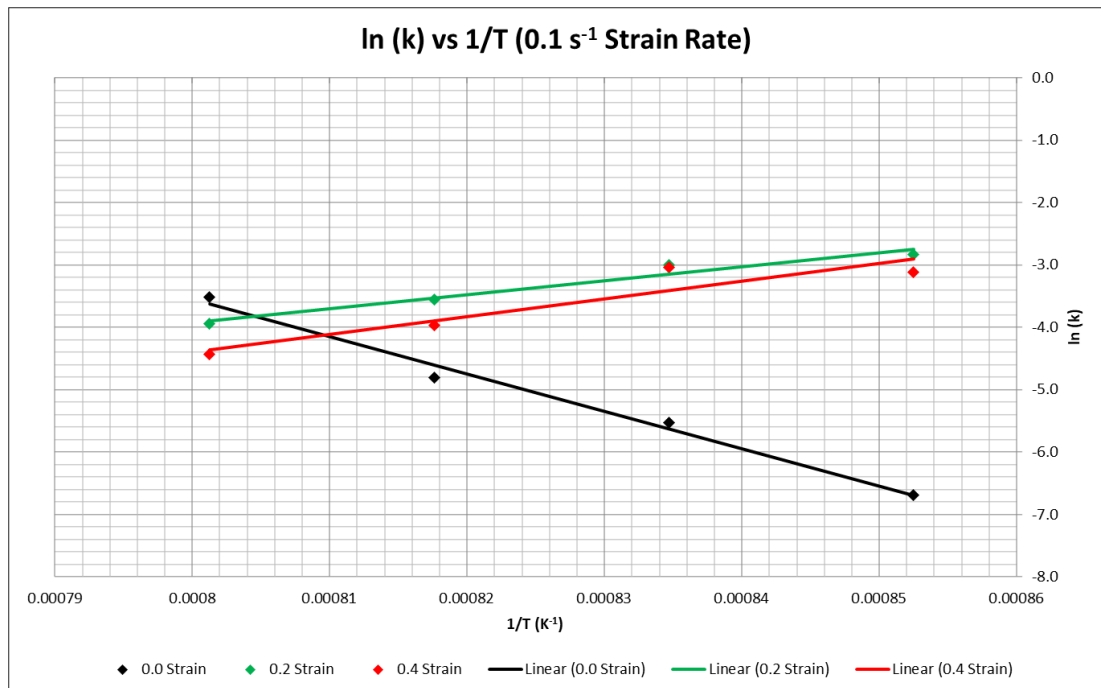


Figure 6.26 – The value of  $\ln(k)$  against  $1/T$  for  $0.1 \text{ s}^{-1}$  strain rate

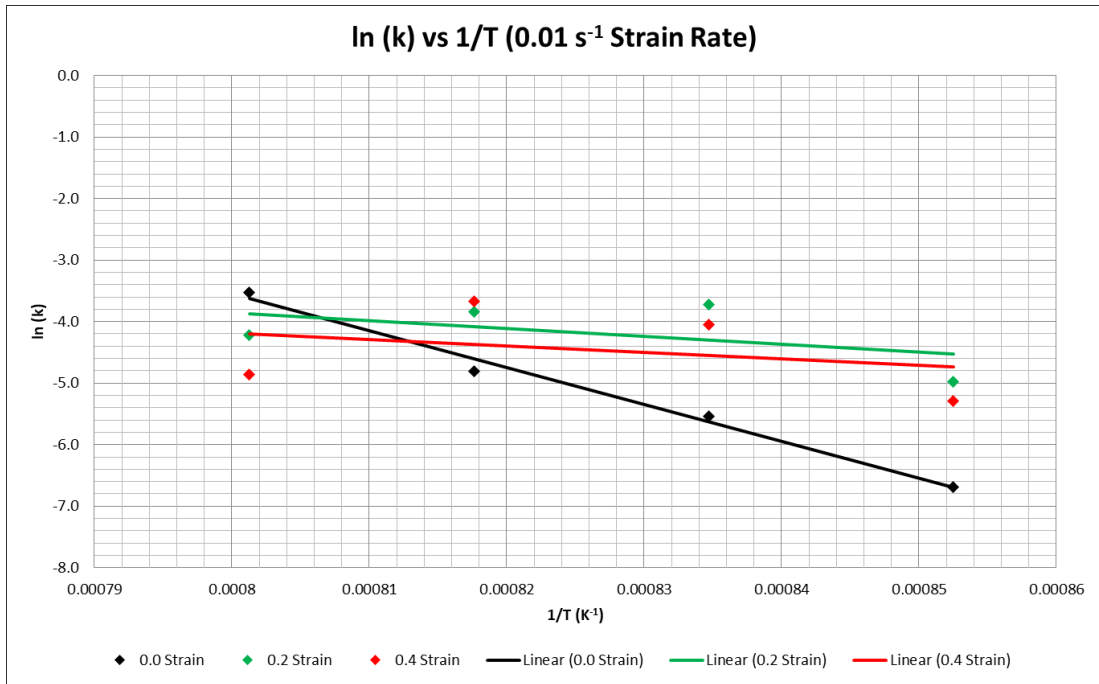


Figure 6.27 – The value of  $\ln(k)$  against  $1/T$  for  $0.01 \text{ s}^{-1}$  strain rate

It can be observed from Figure 6.26 and Figure 6.27 that at 0.0 strain, the value of  $k$  increases as the temperature increases for both strain rates. Conversely at  $0.1 \text{ s}^{-1}$  strain rate in Figure 6.26, and at 0.2 and 0.4 strain, the value of  $k$  decreases as the temperature increases. The  $k$ -values at 0.2 strain are observed to be slightly higher than those at 0.4 strain. At  $0.01 \text{ s}^{-1}$  strain rate in Figure 6.27, the value of  $k$  is observed to slightly increase as the temperature increases, which shows that the value of  $k$  is sensitive to the strain rate.

The rate of  $\eta$  phase precipitation can be described using the Arrhenius equation which is shown below as:

$$k = k_0 e^{\frac{-E_A}{RT}}$$

Where  $k_0$  is the frequency factor,  $E_A$  is the apparent activation energy in J/mol,  $R$  is the universal gas constant and  $T$  is the temperature in Kelvin.

By mathematical rearrangement, the above equation can be presented as:

$$\ln k = \ln k_0 - \frac{E_A}{RT} \quad \text{Equation 6.23}$$

Equation 6.23 can be thought of as a linear equation of the form  $y = mx + c$ , such that:

- $y = \ln k$
- $m = -\frac{E_A}{R}$
- $x = \frac{1}{T}$
- $c = \ln k_0$

At 0.0 strain, the apparent activation energy of  $\eta$  phase precipitation can be determined by obtaining the gradient of the 0.0 strain linear plot as shown in Figure 6.26 and Figure 6.27. By plotting and fitting the 0.0 strain data in Origin 2021, the gradient of the 0.0 strain plot is determined to be -59961.67972, therefore:

$$-59961.67972 = -\frac{E_A}{R}$$

$$E_A = 8.3145 \times 59961.67972$$

$$E_A = 498551.38603 \text{ J} = 498.55 \text{ kJ/mol}$$

$$E_A = 498.55 \text{ kJ/mol}$$

Following the same methodology, the apparent activation energy can be determined for 0.2 and 0.4 strain at both  $0.1 \text{ s}^{-1}$  and  $0.01 \text{ s}^{-1}$  strain rates.

Strain	Strain Rate (s <sup>-1</sup> )	Apparent Activation Energy (kJ/mol)	Adjusted R <sup>2</sup> Value
0.0	N/A	498.55 ± 37.32	0.98338
0.2	0.1	-187.85 ± 28.30	0.93486
0.4		-237.26 ± 67.29	0.79214
0.2	0.01	106.69 ± 129.17	-0.11848
0.4		86.65 ± 187.58	-0.3554

*Table 6.12 – Values of  $E_a$  for each strain and strain rate with adjusted  $R^2$  values*

From Table 6.12, it can be seen that the apparent activation energy decreases in absolute terms as the strain rate decreases. It is unclear why the activation energies at 0.1 s<sup>-1</sup> are negative whereas those at 0.01 s<sup>-1</sup> strain rate are positive and perhaps this could be investigated for future work. However, the data presented at 0.01 s<sup>-1</sup> strain rate has extremely poor adjusted R<sup>2</sup> values, which indicates the unreliability and low confidence in that particular data set.

## **6.5 Summary**

In this chapter, the  $\eta$  phase precipitation kinetics were investigated in deformed material. TTT diagrams were created for material that has been strained at 0.2 and 0.4 strain and with strain rates of 0.1 s<sup>-1</sup> and 0.01 s<sup>-1</sup>.  $\eta$  phase precipitation kinetics were also investigated up to 0.8 strain at 950°C for both strain rates. It has been shown in this study that deformation has markedly increased the  $\eta$  phase precipitation kinetics in comparison to that from the recrystallised strain-free material. However, it is interesting to note that little difference has been observed between 0.2 and 0.4 strain at both strain rates. Between 0.1 s<sup>-1</sup> and 0.01 s<sup>-1</sup> strain rate, it was observed that the  $\eta$  phase precipitation kinetics at the faster strain of 0.1 s<sup>-1</sup> was faster than that at 0.01 s<sup>-1</sup>. The effect of the strain and strain rate on the n and k parameters was explored and an attempt was made to obtain the activation energy of  $\eta$  phase precipitation for the different strains and strain rates. Using the data obtained in this study, a comparison can be made to  $\eta$  phase precipitation kinetics that has been obtained from material that has a larger initial grain size.

## **7 Effect of Initial Grain Size on Precipitation Kinetics**

### **7.1 Introduction**

In this chapter, the effects of the initial grain size (prior to deformation) on the precipitation kinetics of  $\eta$  phase in ATI 718Plus are studied. The effect of strain is also explored on an initial microstructure with a larger austenitic grain size. In order to carry out these investigations, a number of hot torsion tests were performed on material with larger austenite grain size in order to induce deformation within the microstructure of the ATI 718Plus test pieces.

Initially, several torsion test pieces were machined from the as-received ATI 718Plus material. Once these torsion test pieces were produced, they were heat treated at 1010°C for 180 minutes in order to fully solution the existing  $\eta$  phase present within the microstructure and to increase the austenite grain size dramatically.

EBSA analysis was performed in order to determine the grain size after the initial heat treatment at 1010°C for 180 minutes, but prior to the hot torsion test and the subsequent heat treatments shown in Table 7.1. The resultant grain size map is shown in Figure 7.1. The grain size obtained from this EBSA analysis was  $36.2 \mu\text{m} \pm 26.4 \mu\text{m}$  (standard deviation). This corresponds to a grain size of ASTM 6.5, which is significantly larger than the initial grain size that was used in Chapter 5.

The torsion tests were carried out at  $0.01 \text{ s}^{-1}$  strain rate and at a temperature of approximately 1000°C. The applied strain was gradually increased until it had reached 0.6 strain. After the hot torsion test was completed, the test piece was then water quenched immediately. A strain of 0.6 strain was selected for the same reason as was mentioned in Chapter 6; local regions of different strain values (0.2, 0.4, 0.6 and 0.8 strain) could be found within one sample globally strain at 0.6 strain. This is also shown in simulations that were performed in the FORGE simulation software package using the stress-strain flow curves that were generated from the hot torsion tests. As a result of these simulations, a strain map was generated with the temperature, strain and

strain rate conditions applied. These strain maps are shown in Figure 7.2 and Figure 7.3.

After the hot torsion tests were completed, the resultant test pieces were machined into four quarters. These torsion test quarters were then isothermally heat treated from 30 minutes to 720 minutes and from 900°C to 975°C, according to the experimental matrix which is shown in Table 7.1.

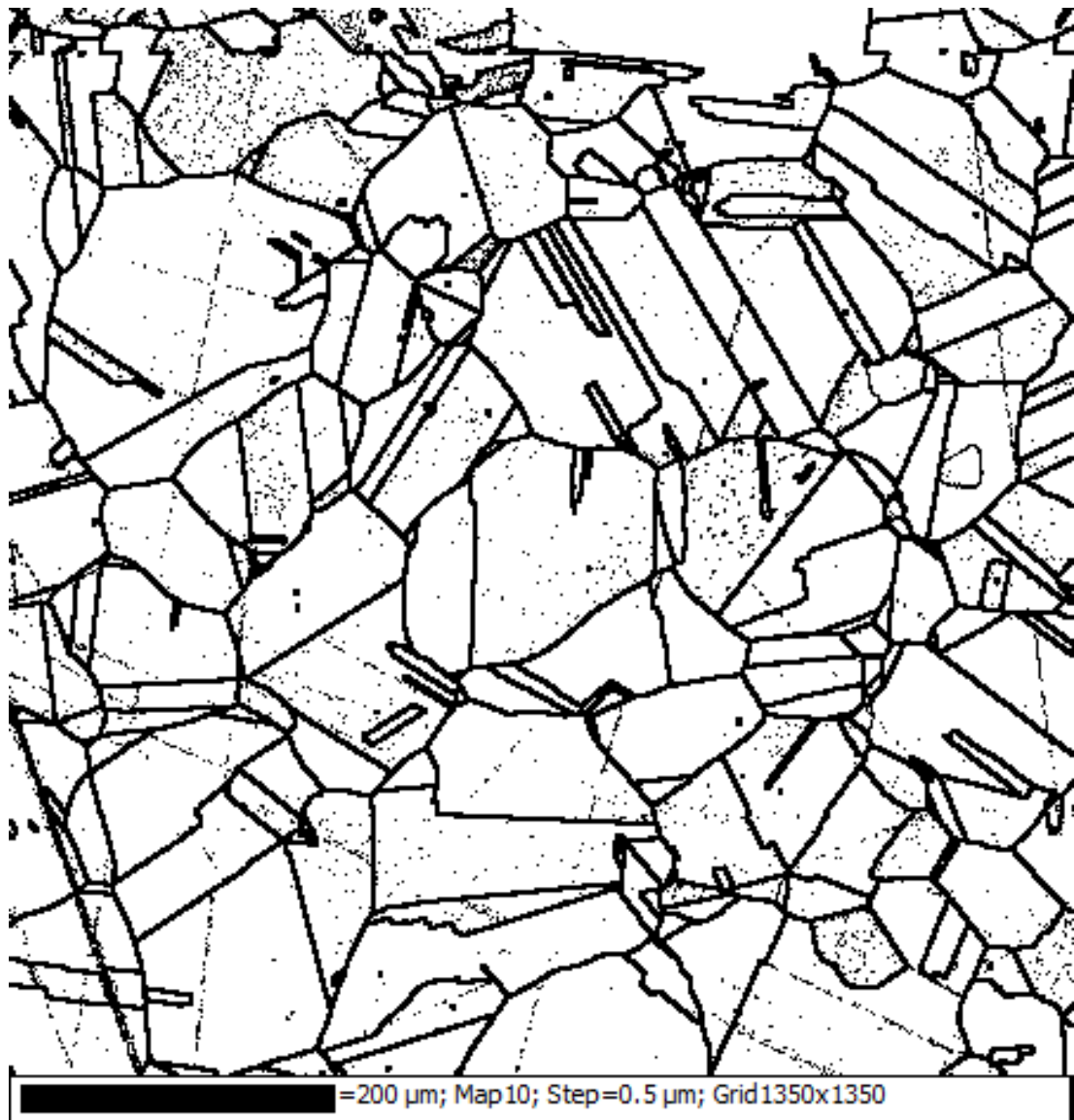


*Figure 7.1 – EBSD grain size map of initial microstructure after solution heat treatment at 1010°C after 180 minutes*

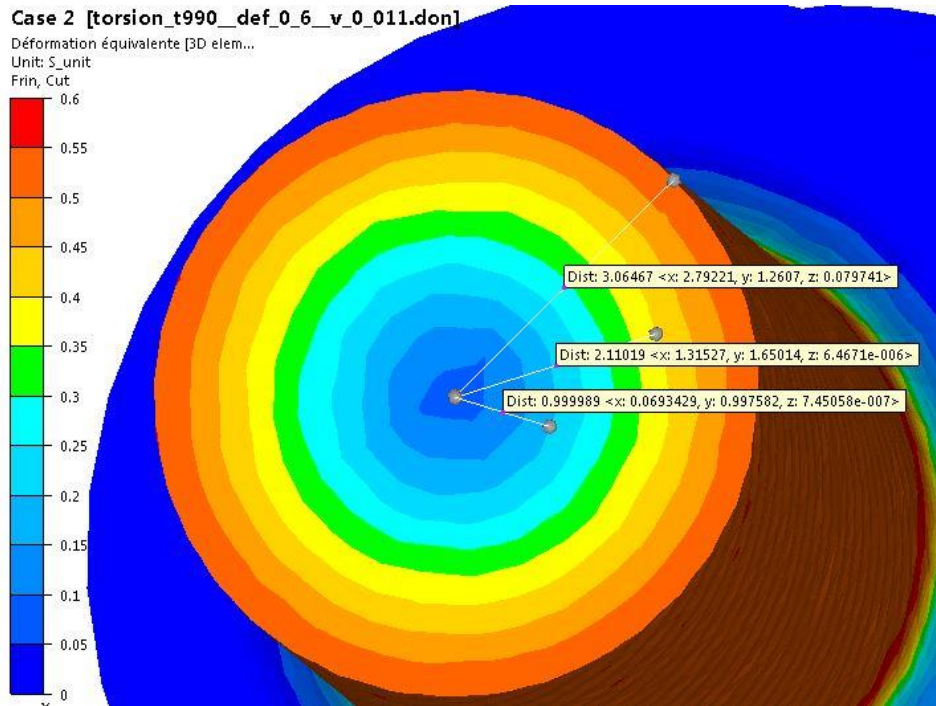


Figure 7.2 – Torsion test strain map at 0.6 global strain with  $0.01\text{ s}^{-1}$  strain rate (middle cut)

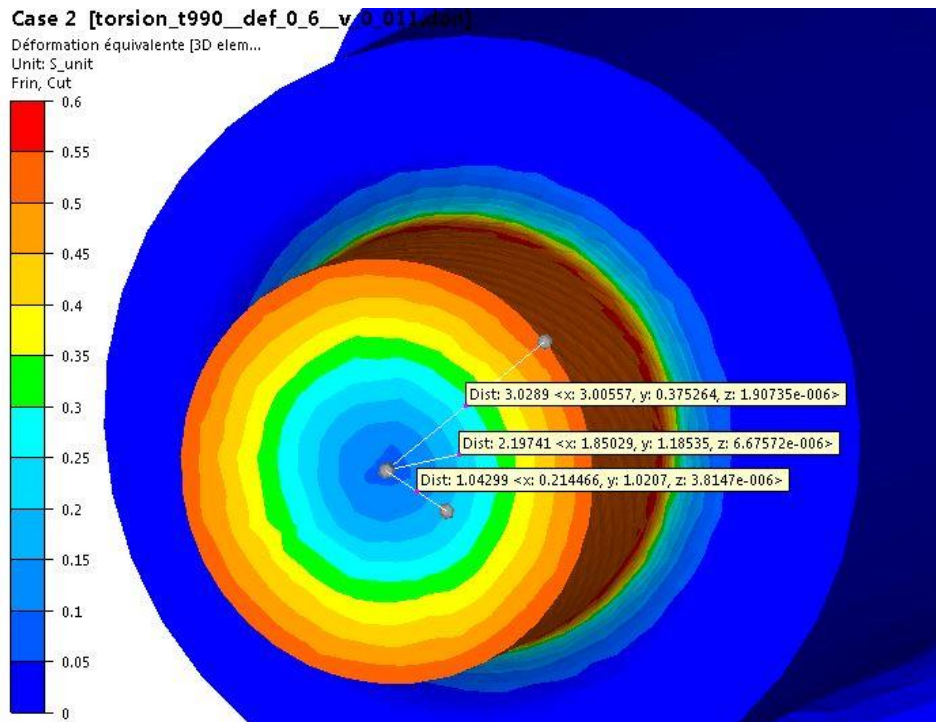


Figure 7.3 – Torsion test strain map at 0.6 global strain with  $0.01\text{ s}^{-1}$  strain rate (end cut)

The entire initial grain size study requires sixteen samples, and since one completed torsion test provides four smaller samples, four hot torsion tests had to be performed.

Temperature (°C)	Time (minutes)			
	0.01 s <sup>-1</sup>			
900	30	60	180	720
925	30	60	180	720
950	30	60	180	720
975	30	60	180	720

*Table 7.1 – Experimental matrix for  $\eta$  phase precipitation kinetics in material with larger initial grain size*

After the heat-treated quarters had gone through the planned heat treatments described in Table 7.1, each smaller sample was then mounted, ground and polished using the techniques and procedures described previously in Chapter 3 Section 3.4.

Using the strain maps mentioned earlier, a number of microstructural images were taken at regions of different strains, specifically 0.2 and 0.4 strain, via the use of an SEM. For the area fraction measurements described later within this chapter, each data point is an average taken from the measurements of three images. It was thought that three images would be sufficient to obtain a good representation of the sample. Also, using three images per data point was more feasible because the image processing technique used to obtain the  $\eta$  phase area fraction (as described in Chapter 3) was considerably time consuming, and due to time constraints more images per data point was not practically possible.

For the aspect ratio, length, and thickness measurements, ten measurements were taken for each data point. This was considered practical as it was thought this would be a good representation of the sample while being feasible at the same time.



## 7.2 Precipitation Kinetics at 0.01 s<sup>-1</sup> Strain Rate

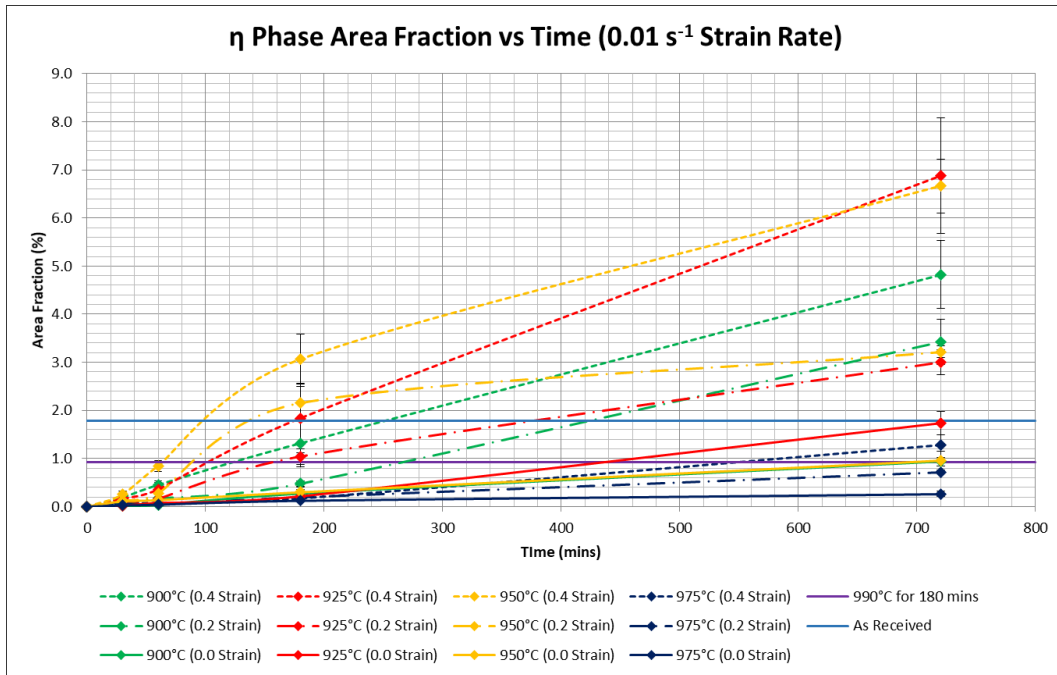


Figure 7.4 –  $\eta$  phase area fraction against time at 0.01 s<sup>-1</sup> strain rate for zero to 0.4 strain and for 900°C to 975°C

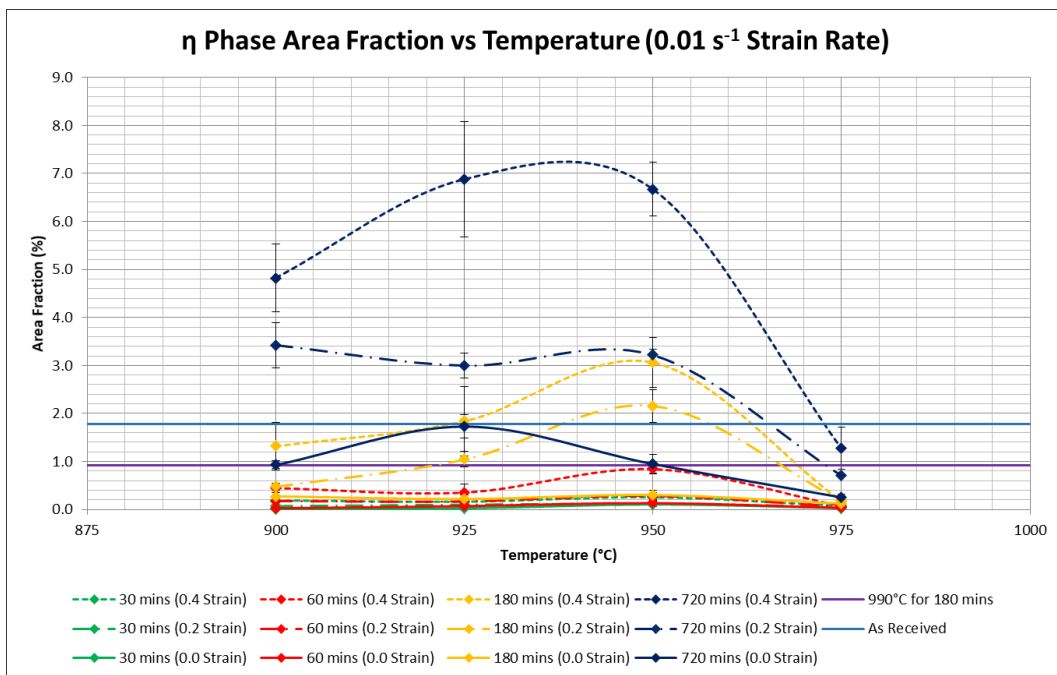


Figure 7.5 –  $\eta$  phase area fraction against temperature at 0.01 s<sup>-1</sup> strain rate for zero to 0.4 strain and for 30 mins to 720 mins

Time (mins)	Area Fraction (%)			
	900°C	925°C	950°C	975°C
0	0.00 ± 0.00	0.00 ± 0.00	0.00 ± 0.00	0.00 ± 0.00
30	0.01 ± 0.00	0.02 ± 0.00	0.11 ± 0.04	0.03 ± 0.01
60	0.03 ± 0.01	0.08 ± 0.01	0.14 ± 0.04	0.04 ± 0.03
180	0.27 ± 0.08	0.22 ± 0.09	0.30 ± 0.11	0.12 ± 0.02
720	0.93 ± 0.09	1.73 ± 0.24	0.96 ± 0.20	0.26 ± 0.05

Table 7.2 –  $\eta$  phase precipitation kinetics at 0.0 strain with  $0.01 \text{ s}^{-1}$  strain rate

Time (mins)	Area Fraction (%)			
	900°C	925°C	950°C	975°C
0	0.00 ± 0.00	0.00 ± 0.00	0.00 ± 0.00	0.00 ± 0.00
30	0.07 ± 0.01	0.10 ± 0.01	0.12 ± 0.06	0.05 ± 0.01
60	0.17 ± 0.02	0.17 ± 0.09	0.28 ± 0.08	0.06 ± 0.01
180	0.48 ± 0.06	1.04 ± 0.16	2.16 ± 0.34	0.19 ± 0.05
720	3.43 ± 0.47	3.00 ± 0.26	3.22 ± 0.12	0.71 ± 0.01

Table 7.3 –  $\eta$  phase precipitation kinetics at 0.2 strain with  $0.01 \text{ s}^{-1}$  strain rate

Time (mins)	Area Fraction (%)			
	900°C	925°C	950°C	975°C
0	0.00 ± 0.00	0.00 ± 0.00	0.00 ± 0.00	0.00 ± 0.00
30	0.19 ± 0.02	0.16 ± 0.05	0.25 ± 0.06	0.08 ± 0.04
60	0.45 ± 0.05	0.36 ± 0.17	0.85 ± 0.11	0.08 ± 0.01
180	1.32 ± 0.49	1.84 ± 0.73	3.07 ± 0.52	0.17 ± 0.06
720	4.82 ± 0.71	6.88 ± 1.20	6.67 ± 0.56	1.28 ± 0.44

Table 7.4 –  $\eta$  phase precipitation kinetics at 0.4 strain with  $0.01 \text{ s}^{-1}$  strain rate

In this section, the results regarding the impact of the initial grain size on the  $\eta$  phase precipitation kinetics are presented. Figure 7.4 displays the  $\eta$  phase area fraction against time at 0 strain, 0.2 strain and 0.4 strain with a strain rate of  $0.01 \text{ s}^{-1}$ , whereas Figure 7.5 shows the  $\eta$  phase area fraction for the aforementioned strain levels against temperature with the same strain rate of  $0.01 \text{ s}^{-1}$ . The numerical values of the data

shown in Figure 7.4 and Figure 7.5 are shown in Table 7.2, Table 7.3 and Table 7.4. The errors shown in the previously shown tables are calculated standard errors.

As is expected and like the results presented in previous chapters, the  $\eta$  phase area fraction increases as the time elapsed increases. Also, as observed in Chapter 6, the amount of  $\eta$  phase is markedly higher in strained material in comparison to strain-free recrystallised material. Interestingly however, there is a major difference in the results presented here and the results presented in Chapter 6. In Chapter 6, no major trend was observed between 0.2 and 0.4 strain at both  $0.1 \text{ s}^{-1}$  (see Figure 6.5 and Figure 6.6) and  $0.01 \text{ s}^{-1}$  (see Figure 6.13 and Figure 6.14) strain rates since the data seem to be uncorrelatable. The same can also be said for the data from 0.2 strain to 0.8 strain at  $950^\circ\text{C}$  at both  $0.1 \text{ s}^{-1}$  and  $0.01 \text{ s}^{-1}$  strain rates (see Figure 6.7 and Figure 6.15 respectively).

However, in the data presented in Figure 7.4 and Figure 7.5, there is a clear correlation that as the strain increases from 0.2 to 0.4, the  $\eta$  phase area fraction increases. This is observed at all temperatures including  $975^\circ\text{C}$  remarkably, since no effect of deformation was observed at  $975^\circ\text{C}$  for the data presented in Chapter 6 in Figure 6.5 and Figure 6.13. It is clearly visible that a correlation exists in which as more induced strain is present within the microstructure, the more precipitation of  $\eta$  phase occurs in this study with a larger initial grain size. In line with previous results, the peak of  $\eta$  phase precipitation lies between  $925^\circ\text{C}$  and  $950^\circ\text{C}$  as is observed in Figure 7.5.

As was done with previous studies in this work, the Origin 2021 software package was used to perform non-linear curve fittings. The Avrami equation was used to fit the data shown in Figure 7.4 and the Levenburg-Marquardt iteration algorithm was used within the Origin 2021 software package for the fitting. The subsequent  $\eta$  phase Avrami equations for zero strain with larger initial grain size are shown from Equation 7.1 to Equation 7.4.

$$900^\circ\text{C} \quad y = 18.46(1 - \exp(-0.00007t^{1.01660})) \quad \text{Equation 7.1}$$

$$925^{\circ}\text{C} \quad y = 15.45(1 - \exp(-0.00001t^{1.49799})) \quad \text{Equation 7.2}$$

$$950^{\circ}\text{C} \quad y = 10.03(1 - \exp(-0.00048t^{0.80963})) \quad \text{Equation 7.3}$$

$$975^{\circ}\text{C} \quad y = 5.88(1 - \exp(-0.00062t^{0.65549})) \quad \text{Equation 7.4}$$

The  $\eta$  phase Avrami equations at 0.2 strain with  $0.01 \text{ s}^{-1}$  strain rate and with larger initial grain size are shown below from Equation 7.5 to Equation 7.8.

$$900^{\circ}\text{C} \quad y = 18.46(1 - \exp(-0.00002t^{1.43969})) \quad \text{Equation 7.5}$$

$$925^{\circ}\text{C} \quad y = 15.45(1 - \exp(-0.00048t^{0.92979})) \quad \text{Equation 7.6}$$

$$950^{\circ}\text{C} \quad y = 10.16(1 - \exp(-0.00463t^{0.68201})) \quad \text{Equation 7.7}$$

$$975^{\circ}\text{C} \quad y = 5.88(1 - \exp(-0.00022t^{0.97083})) \quad \text{Equation 7.8}$$

The  $\eta$  phase Avrami equations at 0.4 strain with  $0.01 \text{ s}^{-1}$  strain rate and with larger initial grain size are shown below from Equation 7.9 to Equation 7.12.

$$900^{\circ}\text{C} \quad y = 18.46(1 - \exp(-0.00037t^{1.01796})) \quad \text{Equation 7.9}$$

$$925^{\circ}\text{C} \quad y = 15.45(1 - \exp(-0.00029t^{1.15576})) \quad \text{Equation 7.10}$$

$$950^{\circ}\text{C} \quad y = 10.03(1 - \exp(-0.00256t^{0.92524})) \quad \text{Equation 7.11}$$

$$975^{\circ}\text{C} \quad y = 5.88(1 - \exp(-0.00002t^{1.41748})) \quad \text{Equation 7.12}$$

Temperature (°C)	Adjusted R <sup>2</sup> Values		
	0.0 Strain	0.2 Strain (0.01 s <sup>-1</sup> Strain Rate)	0.4 Strain (0.01 s <sup>-1</sup> Strain Rate)
900	0.99155	0.99906	0.99992
925	0.99926	0.98899	0.99849
950	0.99596	0.87307	0.98675
975	0.98781	0.99809	0.99297

Table 7.5 – Adjusted R<sup>2</sup> values for Equation 7.1 to Equation 7.12

The adjusted R<sup>2</sup> values of the fitted Avrami equations for 0.0 strain, 0.2 strain and 0.4 strain at 0.01 s<sup>-1</sup> strain rate with larger initial grain size are shown in Table 7.5. The adjusted R<sup>2</sup> values range from 0.87307 to 0.99992 which show that very strong mathematical fits have been obtained for the  $\eta$  phase precipitation kinetic data for this study. This will benefit the accuracy of the TTT curves that will be produced from the Avrami equations listed from Equation 7.1 to Equation 7.12.

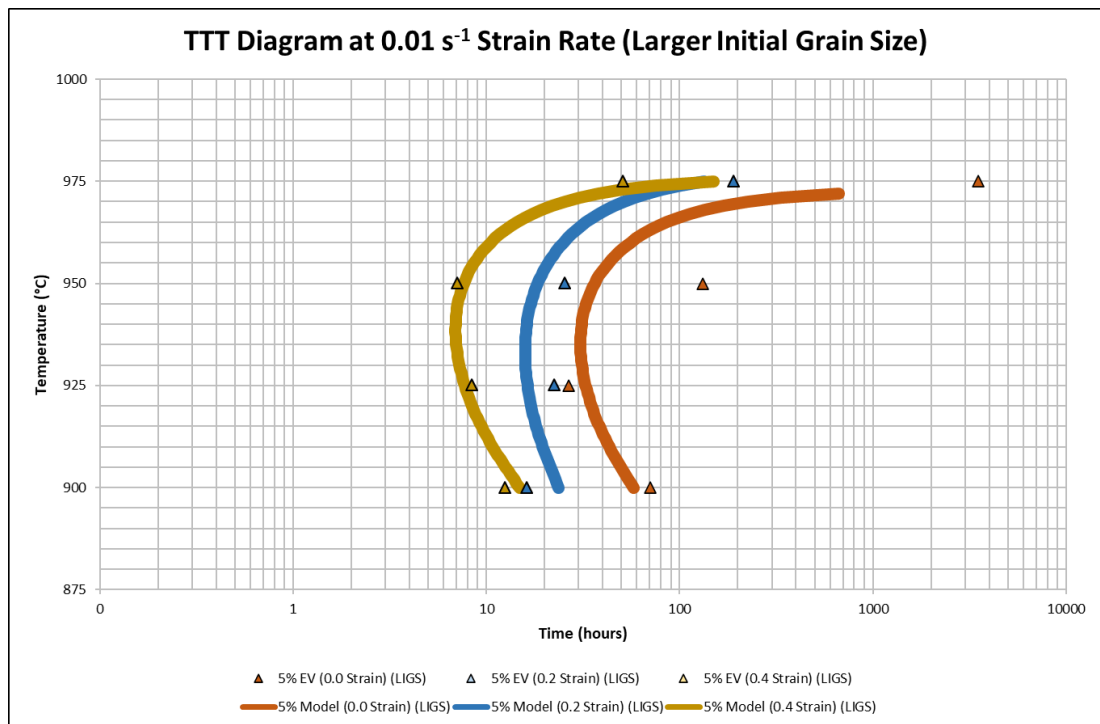


Figure 7.6 – TTT diagrams for 5%  $\eta$  phase area fraction for material with larger initial grain size (LIGS) at zero strain, 0.2 strain and 0.4 strain with 0.01 s<sup>-1</sup> strain rate

The TTT curves at 5%  $\eta$  phase area fraction for 0.0 strain, 0.2 strain and 0.4 strain at  $0.01 \text{ s}^{-1}$  strain rate with larger initial grain size are shown in Figure 7.6. The TTT curves shown in Figure 7.6 were produced using the Avrami equations shown in Equation 7.1 to Equation 7.12. Using Equation 5.9 shown in Chapter 5, the TTT curves were modelled to produce the equations shown below in Equation 7.13, Equation 7.14 and Equation 7.15.

$$\begin{array}{ll} \text{5\% Model} & \tau^{-1} = 0.0015(973 - T)\exp\left[-\frac{(973 - T)^{1.79}}{T + 273}\right] \\ \text{(0.0 strain)} & \end{array} \quad \text{Equation 7.13}$$

$$\begin{array}{ll} \text{5\% Model} & \tau^{-1} = 0.0025(978 - T)\exp\left[-\frac{(978 - T)^{1.72}}{T + 273}\right] \\ \text{(0.2 strain)} & \end{array} \quad \text{Equation 7.14}$$

$$\begin{array}{ll} \text{5\% Model} & \tau^{-1} = 0.0067(976 - T)\exp\left[-\frac{(976 - T)^{1.795}}{T + 273}\right] \\ \text{(0.4 strain)} & \end{array} \quad \text{Equation 7.15}$$

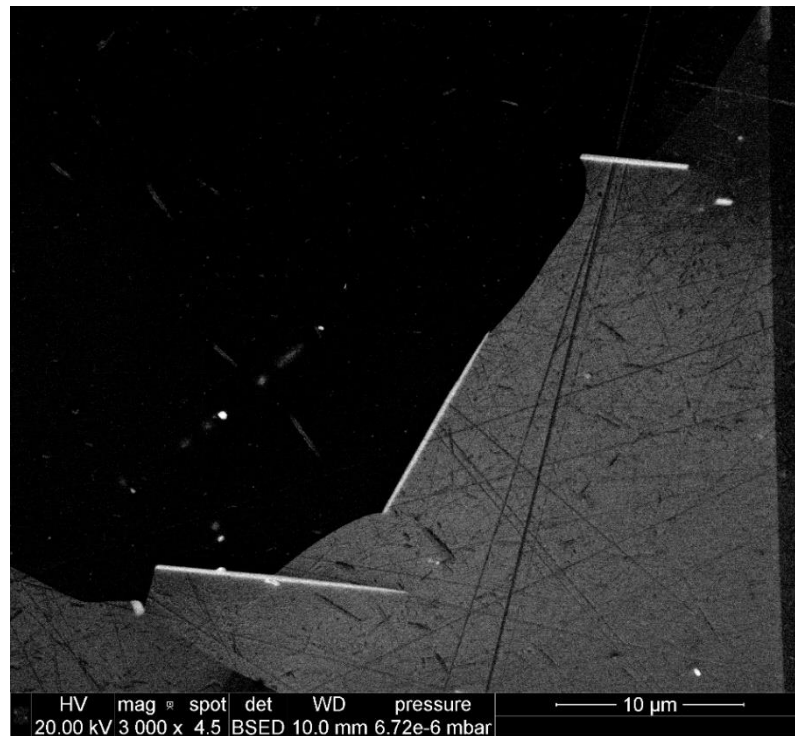


*Figure 7.7 – Microstructure of ATI 718Plus at zero strain with  $0.01 \text{ s}^{-1}$  strain rate and after heat treatment at  $950^\circ\text{C}$  for 720 minutes and with larger initial grain size*

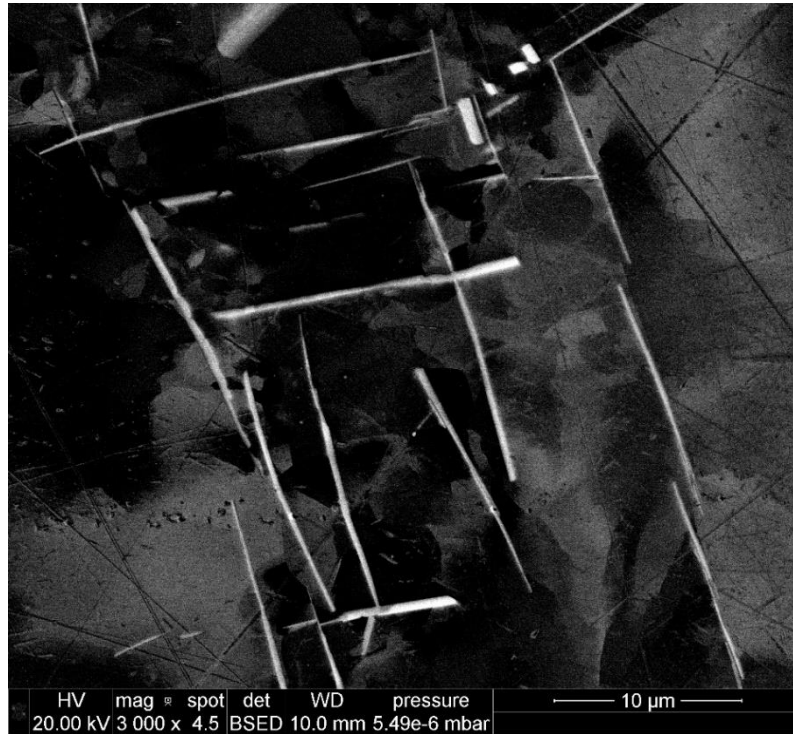


*Figure 7.8 – Microstructure of ATI 718Plus at 0.2 strain with  $0.01\text{ s}^{-1}$  strain rate and after heat treatment at  $950^{\circ}\text{C}$  for 720 minutes and with larger initial grain size*

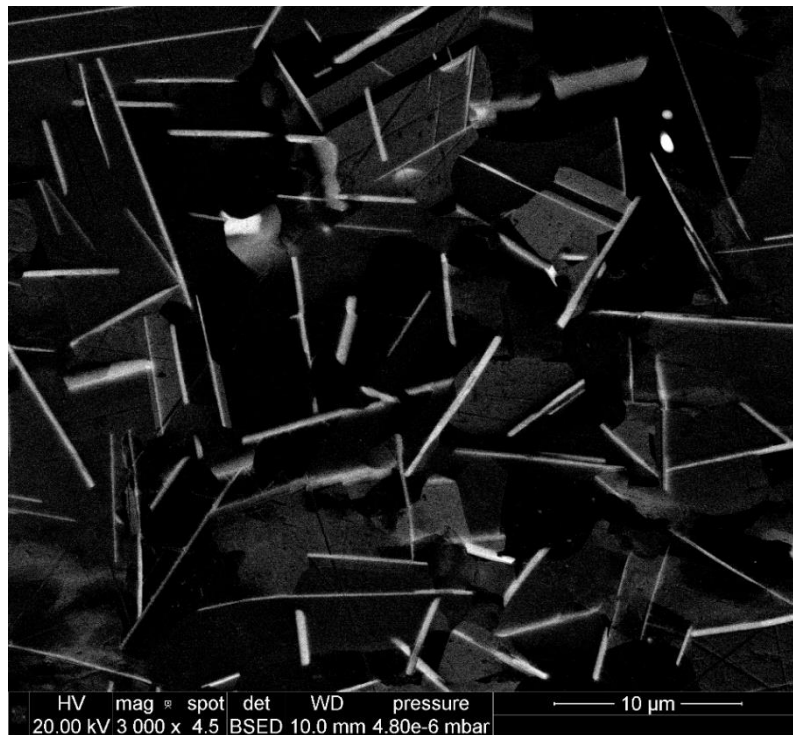


*Figure 7.9 – Microstructure of ATI 718Plus at 0.4 strain with  $0.01\text{ s}^{-1}$  strain rate and after heat treatment at  $950^{\circ}\text{C}$  for 720 minutes and with larger initial grain size*

### 7.3 Aspect Ratio, Length and Thickness

As was done in the recrystallised strain free material condition (Chapter 5), the kinetics of the  $\eta$  phase precipitate length, thickness and aspect ratio was studied in microstructure with larger initial grain size at zero strain. The average  $\eta$  phase precipitate aspect ratio against time is shown below in Figure 7.10 with the numerical values shown in Table 7.6. The average  $\eta$  phase precipitate length against time is shown in Figure 7.11 with the numerical values shown in Table 7.7. Finally, the average  $\eta$  phase precipitate thickness against time is shown in Figure 7.12 with the numerical values shown in Table 7.8.

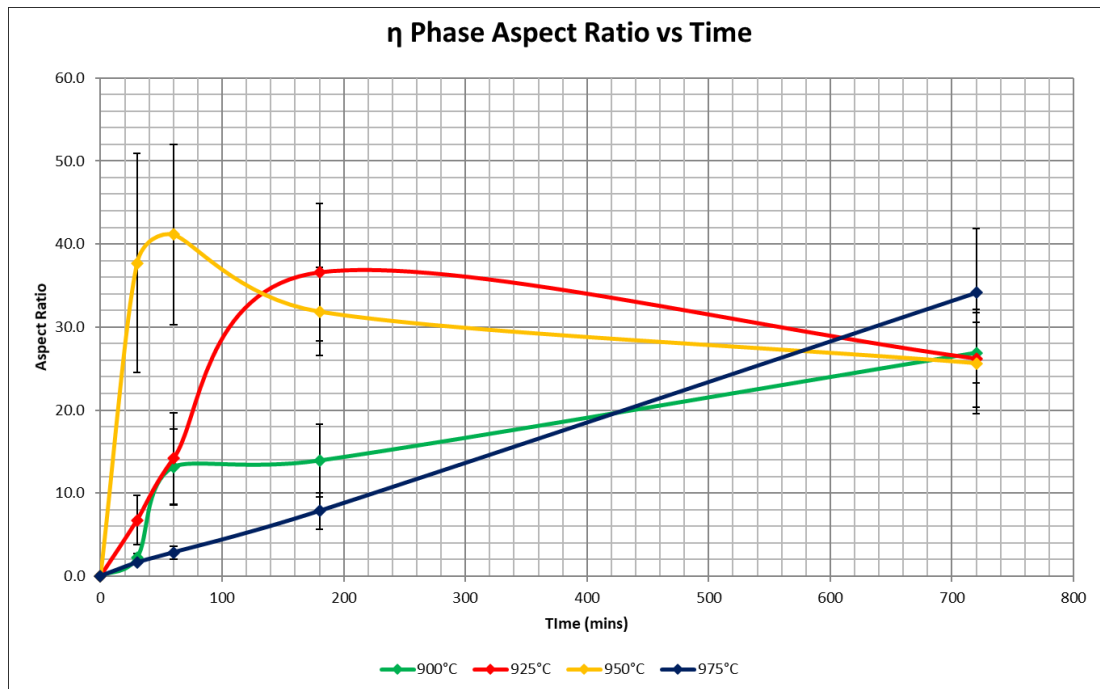


Figure 7.10 –  $\eta$  phase precipitate aspect ratio against time in larger initial grain size material at zero strain



Time (mins)	Aspect Ratio			
	900°C	925°C	950°C	975°C
0	0.00 ± 0.00	0.00 ± 0.00	0.00 ± 0.00	0.00 ± 0.00
30	2.20 ± 0.50	6.73 ± 2.97	37.69 ± 13.17	1.64 ± 0.17
60	13.14 ± 4.61	14.17 ± 5.53	41.13 ± 10.89	2.86 ± 0.78
180	13.91 ± 4.39	36.60 ± 8.25	31.86 ± 5.31	7.86 ± 2.20
720	26.90 ± 3.68	26.21 ± 5.90	25.65 ± 6.08	34.16 ± 7.70

*Table 7.6 – Results of  $\eta$  phase precipitate aspect ratio in larger initial grain size material at zero strain*

For all temperatures studied in this chapter, there is an overall increase in aspect ratio from 0 minutes to 720 minutes. At 925°C and 950°C, there is an initial sharp rise in aspect ratio before decreasing to its final value at 720 minutes. At 925°C, this decrease begins after 180 minutes onwards whereas at 950°C, the decrease begins from 60 minutes onwards. The sharp rises in aspect ratio at 925°C and 950°C reflect the sudden and quick nucleation and growth of  $\eta$  phase precipitates and further confirm that the fastest rates of  $\eta$  phase precipitation occur at (or somewhere between) these temperatures. Eventually, it appears that the aspect ratio tends towards a plateau.

At 900°C, there is a steep rise in aspect ratio from 0 minutes to 60 minutes, after which the aspect ratio continues to increase but a lower rate. At 975°C the aspect ratio appears to steadily increase in a linear fashion. Further data would be required to observe the point when (and if) the aspect ratio tends towards a plateau.

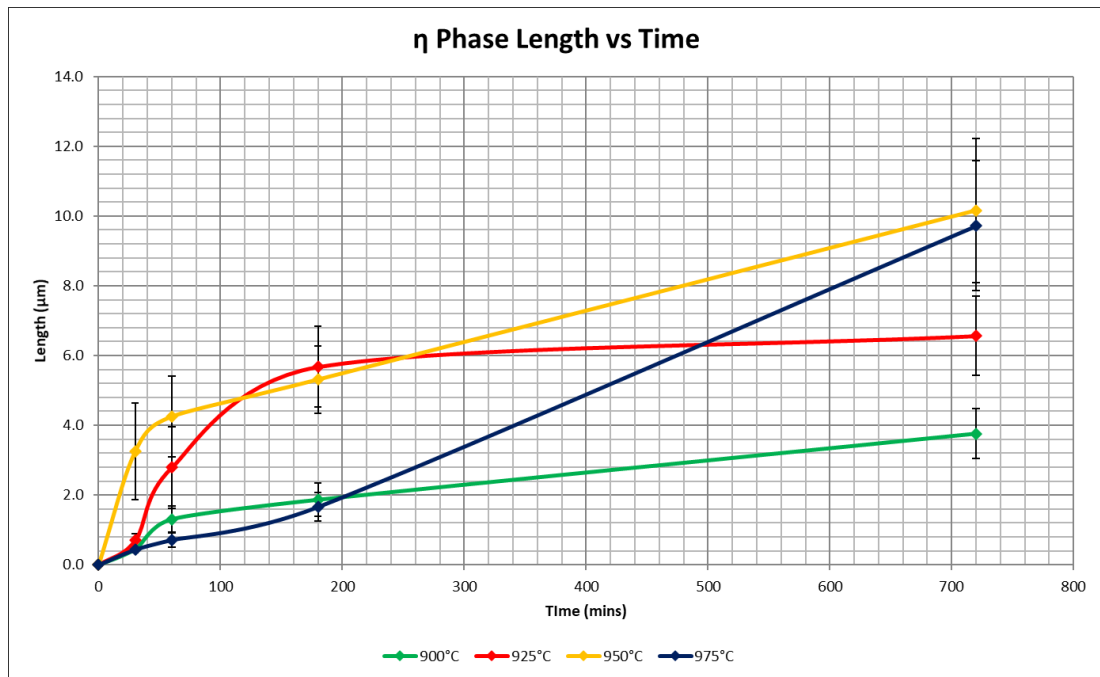


Figure 7.11 –  $\eta$  phase precipitate length against time in larger initial grain size material at zero strain

Time (mins)	Length			
	900°C	925°C	950°C	975°C
0	0.00 ± 0.00	0.00 ± 0.00	0.00 ± 0.00	0.00 ± 0.00
30	0.46 ± 0.09	0.70 ± 0.19	3.25 ± 1.39	0.44 ± 0.10
60	1.31 ± 0.38	2.79 ± 1.17	4.25 ± 1.15	0.72 ± 0.21
180	1.87 ± 0.47	5.68 ± 1.16	5.31 ± 0.96	1.66 ± 0.40
720	3.76 ± 0.71	6.57 ± 1.13	10.16 ± 2.07	9.72 ± 1.87

Table 7.7 – Results of  $\eta$  phase precipitate length in larger initial grain size material at zero strain

In terms of  $\eta$  phase precipitate length, the overall precipitate length increases over time. The largest lengths are observed at 950°C and 975°C at 720 minutes. More data would be required to see the point at which the precipitate length plateaus to a maximum value. At 925°C, the  $\eta$  phase precipitate length appears to tend towards a plateau between 180 minutes and 720 minutes. At 900°C, the  $\eta$  phase precipitate length slowly increases at a lower rate compared to the data observed at 925°C and 950°C. It

is unsure whether it would still increase beyond 720 minutes or plateau to an eventual maximum value.

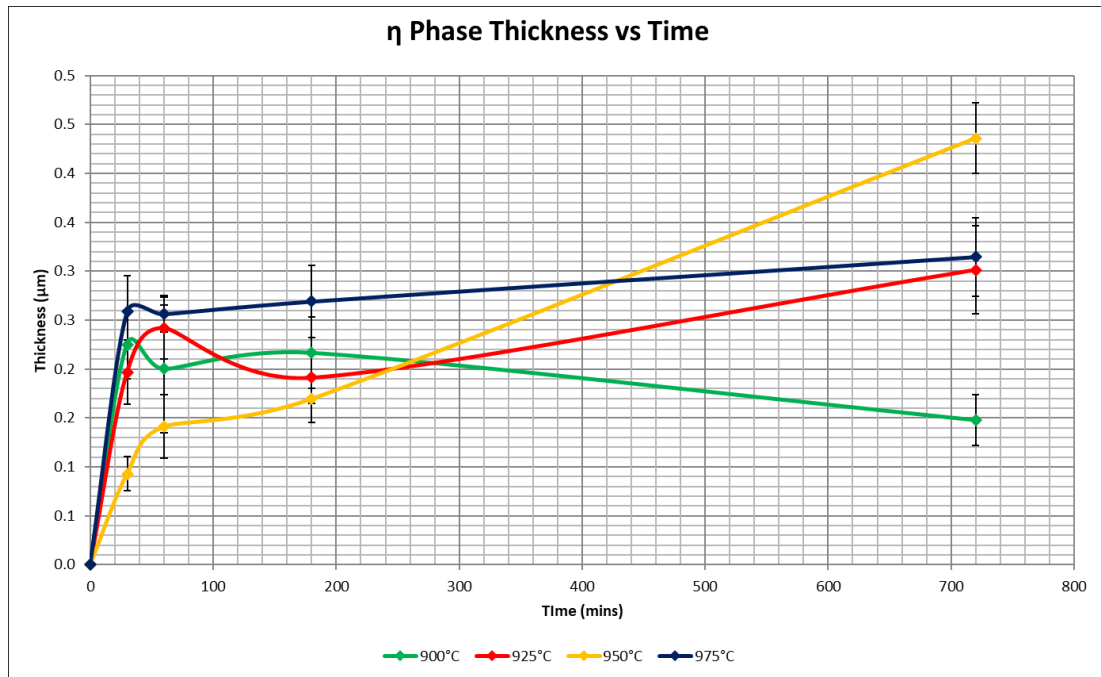


Figure 7.12 –  $\eta$  phase precipitate thickness against time in larger initial grain size material at zero strain

Time (mins)	Thickness			
	900°C	925°C	950°C	975°C
0	0.00 ± 0.00	0.00 ± 0.00	0.00 ± 0.00	0.00 ± 0.00
30	0.23 ± 0.04	0.20 ± 0.03	0.09 ± 0.02	0.26 ± 0.04
60	0.20 ± 0.07	0.24 ± 0.03	0.14 ± 0.03	0.26 ± 0.02
180	0.22 ± 0.04	0.19 ± 0.03	0.17 ± 0.02	0.27 ± 0.04
720	0.15 ± 0.03	0.30 ± 0.05	0.44 ± 0.04	0.31 ± 0.04

Table 7.8 – Results of  $\eta$  phase precipitate thickness in larger initial grain size material at zero strain

At 900°C, 925°C and 975°C, there is a slight drop in thickness after reaching a peak, but the measurements at the peak and the trough still fall within the standard deviation of each other. At 900°C, the thickness decreases from 180 minutes to 720 minutes but again the measurements fall within each other's standard error and may have

plateaued. The  $\eta$  phase precipitate thickness seems to have also reached a plateau at 975°C. At 925°C and 950°C, the  $\eta$  phase precipitate thickness continues to increase from 180 minutes through to 720 minutes.

## 7.4 Discussion

### 7.4.1 Effect of Strain

As observed from the trends in Figure 7.4, Figure 7.5 and Figure 7.6, there is a clear effect of induced strain on the  $\eta$  phase precipitation kinetics on ATI 718Plus material with a larger initial grain size. It can be seen from the TTT diagram (with the larger initial grain size) in Figure 7.6 that the precipitation kinetics becomes significantly faster in the strained material in comparison to the strain-free material. This is expected since the same trend was observed on microstructure with the as-received material grain size (see Chapter 6) and in other published studies (74,77)

Interestingly, in contrast to the results that were observed in Chapter 6, it is observed that as the induced strain increases, the amount of  $\eta$  phase precipitation increases. In Chapter 6, while it is seen that strain is observed to significantly increase the  $\eta$  phase precipitation kinetics in comparison to strain-free material, there was no clear trend from 0.2 strain onward. No correlation was observed between applied strains. However, in this chapter which studies the  $\eta$  phase precipitation kinetics with a larger initial grain size, there is a clear correlation between applied strain levels. As the amount of strain induced into the microstructure increases, the amount of  $\eta$  phase precipitation increases. As the amount of strain increases, the faster the  $\eta$  phase precipitation kinetics becomes as is observed in the TTT diagram in Figure 7.6.

It is unclear as to why the  $\eta$  phase precipitation kinetics becomes faster as the strain increases from 0.2 to 0.4, but not in the deformed material study with the smaller initial grain size (Chapter 6). In Chapter 6, the initial as-received microstructure was heat treated at 990°C for 180 minutes in order to clean the microstructure from the  $\eta$  phase precipitates. However even after this heat treatment, approximately 1% area fraction

of  $\eta$  phase was still present in the microstructure prior to deformation. In this study (Chapter 7), the material was heat treated at 1010°C for 180 minutes in order to encourage grain growth, but this heat treatment had also completely removed any presence of  $\eta$  phase precipitates prior to deformation. It seems that increasing the induced strain amount increases the  $\eta$  phase precipitation kinetics in material with no initial  $\eta$  phase present within the microstructure. In material with some presence of  $\eta$  phase precipitates ( $\approx 1\%$  area fraction), increasing the strain amount in the microstructure does not necessarily increase the  $\eta$  phase precipitation kinetics for strain levels above zero. The reasoning for these findings is unclear and further investigations are required to fully understand this behaviour.

#### 7.4.2 Effect of Initial Grain Size

Figure 7.13 to Figure 7.16 shows the  $\eta$  phase area fraction against time for both the material with as-received initial grain size ( $13.2 \mu\text{m} \pm 5.3 \mu\text{m}$ ) and the material with a larger initial grain size ( $36.2 \mu\text{m} \pm 26.4 \mu\text{m}$ ) for a temperature range from 900°C to 975°C. It is quite clear that increasing the grain size has significantly slowed the  $\eta$  phase precipitation kinetics. This is also observed by comparing the  $\eta$  phase TTT diagrams for both initial grain sizes as seen in Figure 7.17.

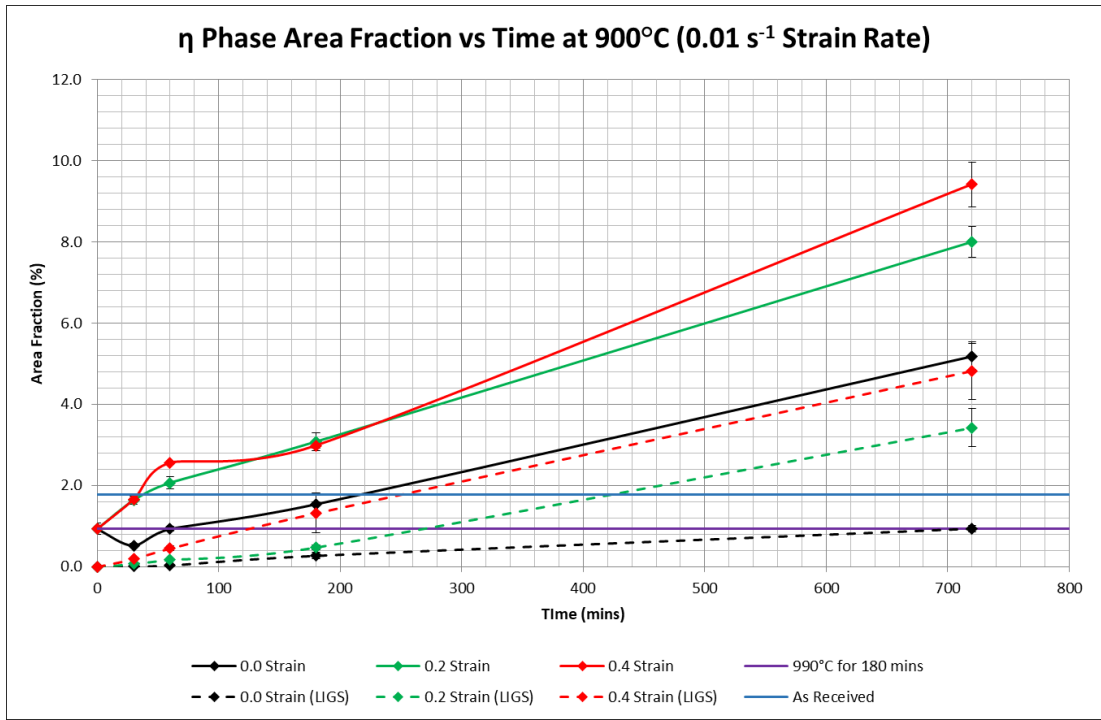


Figure 7.13 –  $\eta$  phase area fraction against time at 900°C for as-received initial grain size material and larger initial grain size material (LIGS)

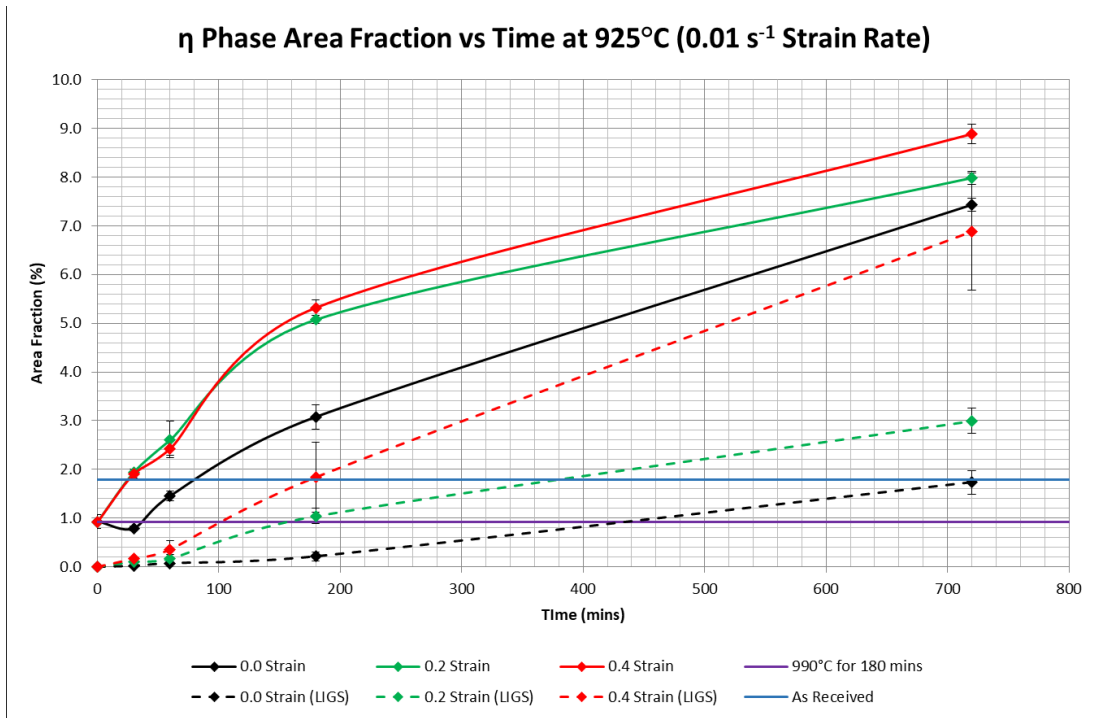


Figure 7.14 –  $\eta$  phase area fraction against time at 925°C for as-received initial grain size material and larger initial grain size material (LIGS)

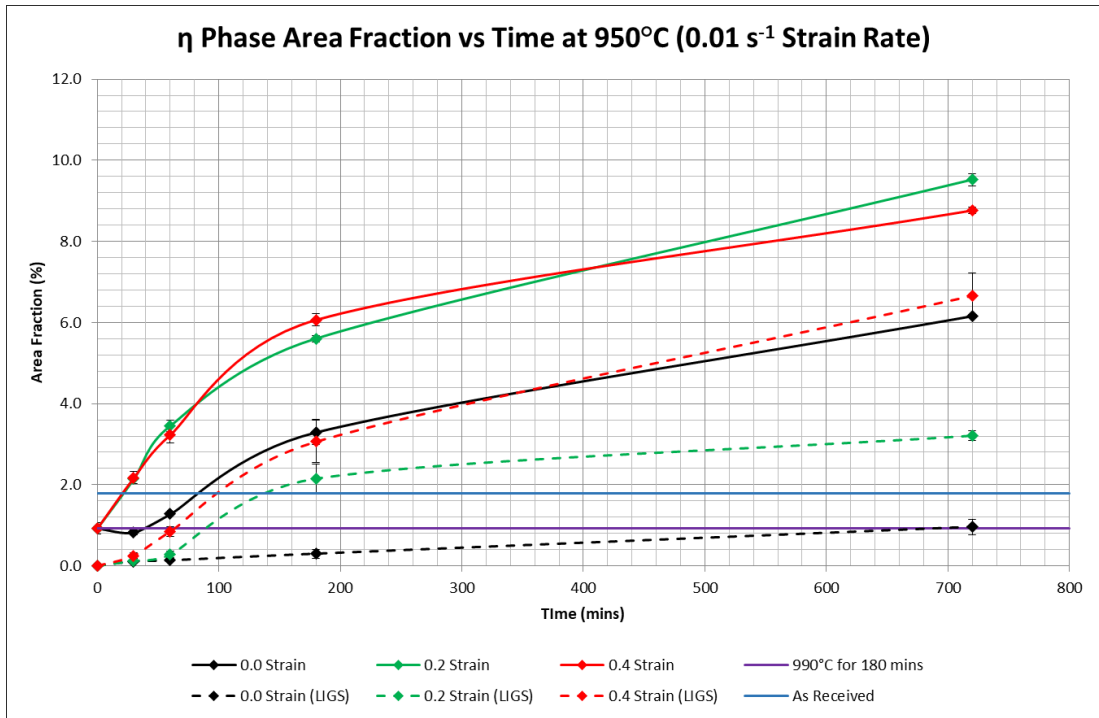


Figure 7.15 – η phase area fraction against time at 950°C for as-received initial grain size material and larger initial grain size material (LIGS)

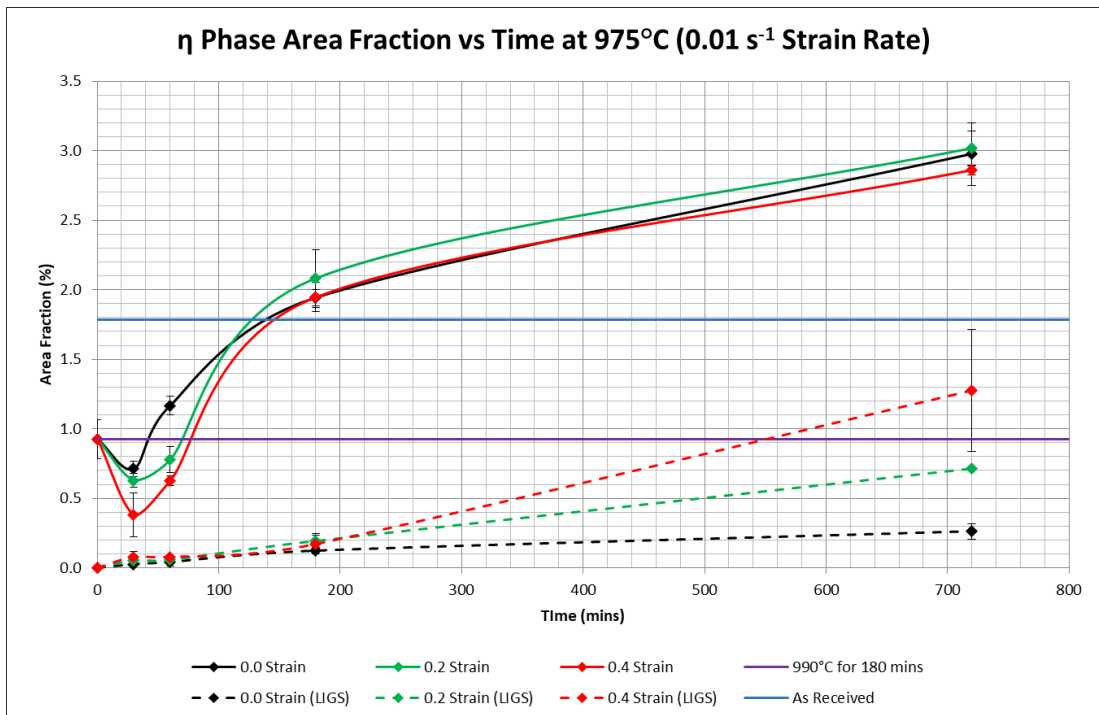


Figure 7.16 – η phase area fraction against time at 975°C for as-received initial grain size material and larger initial grain size material (LIGS)

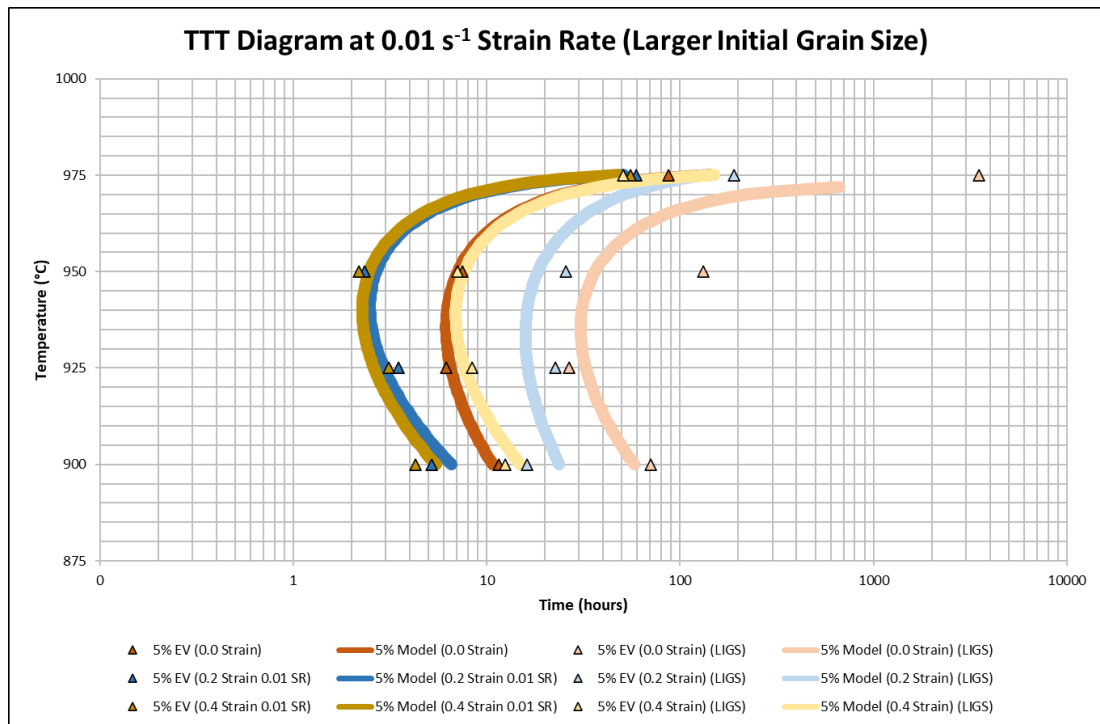


Figure 7.17 – TTT diagrams for 5%  $\eta$  phase area fraction comparing as-received initial grain size material with larger initial grain size material (LIGS)

The reasoning as to why the  $\eta$  phase kinetics have slowed with increasing grain size is as follows. When the grain size of a material increases, there are less grain boundaries present within the microstructure. This means that there is less grain boundary area for the nucleation of  $\eta$  phase precipitates to occur. As for precipitation on twin boundaries and intragranular precipitation (which starts after the commencement of  $\eta$  phase precipitation on the grain boundaries), it seems from the results that it is not enough to keep up with the  $\eta$  phase precipitation kinetics from the as-received initial grain size. The reduction in grain boundary area associated with the larger initial grain size is observed to slow down the  $\eta$  phase precipitation kinetics compared to that from the as-received initial grain size.

On the contrary, a material with a lower grain size means that there are more grains present within the microstructure. Hence, there would be more grain boundary area to nucleate  $\eta$  phase precipitates on.



### 7.4.3 Aspect Ratio, Length and Thickness

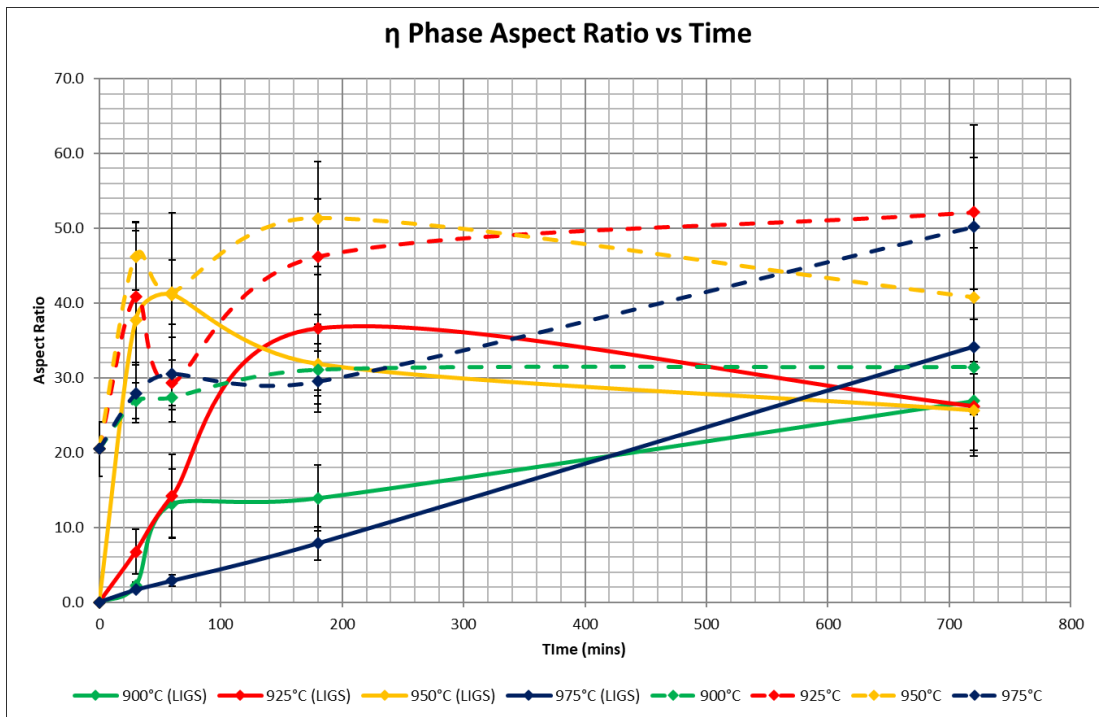


Figure 7.18 –  $\eta$  phase aspect ratio against time for as-received initial grain size material and larger initial grain size material (LIGS)

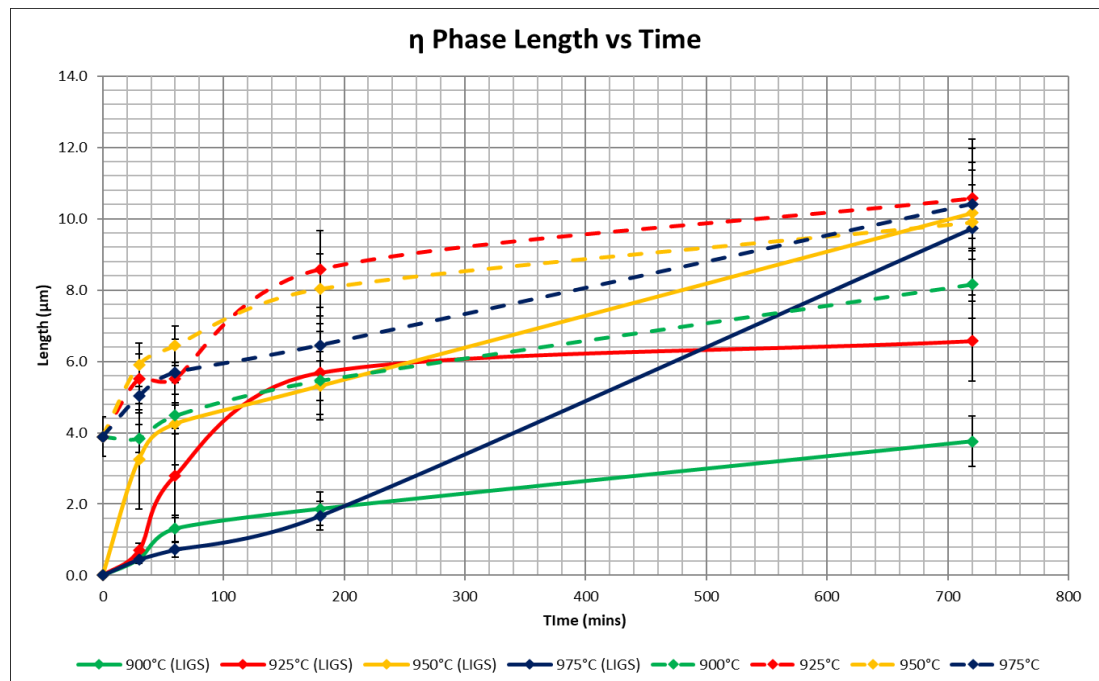


Figure 7.19 -  $\eta$  phase length against time for as-received initial grain size material and larger initial grain size material (LIGS)

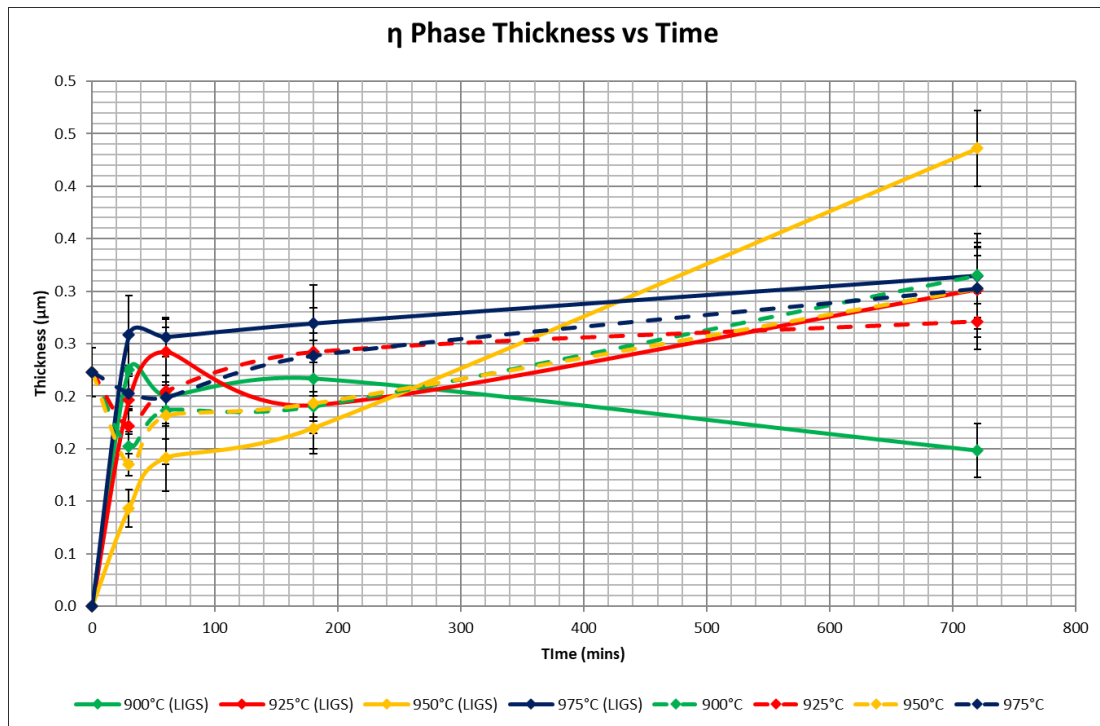


Figure 7.20 -  $\eta$  phase thickness against time for as-received initial grain size material and larger initial grain size material (LIGS)

Figure 7.18, Figure 7.19 and Figure 7.20 show a comparison of the as-received initial grain size microstructure against the larger initial grain size microstructure in terms of  $\eta$  phase precipitate aspect ratio, length, and thickness respectively.

In terms of aspect ratio, the  $\eta$  phase precipitates from the larger initial grain size microstructure appear to have a lower aspect ratio than the  $\eta$  phase precipitates in the as-received initial grain size microstructure. As mentioned previously, the microstructure from the as-received initial grain size microstructure still has approximately 1%  $\eta$  phase area fraction after the heat treatment at 990°C for 180 minutes, whereas the larger initial grain size microstructure was completely solutioned and therefore no  $\eta$  phase precipitates were initially present in the microstructure. Therefore, it is observed that completely solutioning the material appears to provide  $\eta$  phase precipitates with a lower aspect ratio.

From Figure 7.19, it can be generally observed that the  $\eta$  phase precipitate length from the larger initial grain size microstructure is lower than that of the as-received initial

grain size microstructure, although there is not much difference after 720 minutes at 950°C and 975°C. Therefore, this suggests that completely solutioning the material appears to slow the lengthwise growth of the  $\eta$  phase precipitates, which should be investigated further.

The  $\eta$  phase precipitate thickness comparison (Figure 7.20) for both the as-received initial grain size and the larger initial grain size microstructures seems to be scattered and it is difficult to deduce a meaningful correlation from the data. Interestingly, Beaubois et al. (48) had obtained data which indicated that the lateral growth of the  $\delta$  phase precipitates in Inconel 718 is inhibited in solution treated material. However, such a trend is not observed from Figure 7.20 due to the volatile and scattered nature of the data. It is known that the thickness is restricted due to the competition between the  $\eta$  phase precipitates for constituent elements (77) namely aluminium and niobium, which may be a cause for the scattering of the data.

#### 7.4.4 Effect of n and k Parameters

Similar to the analysis shown in Section 6.4.3 in Chapter 6, we can see how the n and k coefficients are affected by time, temperature and strain, and we can then compare this against those from the strain-free  $\eta$  phase precipitation kinetics. Using the same Equation 6.21, we can plot  $\ln \left[ -\ln \left[ 1 - \frac{y}{f_{eq}} \right] \right]$  against time to see how the k and n coefficients behave over time at different temperatures and strains.

Figure 7.21 displays  $\ln \left[ -\ln \left[ 1 - \frac{y}{f_{eq}} \right] \right]$  against time at 950°C and at 0.01 s<sup>-1</sup> strain rate with a larger initial grain size.

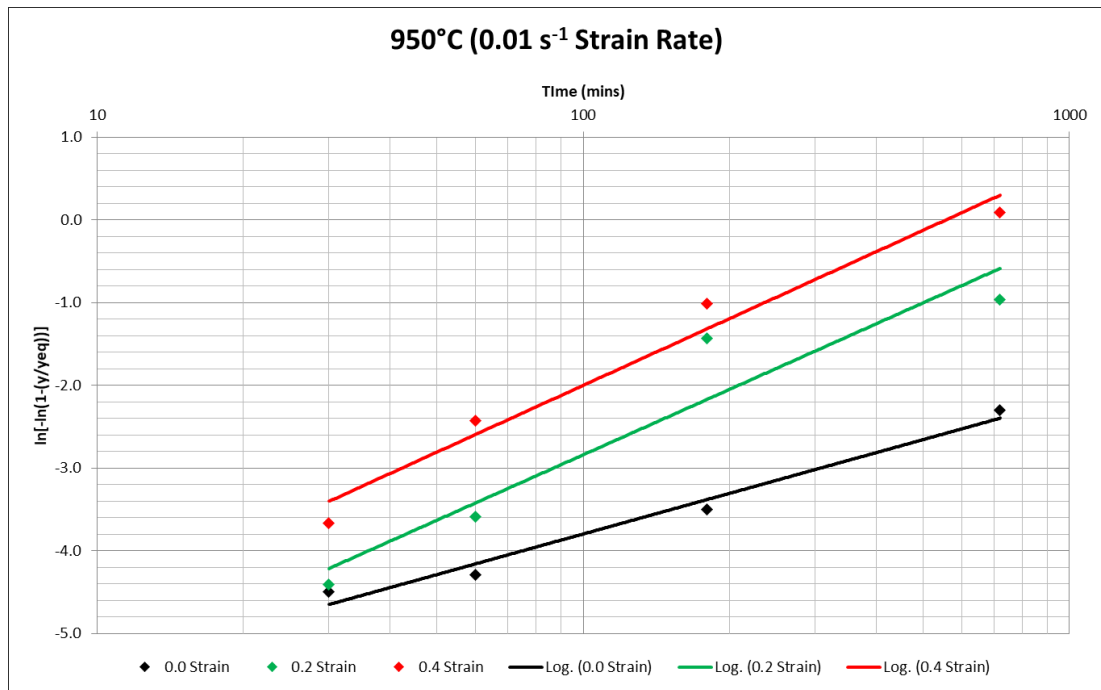
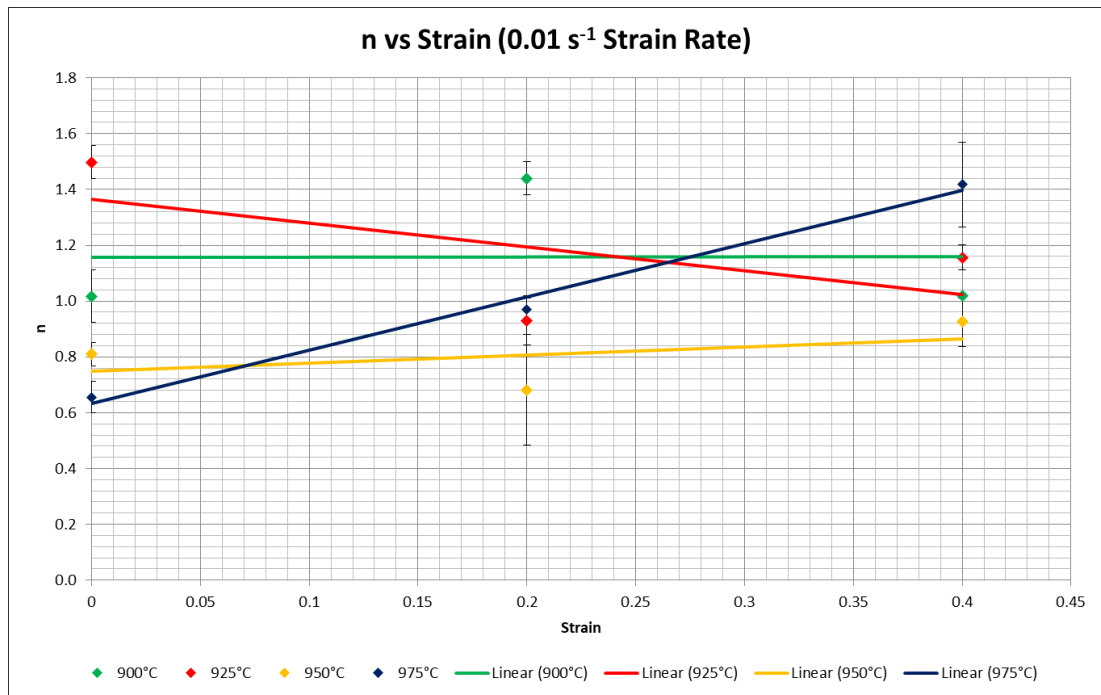


Figure 7.21 –  $\ln\left[-\ln\left[1 - \frac{y}{f_{eq}}\right]\right]$  vs time at 950°C and at 0.01 s<sup>-1</sup> strain rate with larger initial grain size

As is observed from Figure 7.21, the n and k coefficients at 0.2 and 0.4 strain are higher than that at zero strain. Interestingly, the n- and k-values increase as strain increases from zero to 0.4. This is contrast to what was found in Chapter 6 with the material with the smaller initial grain size, where the n- and k-values do not differ much and do not correlate well from any strain above zero. The observation that the n- and k-values increase gradually from zero to 0.4 strain was also found at 900°C, 925°C and 975°C.



*Figure 7.22 – The n-value against strain with  $0.01\text{ s}^{-1}$  strain rate and with larger initial grain size*

The effect of temperature and strain on the n coefficient can also be observed in Figure 7.22 in which the value of n is plotted against strain at a strain rate of  $0.01\text{ s}^{-1}$  with a larger initial grain size. It is observed that at  $900^{\circ}\text{C}$  the value of n stays constant from zero strain to 0.4 strain, while at  $925^{\circ}\text{C}$ , the n-value decreases during the same strain region. At  $950^{\circ}\text{C}$ , the value of n stays somewhat the same and at  $975^{\circ}\text{C}$  the value of n is observed to rise as the strain increases from 0 to 0.4. These trends are very similar to what was observed for the material with the smaller initial grain size.

Using Equation 6.22, the same analysis can be performed as was done in Chapter 6 in which a linear relationship can be derived between the n-value and strain. For the material with the larger initial grain size, the numerical values of  $a_1$ ,  $b_1$  and the adjusted  $R^2$  values are shown in Table 7.9.

Temperature (°C)	$a_1$	$b_1$	Adjusted $R^2$ Value
900	1.01660	$0.43 \pm 0.60$	0.94831
925	1.49799	$-1.25 \pm 0.56$	0.95743
950	0.80963	$0.10 \pm 0.26$	0.97913
975	0.65549	$1.84 \pm 0.09$	0.99847

Table 7.9 – Values of  $a_1$ ,  $b_1$  and adjusted  $R^2$  for material with larger initial grain size

The adjusted  $R^2$  values shown in Table 7.9 show that excellent fittings have been obtained. It is observed that the  $a_1$  value increases from 900°C to 925°C but then drastically reduces from 925°C to 975°C. As mentioned previously, the value of  $a_1$  corresponds to the value of  $n$  in the strain-free recrystallised condition. The results of  $b_1$  are mixed such that there is no correlation between  $b_1$  and temperature. There also does not appear to be any trend between the  $n$ -value and temperature.

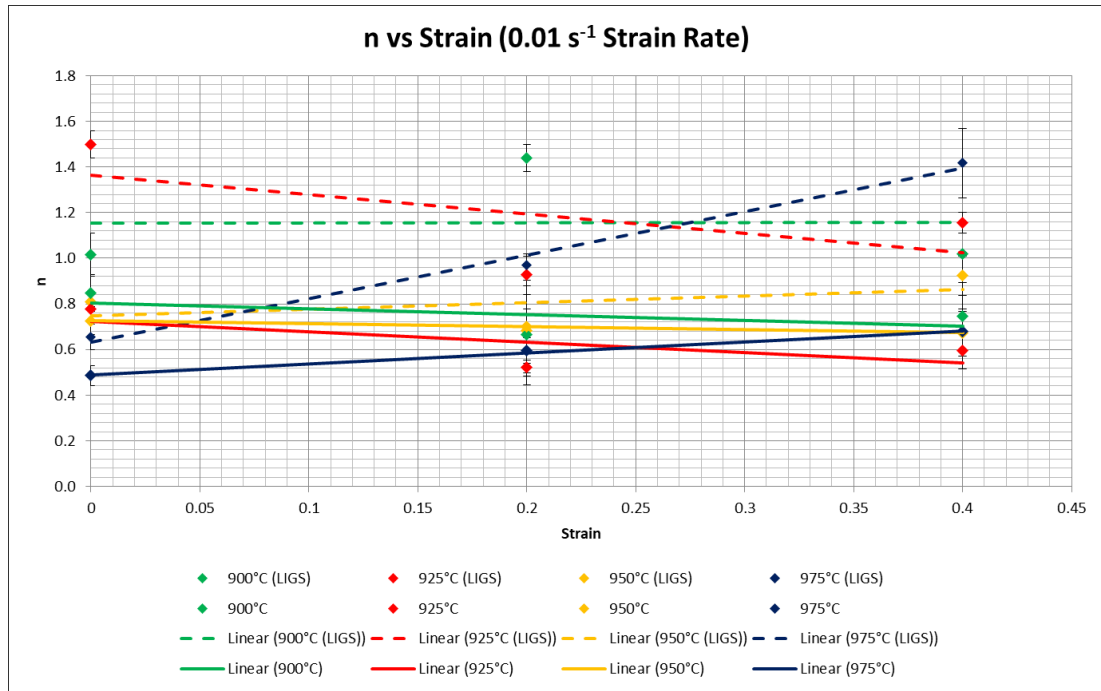


Figure 7.23 –  $n$  against strain for material with larger initial grain size (LIGS) and smaller initial grain size

Figure 7.23 displays a comparison of the  $n$ -value from the material with a smaller initial grain size (Chapter 6) against the material from the larger initial grain size. Interestingly, it can be observed from Figure 7.23 that generally speaking, the  $n$ -values

from the larger initial grain size material are higher than those from the smaller initial grain size material.

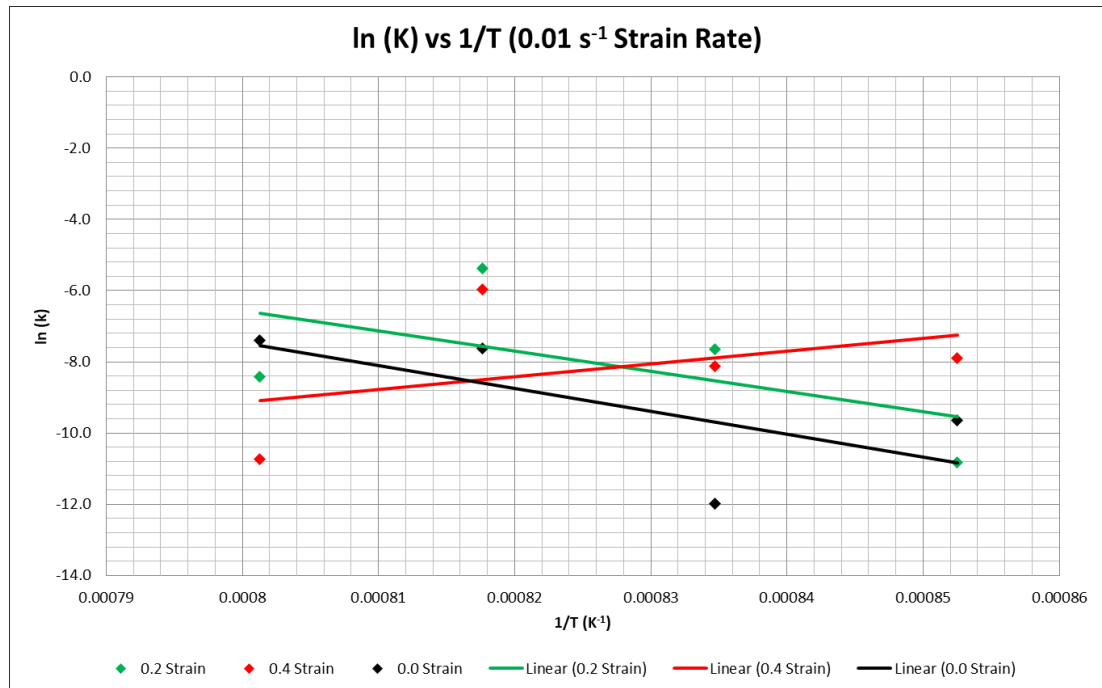


Figure 7.24 – The value of  $\ln(k)$  against  $1/T$  for material with larger initial grain size

The Arrhenius plot for the material with the larger initial grain size is shown in Figure 7.24. It can be observed from Figure 7.24, that for both 0.0 and 0.2 strain, the value of  $k$  increases as the temperature increases, which is the same as what was found in the material used in Chapter 6 with a smaller initial grain size. However, it was interestingly noticed that at 0.4 strain, the value of  $k$  decreases as the temperature increases, which contrasts with the findings at 0.0 and 0.2 strain in this study and the findings in Chapter 6. The reasoning behind this observation is not known and understood at this stage. To further clarify this finding, it would be interesting for future work to obtain values of  $k$  at a wider temperature range. This would allow for more data points to be used to potentially have more confidence in the observed trend. It would also be useful for this analysis to be conducted again to see if similar findings are observed.

It was found from Chapter 6 that the value of  $k$  is sensitive to strain rate, but it would be of interest to see how the initial grain size affects the value of  $k$ .

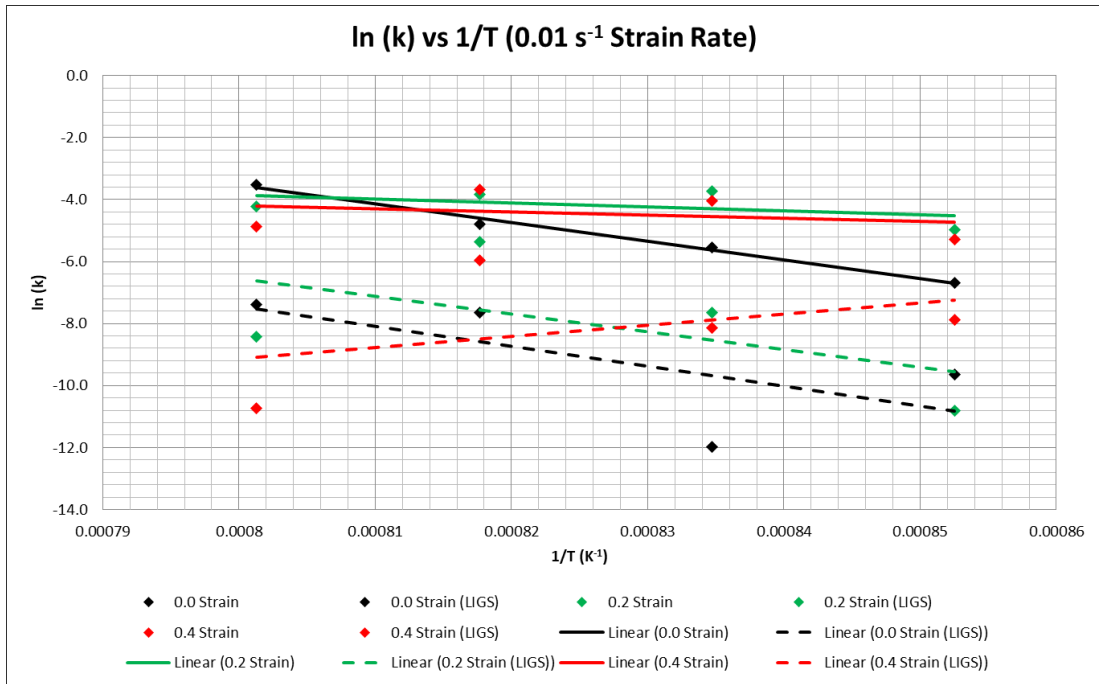


Figure 7.25 –  $\ln(k)$  against  $1/T$  for material with larger initial grain size (LIGS) and smaller initial grain size

Intriguingly, it is observed from Figure 7.25 that the  $k$ -values from the larger initial grain size are lower than the  $k$ -values from the smaller initial grain size, for all strains from 0.0 to 0.4 strain.

By using Equation 6.23 and by performing a similar analysis to that was done in Section 6.4.3, the apparent activation energy of  $\eta$  phase precipitation in the material with the larger initial grain size can be determined. The 0.0 strain data from the larger initial grain size study (0.0 strain line from Figure 7.24) was plotted and fitted in the Origin 2021 software package in order to obtain the gradient. As mentioned previously in Section 6.4.3, the gradient of this line is equal to  $-\frac{E_A}{R}$ . From Origin 2021, the gradient of the 0.0 strain plot from the larger initial grain size material was determined to be -6.43266 therefore:

$$-6.43266 = -\frac{E_A}{R}$$

$$E_A = 8.3145 \times 6.43266$$



$$E_A = 53.48435 \text{ J} = 0.0535 \text{ kJ/mol}$$

$$E_A = 0.0535 \text{ kJ/mol}$$

Following the same methodology, the apparent activation energy can be determined for 0.2 and 0.4 strain at  $0.01 \text{ s}^{-1}$  strain rate for the material with the larger initial grain size.

Strain	Strain Rate ( $\text{s}^{-1}$ )	Apparent Activation Energy (kJ/mol)	Adjusted $R^2$ Value
0.0	N/A	$0.0535 \pm 0.0425$	0.1623
0.2	0.01	$472.93 \pm 496.74$	-0.0322
0.4		$-300.99 \pm 476.98$	-0.25094

*Table 7.10 – Values of  $E_a$  for the larger initial grain size material for each strain at  $0.01 \text{ s}^{-1}$  strain rate with adjusted  $R^2$  values*

As Table 7.10 shows, the apparent activation data obtained at all three strains is incredibly scattered and unreliable, with a very low adjusted  $R^2$  value at 0.0 strain and negative  $R^2$  values at 0.2 and 0.4 strain (which indicates no fitting was obtained). In fact, the data is so poorly fitted to Equation 6.23 that it may be misleading to attempt to compare this to the data obtained for the smaller initial grain size (Table 6.12). The issue here is that the data shown in Figure 7.24 is incredible scattered and does not sufficiently fit Equation 6.23, which then provides inaccurate results when trying to deduce the apparent activation energies. It would be of interest for future work to try to obtain more accurate values of apparent activation energy at the strains, strain rate and initial grain size used in this study.

## 7.5 Summary

In this chapter, the  $\eta$  phase precipitation kinetics was investigated in material that had a larger initial grain size in comparison to the material used in Chapter 5 and Chapter 6. It was clearly observed that the  $\eta$  phase precipitation kinetics in the material with the larger initial grain size was slower than that with the smaller initial grain size. This was observed in microstructures with both 0.2 and 0.4 strain, as well as in microstructure with no strain. Effect of deformation was also investigated in this chapter using the material with the larger initial grain size. TTT diagrams were produced at zero, 0.2 and 0.4 strain with a strain rate of  $0.01 \text{ s}^{-1}$ . It is interesting to observe that the  $\eta$  phase precipitation kinetics became faster as the strain increases from 0 to 0.2 to 0.4. This is in contrast to the material with the smaller initial grain size in Chapter 6, where little difference was observed between 0.2 and 0.4 strain (at both strain rates  $0.1 \text{ s}^{-1}$  and  $0.01 \text{ s}^{-1}$ ). Comparisons were made of the  $\eta$  phase precipitate aspect ratio, length and thickness between the smaller initial grain size material and larger initial grain size material. Also, an attempt was made to see the effect of strain on the  $n$  and  $k$  parameters and activation energies were obtained for  $\eta$  phase precipitation at 0, 0.2 and 0.4 strain. However, the activation energy results were deemed too unreliable.

## **8 Conclusions**

### **8.1 Introduction**

In the present body of work the  $\eta$  phase precipitation kinetics was studied during forging and heat treatment. Hot isothermal compression testing was performed to simulate the effects of forging.  $\eta$  phase precipitation kinetics was studied in the recrystallised strain-free condition as well as in the deformed strained condition. The equilibrium  $\eta$  phase content was studied and the effect of the initial grain size on the  $\eta$  phase precipitation kinetics was investigated.

### **8.2 Equilibrium Study**

#### **8.2.1 Equilibrium Area Fraction**

As part of this study, the equilibrium  $\eta$  phase area fraction was investigated. In order to accelerate the  $\eta$  phase precipitation as much as possible, a number of tensile tests were performed, after which a number of samples were created. Each sample was then heat treated at a particular temperature ranging from 850°C to 975°C. The initial grain size of the tensile test bars was the same as in the as-received material condition. It was observed that the equilibrium  $\eta$  phase area fraction increases from 850°C to reach a peak at 875°C. After this temperature, the equilibrium  $\eta$  phase area fraction decreases gradually from 875°C to 975°C. Due to the acicular nature of many of the  $\eta$  phase precipitates within the microstructures, it was difficult to threshold the microstructural image properly and therefore this is a source of error within the data set for this study.

#### **8.2.2 Aspect Ratio, Length and Thickness**

The aspect ratio of the equilibrium  $\eta$  phase precipitates were observed to fluctuate with increasing and decreasing value as the temperature increases until 925°C (Figure 4.9). Beyond 925°C, the aspect ratio is seen to decrease drastically which indicates that the  $\eta$  phase precipitates at these temperatures are coarser. The

equilibrium  $\eta$  phase length was observed to increase from 850°C to 875°C, beyond which it stays rather constant until 950°C (Figure 4.10). Between 950°C and 975°C, the equilibrium  $\eta$  phase length decreases considerably. The  $\eta$  phase precipitate thickness was observed to stay rather constant from 850°C to 925°C, after which it increases notable from 925°C to 975°C (Figure 4.11).

### **8.3 Recrystallised $\eta$ Phase Precipitation Kinetics**

#### **8.3.1 TTT Diagram**

A TTT diagram displaying the  $\eta$  phase precipitation kinetics in recrystallised strain-free material was produced (Figure 5.13). Samples of as-received ATI 718Plus were heat treated at 990°C for 180 minutes in order to remove the initial  $\eta$  phase precipitates without changing the initial grain size. Approximately 1% area fraction of  $\eta$  phase precipitation was remaining after this heat treatment, therefore the resultant microstructure was not completely “clean” of  $\eta$  phase precipitation. A comparison was made with various TTT diagrams for ATI 718Plus from the existing published literature. The nose of the curve was seen to be between 925°C and 950°C, which is in agreement with the majority of currently published literature.

#### **8.3.2 Aspect Ratio, Length and Thickness**

The  $\eta$  phase precipitate aspect ratio, length and thickness kinetics were also studied. Although the data set in this study is largely scattered, it is generally noted that these characteristics either increase or stay the same as heat treatment time increases. An attempt to compare between intergranular and intragranular precipitates was made. It was found that the thickness of the intragranular precipitates tended to be thinner than those of the intergranular precipitates (Figure 5.34). The intragranular precipitates also were shown to have a larger aspect ratio than those of the intergranular precipitates (Figure 5.32). No correlation between intragranular and intergranular  $\eta$  phase precipitates could be found in terms of length.

## 8.4 Effect of Deformation on $\eta$ Phase Precipitation Kinetics

### 8.4.1 Effect of Strain

High temperature isothermal compression tests were performed on cylindrical samples at 990°C to emulate the industrial forging process for ATI 718Plus at Aubert & Duval. Before the compression tests, the samples were heat treated at 990°C for 180 minutes to remove the initial  $\eta$  phase precipitates in the as-received material condition without increasing the initial grain size too much. Approximately 1% area fraction of  $\eta$  phase precipitates were still present after this heat treatment. During the isothermal compression tests, a global strain of 0.6 was applied, but localised strains of 0, 0.2 and 0.4 within the sample was studied. The strain rates studied were 0.1 s<sup>-1</sup> and 0.01 s<sup>-1</sup>.

It has been clearly shown from the study that deformation markedly impacts the  $\eta$  phase precipitation kinetics for both strain rates studied. From Figure 6.8 and Figure 6.16, the  $\eta$  phase precipitation kinetics in the deformed samples is notable faster in comparison to the  $\eta$  phase kinetics in the recrystallised strain-free material. Interestingly, the  $\eta$  phase kinetics between 0.2 strain and 0.4 strain shows very little difference if at all for both strain rates.

One theory that could be proposed to explain the little variance in  $\eta$  phase precipitation between 0.2 and 0.4 strain is that the maximum possible diffusion of  $\eta$  phase forming elements (namely aluminium and niobium) is reached at 0.2 strain for the data at both 0.1 s<sup>-1</sup> and 0.01 s<sup>-1</sup> strain rates. In other words, the equilibrium state has been reached.

Interestingly at 975°C, no impact on deformation was observed on the  $\eta$  phase precipitation kinetics. This suggests that recrystallisation of the  $\gamma$  matrix has been completed before the onset of  $\eta$  phase precipitation. At 900°C, 925°C and 950°C, a notable increase in  $\eta$  phase precipitation was observed from zero strain to 0.2 and 0.4 strain, which suggests that  $\eta$  phase precipitation occurs before recrystallisation of the  $\gamma$  matrix.

An observation that was made in the study was the sudden drop and rise in  $\eta$  phase area fraction between 0 minutes and 30 minutes. It is unknown at this stage as to the scientific understanding and reasoning as to why this occurs. To verify this finding in future work, a number of samples can be heat treated (at a certain interval) up to 30 minutes after the same deformation process and parameters used in this study. These samples should then be analysed for  $\eta$  phase area fraction in order to assess the trend from 0 to 30 minutes.

#### 8.4.2 Effect of Strain Rate

It was observed from Figure 6.21 that the  $\eta$  phase precipitation kinetics at the higher strain rate of  $0.1 \text{ s}^{-1}$  was faster than the  $\eta$  phase precipitation kinetics at  $0.01 \text{ s}^{-1}$ . A possible explanation could be that a lower strain rate reduces the rate at which dislocations are produced, hence a lower dislocation density would exist in the material being deformed at  $0.01 \text{ s}^{-1}$  in comparison to  $0.1 \text{ s}^{-1}$ . Since dislocations behave as nucleation sites, this would mean that a lower strain rate would provide a lower amount of  $\eta$  phase precipitation.

#### 8.4.3 Effect of n and k Parameters

The effect of deformation on the n-values was observed to be dependent on the temperature. At  $900^\circ\text{C}$  and  $925^\circ\text{C}$ , the n-value was observed to decrease as the strain increases, whereas at  $950^\circ\text{C}$ , the n-value stays somewhat constant. Interestingly, at  $975^\circ\text{C}$ , the n-value is seen to increase as the strain increases. These trends were observed for both  $0.1 \text{ s}^{-1}$  and  $0.01 \text{ s}^{-1}$  strain rates.

To study the effect of deformation on the k-values, Arrhenius plots of  $\ln(k)$  against  $1/T$  were plotted (Figure 6.26 and Figure 6.27). It was observed for both strain rates ( $0.1 \text{ s}^{-1}$  and  $0.01 \text{ s}^{-1}$ ) and strains (0.2 and 0.4) that the value of  $\ln(k)$  decreases as the value of  $1/T$  decreases. Interestingly, the reverse is observed for the data at zero strain. For zero strain, the value of  $\ln(k)$  increases as the value of  $1/T$  decreases.

An attempt was made to determine whether a correlation exists between strain, strain rate and apparent activation energy. It was found that the apparent activation energy decreases as the strain rate increases. It was also seen that the apparent activation energy decreases as the strain increases from 0 to 0.4. However, the adjusted  $R^2$  values at  $0.01 \text{ s}^{-1}$  strain rate are really poor which shows the unreliability and low confidence of the data.

## **8.5 Effect of Initial Grain Size on $\eta$ Phase Precipitation Kinetics**

### **8.5.1 Effect of Strain**

The effect of strain was also studied in the samples with the larger initial grain size. The samples of as-received ATI 718Plus were heat treated at  $1010^\circ\text{C}$  for 180 minutes in order to completely re-solution the existing  $\eta$  phase precipitates and increase the grain size. As expected, the strain has the impact of considerably increasing the  $\eta$  phase precipitation kinetics in comparison to that at zero strain, similar to that observed in Chapter 6 with the as-received initial grain size.

However, an interesting difference is that in the study with the larger initial grain size, the  $\eta$  phase precipitation kinetics becomes faster as the strain increases from 0.2 to 0.4 strain (Figure 7.6). In the study with the as-received initial grain size, the  $\eta$  phase precipitation kinetics at 0.2 and 0.4 strain are almost the same if not have very little differences. It has been suggested that fully re-solutioning the material will allow for the  $\eta$  phase area fraction to increase with increasing strain, but if  $\eta$  phase precipitates are already existing within the microstructure, then the  $\eta$  phase area fraction will be limited at any strain above zero. The reasoning for this theory is unclear at this stage, and further in-depth investigations are required to explore this suggestion.

### **8.5.2 Effect of Initial Grain Size**

It was shown very clearly that increasing the initial grain size of the austenitic  $\gamma$  matrix considerably slows down the  $\eta$  phase precipitation kinetics in comparison to that of

the as-received initial grain size. This can be observed in the TTT diagram shown in Figure 7.17. The reasoning for this finding is that as the grain size increases, there are less grain boundaries present which means that there are less grain boundaries for  $\eta$  phase precipitation to occur from.

### 8.5.3 Aspect Ratio, Length and Thickness

It was observed that the  $\eta$  phase precipitates from the larger initial grain size microstructure appear to have a lower aspect ratio than that from the as-received initial grain size microstructure. It appears that completely solutioning the material and then heat treating subsequently provides  $\eta$  phase precipitates with a lower aspect ratio.

It was also observed that the  $\eta$  phase precipitate length from the larger initial grain size microstructure was lower than that from the as-received initial grain size microstructure. As with the aspect ratio, it shows that fully solutioning the microstructure and then heat treating slows down the longitudinal growth of the  $\eta$  phase precipitates.

In terms of  $\eta$  phase thickness, the data was found to be highly scattered and thus it was not possible to find any meaningful correlation. This could be due to the competition between  $\eta$  phase precipitates for constituent elements for further growth.

### 8.5.4 Effect of n and k Parameters

Like the material with the as-received initial grain size, the effect of deformation on the n-values was observed to be dependent on the temperature. At 900°C, the n-value is seen to stay constant as the strain increases. At 925°C, the n-value was observed to decrease as the strain increases, whereas at 950°C, the n-value stays somewhat constant. Interestingly, at 975°C, the n-value is seen to increase as the strain increases. It was found that generally speaking, the n-values from the material with the larger initial grain size were higher than those from the as-received initial grain size.



It was observed that the value of  $\ln(k)$  increases as the value of  $1/T$  decreases at 0 and 0.2 strain. Surprisingly, the value of  $\ln(k)$  was actually observed to decrease as  $1/T$  decreases for 0.4 strain. This finding is unexplainable at this stage and further work will be required to investigate this. Also, the values of  $\ln(k)$  were noticeably lower for the material with the larger initial grain in comparison than those from the as-received initial grain size.

An attempt was made to obtain the apparent activation energy for  $\eta$  phase precipitation at each strain. Unfortunately, the  $R^2$  values were not good enough for the data to be relied upon and hence no confident correlations could be made.

## **8.6 Future Work**

For future studies, it would be of interest to investigate a number of phenomena which were observed during this project that could not be explained by the author. The first of which is the sudden drop and subsequent increase in  $\eta$  phase area fraction between 0 minutes to 30 minutes. This was especially noticed for  $\eta$  phase area fraction kinetics at  $975^\circ\text{C}$  for both 0.2 and 0.4 strains with  $0.1\text{ s}^{-1}$  and  $0.01\text{ s}^{-1}$  and was also noticed at all temperatures for  $\eta$  phase kinetics for the strain-free recrystallised material (Figure 5.4).

Another result that could be explored for future work is the negative activation energy that was found in Chapter 6. The apparent activation energies at  $0.1\text{ s}^{-1}$  were found to be negative whereas the activation energies at  $0.01\text{ s}^{-1}$  was positive. It was not expected to obtain a negative activation energy in this study because negative activation energies are against the hypothesis of Arrhenius. However, these results could be explored further in future works. Also, the adjusted  $R^2$  values for some of the activation energies obtained in this study were very poor, and perhaps further work can be done to improve on the reliability of these results.

Importantly, it would be significantly interesting to implement these findings on an industrial scale level. This could be achieved via the use of representative large-scale modelling and the implementation of these results in the model.

## References

1. Jeniski R. ATI Jet Engine Applications [Internet]. 2008. Available from: <http://www.slideshare.net/johnpsilk/ati-jet-engine>
2. Kennedy RL. ALLVAC® 718PLUS™, SUPERALLOY FOR THE NEXT FORTY YEARS. In: Loria EA, editor. Superalloys 718, 625, 706 and Derivatives [Internet]. The Minerals, Metals & Materials Society; 2005. p. 1–14. Available from: [http://www.tms.org/Superalloys/10.7449/2005/Superalloys\\_2005\\_1\\_14.pdf](http://www.tms.org/Superalloys/10.7449/2005/Superalloys_2005_1_14.pdf)
3. Uzgur S, Uzunonut Y, Diltemiz F, Kushan MC, Gunay R. STATE-OF-ART TECHNOLOGY ALLVAC 718 Plus SUPERALLOY FOR GAS TURBINE ENGINE PARTS. Adv Mater Res [Internet]. 2011 Feb [cited 2013 May 21];213:131–5. Available from: <http://www.scientific.net/AMR.213.131>
4. Kushan MC, Uzgur SC, Uzunonut Y, Diltemiz F. ALLVAC 718 Plus™ Superalloy for Aircraft Engine Applications. In: Agarwal RK, editor. Recent Advances in Aircraft Technology. 2012. p. 75–96.
5. Donachie MJ, Donachie SJ. Superalloys: A Technical Guide. ASM International; 2002.
6. Reed RC. The Superalloys: Fundamentals and Applications. Cambridge: Cambridge University Press; 2006.
7. ATI. ATI 718Plus® Alloy Specifications [Internet]. 2008. Available from: <https://www.atimetals.com/products/718plus-alloy/Pages/Specifications.aspx>
8. Zhang J, Wu C, Peng Y, Xia X, Li J, Ding J, et al. Hot compression deformation behavior and processing maps of ATI 718Plus superalloy. J Alloys Compd [Internet]. 2020;835:1–12. Available from: <https://doi.org/10.1016/j.jallcom.2020.155195>
9. Jeniski R, Kennedy R. ATI 718Plus® Alloy Background [Internet]. Available from: <https://www.atimetals.com/products/718plus-alloy/background/Pages/default.aspx>
10. Weber JH. Nickel Alloys: Thermal Treatment and Thermomechanical Processing. In: Encyclopedia of Materials: Science and Technology. 2011. p. 6142–4.

11. Jena AK, Chaturvedi MC. The role of alloying elements in the design of nickel-base superalloys. *J Mater Sci.* 1984;19(10):3121–39.
12. Antonov S, Detroids M, Helmink RC, Tin S. Precipitate phase stability and compositional dependence on alloying additions in  $\gamma$ - $\gamma'$ - $\delta$ - $\eta$  Ni-base superalloys. *J Alloys Compd* [Internet]. 2015 Mar [cited 2015 Jan 29];626:76–86. Available from: <http://linkinghub.elsevier.com/retrieve/pii/S092583881402814X>
13. Campbell FC, editor. *Elements of Metallurgy and Engineering Alloys*. ASM International; 2008.
14. Dieter GE. *Mechanical Metallurgy*. SI Metric. Singapore: McGraw-Hill Book Company (UK) Limited; 1988. 751 p.
15. Ogin S. Lecture 11: Strengthening Mechanisms. 2012.
16. Smallman RE, Ngan AHW. *Physical Metallurgy and Advanced Materials*. 2007. 650 p.
17. Barjesteh MM, Abbasi SM, Zangeneh Madar K, Shirvani K. The effect of heat treatment on characteristics of the gamma prime phase and hardness of the nickel-based superalloy Rene ® 80. *Mater Chem Phys* [Internet]. 2019;227(January):46–55. Available from: <https://doi.org/10.1016/j.matchemphys.2019.01.038>
18. Argon AS. *Strengthening Mechanisms in Crystal Plasticity*. Oxford: Oxford University Press; 2008. 404 p.
19. Mouritz AP. Materials and material requirements for aerospace structures and engines. In: *Introduction to Aerospace Materials*. Cambridge; 2012. p. 39–56.
20. FESSLER H. *Design of Machine Elements*. 2nd Editio. Engineering Design. New Delhi; 1966. 203–207 p.
21. Thompson AW, Backofen WA. THE EFFECT OF GRAIN SIZE ON FATIGUE. *Acta Metall.* 1971;19(7):597–606.
22. Cao W-D. SOLIDIFICATION AND SOLID STATE PHASE TRANSFORMATION OF ALLVAC® 718PLUS™ ALLOY. In: Loria EA, editor. *Superalloys 718, 625, 706 and Derivatives* [Internet]. The Minerals, Metals & Materials Society; 2005. p. 165–77. Available from: [http://www.tms.org/Superalloys/10.7449/2005/Superalloys\\_2005\\_165\\_177.pd](http://www.tms.org/Superalloys/10.7449/2005/Superalloys_2005_165_177.pd)

f

23. Cao W-D, Kennedy R. ROLE OF CHEMISTRY IN 718-TYPE ALLOYS - ALLVAC® 718PLUS™ ALLOY DEVELOPMENT. In: Green KA, Pollock TM, Harada H, Howson TE, Reed RC, Schirra JJ, et al., editors. Superalloys 2004. 2004. p. 91–9.
24. Xie X, Wang G, Dong J, Xu C, Cao W-D, Kennedy R. STRUCTURE STABILITY STUDY ON A NEWLY DEVELOPED NICKEL-BASE SUPERALLOY - ALLVAC® 718PLUS™. In: Loria EA, editor. Superalloys 718, 625, 706 and Derivatives [Internet]. The Minerals, Metals & Materials Society; 2005. p. 179–91. Available from: [http://www.tms.org/Superalloys/10.7449/2005/Superalloys\\_2005\\_179\\_191.pdf](http://www.tms.org/Superalloys/10.7449/2005/Superalloys_2005_179_191.pdf)
25. Zickler GA, Schnitzer R, Radis R, Hochfellner R, Schweins R, Stockinger M, et al. Microstructure and mechanical properties of the superalloy ATI Allvac® 718Plus™. Mater Sci Eng A [Internet]. 2009 Oct [cited 2013 May 22];523(1–2):295–303. Available from: <http://linkinghub.elsevier.com/retrieve/pii/S0921509309006534>
26. Ahmadi MR, Povoden-Karadeniz E, Whitmore L, Stockinger M, Falahati a., Kozeschnik E. Yield strength prediction in Ni-base alloy 718Plus based on thermo-kinetic precipitation simulation. Mater Sci Eng A [Internet]. 2014 Jul [cited 2014 Aug 19];608:114–22. Available from: <http://linkinghub.elsevier.com/retrieve/pii/S0921509314005176>
27. Ahmadi MR, Whitmore L, Povoden-Karadeniz E, Stockinger M, Falahati A, Kozeschnik E. Simulation of Yield Strength in Allvac® 718Plus™. Adv Mater Res [Internet]. 2014 May [cited 2014 Jun 5];922:7–12. Available from: <http://www.scientific.net/AMR.922.7>
28. Krakow R, Hardy MC, Rae CMF, Midgley PA. High resolution orientation mapping of secondary phases in ATI 718Plus® alloy. Guédou JY, Choné J, editors. 2nd Eur Symp Superalloys their Appl [Internet]. 2014 Aug 29 [cited 2014 Nov 5];14:5. Available from: <http://www.matec-conferences.org/10.1051/matecconf/20141411002>
29. Whitmore L, Ahmadi MR, Stockinger M, Povoden-Karadeniz E, Kozeschnik

- E, Leitner H. Microstructural investigation of thermally aged nickel-based superalloy 718Plus. *Mater Sci Eng A* [Internet]. 2014 Jan [cited 2014 Jun 5];594:253–9. Available from: <http://linkinghub.elsevier.com/retrieve/pii/S0921509313012653>
30. Pickering EJ, Mathur H, Bhowmik A, Messé OMDM, Barnard JS, Hardy MC, et al. Grain-boundary precipitation in Allvac 718Plus. *Acta Mater* [Internet]. 2012 Apr [cited 2013 May 21];60(6–7):2757–69. Available from: <http://linkinghub.elsevier.com/retrieve/pii/S1359645412000808>
  31. Eurich NC, Bristowe PD. Thermodynamic stability and electronic structure of  $\eta$ -Ni<sub>6</sub>Nb(Al,Ti) from first principles. *Scr Mater* [Internet]. 2014 Apr [cited 2014 Jun 5];77:37–40. Available from: <http://linkinghub.elsevier.com/retrieve/pii/S1359646214000165>
  32. Whitmore L, Leitner H, Povoden-Karadeniz E, Radis R, Stockinger M. Transmission electron microscopy of single and double aged 718Plus superalloy. *Mater Sci Eng A* [Internet]. 2012 Feb [cited 2013 May 30];534:413–23. Available from: <http://linkinghub.elsevier.com/retrieve/pii/S0921509311013281>
  33. Radis R, Zickler GA, Stockinger M, Sommitsch C, Kozeschnik E. NUMERICAL SIMULATION OF THE SIMULTANEOUS PRECIPITATION OF  $\delta$  AND  $\gamma'$  PHASES IN THE NI-BASE SUPERALLOY ATI ALLVAC®718 PLUS™. In: Ott EA, Groh JR, Banik A, Dempster I, Gabb TP, Helmink R, et al., editors. 7th International Symposium on Superalloy 718 and Derivatives. The Minerals, Metals & Materials Society; 2010. p. 569–78.
  34. Viskari L, Stiller K. Atom probe tomography of Ni-base superalloys Allvac 718Plus and Alloy 718. *Ultramicroscopy* [Internet]. 2011 May [cited 2014 Jul 7];111(6):652–8. Available from: <http://www.ncbi.nlm.nih.gov/pubmed/21295914>
  35. Whitmore L, Ahmadi MR, Guetaz L, Leitner H, Povoden-Karadeniz E, Stockinger M, et al. The microstructure of heat-treated nickel-based superalloy 718Plus. *Mater Sci Eng A* [Internet]. 2014 Jul [cited 2014 Jun 3];610:39–45. Available from: <http://linkinghub.elsevier.com/retrieve/pii/S0921509314006236>

36. Radis R, Zickler GA, Stockinger M, Sommitsch C, Kozeschnik E. INTERACTION OF THE PRECIPITATION KINETICS OF  $\delta$  AND  $\gamma'$  PHASES IN NICKEL-BASE SUPERALLOY ATI ALLVAC® 718PLUS™. Mater Sci Forum. 2010;638–642:2712–7.
37. Ennis PJ. Nickel-base alloys for advanced power plant components. In: Shibli A, editor. Coal Power Plant Materials and Life Assessment: Developments and Applications [Internet]. Cambridge: Woodhead Publishing; 2014 [cited 2014 Nov 5]. p. 147–67. Available from: <http://dx.doi.org/10.1533/9780857097323.1.147>
38. Laurence A, Cormier J, Villechaise P, Billot T, Petinari-sturmel F, Hantcherli M, et al. IMPACT OF THE SOLUTION COOLING RATE AND OF THERMAL AGING ON THE CREEP PROPERTIES OF THE NEW CAST & WROUGHT RENÉ 65 Ni-BASED SUPERALLOY. In: 8th International Symposium on Superalloy 718 and Derivatives. 2014. p. 333–48.
39. Devaux A, Helstroffer A, Cormier J, Villechaise P, Douin J, Hantcherli M, et al. Effect of Aging Heat-Treatment on Mechanical Properties of AD730™ Superalloy. In: 8th International Symposium on Superalloy 718 and Derivatives [Internet]. 2014. p. 521–35. Available from: <http://doi.wiley.com/10.1002/9781119016854.ch41>
40. Kennedy R, McDevitt E. Metallurgy of ATI 718Plus Alloy. Advanced Materials & Processes. 2008;32–3.
41. Devaux A, Naze L, Molins R, Pineau A, Organista A, Guedou JY, et al. Gamma double prime precipitation kinetic in Alloy 718. Mater Sci Eng A. 2008;486(1–2):117–22.
42. Bhadeshia HKDH. Nickel Based Superalloys [Internet]. 2003. Available from: [www.msm.cam.ac.uk/phase-trans/2003/Superalloys/superalloys.html](http://www.msm.cam.ac.uk/phase-trans/2003/Superalloys/superalloys.html)
43. Ott EA, Groh J, Sizek H. Metals Affordability Initiative: Application of Allvac Alloy 718Plus® for Aircraft Engine Static Structural Components. In: Loria EA, editor. Superalloys 718, 625, 706 and Derivatives [Internet]. The Minerals, Metals & Materials Society; 2005. p. 35–45. Available from: [http://www.tms.org/Superalloys/10.7449/2005/Superalloys\\_2005\\_35\\_45.pdf](http://www.tms.org/Superalloys/10.7449/2005/Superalloys_2005_35_45.pdf)
44. Azadian S, Wei L-Y, Warren R. Delta phase precipitation in Inconel 718. Mater

- Charact [Internet]. 2004 Sep [cited 2014 Nov 17];53(1):7–16. Available from: <http://linkinghub.elsevier.com/retrieve/pii/S1044580304001603>
45. Zhang HY, Zhang SH, Cheng M, Li ZX. Deformation characteristics of  $\delta$  phase in the delta-processed Inconel 718 alloy [Internet]. Vol. 61, Materials Characterization. 2010. p. 49–53. Available from: <http://dx.doi.org/10.1016/j.matchar.2009.10.003>
  46. Huang Y, Langdon TG. The evolution of delta-phase in a superplastic Inconel 718 alloy. *J Mater Sci*. 2007;42(May 2006):421–7.
  47. Dehmas M, Lacaze J, Niang A, Viguier B. TEM Study of High-Temperature Precipitation of Delta Phase in Inconel 718 Alloy. *Adv Mater Sci Eng* [Internet]. 2011 [cited 2013 Aug 13];2011:1–9. Available from: <http://www.hindawi.com/journals/amse/2011/940634/>
  48. Beaubois V, Huez J, Coste S, Brucelle O, Lacaze J. Short term precipitation kinetics of delta phase in strain free Inconel\* 718 alloy. *Mater Sci Technol* [Internet]. 2004 Aug 1 [cited 2013 Sep 27];20(8):1019–26. Available from: <http://openurl.ingenta.com/content/xref?genre=article&issn=0267-0836&volume=20&issue=8&spage=1019>
  49. Radavich JF, Coutts Jr WH. FACTORS AFFECTING DELTA PHASE PRECIPITATION AND GROWTH AT HOT WORK TEMPERATURES FOR DIRECT AGED INCO 718. In: *Superalloys 1984*. 1984. p. 497–507.
  50. Cai D, Zhang W, Nie P, Liu W, Yao M. Dissolution kinetics of  $\delta$  phase and its influence on the notch sensitivity of Inconel 718. *Mater Charact* [Internet]. 2007 Mar [cited 2014 Jul 27];58(3):220–5. Available from: <http://linkinghub.elsevier.com/retrieve/pii/S1044580306001215>
  51. Valle LCM, Araújo LS, Gabriel SB, Dille J, De Almeida LH. The Effect of  $\delta$  Phase on the Mechanical Properties of an Inconel 718 Superalloy. Vol. 22, *Journal of Materials Engineering and Performance*. 2013. p. 1512–8.
  52. Zhang S-H, Zhang H-Y, Cheng M. Tensile deformation and fracture characteristics of delta-processed Inconel 718 alloy at elevated temperature. *Mater Sci Eng A* [Internet]. 2011;528(19–20):6253–8. Available from: <http://www.sciencedirect.com/science/article/pii/S092150931100517X%5Cnh>  
<http://www.sciencedirect.com/science/article/pii/S092150931100517X/pdf?md>



5=ad73a28740958483b905141bc013234b&pid=1-s2.0-S092150931100517X-main.pdf

53. Unocic KA, Hayes RW, Mills MJ, Daehn GS. Microstructural Features Leading to Enhanced Resistance to Grain Boundary Creep Cracking in ALLVAC 718Plus. *Metall Mater Trans A*. 2010;41(2):409–20.
54. Kuo CM, Yang YT, Bor HY, Wei CN, Tai CC. Aging effects on the microstructure and creep behavior of Inconel 718 superalloy. *Mater Sci Eng A*. 2009;510–511:289–94.
55. Agnoli A, Bernacki M, Logé R, Franchet J-M, Laigo J, Bozzolo N. UNDERSTANDING AND MODELING OF GRAIN BOUNDARY PINNING IN INCONEL 718. In: *Superalloys 2012*. The Minerals, Metals & Materials Society; 2012.
56. Radavich JF, Carneiro T. A Microstructural Study of Alloy 718 Plus™. In: Loria EA, editor. *Superalloys 718, 625, 706 and Derivatives*. The Minerals, Metals & Materials Society; 2005. p. 329–40.
57. Stotter C, Sommitsch C, Wagner J, Leitner H, Letofsky-Papst I, Zickler GA, et al. Characterization of  $\delta$ -phase in superalloy Allvac 718Plus™. *Int J Mater Res*. 2008;2008(4):376–80.
58. Andersson J, Sjöberg GP, Viskari L, Chaturvedi M. Effect of different solution heat treatments on hot ductility of superalloys Part 2 - Allvac 718Plus. *Mater Sci Technol* [Internet]. 2012 Jun 1 [cited 2013 Jul 9];28(6):733–41. Available from: <http://openurl.ingenta.com/content/xref?genre=article&issn=0267-0836&volume=28&issue=6&spage=733>
59. Vishwakarma KR, Richards NL, Chaturvedi MC. HAZ MICROFISSURING IN EB WELDED ALLVAC 718 PLUS™ ALLOY. In: Loria EA, editor. *Superalloys 718, 625, 706 and Derivatives*. The Minerals, Metals & Materials Society; 2005. p. 637–48.
60. Scheriber K, Loehnert K, Singer RF. Opportunities and Challenges for the New Nickel Base Alloy 718Plus™.
61. Andersson J, Hatami S, Sjöberg G. Notch Sensitivity and Intergranular Crack Growth in the Allvac 718Plus Superalloy. In: *18th ISABE Conference*. Beijing; 2007.

62. Viskari L, Cao Y, Norell M, Sjöberg G, Stiller K. Grain boundary microstructure and fatigue crack growth in Allvac 718Plus superalloy. *Mater Sci Eng A* [Internet]. 2011;528(6):2570–80. Available from: <http://dx.doi.org/10.1016/j.msea.2010.11.080>
63. Xie X, Xu C, Wang G, Dong J, Cao W-D, Kennedy R. TTT DIAGRAM OF A NEWLY DEVELOPED NICKEL-BASE SUPERALLOY - ALLVAC® 718PLUS™. In: Loria EA, editor. *Superalloys 718, 625, 706 and Derivatives*. The Minerals, Metals & Materials Society; 2005. p. 193–202.
64. Wang M, Du J, Deng Q, Tian Z, Zhu J. Effect of the precipitation of the  $\eta$ -Ni<sub>3</sub>Al<sub>0.5</sub>Nb<sub>0.5</sub> phase on the microstructure and mechanical properties of ATI 718Plus. Vol. 701, *Journal of Alloys and Compounds*. 2017. p. 635–44.
65. Tang L, Zhang H, Guo Q, Liu C, Li C, Liu Y. The precipitation of  $\eta$  phase during the solution treatments of Allvac 718Plus. Vol. 176, *Materials Characterization*. 2021.
66. Alabbad B, Tin S. Effect of grain boundary misorientation on  $\eta$  phase precipitation in Ni-base superalloy 718Plus. Vol. 151, *Materials Characterization*. 2019. p. 53–63.
67. Porter DA, Easterling KE. *Phase Transformations in Metals and Alloys*. 2nd Editio. London: Chapman & Hill; 1992. 440 p.
68. Zyka J, Hlous J, Podhorna B, Dobrovska J, Hrbacek K. HEAT TREATMENT AND PROPERTIES OF NICKEL SUPERALLOY 718PLUS. In: *METAL 2010*. 2010.
69. Chamanfar A, Sarrat L, Jahazi M, Asadi M, Weck A, Koul a. K. Microstructural characteristics of forged and heat treated Inconel-718 disks. *Mater Des* [Internet]. 2013;52:791–800. Available from: <http://dx.doi.org/10.1016/j.matdes.2013.06.004>
70. Liu WC, Chen ZL, Yao M. Effect of Cold Rolling on the Precipitation Behavior of  $\delta$  Phase in INCONEL 718. *Metall Mater Trans A* [Internet]. 1999;30A(January):31–40. Available from: <http://link.springer.com/article/10.1007/s11661-999-0193-7>
71. Mei Y, Liu Y, Liu C, Li C, Yu L, Guo Q, et al. Effects of cold rolling on the precipitation kinetics and the morphology evolution of intermediate phases in

- Inconel 718 alloy. *J Alloys Compd* [Internet]. 2015;649:949–60. Available from: <http://linkinghub.elsevier.com/retrieve/pii/S0925838815305466>
72. Wang Y, Shao WZ, Zhen L, Zhang BY. Hot deformation behavior of delta-processed superalloy 718. *Mater Sci Eng A* [Internet]. 2011 Mar [cited 2014 Aug 15];528(7–8):3218–27. Available from: <http://linkinghub.elsevier.com/retrieve/pii/S0921509311000219>
  73. Wei X, Zheng W, Song Z, Lei T, Yong Q, Xie Q. Strain-induced Precipitation Behavior of  $\delta$  phase in Inconel 718 Alloy. *J Iron Steel Res Int*. 2014;21(3):375–81.
  74. McDevitt E. EFFECT OF TEMPERATURE AND STRAIN DURING FORGING ON SUBSEQUENT DELTA PHASE PRECIPITATION DURING SOLUTION ANNEALING IN ATI 718PLUS® ALLOY. 7th Int Symp Superalloy 718 Deriv. 2010;307–19.
  75. Covarrubias O. Microstructural and Mechanical Effects of Thermo-Mechanical Processing on ATI 718Plus® Contoured Rings. *Adv Mater Res* [Internet]. 2011 Jul [cited 2014 Sep 2];278:271–6. Available from: <http://www.scientific.net/AMR.278.271>
  76. Casanova A, Martín-Piris N, Hardy M, Rae C. Evolution of secondary phases in alloy ATI 718Plus® during processing. In: 2nd European Symposium on Superalloys and their Applications [Internet]. 2014 [cited 2014 Nov 3]. p. 6. Available from: <http://www.matec-conferences.org/10.1051/matecconf/20141409003>
  77. Casanova A, Hardy M, Rae CMF. MORPHOLOGY AND KINETICS OF GRAIN BOUNDARY PRECIPITATION IN ALLOY ATI 718PLUS®. In: 8th International Symposium on Superalloy 718 and Derivatives. 2014. p. 573–86.
  78. Eiselstein H. Metallurgy of a columbium-hardened nickel-chromium-iron alloy. *Adv Technol Stainl Steels Relat Alloy*. 1965;
  79. Boesch WJ, Canada HB. Precipitation Reactions and Stability of Ni<sub>3</sub>Cb in Inconel Alloy 718. In: International Symposium on Structural Stability in Superalloys (1968). 1968. p. 579–96.
  80. Kirman I, Warrington DH. The precipitation of Ni<sub>3</sub>Nb phases in a Ni-Fe-Cr-Nb alloy. *Metall Trans*. 1970;1(10):2667–75.

81. Decker R, Sims C. Metallurgy of Nickel-Base Alloys. In: Superalloys 1972 (Second International Symposium). 1972. p. 33–77.
82. Sundararaman M, Mukhopadhyay P, Banerjee S. Precipitation of the  $\delta$ -Ni<sub>3</sub>Nb phase in two nickel base superalloys. Metall Trans A. 1988;19(3):453–65.
83. Burger JL, Biederman RR, Coutts WH. THE EFFECTS OF STARTING CONDITION ON THE AGING RESPONSE OF AS-FORGED ALLOY 718. In: Superalloy 718 Metallurgy and Applications (1989). 1989. p. 207–17.
84. Oradei-Basile A, Radavich JF. A CURRENT T-T-T DIAGRAM FOR WROUGHT ALLOY 718. In: Superalloys 718, 625 and Various Derivatives (1991) [Internet]. 1991. p. 325–35. Available from: [http://www.tms.org/Superalloys/10.7449/1991/Superalloys\\_1991\\_325\\_335.pdf](http://www.tms.org/Superalloys/10.7449/1991/Superalloys_1991_325_335.pdf)
85. Sommitsch C, Stotter C, Leitner H, Mitsche S, Letofsky-Papst I, Stockinger M.  $\delta$ -PHASE CHARACTERIZATION OF SUPERALLOY ALLVAC 718PLUS™. In: Volume 2: Materials Characterization, Computation and Modelling. The Minerals, Metals & Materials Society; 2008. p. 63–8.
86. Zickler GA, Radis R, Schnitzer R, Kozeschnik E, Stockinger M, Leitner H. The Precipitation Behavior of Superalloy ATI Allvac 718Plus. Adv Eng Mater [Internet]. 2010 Apr 1 [cited 2013 May 21];12(3):176–83. Available from: <http://doi.wiley.com/10.1002/adem.200900282>
87. Agnoli A, Bernacki M, Logg R, Franchet JM, Laigo J, Bozzolo N. Selective Growth of Low Stored Energy Grains During  $\delta$  Sub-solvus Annealing in the Inconel 718 Nickel-Based Superalloy. Metall Mater Trans A Phys Metall Mater Sci. 2015;46(9):4405–21.
88. Messé OM, Barnard JS, Pickering EJ, Midgley PA, Rae CMF. On the precipitation of delta phase in ALLVAC® 718Plus. Philos Mag [Internet]. 2014 Mar 5 [cited 2014 Jun 5];94(10):1132–52. Available from: <http://www.tandfonline.com/doi/abs/10.1080/14786435.2013.878052>
89. Sjoberg G, Ingesten N-G, Carlson RG. Grain Boundary  $\delta$ -phase Morphologies, Carbides and Notch Rupture Sensitivity of Cast Alloy 718. In: Superalloys 718, 625 and Various Derivatives (1991) [Internet]. 1991. p. 603–20. Available from:

[http://www.tms.org/Superalloys/10.7449/1991/Superalloys\\_1991\\_603\\_620.pdf](http://www.tms.org/Superalloys/10.7449/1991/Superalloys_1991_603_620.pdf)

90. Koul AK, Au P, Bellinger N, Thamburaj R, Wallace W, Immarigeon J-P. DEVELOPMENT OF A DAMAGE TOLERANT MICROSTRUCTURE FOR INCONEL 718 TURBINE DISC MATERIAL. In: Superalloys 1988 (Sixth International Symposium). 1988. p. 3–12.
91. Hayes R, Thompson E, Johnson K, Aichlmayr A. Effect of heat treatment on the combination stress-rupture properties of allvac 718plus™. Mater Sci Eng A. 2009;510–511:256–61.
92. Yeh A-C, Lu K-W, Kuo C-M, Bor H-Y, Wei C-N. EFFECT OF SERRATED GRAIN BOUNDARIES ON THE CREEP PROPERTY OF INCONEL 718 SUPERALLOY. In: Superalloy 718 and Derivatives (2010). 2010. p. 825–35.
93. Ghosh S, Yadav S, Das G. Study of standard heat treatment on mechanical properties of Inconel 718 using ball indentation technique. Mater Lett. 2008;62(17–18):2619–22.
94. Sims CT, Stoloff NS, Hagel WC. Superalloys II: High-Temperature Materials for Aerospace and Industrial Power. New York; 1987. 640 p.
95. Cheng YL, Atkinson H, Strang A. Effects of High Temperature Exposure on the Microstructure and Properties of ATI 718Plus®. HKIE Trans [Internet]. 2011;18(3):1–4. Available from: <http://www.scopus.com/inward/record.url?eid=2-s2.0-80355126574&partnerID=40&md5=b011bca25a41d31c647630c191e1e297>
96. Singh RP, Hyzak JM, Howson TE, Biederman RR. Recrystallization Behavior of Cold Rolled Alloy 718. In 1991. p. 205–15.
97. Gabb TP, Telesman J, Garg A, Lin P, Provenzano V, Heard R, et al. Grain boundary engineering the mechanical properties of allvac 718Plus™ superalloy. In: 7th International Symposium on Superalloy 718 and Derivatives 2010. 2010. p. 255–69.
98. Sommitsch C, Huber D, Ingelman-Sundberg F, Mitsche S, Stockinger M, Buchmayr B. Recrystallization and grain growth in the nickel-based superalloy Allvac 718Plus. Int J Mater Res. 2009;2009(8):1088–98.